

**Synthesis of Aggregation Induced Emission Enhancement  
based Low Dimensional Organic Materials and their  
Potential Use as Sensor**

By  
**Prativa Mazumdar**

**A THESIS SUBMITTED TO  
VIDYASAGAR UNIVERSITY  
FOR THE AWARD OF THE DEGREE OF  
DOCTOR OF PHILOSOPHY  
(SCIENCE)**

*Department of Chemistry & Chemical Technology  
Vidyasagar University  
Paschim Medinipur, West Bengal  
PIN-721102*

**2016**



# *Dedicated*

*To my  
Mom and Dad,  
I could never have done  
this without your faith, support and constant  
encouragement. Thank you for teaching me  
to believe in myself, in  
God and in my  
dreams.*

**Prof. Ajay Misra**  
**Dept. of Chemistry & Chemical Tech.**  
**Vidyasagar University**  
**Midnapore (w) - 721102**  
[ajaymsr@yahoo.co.in](mailto:ajaymsr@yahoo.co.in)

---



## CERTIFICATE

This is to certify that the research work presented in this thesis entitled, “*Synthesis of Aggregation Induced Emission Enhancement based Low Dimensional Organic materials and their potential use as Sensor*” was carried out under my supervision in Department of Chemistry & Chemical Technology, Vidyasagar University, Midnapore and is the bonafied record of work done by **Ms. Prativa Mazumdar**. This work is original and has not been submitted for any other degree or diploma of this or any other University.

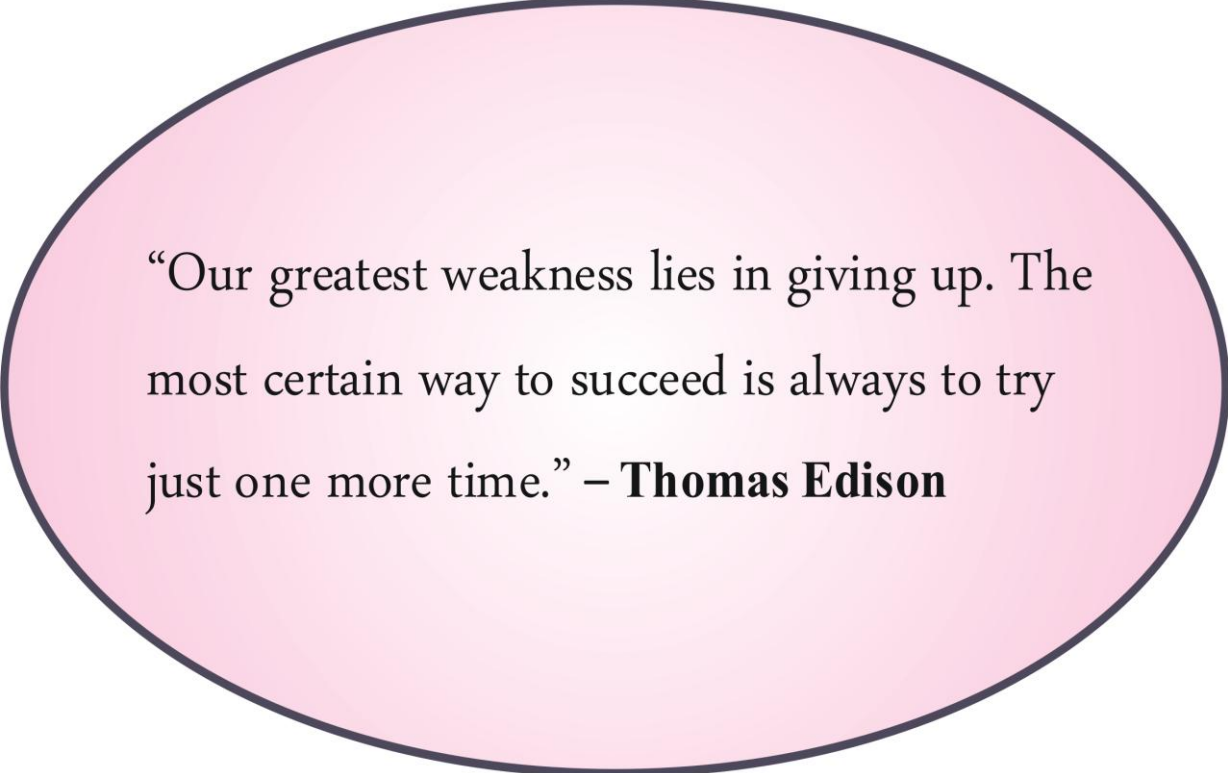
Date:

(Prof. Ajay Kumar Misra)  
Research Guide

---

**Department of Chemistry and Chemical Technology, Vidyasagar University,  
Midnapore-721102, INDIA**

Phone: +91-3222-276554/276555/276557/276558 Extn. 437, Fax: +91-3222-275329



“Our greatest weakness lies in giving up. The most certain way to succeed is always to try just one more time.” – **Thomas Edison**

## DECLARATION

*The research work embodied in this thesis entitled “Synthesis of Aggregation Induced Emission Enhancement based Low Dimensional Organic materials and their potential use as Sensor” has been carried out by me under the supervision of Prof. Ajay Kumar Misra in Department of Chemistry & Chemical Technology, Vidyasagar University, Midnapure. This work is original and no part of the work has been submitted at this University or anywhere by me or any other person in part or full for any degree.*

*Date:*

*(Prativa Mazumdar)*

# Acknowledgement

This thesis represents not only my work at the keyboard; it is a milestone of work in the Department of Chemistry and Chemical Technology, Vidyasagar University. My experience at here has been nothing short of amazing. I have been given unique opportunities and taken advantage of them. So this thesis is also the result of many experiences I have encountered from dozens of remarkable individuals who I wish to acknowledge. First and foremost I take this opportunity to convey my deep sense of gratitude and regards to my supervisor, **Prof. Ajay Kumar Misra**, for introducing me to such an interesting and advanced field of research. He has been supportive since the days I began working. His invaluable guidance, advice, technical discussion and clarification kept me inspired throughout the rough road to finish this thesis. During this long journey even in many difficult times also, he gave me the moral support and the freedom I needed to move on. It was a valuable experience to work with and learn so many things from him both as a scientist and as a human being. It has been a great honour to work with him.

I express my deep sense of gratitude to Hon'ble Vice chancellor, Prof. Ranjan Chakrabarti and Registrar, Dr. Jayanta Kishore Nandi for providing various facilities.

I convey my deep regards to Prof. Sayed Sirajul Islam, Prof. Braja Gopal Bag, Prof. Amiya Kumar Panda, Dr. Sudipta Dalai, Dr. Sumita Roy, Dr. Subal Chandra Manna and Dr. Moidul Hossain for their moral support, affection and encouragement throughout my research career.

I would like to thank my lab mates Dr. Harekrishna Bar, Dr. Dipak Kumar Bhui, Dr. Gobinda Prasad Sahoo, Dr. Sankar Prasad De, Dr. Sankarlal Ash, Dr. Hasibul Beg, Mr. Sadhan Samanta, Mr. Ashim Maity, Mr. Debasish Das, Mr. Debkumar Mondal, Mr. Samir Maity, Mr. Milan Shyamal and Mr. Rakesh Maity for their generous assistance in each moment.

I am also thankful to Mr. Bibhas Panda, Mr. Subrata Hazra, Mr. Ranjit Majhi in our department and Mrs. Anindita Maiti, Mr. Dipankar Mandal in USIC for their cooperation.

I greatly acknowledge to the Central Research Facility (CRF), IIT Kharagpur, India for XRD study, Prof. Sanjib Ghose, Presidency University, Kolkata, India, Prof. Nilmony Sarkar, Department of Chemistry, IIT Khargapur, India for lifetime study, Prof. Dipankar Chattopadhyay, Nano centre, Calcutta University, Kolkata, India for FE-SEM study and USIC, Vidyasagar University, Midnapur, India for UV-VIS, Fluorescence, Optical Microscopic study. I also greatly acknowledge to the Departmental facility of our University for SEM study.

I am thankful to Council of Scientific and Industrial Research (CSIR), Department of Science and technology (DST), University Grand Commission (UGC), New Delhi and Government of India, for financial assistance.

Last but never the least I feel a deep sense of gratitude for my loving father, Sri Nirmalendu Mazumdar, and my sweet mother, Smt. Banasree Mazumdar, who were always proud of me. They have been the source of love and energy ever since. I dedicated my thesis to my parents. Without their constant support and inspiration it would have been impossible for me to be where I am at present.

Date:

Place: Midnapur, India

*(Prativa Mazumdar)*

# Abbreviations

ACQ	Aggregation caused quenching
AFM	Atomic Force Microscope
AIDS	Acquired immuno deficiency syndrome
AIE	Aggregation induced emission
AIEE	Aggregation induced emission enhancement
AILEE	Aggregation induced locally excited emission
BA	Bathophenanthroline
BDBA	5,5'-bidibenzo-7-annulenyldiene
BODIPY	Ttriphenylamine–boradiazaindacene
BPQ	6,7-dimethyl-2,3-bis-(2-pyridyl)-quinoxaline
BQN	2,2'-biquinoline
BSE	Back scattered electron
BZP	4,4'-Bis(diethylamino)benzophenone
CA	Cyanuric acid
CH	Cyclohexane
CHEQ	Chelation induced fluorescence quenching
ChS	Chondroitin sulfates
CIBE	Crystal induced blue emission
CIE	Crystal induced emission
CIF	Crystal Information File
CIL	Carbamate ionic liquid
CIP	Crystal induced phosphorescence
CMC	Critical Micelle Concentration
CN-TFMBE	1-Cyano-trans-1,2-bis(3,5-bistrifluoromethyl-biphenyl)ethylene
COT	dibenzo-Cyclooctatetraene
CP3E	1-(4-pyridinyl)-1-phenyl-2-(9-carbazolyl) ethane
CSA	Camphorsulfonic acid
CTAB	Cetyl trimethyl ammonium bromide
CT	Charge Transfer
CuAAC	Copper alkyne-azide coupling
D-A	Donor- Acceptor
DBM	Dibenzoylmethane
DCM	Dichloromethane
DD	Dual descriptor
DFT	Density Function Theory
DMF	N,N-Dimethyl formamide
DNA	Deoxy ribonucleic acid
DNBS-CSA	2-(2,4-dinitrobenzenesulfonyl)-5-chlorosalicylaldehydeazine
DOL	Degree of leveling
DP	Diphenyl-2-pyrazoline
DPA	Dipropylamine
EDOT	3,4-ethylenedioxythiophene



E-DPN	Electrochemical Dip-Pen Nanolithography
ESIPT	Excited state intramolecular proton transfer
FESEM	Field emission scanning electron microscope
FETs	Field-effect transistors
FOM	Fluorescent organic material
GO	Graphene oxide
HA	Hyaluronic acid
Hcy	Homocysteine
HF	Hartee Fock
HLB	Hydrophilic-lypophilic balance
HOMO	Highest occupied molecular orbital
HPS	Hexaphenylsilole
ICT	Intramolecular charge transfer
ILCT	Intraligand charge transfer
ISC	Intra system crossing
JAF	J-aggregate formation
LASER	Light amplification by stimulated emission of radiation
LE	Locally excited
LED	Light emitting diode
LFPs	Latent fingerprints
LMOG	Low molecular mass organogelators
LRD	Local reactivity descriptors
LUMO	Lowest unoccupied molecular orbital
M	Melamine
MC	Methyl cellulose
MM	Molecular Mechanics
MO	Molecular orbital
MOF	Metal organic framework
MPA	Mercapto propionic acid
MRI	Magnetic resonance imaging
MWCNT	Multi walled carbon nanotubes
Na-AOT	Sodium di-(ethyl hexyl sulfosuccinate)
NaBH <sub>4</sub>	Sodium borohydride
NLO	Nonlinear optical properties
NTA	Nitrile triacetic
OFET	Organic field-effect transistor
OLED	Organic light emitting diodes
OPV	Organic photovoltaic
OTS	Octadecyltrichlorosilane
PAMAM	Poly(amidoamine)
PEG	Poly ethylene glycol
PL	Photoluminescence
PLM	Polarizing Microscopes
PMT	Photomultiplier tube
ppb	parts-per-billion
ppm	parts-per-million

PTZ-BZP	10-hexyl-3,7-bis(7-phenylbenzo[1,2,5]thiadiazol-4-yl)-10H-phenothiazine
PVA	Poly vinyl alcohol
PVD	Physical vapour deposition
PVP	Poly vinyl pyrrolidine
QM	Quantum Mechanics
RIM	Restricted Intramolecular motion
RIR	Restricted Intramolecular rotation
RIV	Restricted Intramolecular vibration
RNA	Ribonucleic acid
SDS	Sodium dodecyl sulphate
SE	Secondary electron
SEM	Scanning electron microscope
TAA	Thio acetamide
TAP	2,4,6-triaminophenol
TCNQ	7,7',8,8'-tetracyanoquinodimethane
TCSPC	Time correlated single photon counting
TDDFT	Time dependent density functional theory
THBA	10,10',11,11'-tetrahydro-5,5'-bidibenz-7-annulenyldiene
THF	Tetra Hydro Furan
TICT	Twisted intramolecular charge transfer
TNP	2,4,6-trinitrophenol
TNT	2,4,6-Trinitrotoluene
TPE	Tetra phenyl ethane
TPFI	Two photon fluorescence imaging
TSC	Tri-sodium citrate
TTF	Tetrathiafulvalene
UFP	Ultrafine particles
UV	Ultra violet
UV-VIS-NIR	Ultraviolet-Visible-Near Infrared
XC	Exchange-correlation
XRD	X-ray diffraction

# An Overview of Thesis

This thesis entitle “*Synthesis of Aggregation Induced Emission Enhancement based Low Dimensional Organic materials and their potential use as Sensor*” contains the work carried out in the Department of Chemistry and Chemical Technology, Midnapore, Paschim Medinipur, Pin-721102, India under the supervision of Prof. Ajay Kumar Misra. This thesis comprises eight chapters.

## Chapter I:

Luminogenic materials with aggregation-induced emission enhancement (AIEE) attributes have attracted much interest since the debut of the AIEE concept in 2001. In this chapter, recent progress in the area of AIEE research is summarized. Typical examples of AIEE systems are discussed, from which their structure–property relationships are derived. Through mechanistic decipherment of the photophysical processes, structural design strategies for generating new AIEE luminogens are developed. Technological, especially optoelectronic and biological applications of the AIEE systems are exemplified to illustrate how the novel AIEE effect can be utilized for high-tech innovations.

## Chapter II:

This chapter describes various synthetic methods of low dimensional organic particles that have been developed over the few years. Different stabilization processes are also described in this chapter.

## Chapter III:

This chapter briefly discuss the characterization techniques of the synthesize low dimensional materials using scanning electron microscopy (SEM), Optical, polarising and fluorescence microscopy analysis, X-ray diffraction (XRD) spectroscopy, Single crystal X-

ray diffraction, UV-Vis spectroscopy, Fluorescence spectroscopy, Time correlated single photon counting spectroscopy (TCSPC).

#### Chapter IV:

This chapter consists of the theory of computational background *i.e.* Schrödinger Equation, Born-Oppenheimer approximation, Molecular Mechanics, Electronic Structure Methods, Semi-empirical Quantum Chemistry Methods, Hartree-Fock Methods, Density Functional theory, Time dependent Density functional theory, basis sets and Fukui Parameter etc.

#### Chapter V:

This chapter presents that Bathophenanthroline (BA) microstructures of various morphologies have been synthesized using reprecipitation method. Morphologies of the particles are characterized using optical and scanning electron microscopic (SEM) study. Aqueous dispersion of BA microstructures show aggregation induced emission enhancement (AIEE) compare to BA in good solvent, THF. This luminescent property of aggregated BA hydrosol is used for selective detection of trace amount of mercury ion ( $\text{Hg}^{2+}$ ) in water. It is observed that  $\text{Hg}^{2+}$  ions can quench Photoluminescence (PL) intensity of BA aggregates even at very low concentration compare to other heavy metal ions *e.g.* Nickel ( $\text{Ni}^{2+}$ ), Manganese ( $\text{Mn}^{2+}$ ), Cadmium ( $\text{Cd}^{2+}$ ), Cobalt ( $\text{Co}^{2+}$ ), Copper ( $\text{Cu}^{2+}$ ), Ferrous ( $\text{Fe}^{2+}$ ), Zinc ( $\text{Zn}^{2+}$ ). This strong fluorescence quenching of aggregated BA in presence of  $\text{Hg}^{2+}$  ions has been explained as complex interplay between ground state complexation between BA and  $\text{Hg}^{2+}$  ions and external heavy atom induced perturbation by  $\text{Hg}^{2+}$  ion on the excited states of fluorophore BA.

## Chapter VI:

Optical emission from a luminogen in solid state is generally red shifted with respect to its solution phase emission. But in this chapter we report exceptionally large blue shifted enhanced emission from aggregated hydrosol of 4,4'-bis(diethylamino)benzophenone (BZP) compare to its solution phase emission in any good solvent. This exceptional blue emission from aggregated structure of BZP arises from its locally excited states with the concomitant suppression of twisted intramolecular charge transfer (TICT) motion. This is known as aggregation induced locally excited (AILE) state emission. A broad red shifted emission is also observed in case of larger aggregated structure of BZP and it originates from the excited intramolecular charge transfer (ICT) state of planar BZP. Morphology of the aggregated BZP is also studied by scanning electron and optical microscopic study. This AILE emission of the luminogen is used for sensing glucose in aqueous solution at very low concentration. The quenching of AILE in presence of glucose has been explained due to hydrogen bonded complexation between glucose and BZP molecule present at the surface of the aggregated structure and is responsible for crystal softening *i.e.* loosening of crystal packing.

## Chapter VII:

This chapter describes a heteroatom containing organic fluorophore 6,7-dimethyl-2,3-bis-(2-pyridyl)-quinoxaline (BPQ) is weakly emissive in solution but its emission property is highly enhanced in the aggregated state due to restriction of intramolecular rotation (RIR) and large amplitude vibrational modes, demonstrating the phenomena, aggregation induced emission enhancement (AIEE). It has strong proton capture capability, allowing reversible fluorescence switching in basic and acidic medium and the emission color changes from blue to green in aggregated state through protonation. It has been explained as competition between intramolecular charge transfers (ICT) and the AIEE phenomena at lower pH range (pH~1-4). Such behavior enables it as a fluorescent pH sensor for detecting acidic and basic

medium. Morphologies of the particles are characterized using optical and scanning electron microscopic (SEM) study. The turn off fluorescence property of aggregated BPQ has been utilized for selective detection of picric acid and the fluorescence quenching is explained due to ground state complexation with strong quenching constant,  $7.81 \times 10^4 \text{ M}^{-1}$ .

### Chapter VIII:

This chapter presents a novel material showing aggregation induced enhanced emission (AIEE) is developed by reprecipitation method using 2,2' biquinoline (BQN) in aqueous medium. Morphologies of the particles are characterized using optical and scanning electron microscopic (SEM) study. The selective fluorescence and absorbance response of aggregated BQN towards  $\text{Zn}^{2+}$  and  $\text{H}^+$  have been explained due to ground state complexation and protonation of BQN with  $\text{Zn}^{2+}$  and  $\text{H}^+$  respectively. Protonated BQN exhibits charge transfer character in transoid form with yellowish green emission but in BQN- $\text{Zn}^{2+}$  complex, BQN changes to cis planer conformation and displays considerable intra ligand charge transfer (ILCT) character with sky blue color under UV excitation. A 2:1 BQN- $\text{Zn}^{2+}$  complex have been confirmed using Job's plot. Our study revealed that BQN hydrosol act as selective turn-on fluorescence sensor for  $\text{Zn}^{2+}$  ion both in acidic and alkaline medium. Further, the proton induced charge transfer character and the proposed binding modes of the receptor with  $\text{Zn}^{2+}$  have been supported by DFT based computational study.

# Table of Contents

Content	Pages
<b>Chapter 1</b>	<b>1-43</b>
<b>Introduction</b>	
1.1. Low dimensional materials	2
1.2. Bulk materials and Low dimensional materials	3
1.3. Classification of Low dimensional particles	5
1.3.1. Nanoparticles	5
1.3.2. Microparticles	6
1.4. AIEE based low dimensional materials	7
1.5. Mechanism of AIEE phenomena	9
1.5.1. Restriction of intramolecular rotation (RIR)	9
1.5.2. Restriction of intramolecular vibration (RIV)	11
1.5.3. Restriction of intramolecular motion (RIM)	12
1.6. AIEEgen Systems	13
1.6.1. Hydrocarbon AIEEgens	13
1.6.2. Hetero atom containing AIEEgens	14
1.6.3. Macromolecular AIEEgens	18
1.6.4. Metal Complex AIEEgens	21
1.6.5. Unorthodox AIEEgens	22
1.7. AIEE and TICT	23
1.8. Technological Application	25
1.8.1. Biological Probes	25
1.8.2. Chemical Sensing	28
1.8.3. Optoelectronic Systems	32
1.8.4. Stimuli Responses	36
References	40
<b>Chapter 2</b>	<b>44-63</b>
<b>Synthesis of Low Dimensional Organic Particles: A General Overview</b>	
2.1. Introduction	45
2.2. Top-Down method	46
2.2.1. Electro spinning Method	46
2.2.2. LASER ablation approach	47
2.2.3. Direct Condensation Method	48
2.2.4. Molecular beam deposition Method	49
2.2.5. Physical vapour deposition Method	49
2.3. Bottom-Up method	49
2.3.1. Reprecipitation Method	52
2.3.2. Chemical reduction Method	54
2.3.3. Microemulsion Method	54

2.3.4. Hydrothermal or Solvothermal Method	55
2.3.5. Sonochemical Method	56
2.3.6. Sol-gel Method	56
2.3.7. Post Chemistry Method	57
2.3.8. Direct writing Method	57
2.3.9. Microwave Method	58
2.4. Stabilization of Microparticles	58
2.4.1. Soft Template Method	59
2.4.2. Hard Template Method	59
References	61

## **Chapter 3 Characterization Techniques 64-88**

3.1. UV-vis Spectroscopy	65
3.2. Fluorescence Spectroscopy	67
3.3. Time-resolved Fluorescence Measurements	71
3.3.1. Time correlated single photon counting : Picosecond setup	71
3.3.2. Deconvolution procedure	72
3.4. Spectroscopic Study of molecular assemblies	73
3.4.1. H- vs. J-aggregates	74
3.4.2. $\pi$ -stack vs. herringbone	75
3.5. Scanning Electron microscope (SEM)	75
3.6. Optical, Polarizing and Fluorescence microscopy analysis	77
3.6.1. Optical microscopy study	79
3.6.2. Polarizing microscopy study	79
3.6.3. Fluorescence microscopy study	80
3.7. X-ray diffraction (XRD)	81
3.8. Single-crystal X-ray diffraction	83
References	88

## **Chapter 4 Computational Study 89-110**

4.1. Introduction	90
4.2. Schrödinger Equation	91
4.2.1. Time Dependent Equation	93
4.2.2. Time Independent Equation	94
4.3. Born-Oppenheimer approximation	95
4.4. Molecular Mechanics	96
4.5. Electronic Structure Methods	97
4.6. Semi-empirical Quantum Chemistry Methods	97
4.7. Ab initio Quantum Chemistry Methods	98
4.8. Hartree-Fock Methods	99
4.9. Density Function Theory (DFT)	100
4.9.1. Time Dependent Density Functional	101



	Theory (TDDFT)	
	4.9.2. Success of Density Functional Theory	102
4.10. Basis sets		103
	4.10.1. Minimal basis sets	104
	4.10.2. Split-valence basis sets	105
	4.10.3. Pople basis sets	105
4.11. Fukui Parameter		106
4.12. Computable Properties		108
4.13. Conclusion		109
References		110
<b>Chapter 5</b>	<b>Aggregation Induced Emission Enhancement from Bathophenanthroline Micro Structures and Its Potential use as Sensor of Mercury ions in Water</b>	<b>111-129</b>
5.1. Introduction		112
5.2. Experimental		113
	5.2.1. Materials	113
	5.2.2. Luminogen Preparation	113
	5.2.3. Characterization	114
	5.2.4. Computational Method	114
5.3. Result and Discussion		115
	5.3.1. SEM Study	115
	5.3.2. Optical Microscopic Study	116
	5.3.3. XRD Study	116
	5.3.4. UV-vis Study	117
	5.3.5. Emission Study	118
	5.3.6. Time Resolved Fluorescence Study	121
	5.3.7. Mechanism of AIEE effect	122
5.4. Mercury Sensor		125
5.5. Conclusion		127
References		129
<b>Chapter 6</b>	<b>Aggregation induced emission enhancement of 4,4' bis(diethylamino) benzophenone with an exceptionally large blue shift and its potential use as glucose sensor</b>	<b>130-152</b>
6.1. Introduction		131
6.2. Experimental		133
	6.2.1. Materials	133
	6.2.2. Fluorogen Preparation	133

6.2.3. Characterization	133
6.2.4. Computational Method	134
6.3. Result and Discussion	134
6.3.1. UV-vis Study	134
6.3.2. Emission Study	137
6.3.3. Time Resolved Fluorescence Study	141
6.3.4. Mechanistic Discussion	143
6.3.5. SEM and Optical Microscopic Study	147
6.4. Glucose Sensor	149
6.5. Conclusion	150
References	152

**Chapter 7 Proton triggered emission and selective sensing of picric acid by the fluorescent aggregates of 6,7-dimethyl-2,3-bis-(2-pyridyl)-quinoxaline 153-179**

7.1. Introduction	154
7.2. Experimental	156
7.2.1. Materials	156
7.2.2. Preparation of aggregates	157
7.2.3. Characterization	157
7.2.4. Computational Method	158
7.3. Result and Discussion	158
7.3.1. UV-vis Absorption Properties	158
7.3.2. Photoluminescence study	161
7.3.3. SEM Study	163
7.3.4. Optical Microscopic Study	164
7.3.5. Crystallographic Study	165
7.3.6. pH dependent photophysical Properties	167
7.3.7. Time resolved Fluorescence study	170
7.3.8. Mechanism of proton triggered tuning AIEE and ICT effect	172
7.4. Picric acid Sensor	175
7.5. Conclusion	177
References	179

**Chapter 8 Proton induced green emission from AIEE active 2,2' biquinoline hydrosol and its selective fluorescence turn-on sensing property towards Zn<sup>2+</sup> ion in Water 180-202**

8.1. Introduction	181
-------------------	-----

8.2. Experimental	183
8.2.1. Materials	183
8.2.2. Preparation of aggregates	183
8.2.3. pH dependent experiment	184
8.2.4. Characterization	184
8.2.5. Computational Method	185
8.3. Result and Discussion	185
8.3.1. Absorption Study	185
8.3.2. Aggregation induced emission enhancement effect	186
8.3.3. SEM and Optical Microscopic study	189
8.4. Proton and Zinc (II) sensor	190
8.4.1. Proton induced photophysical properties	190
8.4.2. Fluorogenic Zinc (II) Sensing	192
8.4.3. Time resolved emission study	197
8.4.4. Density Functional Theory based Computational Study	198
8.5. Conclusion	201
References	202

## List of Publications

203-204

*CHAPTER*

**1**

**Introduction**

## 1.1. Low dimensional materials:

Low dimensional materials are those that possess at least one physical boundary small enough to confine the electrons. This quantum confinement reduces the dimensionality of the material and imparts unique and novel properties that are not seen in their bulk form. They belong to the intermediate states that fill the gap between bulk materials and single molecules. These very small objects measure, less than 100 nanometers and up to some tens of micrometers. Those of interest in this thesis are made of molecules that exhibit particular photophysical or photochemical properties. Thousand years back, the people of 9<sup>th</sup> century in Mesopotamia first introduce the application of nanoparticles without knowing its science. The artisans prepared a colorful paint by mixing copper and silver salt in vinegar, ochre and clay on the surface of pottery and heated to have colorful metallic glitter that was nothing but metallic nanoparticles. During Middle Ages and Renaissance artists and craftsmen used nanomaterials gold and copper by luster technique. Recently several researchers have revealed size-tunable optoelectronic properties of organic nanoparticles and their high potential for novel electronic devices. In the case of organic compounds, their electronic and optical properties are fundamentally different from those of semi conductors and metals due to their weak intermolecular interactions and the small radius of the Frenkel exciton. Through scientific advancement the hidden science and logic revealed in tiny particles and a new branch of science opened as material science of low dimensional materials.

The ultrafine particles (UFP) named as nanoparticles or microparticles considering the scaling parameter. The word ‘nano’ derived from Greek word ‘dwarf’ which means the things of one billionth ( $10^{-9}$ ) of a meter in dimension. Since Prof. Richard Feynman presented (1959) his famous lecture entitled “There’s plenty of rooms at the rooms”, the focus of research shifted from molecule or bulk materials to their low dimensional state. The material or structures of inorganic or organic materials having either dimension one nano meter to thousands micrometer are generally called low dimensional materials. The physiochemical properties of many conventional bulk materials changes to their low dimensional due to greater surface area per volume than the bulk substances.

### **1.2. Bulk materials and Low dimensional materials:**

When some materials are reduced to low dimension they have different and unique properties from their bulk counterpart. The optical and electronic properties of bulk counterpart alter chemical reactivity’s may increase or decreased by transforming into low dimensional materials. Low dimensional materials have large fraction of surface atoms, high surface energy, spatial confinement, reduced imperfections, which do not exist in bulk counterpart. A molecule at the surface of a bulk material is different from a molecule of the same element inside the bulk. Moreover, a molecule at the smooth surface of a single crystal is different from a molecule at the surface of a small cluster of the same element. There are basically two types of size-dependent effects [1, 2], smoothly scalable ones which are related to the fraction of atoms at the surface and quantum effects which show discontinuous behaviour due to completion of shells in systems with delocalised electrons. The surface of a sphere scales with the square of its radius  $r$ , but its volume scales with  $r^3$ .

The total number of atoms ‘N’ in this sphere scales linearly with volume. The fraction of atoms at the surface is called dispersion ‘F’, and it scales with surface area divided by

volume, *i.e.* with the inverse radius or diameter, and thus also with  $N^{-1/3}$ . Basically the same relation holds for long cylinders of radius  $r$  and for thin plates of thickness  $d$ . For cubes of  $n$  atoms along an edge and a total of  $N = n^3$  atoms, where the number of atoms at the surface is  $6n$  corrected for double counts at the 12 edges and for reinstalling the 8 corners. For large  $N$  the edge and corner corrections become negligible, leading to the  $N^{-1/3}$  scaling:

$$F = \frac{6n^2 - 12n + 8}{n^3} = \frac{6}{N^{1/3}} \left( 1 - \frac{2}{N^{1/3}} + \frac{8}{6N^{2/3}} \right) \approx \frac{6}{N^{1/3}}$$

All particles which depend on the dispersion of particles lead to a straight line when plotted against  $N^{-1/3}$  (Fig 1.1).

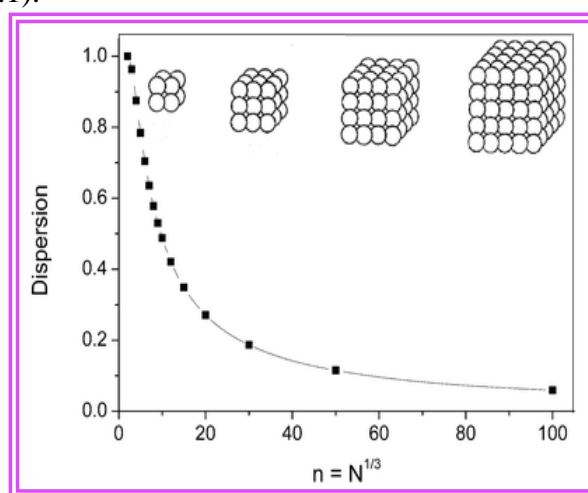


**Figure 1.1: Evolution of the dispersion (F) as a function of  $n$  for cubic clusters up to  $n = 100$  ( $N = 106$ ). Reproduce with permission from Ref. [1] copyright © Royal Society of Chemistry.**

Due to small dimension of low dimensional materials and large surface to volume ratio, makes large fraction of molecules present at the surface. The behaviour of low dimensional materials can better be explained from their surface and interface property. In bulk materials, only small amount of molecules will be present near or at the surface or interface, like crystal boundary, whereas in low dimensional materials, half or more molecules will be near the interface. For this reason property such as energy levels, electronic structure and reactivity is quite different from the bulk.

### 1.3. Classification of Low dimensional particles:

Low dimensional particles are classified into two main groups depending on the size:

(a) Nanoparticles

(b) Microparticles

**1.3.1. Nanoparticles:** Nanoscience and nanotechnology primarily deal with the synthesis, characterization, exploration and exploitation of nano structured materials. These materials are characterized by at least one dimension in the nanometer ( $1\text{nm}\sim 10^{-9}\text{m}$ ) range. Nanostructures constitute a bridge between molecules and micro systems. Scientists have shifted their attention to developed organic nanoparticles in last few years. The number of studies of organic nanoparticles has been increasing because of the diversity of organic molecules; there is a tendency to extend the research on nanoparticles from metals and semiconductors into the organic field, especially into general organic molecules. The development of organic low-dimensional nanostructures was inspired by their unique optical and electronic properties and the potential applications in fabricating nano devices, such as optoelectronic and field-effect transistors. Organic nanoparticles are self-assembled into highly aligned super lattice at room temperature and these are implemented to better performance of organic light emitting diodes (OLED). In addition, morphology also plays an influential role in determining the properties of organic nanostructures. Single-crystal one-dimensional (1-D) nanostructures of [2 (p-dimethyl amino phenyl)ethenyl]-phenyl-methylene-propane-dinitrile, 9, 10-bis(4-(N-carbazolylphenyl) anthracene, Triphenylene, 9-anthracene carboxylic acid [3-5] etc have been prepared by a simple solution process or solid phase synthesis method. For example, organic nanoparticles were successfully fabricated by reprecipitation, microemulsion, thermal evaporation, laser ablation etc. One-dimensional (1D) organic nanostructures such as rods, wires and tubes were prepared through physical



vapor deposition, self-organization and template method [6-8] etc., while organic nanoflowers were synthesized via induction of coordination and intermolecular interactions.

**1.3.2. Microparticles:** Size of these materials is in the micrometer (1 $\mu$ m to 100 $\mu$ m) range. Microstructures constitute a bridge between nanoparticles and infinite bulk systems. Commercial microparticles are available in a wide variety of materials, including ceramics, glass, polymers and metals. Microparticles used in daily life include pollen, sand, dust, flour, and powdered sugar. Microparticles have a much larger surface-to-volume ratio than at the nanoscale and thus their behaviors are quite different. Microspheres are spherical microparticles and are used where consistent and conventional particle surface area is important. In biological systems, microparticles are small membrane bound vesicles circulating in the blood derived from cells that are in contact with the bloodstream such as platelets and endothelial cells. Because they retain the signature of membrane protein composition of the parent cell, microparticles carry useful information and can be detected and characterized by flow cytometry.

Functionalized organic microparticles are one of the most interesting topics of the present materials science, which significantly offer large variability in their composition and physical properties. Their chemical and photo physical stability differ widely than that of the isolated molecules and display their characteristic optical and optoelectronic properties. Therefore, they are of considerable interest for various potential applications in the field of biological sensor, photocatalyst, OLEDs, optical devices etc. [9-11]. The interaction in organic materials is basically weak interactions forces like hydrogen bond,  $\pi$ - $\pi$  stacking, van der Waals contacts and charge transfer interactions etc. Much effort has been devoted to synthesize organic microparticles having various size and shapes. This includes zero dimensional (0-D) spherical or tetrahedral quantum dots [12,13], one-dimensional (1-D)

nanorods and wires from small organic compound [14] and two-dimensional (2-D) nanoplates [15], nanoribbon and nanotube [16], microcapsule [17], organic nano flower [18], sub-microtube [19] etc. Organic-inorganic hybrid microcapsules may find applications in biomedical and biosensing fields. Organic microparticles like 1-phenyl-3-((dimethyl amino)stryl)-5-((dimethyl amino)phenyl)-2 pyrazoline [20], 1,3-diphenyl-5-(2-anthryl)-2-pyrazoline, 1,3-diphenyl-5-pyrenyl-2 pyrazoline [21], 1-cyano-trans-1,2-bis-(4-methyl-biphenyl)ethylene, 2,4,5-triphenylimidazole [22], 1-cyano-trans-1,2 bis(3',5'-bistrifluoromethyl-biphenyl)ethylene, 1-Pyrene-carboxaldehyde, Pyrene, Anthracene, 9,10-diphenylanthracene, perylene, 2-cyano-3(4-(diphenylamino)phenyl)acrylic acid [23-25] etc are mainly prepared by reprecipitation method, physical vapour deposition, microemulsion, ultra-sonication, template method, self-organization [26,27]etc. Porphyrin-silica microparticle conjugates as an efficient tool for the photo sensitized disinfection of water contaminated by bacterial pathogens.

#### **1.4. AIEE based low dimensional materials:**

Photoluminescence is one of the possible photophysical phenomena resulting from interaction of light with matter. Low dimensional fluorescent inorganic semiconductor or metal particles have attracted considerable research interests due to their unique properties originating from quantum-size effects. They have been extensively investigated for various potential applications including the fluorescent biological labels, photovoltaic cells, light-emitting diodes (LED) and optical sensors. As far as the application is concerned, fluorescent organic materials (FOM) are expected to hold the higher potentials because FOM allow much more variability and flexibility in molecule synthesis and their aggregates preparation.

About half century ago, Förster and Kasper discovered that the fluorescence of pyrene was weakened with an increase of its concentration in solution. Studies have shown that the

fluorescence of many aromatic luminophores became weaker or even completely quenched in concentrated solutions or in the solid state (Fig.1.2). This common photo physical phenomenon is widely known as aggregation-caused quenching (ACQ) of light emission [28]. This effect was found to be caused by the molecules especially those with disc-like shapes, experience strong  $\pi$ - $\pi$  stacking interactions and formation of sandwich-shaped excimers and exciplexes aided by the collision interactions between the aromatic molecules in the excited and ground states, which are now known to be common to most aromatic hydrocarbons and their derivatives, as summarized by Birks in his classic book on “*Photophysics of Aromatic Molecules*” in 1970 [29]. The ubiquitous concentration quenching effect has forced researchers to study and utilize fluorophores in solution phase but that causes many problems. Numerous processes have been employed and many approaches have been developed to prevent the luminophores from aggregating, but these efforts have met with only limited success. The difficulty lies in the fact that chromophore aggregation is an intrinsic natural process when luminophore molecules are located in close vicinity in the condensed phase.

Exactly opposite to the ACQ effect, in 2001 Tang and Park observed a unique luminogen system in which luminogen plays a constructive instead of destructive role in the luminescence process [30, 31]. Hexaphenylsilole (HPS) is nonemissive when its molecules are dissolved in a good solvent, such as tetrahydrofuran (THF) or a THF/water mixture with a fraction of water ( $f_w$ ) lower than 80%. Its fluorescence is turned on when  $f_w$  reaches ~80% (Fig.1.2). As water is a poor solvent for the hydrophobic siloles luminogen, addition of water to THF cause the siloles molecules to aggregate in aqueous media [32]. Since the light emission is induced by aggregate formation, they coined the term aggregation induced emission enhancement (AIEE) for the phenomenon. In the last decade, a large variety of

molecules with propeller shapes has been found to show the AIEE effect, indicating that AIEE is a general photophysical phenomenon.

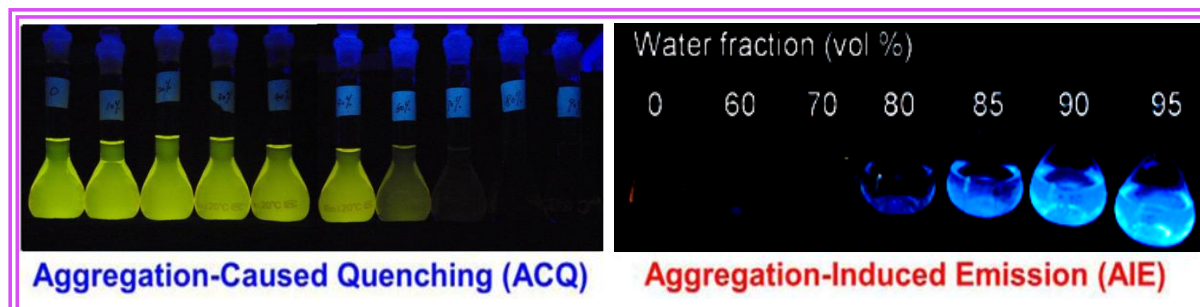


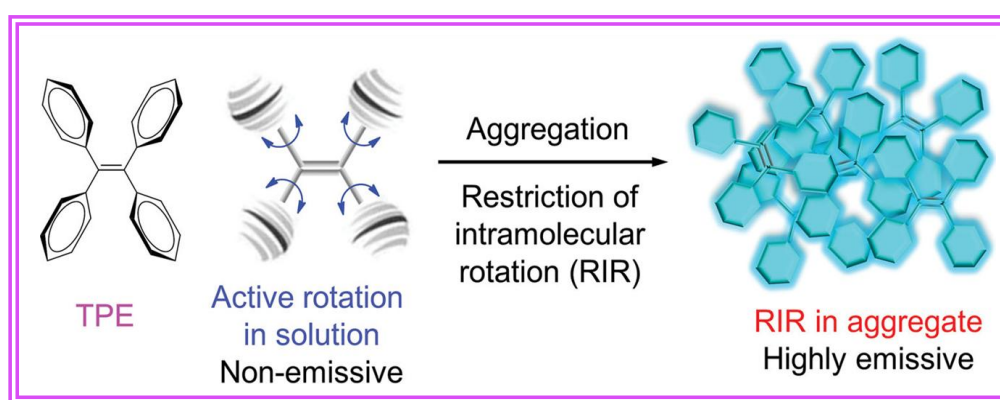
**Figure 1.2:** Fluorescence photographs of solutions or suspensions of (left) perylene ( $20\mu\text{M}$ ) and (right) hexaphenylsilole (HPS;  $20\mu\text{M}$ ) in THF/water mixtures with different fractions of water ( $f_w$ ), showing typical ACQ and AIEE effects, respectively. Reproduce with permission from Ref. [32] copyright © Royal Society of Chemistry.

## 1.5. Mechanism of AIEE phenomena:

The coinage of the AIEE concept in 2001, researchers has shown persistent thirst for learning the real mechanistic causes for the AIEE phenomena. A number of mechanistic pathways have been hypothesized, including conformational planarization, J-aggregate formation, E/Z isomerization, twisted intramolecular charge transfer (TICT) and ESIPT. None of them can be fully supported by the experimental data. To avoid these ambiguities, the experimental and theoretical works were done to provide solid proof to the three main hypotheses from the mechanistic viewpoints of the AIEE effects, *i.e.* Restriction of intramolecular rotation (RIR), Restriction of intramolecular vibration (RIV) and Restriction of intramolecular motion (RIM).

**1.5.1. Restriction of intramolecular rotation (RIR):** Fundamental physics teaches us that any movement, whether it is microscopic or macroscopic, consumes energy. Molecular motions include rotations and vibrations. Tetraphenylethene (TPE) is a well-studied AIEEgen (Scheme 1.1) in which four phenyl rings are linked to a central ethene rod

through single bonds and have great freedom to rotate against the ethene stator. The isolated molecules of TPE in a dilute solution can undergo active intramolecular rotations, which serves as a relaxation channel for the excited states to non-radiatively decay to the ground state. In aggregate state, however, the intramolecular rotations are restricted due to the involved physical constraint, which blocks the radiation less relaxation channel and opens the radiative decay pathway [33]. Arylenevinylene luminogens containing big dibenzosuberene terminals and anthracene cores [34, 35] are non-planar in conformation and propeller-like in shape and show marked AIEE effect.

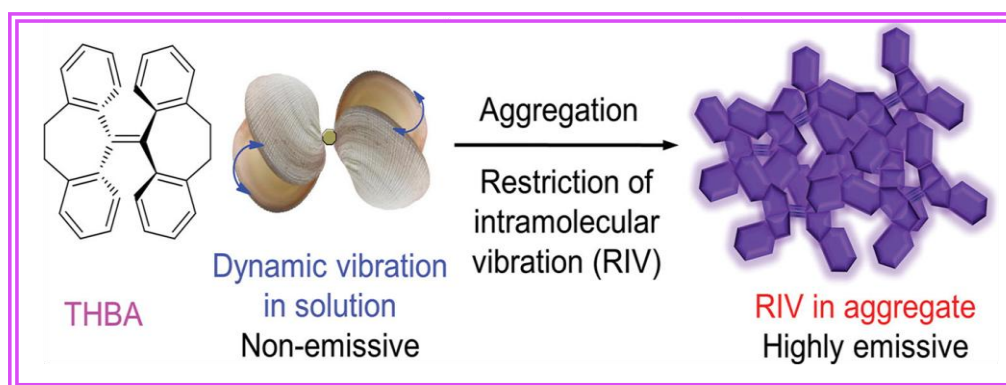


**Scheme 1.1: Propeller-shaped tetraphenylethene (TPE) is non-luminescent in a dilute solution but becomes emissive in aggregated state, due to the restriction of intramolecular rotation (RIR).**

The above analysis implies that the RIR process is responsible for the AIEE phenomena of molecular rotor systems. Theoretical calculations and simulations on the low-frequency intramolecular motions also support the RIR mechanism. Using the vibration correlation function formalism coupled with first-principles calculations under displaced/distorted harmonic oscillator approximation, the radiative and radiation less decay processes of AIEEgens have been studied. The solid-state packing effects on the radiative and non-radiative decays have been revealed by a combined quantum mechanics and classical molecular mechanics (QM/MM) study. These investigations provide supportive evidences to the RIR process and clearly define the role of low-frequency motions in the radiation less

decay processes. The aggregation tends to significantly slow down the non-radiative relaxation process and populate the radiative decay species.

**1.5.2. Restriction of intramolecular vibration (RIV):** As the AIEE study advances, new AIEEgens are discovered, whose AIEE processes cannot be explained by the RIR mechanism. 10,10',11,11'-tetrahydro-5,5'-bidibenz-7-annulenyldiene (THBA) and 5,5'-bidibenzo-7-annulenyldiene (BDBA) is such examples [36,37]. THBA has no rotatable units, as its phenyl rings are locked by central C=C bond. However, it is non-emissive in solution but highly luminescent as an aggregate. So RIV is envisioned to be responsible for the AIEE effect of this molecule.



**Scheme 1.2: Shell like THBA is non-luminescent in a dilute solution but becomes emissive in aggregated state, due to the restriction of intramolecular vibration (RIV).**

Further investigations testify that the vibrational motions of the phenyl rings are the source of the exciton energy consumption. QM/MM modeling results clearly show that the isolated THBA has six normal modes that consume significant amounts of excited-state energy ( $\sim 5679\text{cm}^{-1}$ ). In comparison, for THBA in the cluster, there are only three normal modes consuming significant amounts of excited-state energy ( $\sim 4016\text{cm}^{-1}$ ). In the cluster, the combination of a decrease in the number of vibrational normal modes and a loss of  $\sim 30\%$  in the exciton energy consumption due to RIV enables THBA to decay radiatively, leading to the observed AIEE effect (Scheme 1.2).

Iyoda *et al.* have reported a dibenzocyclooctatetraene (COT) based AIEEgen. These COT based molecules can undergo various vibrational ring inversions, giving different boat/chair-shaped conformations [38]. Such intramolecular motions non-radiatively dissipate the excited-state energy, resulting in the non-emissive solution state. In the crystal state, the conformational changes of the COT units are restricted by packing and hampering the intramolecular vibrations from occurring. The non-planar structure hinders the intermolecular  $\pi$ - $\pi$  stacking interactions. These two effects collectively make the crystals luminescent. This illuminates that in addition to rotations, vibrations (in-plane/out-of-plane bending, flapping, stretching, scissoring, wagging, twisting, rocking, etc.) can also expend excited-state energy.

**1.5.3. Restriction of intramolecular motion (RIM):** In a system, where both RIR and RIV are involved, the luminogen must be AIEE active by restricting intramolecular motion (RIM). 10-hexyl-3,7-bis(7-phenylbenzo[1,2,5]thiadiazol-4-yl)-10H-phenothiazine (PTZ-BZP) which has a nonplanar butterfly-like conformation, is non-luminescent in solution but emits bright red fluorescence in presence of water, clearly showing an AIEE effect [39]. In the isolated state, there are two major radiationless channels consuming its excited-state energy: (i) the rotational motions of the benzothiadiazole and phenyl rings and (ii) the vibrational motions of the phenothiazine core. The aggregate formation confines the intramolecular motions of the rotatable and vibratable units and thereby turns on the emission. The RIM process hence accounts for the AIEE attribute of this compound. 11,11,12,12,-Tetracyano-9,10-anthraquinodimethane, Oxacalixarene 33 are the example of AIEE active molecule whose emission is enhanced by RIM mechanism [40,41]. So the RIM mechanism is the unification of the RIR and RIV mechanisms. A simple, fundamental idea of RIM is that the RIR and RIV mechanisms are not mutually exclusive but instead can work together to bring about the AIEE phenomenon.

## 1.6. AIEEgen Systems:

With the increasing research interest in the field of AIEE, the development of new AIEEgens has also significantly progressed. From pure hydrocarbons to heteroatomic compounds, from small molecules to macromolecules, from organic to inorganic or metallo-organic, the variety of AIEEgens has maintained a continual growth.

**1.6.1. Hydrocarbon AIEEgens:** Pure hydrocarbon systems remain an important class of AIEEgens for a variety of reasons. Without the presence of heteroatoms, their properties, *e.g.*, chemical, electro, photophysical are relatively easier to study, thus providing simpler systems for structure-property relationship analyses and mechanism decipherment. TPE is the best-known hydrocarbonic AIEEgen and has been extensively used for mechanistic studies and ACQ-to-AIEE transformation [42]. Diphenyldibenzofulvene [43], 9,10-distyrylanthracene [44] and substituted 1,4-distyrylbenzene derivatives [45] are also the well known example of hydrocarbonic AIEEgens. Shimizu *et al.* have reported a series of new AIEEgens, (1E,3E,5E)-1,3,4,6-Tetraarylhexa-1,3,5-trienes [46]. Vertical phenyl rings of these compounds adopt an almost orthogonal conformation with respect to the conjugated core with dihedral angles falling in the range of 82.31° and 99.82° because of the steric repulsion interactions of the hydrogen atoms at the ortho-position of these phenyl rings with the neighboring hydrogen atoms on the hexa-1,3,5-trienes core. Due to a much weaker conjugation, these vertically positioned phenyl rings can easily rotate to consume excited-state energy and subsequently quenches emission intensity in the isolated state. In the aggregate state, the orthogonal phenyl rings together with the slightly twisted horizontal phenyl rings impair detrimental  $\pi$ - $\pi$  stacking interactions, which work jointly with the RIR process to turn on the emission. Similar to the previous compounds, a series of modifications have been made using it as a building block and the resulting derivatives have also been



reported to be AIEE-active. A variety of hydrocarbonic systems have been studied starting from phenyl rings decorating conjugated linear to cyclic cores, then from smaller to larger aromatic cores and rotors, and finally from systems that are AIEE-active because of RIR principle to those due to RIV and RIM processes.

**1.6.2. Hetero atom containing AIEEgens:** The hydrocarbonic AIEEgens enjoy simplicity in structure and accessibility in synthesis. They can function as excellent models for the mechanistic study of AIEE effects. The categories of the pure hydrocarbon systems are limited. Incorporation of heteroatoms into AIEEgens will definitely enrich the variety of AIEE systems.

➤ **Pentacyclic Compound:** Heteroatom-bridged cyclopentadienes which are often referred to as heteroles have drawn extensive attention, due to their unique electronic structures and optoelectronic characteristics. Many heteroles are found to be AIEE-active, such as silacyclopentadienes (silole), one of the well-studied AIEEgens. Germoles are heavier group-14 congeners of siloles. More recently, AIEE-active 1,1-disubstituted 2,3,4,5-tetraphenylgermole, has been developed by Braddock-Wilking *et al* [47]. Their single crystal structures have highly distorted configurations with the substituted phenyl rings twisted out of the pentacyclic cores. In the aggregate state, the quantum yield of this compound is 65 times higher than that of its acetone solution. Similar to its silole counterparts, the rotations of the phenyl rings on the germole ring cores quickly relax the excited state via non-radiative channels. Upon aggregation, the activation of RIR and the lack of intermolecular  $\pi$ - $\pi$  stacking interaction give rise to the enhanced emission. Benzyl-Phospholium Acenes, tetraphenyl-substituted Thiophene, Polytellurophenes are well known AIEEgens [48-50].

➤ **Boron Compounds:** Due to the unique electronic nature and chemical characteristics of boron, organoboron species always possess highly useful properties, especially the optoelectronic properties. Conventional organoboron systems are often afflicted by the ACQ effect, which limits their practical applications. Delightfully, the novel AIEE phenomenon has casted a new light on the organoboron research. Recently, some boron diketonates have shown AIEE activity [51-52]. Difluoroboron diketonate derivative exhibits an array of interesting luminescence properties, such as mechanochromism, thermochromism and chromochromism. Owing to its D-A nature, displays solvatofluorochromism properties, with emission red-shifting as solvent polarity increases. It is nearly nonluminescent in isolated state due to the cooperative effects of the high solvent polarity and active intramolecular motions. In solid state, it becomes highly emissive exemplifying AIEE behavior. The central difluoro dioxaborinane is not completely planar and the  $\text{BF}_2$  moiety is warped out of the central core, indicating vigor vibrational motions of the  $\text{BF}_2$  in the isolated state. Therefore, the AIEE feature of it should be ascribed to the RIM process. In the aggregate state, the rotations of the aryls and the vibrations of the  $\text{BF}_2$  segment are restricted, and the emission is hence turned on. Linking triphenylamine (TPA) and phenanthroline to o-carborane moiety are also AIEE active luminogen [53,54].

➤ **Schiff Base:** AIEE-active Schiff bases are a newly emerging class of AIEEgens. With its straightforward chemistry, it is easy for Schiff bases to link rotatable moieties via single bonds, making them promising candidates for AIEE research. Tian *et al.* have synthesized Schiff base derivative from hydrazine and an aldehyde-substituted aza-crown-ether [55]. The structure is featured with two conjugated moieties linked by a rotatable N–N single bond instead of a C–C bond and rotatable flexible substituents *i.e.* bulky aza-crown-ether units. In molecular phase, this compound only faintly luminesces but in the aggregate state, an 88.9-

fold increase in emission has been observed, implying its AIEE activity. The aza-crown-ethers are found to play two important roles in the AIEE effect. In the isolated state, the rotations and vibrations of the big aza-crown-ether rings work collaboratively with the rotation of phenyl rings to dissipate the excited-state energy. In the aggregate state, the bulky character of the azacrown-ethers prevents intermolecular  $\pi$ - $\pi$  stacking interactions and result emission enhancement. The second reason is, azacrown-ethers also direct the molecules to pack in a way that aids in rigidifying the molecules. The rigidification occurs at two sites: the first one is between two neighboring ether moieties and a phenyl ring unit; the second one is between the central conjugated segment ( $-\text{C}=\text{N}-\text{N}=\text{C}-$ ) and its two neighboring phenyl rings. With the help of multiple strong  $\text{C}-\text{H}\cdots\pi$ ,  $\text{C}-\text{H}\cdots\text{O}$ , and  $\text{C}-\text{H}\cdots\text{N}$  interactions, the rotations of the aza-crown-ethers and the  $\text{N}-\text{N}$  bond are restricted and the radiative pathways are hence activated, resulting in the enhanced emission. TPA substituted heterocycles, Diaminomaleonitrile-functionalized Schiff base also exhibits interesting AIEE properties [56,57].

➤ **Hydrogen Bonding System:** As an important non-covalent force, hydrogen-bonding (H-bonding) has been recognized to be of significance in the field of photophysics research. Intramolecular H-bonding has its ability to aid in the rigidification of the AIEE molecules and minimize the non-radiative energy losses to either turn on or enhance emission. N-(4-(benzo[d]oxazol-2-yl)-phenyl)-4-tert-butyl benzamide, is a simple and representative example that contains hydrogen-bonding by incorporating an amide moiety into its structure [58]. In molecular phase, the light emission from this solution is rather weak due to dynamic intramolecular rotations which effectively dissipate the excited-state energy. But in aggregated state the hydrogen bonding between molecules starts to form. From its crystal structure it can be seen that there are four molecules per unit cell, exhibiting cross

stacking by means of two kinds of interactions, *i.e.*, the H-bonding associated with the carbonyl groups and C–H $\cdots$  $\pi$  interactions.

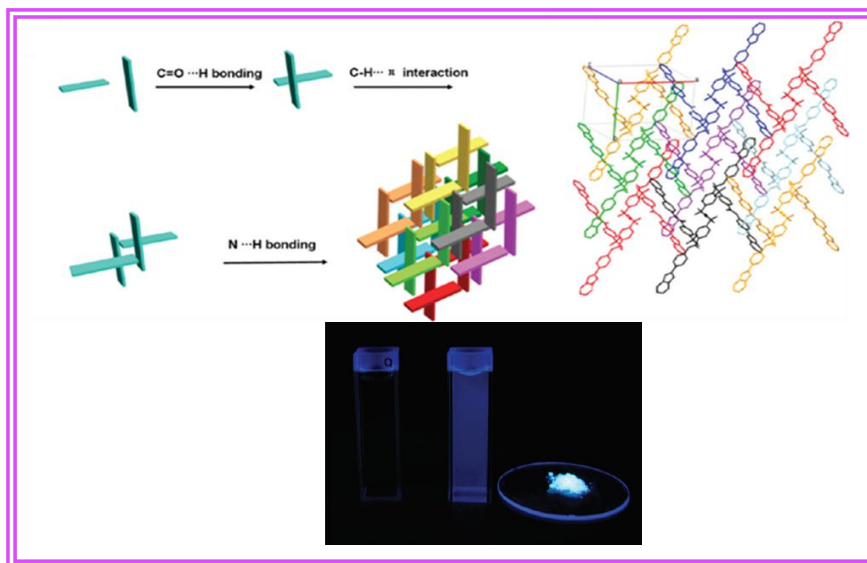


**Figure 1.3:** AIEE-active hydrogen-bonding-containing compound N-(4-(benzo[d]oxazol-2-yl)-phenyl)-4-tert-butylbenzamide. Reproduce with permission from Ref. [58] copyright © American Chemical Society.

A pair of molecules is initially stacked in an edge-to-edge mode forming an X-shaped dimer. Two such X-dimers are then edge-to-face connected with each other via strong C–H $\cdots$  $\pi$  bonds, forming a #-shaped tetramer in a unit cell. These #-aggregates are further interconnected by intermolecular N $\cdots$ H interactions between the nitrogen atom on the oxazole ring and hydrogen atoms of the aryl ring or amide on the neighboring molecules, expanding into a 3D network (Fig.1.3). These intermolecular interactions together with the physical constraints resulting from aggregation stiffen the molecular conformation and restrict the intramolecular motions and thus switch on the luminescence. In addition to the amide groups, other H-bonding motifs such as carboxyl, amine, imide, and sulfonyl groups have also been utilized to construct H-bonding-containing AIEE systems [59-61].

➤ **Miscellaneous System:** This section introduces heteroatom systems which are not belong to the above categories. Some of the luminogens can emit light of multiple colours.

Aggregates of butterfly-shaped pyran derivative formed in THF–water mixtures with 40%, 90% and 99% water emit green, orange and red light, respectively (Fig.1.4). Chiral cholesteryl wings attached to the pyran skeleton of this molecule and self-assemble to form crystalline, helical aggregates under appropriate conditions, which emit polarized light with high efficiency. The organizational assembly of the cholesteryl units is sensitive to environment condition. So at different water fraction, the aggregation mode will be different and as a result of this multiple colours are observed [62].

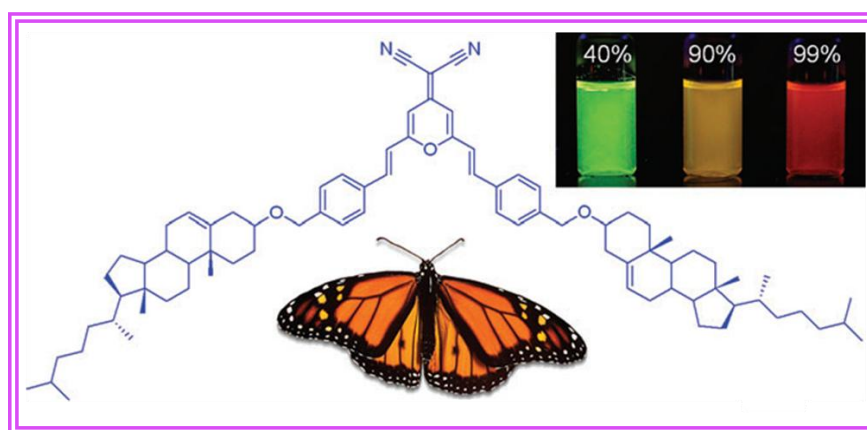


**Figure 1.4: Chemical structure of 2-{2,6-Bis[4-(cholesteryloxymethyl)styryl]-4H-pyran-4-ylidene}malononitrile and photograph of its aggregates at different water fraction. Reproduce with permission from Ref. [62] copyright © American Chemical Society.**

**1.6.3. Macromolecular AIEEgens:** With great success in developing small molecular AIEEgens, considerable progress has also been achieved regarding the exploration of macromolecular AIEE systems. As a matter of fact, macromolecular materials possess quite a few advantages over small molecule materials *i.e.* there are numerous possibilities to tune the molecular structure, topology, and morphology as well as functionalities of the macromolecular systems, which are hard to realize in small molecule systems.

➤ **Main Chain Polymers:** The core design strategy of AIEE-active macromolecules is to incorporate typical AIEEgens, into the polymer architectures. Pure TPE-based full-conjugated polymer is produced in high yields and moderate molecular weights by joining

the TPE units together via Suzuki coupling. It inherits the AIEE attribute from its TPE monomer which has very low intensity. When the polymeric molecules are induced to aggregate, the fluorescence intensity shows a general tendency to increase [63]. This polymer bears two interesting properties owing to its TPE backbone. For one thing, the polymer is highly soluble in solution, and for another, it is also strongly emissive in the aggregate and solid states due to the presence of highly twisted nature of the TPE modules prevent strong  $\pi$ - $\pi$  stacking interactions between the aromatic rings.

➤ **Side Chain Polymers:** In addition to the AIEE-active linear polymers, researchers have also successfully created side chain polymeric AIEEgens. Polyacetylenes which possess rigid and well-conjugated backbones have also been functionalized with AIEEgens as their side groups to create AIEE-active conjugated polymers [64]. The polymerization of acetylene monomers with aminated TPE units at their terminals using organo-rhodium as catalysts generates TPE-functionalized luminogen with an E-conformation. In the aggregate state, the polymer emits bright yellow fluorescence which is 56-fold stronger than the negligible emission of its in THF solution. In this compound, the polymer backbone and the TPE pendants are separated by flexible alkyl spacers, hence providing enough freedom for the TPE moieties to undergo active intramolecular rotations and facilitate the emission quenching in the isolated state. Upon aggregation, such intramolecular motions become restricted by RIR, rendering the polymer highly emissive. The well-known reversible addition-fragmentation chain transfer (RAFT) polymerization, a kind of living radical polymerization for vinyl compounds, has been used to synthesize TPE-pendent homopolymer [65]. Tetraphenylthiophene introduced to vinyl polymer as side chain pendant via radical polymerization and also exhibit AIEE activity [66]. Another study shows that, attachment of diphenylquinoline units to the vinyl polymers can't enhance emission but the addition of

camphorsulfonic acid (CSA), greatly affects the photophysical properties of polymer. The CSA molecules form complexations with the diphenylquinoline units [67]. The bulky nature of the CSA molecules is able to hinder the intramolecular rotations and make it AIEE active.

➤ **Dendrimer system:** Dendrimers are hierarchically branched macromolecules with multiple chains and branching units emanating from a single core. In light of the special conformation feature of dendrimers and the unique emission character of AIEEgens, a family of novel dendritic AIEE systems has been constructed in pursuit of developing more functional materials. Dendritic phosphole oxides prepared through the convergent strategy from the corresponding benzyl bromides are representatives of the first group of AIEE dendrimers [68]. The phosphole oxide core is a typical AIEEgen showing negligible fluorescence in the solution state but 5.2-fold emission enhancement is observed in the aggregate state. For each successive generation of the dendrimer, a pair of benzyloxyl groups branch out from each of the previous aryl ring. For first generation, emission enhancement is not strong due to lack of restriction of rotation in aggregated state but for second generation, great restriction on the intramolecular motions in the aggregate state, enabling it to show the most significant AIE effect with intense green emission. As the generation increases, more dendrons are attached to the core, resulting in larger steric crowdedness that makes the intramolecular motion restricted in solution state also. This leads to a higher solution-state emission and reduce the AIE effect. TPE-containing dendrimers, poly(amidoamine) (PAMAM) dendrimers peripherally decorated with TPE moieties are also well known AIEE active dendrimer [69,70].

➤ **Hyperbranched Polymers:** Hyperbranched macromolecular systems possess similar architectures and properties as dendrimers but enjoy much simpler syntheses. Hyperbranched polymers are intrinsically crowded in their molecular structures and thus it is

really difficult to obtain a hyperbranched polymer which is non-emissive in solution but strongly luminescence in the aggregate state. But after the discovery of AIEE features, this limitation can be overcome. Triazides with varying spacer lengths were designed and integrated into the hyperbranched structures by the well established copper alkyne-azide coupling (CuAAC) click polymerization with the diyne modified TPE derivative, readily furnishing 1,4-regioregular hyperbranched polytriazoles [71]. These polymers are well soluble in most of the common organic solvents and practically non-emissive in the isolated state. The photoluminescence is continuously boosted with aggregation, suggesting the AIEE characteristics of these two polymers. Such remarkable AIEE features are ascribed to their innovative spring-like architectures. The function of the alkyl spacers is to introduce flexibility into this luminogenic hyperbranched system. When molecularly isolated in good solvents, these alkyl arms are fully stretched and enlarge the distances between the TPE moieties ensuring enough freedom for the intramolecular motions. But in aggregated state, the flexible and hydrophobic polymer branches become agglomerate and the bulky spheres are induced to compress into smaller ones. The reduced space freedom severely constrains the intramolecular motions, resulting in AIEE effect. Besides the nonconjugated hyperbranched polymeric systems conjugated hyperbranched polymers synthesized through the TaBr<sub>5</sub>-catalyzed cyclotrimerization of a diyne-functionalized TPE derivative are also exhibit AIEE characteristics [72].

**1.6.4. Metal Complex AIEEgens:** Metal complexes or coordination complexes refer to chemical compounds containing at least one bond (*i.e.* coordination bond) between atoms of an organic ligand and a metal center. From this viewpoint, the Metal organic fluorophores (MOFs) are in nature one type of metal complex. Similar to many organic systems, light emissions of metallic organic luminophores also often meet with ACQ problems.



Delightedly, AIEE effects have been observed in a number of metal complexes. The incorporation of transition metals has made it possible to take advantages of the electronic properties of the metal species such as the transitions of triplet excited states to easily access phosphorescence.

Liu *et al.* reported a series of di isocyano benzene-based dinuclear gold(I) complexes which differ only in the ether bridge linking the two identical arms have been synthesized [73]. This is nonemissive in a variety of organic solvents but can be gradually induced to luminescence by adding poor solvent like water. A 538-fold emission enhancement is observed in aggregated state indicative of the AIEE activity. Such an AIEE effect is attributed to the RIR process caused by the strengthened physical constraints in the aggregate/solid state. Che *et al.* reported that an Pt(II) complex in molecular phase is virtually non-phosphorescent [74]. But in aggregated state, the emission is enhanced by 7.5 times and red-shifted. It is hypothesized that the intramolecular hydrophobic folding of the *o*-phenyleneethynylene chain is responsible for its solvatochromic phosphorescence. The similar phenomenon was observed by Lu *et al.* in the Re(I) complex systems [75].

**1.6.5. Unorthodox AIEEgens:** For organic compounds, one of the most important prerequisites for their luminescence is the large enough electronic conjugation. Recently a class of unorthodox system that does not possess conventional chromophores and bond conjugations but still have been found to exhibit a marked AIEE effect [76]. (R)-diethyl-1,2,3-triphenyl-1,2,3,6-tetrahydropyrimidine-4,5-dicarboxylate, is non-emissive in solution but luminescence brightly as crystals [77]. Examination on its crystal packing reveals that the electron-rich oxygen and nitrogen atoms with lone pairs are spatially arranged in close proximity. Such a through-space electronic interaction yields a conjugated chromophore or luminogen. In the solution state, the dynamic rotations of the aryl and ester units as well as

the active vibrations of the tetrahydro pyrimidine ring and carbonyl bonds consume the excited-state energy via nonradiative decay channels. In addition to the fluorescent system, similar electronic communication fashion has also been observed in some phosphorescent systems. Crystal induced phosphorescence (CIP) property at room temperature includes carbonyl-rich and halogenated species like different benzophenone derivatives. These compounds show no luminescence when they are dissolved in good solvents, because in these isolated states, intramolecular motions effectively annihilate their triplet excitons through nonradiative decay pathways. The benzophenone derivatives *e.g.* methyl 4-bromobenzoate and 4,4'-dibromobiphenyl show different colors in their phosphorescent emissions varying from blue to green to orange and their quantum yield increases from 0.001% to 39.7% and 12.4% respectively. These high quantum yields are first and foremost a result of the strengthened rigidity in molecular conformations due to crystallization. The crystal packing of these compounds has evidenced the existence of extensive strong intermolecular interactions, such as C–H···O, N–H···O and C–H··· $\pi$  hydrogen bonds, C–H···X (X = F, Cl or Br) halogen bonds and C–Br···C–Br interconnects leading to the turn-on in phosphorescence. Lifetimes of these molecules are from 19.2 $\mu$ s to 4.8ms [78].

### 1.7. AIEE and TICT:

Like AIEE, TICT is associated with intramolecular rotation or twisting. However, unlike AIEE, TICT results in PL diminution. TICT generally occurs in a luminogen system containing donor (D) and acceptor (A) units with push–pull interactions. In a polar solvent, the charge-separated conformation resulting from intramolecular twisting is stabilized by the solvation effect, whose excited state often decays non-radiatively. This is a drawback if one wishes to use the luminogen as a fluorescent biosensor, because biological processes basically occur in aqueous medium. The emission colour of an AIEE luminogen is scarcely

affected by solvent polarity, whereas that of a TICT luminogen typically bathochromically shifts with increasing solvent polarity, as polar solvents alter its ground and excited states and narrow its energy gap [79,80]. When polar heteroatoms, especially D/A groups, are introduced into an AIEE system, the TICT process comes into play.

Triphenylamine-boradiazaindacene (BODIPY) contains a D-A pair with multiple aryl rotors [81]. This structural feature is likely to make it both AIEE and TICT active. As shown in the upper panel of Fig. 1.5, the PL color of it is very sensitive to the solvent polarity. As the solvent is changed (hexane - toluene - chloroform - methanol), its PL color is changed accordingly (green -yellow - red - infrared).

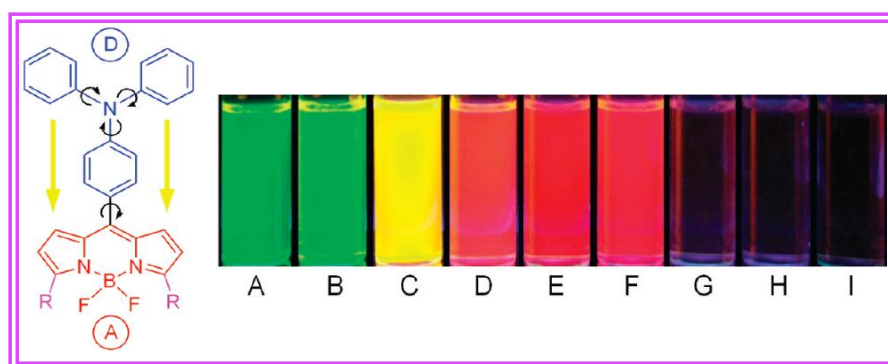


**Figure 1.5: Photographs of boradiazaindacene (BODIPY) derivatives taken under illumination of a UV lamp in solvents with increasing polarity (from left to right): (A) hexane, (B) cyclohexane, (C) toluene, (D) chloroform, (E) ethyl acetate, (F) THF, (G) ethanol, (H) acetonitrile, and (I) methanol. Reproduce with permission from Ref. [81] copyright © American Chemical Society.**

Blending water with THF in different ratios gives aqueous mixtures with varying solvent polarity and solvating power. BODIPY gives a PL spectrum in pure THF, which is dramatically weakened in intensity and is red-shifted in the THF-water mixture with 10% water, due to an increase in solvent polarity. The emission remains weak when the water content in the THF-water mixture is increased to 70%, after which the PL intensity starts to increase, accompanied by a blue-shift in the PL peak with a prominent variation in colour with 70-fold higher in intensity (Fig. 1.6). When the water content is increased, the aqueous

mixture becomes more polar. So the emission from the TICT luminogen should be monotonically decreased and red-shifted. At a certain point with an appreciably high water content, the solvating power of the aqueous mixture has deteriorated to such an extent that it cannot dissolve all the luminogen molecules any more. Some of the molecules thus begin to aggregate into nanoparticles, whose polarity inside is lower than that outside and AIEE effect become predominant over TICT effect.

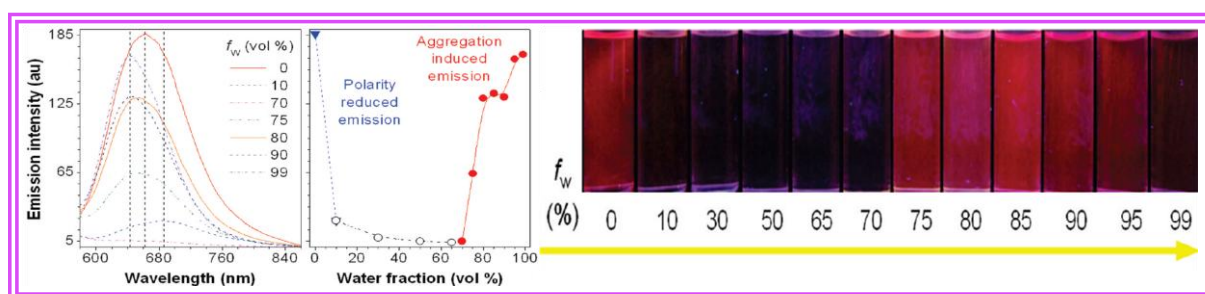


**Figure 1.6: Photographs of BODIPY in THF/water mixtures with different fractions of water ( $f_w$ ) taken under UV illumination. Emission spectra of this in the THF/water mixtures and plot of maximum emission intensity versus water fraction in the aqueous mixture. Reproduce with permission from Ref. [81] copyright © American Chemical Society.**

## 1.8. Technological Application:

These AIEE materials have in turn brought forth plentiful technological innovations. The AIEE effect provides exhilarating possibilities for empowering new sensing systems that operate in a luminescence turn-on fashion. As efficient solid emitters with good thermal- and photo-stabilities, AIEEgens definitely fill the bill and are promising materials for the fabrication of high performance optoelectronic devices. Numerous efforts have been devoted to the utilities of AIEE materials in a wide variety of high-tech areas.

**1.8.1. Biological Probes:** Biological area itself is a vast and appealing research field.

There are uncountable species which are vital to living things need to be detected and numerous events biotechnology, healthcare of human beings (*e.g.*, clinical diagnostic

examinations, treatment monitoring), fermentation industry, as well as food and pharmaceutical industries, etc need to be unveiled and monitored. Luminescence as a technique is a perfect choice for the applications in biological areas, in the light of its rich advantages such as superior sensitivity, high selectivity, fast response, low background noise, simplicity, and so on. AIEE has been proven to be a powerful approach for sensitive and specific biosensing.

Glucose is an important biomolecule as a basic necessity of living organism and a pervasive fuel for biological processes. The abnormal levels of glucose in body fluids such as human blood or urine signify biological dysfunctions. Phenylboronic acid is an alcohol-affinitive moiety that can reversibly react with diols in aqueous media and hence can be employed as synthetic receptors for carbohydrates. TPE is easily functionalized with two boronic acid groups. The obtained TPE-diboronic acid adduct is immiscible in neutral water and its suspended aggregates show bright blue emission. But at higher pH, the emission begins to decrease and becomes fairly weak because the compound ionizes and become soluble. Turn-on detection of glucose is achieved by adding glucose into a solution of pH~10.5. The cis-1,2-diol and cis-5,6-diol units of the glucose react with the boronate moieties of it affording either cyclic or linear oligomers [82]. The oligomers formation restricts the phenyl ring motions of the TPE units and thus switches on the emission. The selective emission enhancement ensures the occurrence of oligomerization of it with two cis-diol moiety of glucose. In contrast, fructose, galactose, and mannose only possess a single cis-diol. As a result, it is end-capped with two monosaccharide units which are no longer reactive to boronic acid. The intramolecular motions of TPE units in such small adducts are not sufficiently restricted and still able to efficiently dissipate the excited-state energy via non-radiative channels, hence resulting in the small emission enhancement.

Different biological thiols such as cysteine, Glutathione etc are also decisive in maintaining the appropriate oxidation-reduction states of proteins, cells, and organisms. The abnormal levels of these biothiols are indicative of a number of diseases, such as liver damage, skin lesions, slow growth, neurodegenerative diseases, cancers, and acquired immunodeficiency syndrome (AIDS) etc [83-87]. Homocysteine (Hcy) is another primary biothiol which causes a significant risk factor for cardiovascular diseases, renal dysfunction, and Alzheimer's disease in its high level. Tong *et al.* have developed a novel AIEEgen based turn-on fluorescent probe, 2-(2,4-dinitrobenzenesulfonyl)-5-chlorosalicylaldehydeazine (DNBS-CSA) [88]. Utilizing the AIEE effect, such thiol detection can be performed on test paper and the detection is thiol-specific, so no emission enhancement is observed with the addition of amino acids without thiol group. Using this AIEE based method in addition to the thio based amino acid, other basic amino acids, such as arginine and lysine, can also be detected [89].

Numerous biomolecules such as polysaccharides, DNA, and phospholipids exist in the form of charged species. Heparin is recognized as one of the most negatively charged biological molecules. AIEEgen integrated graphene oxide (GO) was used for better selective sensitivity. GO is a fluorescence quencher so addition of AIEE probe, it will tightly bind with the molecules via  $\pi$ - $\pi$  interaction, resulting in greatly weakened fluorescence. The mixture begins to fluoresce when heparin is added, because the heparin detaches the probe molecules from the surface of GO and forms electrostatic complex with them and switches on the green fluorescence. The addition of chondroitin sulfates (ChS) and hyaluronic acid (HA) cannot "light up" the emission of probe, because their electrostatic attraction power is not strong enough to seize the probe molecules from GO surface [90].

Together with proteins, nucleic acids including DNA and RNA are the most important biological macromolecules, essential for all known forms of life. The detection of nucleic

acids is of great importance in genetic engineering, forensics, and bioinformatics in terms of its crucial roles in various physiological processes. AIEEgen-labeled nucleotide [5-(3-aminoallyl)-2-deoxyuridine-5-triphosphate does not undergo self-quenching in fluorescence even with a degree of leveling (DOL) 10 times higher than that was ever reported. Such highly fluorescent DNAs can be further used as probes for various bioassays such as gene detection [91].

**1.8.2. Chemical Sensing:** Sensing refers to the detection of a particular entity, by a specialized system, namely, sensor or probe. Sensors are used in daily life and have been utilized in various areas including medicine, industry and environmental protection and control etc. The AIEE systems utilized for ion detection, pH sensing, gas detection, explosive detection, peroxide sensing, hazardous species detection, fingerprint visualization, chiral recognition, viscosity evaluation, conformation probing, self-assembly monitoring and morphology visualization.

➤ **Ions:** Ion detection has occupied a large portion of chemosensing, and it can be further classified into cation and anion detection. As a monovalent metal ion,  $K^+$  has attracted tremendous research interest for its extremely important roles in diverse physiological activities and biological functions. The sensitive detection of  $K^+$  is of great significance. Liu and Zhang *et al.* integrated TPE core functionalized with four crown ether moieties via thiol-ene click reaction affording the targeted probe. In molecular phase this probe is non emissive but upon the addition of  $K^+$ , intense fluorescent signal was detected [92]. The turn-on response originated from the aggregation induced by the  $K^+$  mediated cross-linking through the formation of  $K^+$ /crown ether (1/2 molar ratio) molecular recognition complex in a sandwiched fashion. This AIEE-based probe for  $K^+$  achieved a detection limit of  $\sim 1.0\mu M$  and showed excellent selectivity over other common metal ions including  $Li^+$ ,  $Na^+$ ,  $NH_4^+$ ,  $Ca^{2+}$ ,

$\text{Mg}^{2+}$ , and  $\text{Pb}^{2+}$ . Through combining the AIEE feature of TPE derivatives and the reaction of  $\text{CN}^-$  with the indolium group, a selective and sensitive fluorescence turn-on detection of  $\text{CN}^-$  was established with a simple AIEEgen by Zhang *et al.* Carrying a positively charged indolium moiety, AIEEgen was well dissolved in aqueous solution and showed very weak fluorescence [93]. The indolium moiety not only conferred the water solubility but also induced with selective recognition ability to  $\text{CN}^-$  via the specific reaction to afford  $\text{CN}^-$  adduct, which was highly hydrophobic and hence formed aggregates in the aqueous media, ultimately switching on the fluorescence.

➤ **pH:** pH is crucial to all life forms. A subtle variation in environmental pH can even devastate quite a few plant and animal lives. Acidification of soils, streams, lakes, and seawater caused by acid rain, excessive human activities, and untreated sewage can induce ecological disasters, which might further lead to the extinction of individual species, reduction of biodiversity, the elimination of specific strains, etc. Additionally, pH value is also a critical factor for medicines, foods, and drinking water, etc. Amongst various analytical methods for monitoring the pH level, fluorescence-based techniques have caught special attention for its superior sensitivity, rapidity, portability, etc. Since the pH detection should be carried out preferably in aqueous solution, AIEEgens would be better choices for their unique solution and aggregate-state behaviors. 1-(4-pyridinyl)-1-phenyl-2-(9-carbazolyl) ethane ( $\text{CP}_3\text{E}$ ) is AIEE-active and features the TICT property because of the D-A interaction between the carbazolyl and pyridinyl blocks.  $\text{CP}_3\text{E}$  showed an intense blue emission in the aggregated state owing to its AIEE character, whilst its protonated state exhibited dim yellow fluorescence due to a much stronger ICT effect [94]. The light emission of  $\text{CP}_3\text{E}$  can be reversibly switched between dark and blue states by repeated protonation and deprotonation, thus enabling  $\text{CP}_3\text{E}$  to function as a fluorescent probe for pH sensing in both the solution and



solid states as well as a sensor for detecting organic vapors with high acidity or basicity. The change in electron affinity of the pyridinyl unit and molecular conformation of CP<sub>3</sub>E upon protonation was believed to account for such sensing process.

➤ **Gases:** AIEE-based systems have been smartly designed to satisfy the applications for the sensing of some special gases, such as carbon dioxide (CO<sub>2</sub>), primary amine gas, and hydrogen sulfide (H<sub>2</sub>S). CO<sub>2</sub> sensing has great societal implications, because CO<sub>2</sub> is a component of gas mixtures that are released from many natural and anthropogenic activities and it has huge impacts on globe climate and human well-being. Especially, it has been widely accepted that CO<sub>2</sub> is closely associated with the global greenhouse effect. Enlightened by the fact that bubbling CO<sub>2</sub> through an amine solution can furnish a carbamate ionic liquid (CIL) resulting in the increases in polarity and viscosity, the CO<sub>2</sub>-induced in-situ generation of CIL has been made full use of to arouse the fluorescence response from the AIEEgen. HPS was dissolved in dipropylamine (DPA), affording a non-luminescent solution. Purging the DPA solution of HPS with a stream of CO<sub>2</sub>, a CIL was readily yielded via the reaction between CO<sub>2</sub> and DPA and the green fluorescence from the mixture was observed. With the increasing amount of CO<sub>2</sub>, the fluorescence was intensified [95].

➤ **Explosives:** There is a recent rise in concerns on global terror threats and anti-terrorism activities, making the sensitive detection of trace explosive materials and their precursors in security screening processes highly and urgently demanded. The development of reliable methods and processes for this purpose thus has antiterrorism and homeland-security implications. AIEE elements have been exploited to develop highly-performed fluorescent chemosensors for explosives. Fang *et al.* have fabricated a composite film by doping the aggregates of Hexaphenyl sillole (HPS) into a chitosan film via physical process, which is very stable and highly emissive due to the AIEE feature of HPS. The fluorescence of

such composite film can be sensitively and selectively quenched by Picric acid (PA) with a detection limit as low as  $\sim 2.1 \times 10^{-8}$  M [96].

➤ **Fingerprints:** Latent fingerprints (LFPs) at the crime scene are very crucial clues in forensic investigations due to their uniqueness and stableness. The uniqueness is identified by careful study of their ridge and groove characteristics, such as enclosure, island, bifurcation and ridge ending [97]. Su's group has recently carried out a systematic work to explore the possibility of identifying and visualizing LFPs on the basis of AIEEgens. As shown in Fig.1.7, AIEEgens TPE, HPS and HPS derivatives have been individually employed as a fluorescent visualizing agent. A versatile procedure has been established for the AIEEgen-based fingerprints developing processes.

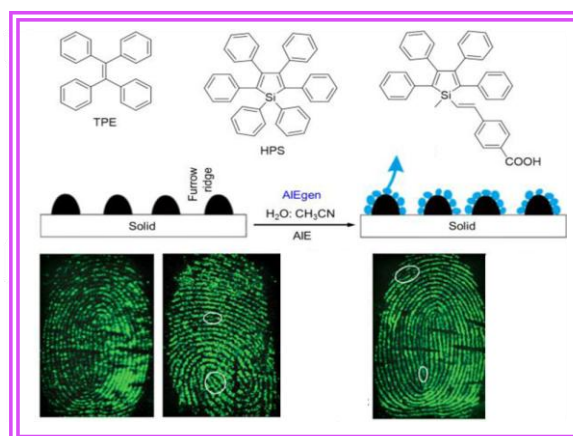


**Figure 1.7: Representative AIEEgens which have been used for the recognition and visualization of latent fingerprints and the illustration of working principle. Fluorescence images of sebaceous fingerprints on microscopic glass, stainless steel sheet, and aluminum foil (from left to right) developed by the AIEE of TPE aggregates. Reproduce with permission from Ref. [98] copyright © Royal Society of Chemistry.**

Sebaceous fingerprints were obtained by gently rubbing the fingertips of the volunteers over the forehead and nose and then stamping them directly onto different substrates with a minimal pressure. The substrates bearing the sebaceous prints were immersed into the acetonitrile/water mixtures of AIEEgens with different water fractions and incubated under stirring for 5 min; rinsed with a copious amount of ultrapure water and dried

under argon stream; then these substrates were positioned in the dark box of a ChemiScope 2850 fluorescence imaging system for observation. As these AIEEgens are lipophilic, thereby their aggregates preferentially adhere to the fingerprint ridges via hydrophobic interactions. The fingerprint ridges hence strongly fluoresced under UV illumination and the visual contrast was significantly enhanced by the AIEE effect of TPE, HPS and HPS derivatives [98].

**1.8.3. Optoelectronic Systems:** Optoelectronic devices refer to electrical-to-optical or optical-to electrical transducers that use such devices in their operation. Optoelectronic devices are the key and core component of optoelectronic technology, a cutting-edge research field in modern photoelectric and microelectronics technologies and also an important constituent part of information technology. In photo electronic areas, the light emitting materials can be used to serve various purposes and in most cases, the luminogens are utilized in the solid state. Thus, AIEEgens are ideal candidates for optoelectronic applications.

➤ **Organic Light-Emitting Diodes (OLEDs):** OLEDs have attracted tremendous attention because of their huge potentials in such applications as new display devices and solid state lighting. With the aim of attaining efficient full-color display and white light illumination, AIEEgens with emission colors covering the whole range of visible lights have been designed and synthesized. Directly hooking up the two TPE units through a para linkage gave rise to bis adduct pTPE-pTPE, which was found to show a sky blue EL with a maximum ( $\lambda_{em}$ ) at 488nm [99]. Multilayer OLED with a configuration of ITO/NPB (60nm)/ pTPE-pTPE (20nm)/TPBi (10nm)/Alq<sub>3</sub> (30 nm)/LiF (1nm)/Al (100nm) showed fairly good EL performance with a low turn-on bias ( $V_{on}$ ) down to ~4V, brilliant luminance up to 11180cd

$\text{m}^{-2}$  at 15V, and current efficiency ( $\eta_{\text{C,max}}$ ) and external quantum efficiency ( $\eta_{\text{ext,max}}$ ) reaching to  $7.26\text{cd A}^{-1}$  and 3.17%, respectively, at a bias of 6V.

➤ **Organic Field-Effect Transistors (OFETs):** The research field of OFETs is very active, with newly synthesized and tested organic compounds. Since electric current flows through such a transistor, it can be utilized as a light-emitting device, thus integrating current modulation with light emission. In this regard, AIEEgens are expected to be advantageous to the conventional OFET materials in terms of its efficient solid-state light emission. The emission colors of these luminogens vary from cyan to red and then to NIR. Tang and Miao *et al.* further investigated a good AIEEgen 1,2-bis[4'-(diphenylamino)biphenyl-4-yl]-1,2-diphenylethene for OFET application [100]. A high HOMO energy level (-5.15eV), which was close to the work function of metallic gold (-5.10eV) and favorable for the fabrication of OLEDs and OFETs, was determined. The hole mobility was estimated to be  $5.2 \times 10^{-4} \text{ cm}^2 \text{ V}^{-1} \text{ s}^{-1}$ , which was higher than that of N, N- diphenyl-N,N-bis(3-methylphenyl)-1,1-biphenyl-4,4-diamine, a well-known hole transporting material, under the same test conditions. The FETs were fabricated by depositing 60nm thick films onto silicon wafers which had been pretreated with self-assembled monolayer of octadecyltrichlorosilane (OTS) through thermal evaporation under high vacuum. The transfer I-V curve of this compound recorded under optimized conditions is exhibited, from which field-effect mobility up to  $2.6 \times 10^{-3} \text{ cm}^2 \text{ V}^{-1} \text{ s}^{-1}$  was calculated in the saturation regime using a specific equation. Moreover, the on/off ratio of the drain current acquired between 0 and -50V gate bias from the transfer I-V curve was larger than  $2 \times 10^4$ . Combining its OFET performance with its efficient photoluminescence and EL find an array of applications in organic electronics and optics.

➤ **Optical Waveguides:** Luminescent materials with optical waveguiding properties are a class of attractive functional materials. A large variety of AIEEgens possessing optical

waveguide effects with their emission color spanning the whole visible spectral region have been developed. Di(p-methoxyphenyl)dibenzofulvene, has been reported to be a member of this family [101]. This compound can emit blue light at wavelength 466nm. The microrods of it displayed remarkable optical waveguiding behaviors, with brighter luminescence at the rod-ends than the rod-bodies (Fig.1.8). When the microrods were excited with a focused laser at different local positions along the length of the microrods, characteristics of active waveguides were clearly observed. The optical loss coefficient values for microrods of it were estimated to be  $76.5 \text{ dB mm}^{-1}$ .

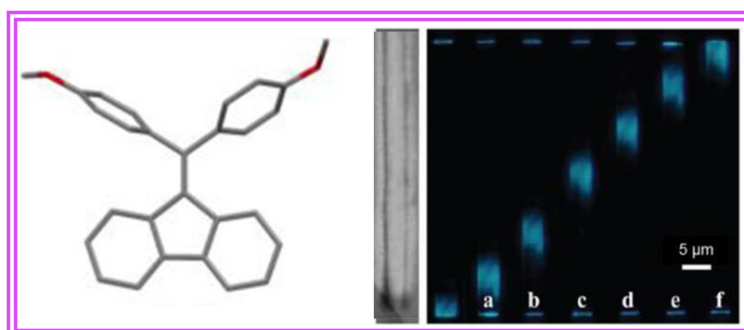


**Figure 1.8: Crystal structure of Di(p-methoxyphenyl)dibenzofulvene and PL image of microstructure at six different positions, excited with a focused UV laser. Reproduce with permission from Ref. [101] copyright © Wiley-VCH Verlag GmbH & Co. KGaA.**

➤ **Self-Assembly Systems:** Self-assembly is an interesting process that has attracted tremendous research interest. When such a process is related to fluorescent molecules, it provides opportunities for the manufacture of miniaturized high-performance photonic and electronic devices. A silole based AIEEgen derivative 2,5-Bis(triphenylsilylethynyl)-3,4-diphenylsiloles could easily generate ordered microstructures through a simple natural admixing and the subsequent evaporation of its solvent (Fig. 1.9). The addition of poor solvent into the molecular solution of silole derivative afforded thin 1D nanorods at the solvent interface. The fibrils were nanoscaled in diameter and tens of micrometers in length. Further gathering of the microrods resulted in the formation of bundles [102]. Majority of the rods are uniformly arranged in a parallel fashion, through side-by-side self-assembly.

The well-organized cables exhibited strong green light, especially at the cross sections. The self-assembly process driven by  $\pi$ - $\pi$  interactions together with the intense light emission makes the luminogen a promising candidate in the fabrication of miniature optoelectronic devices.

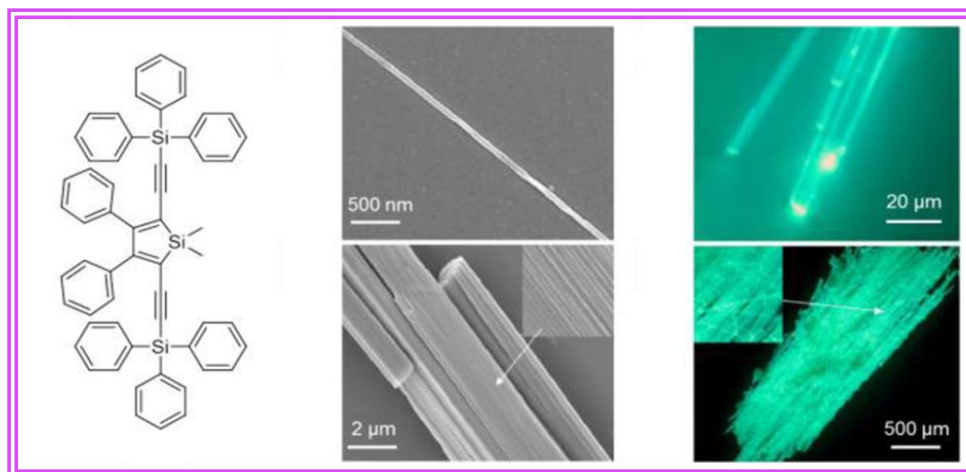


**Figure 1.9: Silole derivative and SEM images of the morphologies and corresponding confocal fluorescence images of the aggregates. Reproduce with permission from Ref. [102] copyright © Wiley-VCH Verlag GmbH & Co. KGaA.**

➤ **Photovoltaics:** Photovoltaics are also known as solar cells, which generate electric power by converting energy from the sun into a flow of electrons. Owing to its great impacts on environments and economics, photovoltaics are now, after hydroenergy and wind power, the third most important renewable energy sources in terms of globally installed capacity. The solar cells based on cadmium telluride (CdTe) are one class of currently widely used solar cells. The D-A conjugated fluorophores consist of TPE and malononitrile components with different aromatic rings as conjugating bridges [103]. The ICT and AIEE effects of these fluorophores resulted in large Stokes shifts and high quantum yield in solid medium (*e.g.*, PMMA matrix). With desirable photophysical properties these compounds had significantly improved the spectral response of the CdTe solar cells to photons in short-wavelength region (<500nm) when these fluorophores were doped in PMMA films as (light-emitting down-

shifting) LDS materials. Ultimately, when these AIEEgen-doped PMMA films were applied to the surfaces of the solar cells, the measured short circuit current density ( $J_{sc}$ ) was dramatically enhanced by a magnitude of 6-10%. Such work might suggest that the applications of AIEgens in the photovoltaic area are not restricted to the use as photovoltaic-active materials.

**1.8.4. Stimuli Responses:** Molecular systems that change their properties in response to a single stimulus or multiple stimuli are called stimuli responsive materials. The luminescence properties alter in response to the external stimuli or environmental variations, such as mechanical force, temperature (thermal treatment), fuming (vapor), photonic irradiation (light), solvent polarity, electric field and so on.

➤ **Force:** Mechanochromism refers to a phenomenon in which the luminescence of a luminophore changes with mechanical force. Materials exhibiting mechanochromism are widely utilized in sensors, memory chips, optical storage, and security inks, optoelectronic devices, and so forth. Such a chromic effect has been commonly observed in a great quantity of AIEEgens. Incorporation of two (6-phenoxyhexyl)-1H-1,2,3-triazole moieties into a TPE system by click reaction generated a luminogen [104]. The as-prepared solid emitted a pure blue light at 447 nm. Upon grinding, the emission maximum was red shifted to 477 nm, due to the morphological transition from the crystalline to the amorphous phase. The thermal annealing or vapor fuming with a polar solvent readily recovered the fluorescence. The writing-erasing process clearly demonstrated its potential for practical applications such as being utilized as a security ink for rewritable information storage system.

➤ **Heat:** Heat driven fluorescence switches can be easily realized in AIEE-active systems. Fabricating AIEEgen-based organic gelators is an effective and frequently-used approach to achieve thermo responsive AIEE systems. The AIEE-active gold(I) complex is

highly sensitive to temperature [105]. The photoluminescence spectra of this crystal displayed two emission bands at 407 and 428 nm, respectively, which were assigned to the fluorescence from the intra-ligand localized  $\pi\text{-}\pi^*$  excited state. Gentle heating ( $>55^\circ\text{C}$ ) of the sample on a slender piece of glass resulted in a broad emission band peaked at 530 nm (Fig. 1.10). The aurophilic interactions might be the cause for the generation of new ligand-to-metal charge transfer in excited state. When the temperature dropped to  $25^\circ\text{C}$ , the solid showed an emission band similar to that of the original sample. The blue-to-yellowish green fluorescence switching was repeatable and could be implemented by consecutive heating and cooling cycles in the temperature range of  $25\text{-}59^\circ\text{C}$ .

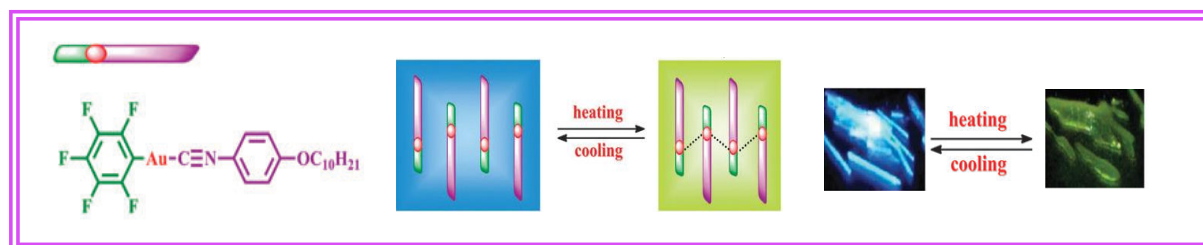


**Figure 1.10: AIEE based gold complex and its luminescence change before heating and after heating with fluorescent images under 365 nm UV illumination. Reproduce with permission from Ref. [105] copyright © Royal Society of Chemistry.**

➤ **Vapour:** AIEE-involved systems have been found to exhibit vapochromism. *o*-carborane containing poly(fluorene) show response to solvent vapors materials (Fig. 1.11). This polymer in the solid state underwent a change in its emission wavelength when exposed to organic solvents or their vapors, shifting from bright green to shade of yellow, orange, or red depending on the solvent used [106]. The shift correlated most closely to the polarity of the solvent vapor, and the higher the solvent polarity, the larger the red-shift in the emission would be. Such phenomenon is similar to the solvatochromism observed for some luminescent molecules in the solution phase. When exposed to solvent vapors, the emission



intensity also became lower, which was likely associated with the activation of the intramolecular motions of the o-carborane systems.

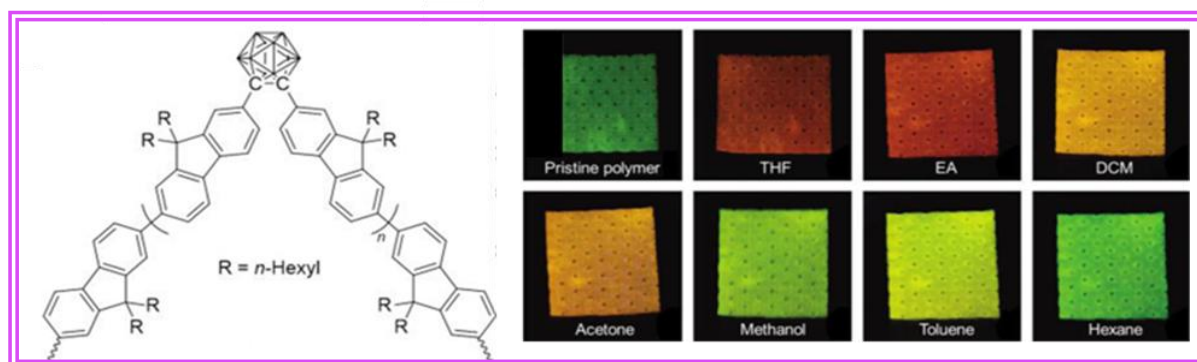


**Figure 1.11: Chemical structure of carborane-containing poly-(fluorene) and its response to solvent vapors. Reproduce with permission from Ref. [106] copyright © American Chemical Society.**

➤ **Photons:** Photo-responsive materials have been widely applied in many technological fields especially those related to biological applications such as super-resolution imaging and macromolecular movement tracking. Tang *et al.* recently developed a photoactivatable system in which caged AIEEgen was constructed by capping a TPE derivative with a 2-nitrobenzene group [107]. Caged TPE was practically non-luminescent both in solution and aggregate states as a result of photoinduced electron transfer. In the presence of UV irradiation, the quenching (*i.e.*, 2-nitrobenzene) moiety was removed from it, thus allowing the TPE motif in the resulting product to emit intensively in the aggregate state. The photoresponsive capability of this material makes it useful for practical applications in such as photopatterning and anticounterfeiting.

➤ **Multiplex:** AIEE systems which can respond to multi stimuli have been developed and reported. AIEE-active luminogen was made by employing TPE as a building block and introducing 6-hydroxylbenzothiazole as an acid-specific reaction site [108]. Benefiting from its AIEE characteristic, solid powder of this material emitted a bright blue light peaked at 454 nm ( $B_1$  form). Fuming the sample with HCl vapor dramatically changed the emission from

blue to yellow at 550 nm ( $Y_1$  form), indicative of its pH-responsive capability. Exposed to  $NH_3$  vapor, the initial blue emissive  $B_1$  state was fully restored. This reversible fluorescence switching was associated with the corresponding protonation and deprotonation (Fig.1.12).

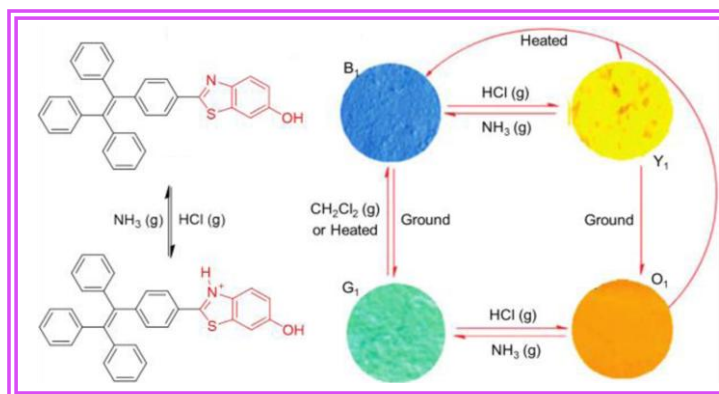


**Figure 1.12: AIEEgen-based smart material showing multi stimuli responsiveness. Reproduce with permission from Ref. [108] copyright © Royal Society of Chemistry.**

Mechanical stimuli such as grinding could readily shift the blue fluorescence of the pristine solid powder to green with a maximum at 492 nm ( $G_1$  form). Solvent fuming enabled the full recovery of the original  $B_1$  state, suggesting that the mechanochromic effect was reversible. The ground sample ( $G_1$  form) preserved the property of protonation deprotonation and hence was also pH-responsive. Upon fumigation of HCl vapor, the green luminescence was turned into orange light ( $O_1$  form) at around 565 nm. In presence of  $NH_3$  the green state reappeared. When the  $Y_1$  powder was ground, its fluorescence was converted to orange similar to that of the  $O_1$  form. In this way, a reversible four-color luminescence switching built upon a single AIEEgen in the solid state has been achieved (Fig.1.15).

The AIEE research is fast developing in recent years, resulting in the accumulation of a wealth of information on structural design of AIEE luminogens and mechanistic understanding of AIEE processes.

## References:

1. E. Roduner, *Nanoscopic Materials: Size-Dependent Phenomena*. The Royal Society of Chemistry, Cambridge, **2006**.
2. J. Jortner, *Z. Phys. D: At., Mol. Clusters* 24, **1992**, 247.
3. X. Zhang, X. Zhang, K. Zou, C.S. Lee and S.T Lee, *J. Am. Chem. Soc.* 129, **2007**, 3527.
4. H. Wang, X. Xu, A. Kojtari and H.F. Ji, *J. Phys. Chem. C* 115, **2011**, 20091.
5. J.Y. Hu, Y.J. Pu, F. Satoh, S. Kawata, H. Katagiri, H. Sasabe and J. Kido, *Adv. Funct. Mater.* 24, **2014**, 2064.
6. H. Liu, Y. Li, S. Xiao, H. Gan, T. Jiu, H. Li, L. Jiang, D. Zhu, D. Yu, B. Xiang and Y. Chen, *J. Am. Chem. Soc.* 125, **2003**, 10794.
7. A. Peng, D. Xiao, Y. Ma, W. Yang and J. Yao, *Adv. Mater.* 17, **2005**, 2070.
8. L. Zang, Y. Che and J.S. Moore, *Acc. Chem. Res.* 41, **2008**, 1596.
9. A. Jana, K.S.P. Devi, T.K. Maiti and N.D. Pradeep Singh, *J. Am. Chem. Soc.* 134, **2012**, 7656.
10. C. Sanchez, P. Belleville, M. Popall and L. Nicole, *Chem. Soc. Rev.* 40, **2011**, 696.
11. T.M. Figueira-Duarte and K. Mullen, *Chem. Rev.* 111, **2011**, 7260.
12. B.K. An, S.K. Kwon, S.D. Jung and S.Y. Park, *J. Am. Chem. Soc.* 124, **2002**, 14410.
13. K. Panthi, R.M. Adhikari and T. H. Kinstle, *J. Phys. Chem. A* 114, **2010**, 4550.
14. H. Yu and L. Qi, *Langmuir* 25, **2009**, 6781.
15. K. Ujiye-Ishii, E. Kwon, H. Kasai, H. Nakanishi and H. Oikawa, *Cryst. Growth & Des.* 8, **2008**, 369.
16. C. Shi, Z. Guo, Y. Yan, S. Zhu, Y. Xie, Y. S. Zhao, W. Zhu and H. Tian, *ACS Appl. Mater. Interfaces* 5, **2013**, 192.
17. Z. Wang, H. Mohwald and C. Gao, *ACS Nano*, 5, **2011**, 3930.
18. Y. S. Zhao, W. Yang, G. Zhang, Y. Ma and J. Yao, *Colloids Surf. A* 277, **2006**, 111.
19. Y. S. Zhao, W. Yang, D. Xiao, X. Sheng, X. Yang, Z. Shuai, Y. Luo and J. Yao, *Chem. Mater.* 17, **2005**, 6430.
20. Z. Zhang, G. Li, Y. Ma and J. Shen, *Mater. Chem. Phys.* 82, **2003**, 613.
21. H. Fu, B. H. Loo, D. Xiao, R. Xie, X. Ji, J. Yao, B. Zhang and L. Zhang, *Angew. Chem.* 41, **2002**, 1433.
22. B.K An, S.K Kwon, S.D Jung and S.Y. Park, *J. Am. Chem. Soc.* 124, **2002**, 14410.
23. Z. Wang, M. Liu, Y. Xie and C. Gao, *J. Mater. Chem.* 22, **2012**, 2855.
24. A. Datar, K. Balakrishnan, X. Yang, X. Zuo, J. Huang, R. Oitker, M. Yen, J. Zhao, D.M. Tiede and L. Zang, *J. Phys. Chem. B* 110, **2006**, 12327.
25. S.P. Anthony and S.M. Draper, *J. Phys. Chem. C* 114, **2010**, 11708.
26. Y.S. Zhao, D. Xiao, W. Yang, A. Peng and J. Yao, *Chem. Mater.* 18, **2006**, 2302.
27. C. Zhang, Y. Yan, Y.S. Zhao and J. Yao, *Annu. Rep. Prog. Chem., Sect. C: Phys. Chem.* 109, **2013**, 211.
28. T. Förster and K. Kasper, *Z. Phys. Chem. (Muenchen, Ger.)* 1, **1954**, 275.
29. J. B. Birks, Ed.; Wiley: London, *Photophysics of Aromatic Molecules*; **1970**.
30. J. Luo, Z. Xie, J. W. Y. Lam, L. Cheng, B. Z. Tang, H. Chen, C. Qiu, H. S. Zhan, X. Kwok and Y. Liu, *Chem. Commun.*, **2001**, 1740.
31. B.K. An, S.K. Kwon, S.D. Jung and S. Y. Park, *J. Am. Chem. Soc.*, 124, **2002**, 14410.
32. Y. Hong, J.W. Y. Lam and B. Z. Tang, *Chem. Soc. Rev.*, 40, **2011**, 5361.

33. Z. Zhao, J. W. Y. Lam and B. Z. Tang, *J. Mater. Chem.*, **22**, **2012**, 23726.
34. Z. Wang, H. Shao, J. Ye, L. Tang and P. Lu, *J. Phys. Chem. B*, **109**, **2005**, 19627.
35. H. Jiating, X. Bin, C. Feipeng, X. Haijian, L. Kunpeng, Y. Ling and T. Wenjing, *J. Phys. Chem. C*, **113**, **2009**, 9892.
36. J. Luo, K. Song, F. I. Gub and Q. Miao, *Chem. Sci.*, **2**, **2011**, 2029.
37. N. L. C. Leung, N. Xie, W. Yuan, Y. Liu, Q. Wu, Q. Peng, Q. Miao, J. W. Y. Lam and B. Z. Tang, *Chem. Eur. J.*, **20**, **2014**, 15349.
38. T. Nishiuchi, K. Tanaka, Y. Kuwatani, J. Sung, T. Nishinaga, D. Kim and M. Iyoda, *Chem. Eur. J.* **19**, **2013**, 4110.
39. L. Yao, S. Zhang, R. Wang, W. Li, F. Shen, B. Yang and Y. Ma, *Angew.Chem., Int. Ed.* **53**, **2014**, 2119.
40. J. Liu, Q. Meng, X. Zhang, X. Lu, P. He, L. Jiang, H. Dong and W. Hu, *Chem. Commun.* **49**, **2013**, 1199.
41. C. Zhang, Z. Wang, S. Song, X. Meng, Y.S. Zheng, X.L. Yang and H.B. Xu, *J. Org. Chem.* **79**, **2014**, 2729.
42. W. Z. Yuan, P. Lu, S. Chen, J. W. Y. Lam, Z. Wang, Y. Liu, H. S. Kwok and B. Z. Tang, *Adv. Mater.* **22**, **2010**, 2159.
43. C. Deng , Y. Niu , Q. Peng , A. Qin , Z. Shuai and B. Z. Tang , *J. Chem.Phys.* **135**, **2011**, 14304.
44. H. Jiating, X. Bin, C. Feipeng, X. Haijian, L. Kunpeng, Y. Ling and T. Wenjing, *J. Phys. Chem. C* **113**, **2009**, 9892.
45. C. J. Bhongale, C. W. Chang, C. S. Lee, E. W. G. Diau and C. S. Hsu, *J. Phys. Chem. B* **109** , **2005** , 13472.
46. M. Shimizu, H. Tatsumi, K. Mochida, K. Shimono and T. Hiyama, *Chem.-Asian J.* **4**, **2009**, 1289.
47. T. L. Bandrowsky, J. B. Carroll and J. Braddock-Wilking, *Organometallics*, **30**, **2011**, 3559.
48. Y. Ren and T. Baumgartner, *Inorg.Chem.* **51**, **2012**, 2669.
49. C. T. Lai and J. L. Hong, *J. Phys. Chem. B* **114**, **2010**, 10302.
50. A. A. Jahnke and D. S Seferos., *Macromol. Rapid Commun.* **32**, **2011**, 943.
51. P. Galer, R. C. Korosec, M. Vidmar and B. Sket, *J. Am. Chem. Soc.* **136**, **2014**, 7383.
52. X. Cheng, D. Li, Z. Zhang, H. Zhang and Y. Wang, *Org. Lett.* **16**, **2014**, 880.
53. S. Inagi, K. Hosoi, T. Kubo, N. Shida, T. Fuchigami, *Electrochemistry* **81**, **2013**, 368.
54. K. Kokado, A. Nagai and Y. Chujo, *Tetrahedron Lett.* **52**, **2011**, 293.
55. Z. Yu, Y. Duan, L. Cheng, Z. Han, Z. Zheng, H. Zhou, J. Wu and Y. Tian, *J. Mater. Chem.* **22**, **2012**, 16927.
56. G. Liu, M. Yang, L. Wang, J. Zheng, H. Zhou, J. Wu and Y. Tian, *J. Mater. Chem. C* **2**, **2014**, 2684.
57. T. Han, Y. Hong, N. Xie, S. Chen, N. Zhao, E. Zhao, J. W. Y. Lam, H. H. Y. Sung, Y. Dong and B. Tong, *J. Mater. Chem. C* **1**, **2013**, 7314.
58. Y. Qian, M. Cai, X. Zhou, Z. Gao, X. Wang, Y. Zhao, X. Yan, W. Wei, L. Xie and W. Huang, *J. Phys. Chem. C*, **116**, **2012**, 12187.
59. Y. Zhao, H. Lin, M. Chen and D. Yan, *Ind. Eng. Chem. Res.* **53**, **2014**, 3140.
60. H. M. Krishna Murthy and M. Vijayan, *Acta Crystallogr., Sect. B: Struct. Crystallogr. Cryst. Chem.* **35**, **1979**, 262.
61. T. Beppu, S. Kawata, N. Aizawa, Y.J. Pu, Y. Abe, Y. Ohba and H. Katagiri, *ChemPlusChem* **79**, **2014**, 536.
62. H. Tong, Y. Hong, Y. Dong, Y. Ren, M. Halussler, J. W. Y. Lam, K. S. Wong, and B. Z. Tang, *J. Phys. Chem. B*, **111**, **2007**, 2000.

63. R. Hu, J. L. Maldonado, M. Rodriguez, C. Deng, C. K. W. Jim, J. W. Y. Lam, M. M. F. Yuen, G. Ramos-Ortiz and B. Z. Tang, *J. Mater. Chem.* 22, **2012**, 232.
64. W. Z. Yuan, H. Zhao, X. Y. Shen, F. Mahtab, J. W. Y. Lam, J. Z. Sun and B. Z. Tang, *Macromolecules* 42, **2009**, 9400.
65. C. Ma, Q. Ling, S. Xu, H. Zhu, G. Zhang, X. Zhou, Z. Chi, S. Liu, Y. Zhang and J. Xu, *Macromol. Biosci.* 14, **2014**, 235.
66. R.H. Chien, C.T. Lai and J. L. Hong, *J. Phys. Chem. C* 115, **2011**, 5958.
67. C. A. Chou, R. H. Chien, C. T. Lai and J. L. Hong, *Chem. Phys. Lett.* 501, **2010**, 80.
68. K. Shiraishi, T. Kashiwabara, T. Sanji and M. Tanaka, *New J. Chem.* 33, **2009**, 1680.
69. G. Huang, B. Ma, J. Chen, Q. Peng, G. Zhang, Q. Fan and D. Zhang, *Chem. - Eur. J.* 18, **2012**, 3886.
70. Y. Zeng, P. Li, X. Liu, T. Yu, J. Chen, G. Yang and Y. Li, *Polym. Chem.* 5, **2014**, 5978.
71. J. Wang, J. Mei, W. Yuan, P. Lu, A. Qin, J. Sun, Y. Ma and B. Z. Tang, *J. Mater. Chem.* 21, **2011**, 4056.
72. R. Hu, J. W. Y. Lam, J. Liu, H. H. Y. Sung, I. D. Williams, Z. Yue, K. S. Wong, M. M. F. Yuen and B. Z. Tang, *Polym. Chem.* 3, **2012**, 1481.
73. J. Liang, Z. Chen, L. Xu, J. Wang, J. Yin, G.A. Yu, Z. N. Chen and S. H. Liu, *J. Mater. Chem. C*, 2, **2014**, 2243.
74. M. X. Zhu, W. Lu, N. Y. Zhu and C. M. Che, *Chem.-Eur. J.*, 14, **2008**, 9736.
75. B. Manimaran, P. Thanasekaran, T. Rajendran, R. J. Lin, I. J. Chang, G. H. Lee, S. M. Peng, S. Rajagopal and K. L. Lu, *Inorg. Chem.*, 41, **2002**, 5323.
76. J. Mei, Y. Hong, J. W. Y. Lam, A. Qin, Y. Tang, and B. Z. Tang, *Adv. Mater.* 26, **2014**, 5429.
77. Q. Zhu, L. Huang, Z. Chen, S. Zheng, L. Lv, Z. Zhu, D. Cao, H. Jiang and S. Liu, *Chem. - Eur. J.* 19, **2013**, 1268.
78. W. Z. Yuan, X.Y. Shen, H. Zhao, J. W. Y. Lam, L. Tang, P. Lu, C. Wang, Y. Liu, Z. Wang, Q. Zheng, J. Z. Sun, Y. Ma and B. Z. Tang, *J. Phys. Chem. C* 114, **2010**, 6090.
79. K. Bhattacharyya and M. Chowdhury, *Chem. Rev.*, 93, **1993**, 507.
80. H. Tong, Y. Dong, M. Haeussler, Y. Hong, J. W. Y. Lam, H. H. Y. Sung, I. D. Williams, H. S. Kwok and B. Z. Tang, *Chem. Phys. Lett.*, 428, **2006**, 326.
81. R. Hu, E. Lager, A. A. Aguilar, J. Liu, J. W. Y. Lam, H. H. Y. Sung, I. D. Williams, Y. Zhong, K. S. Wong, E. P. Cabrera, and B. Z. Tang, *J. Phys. Chem. C* 113, **2009**, 15845.
82. Y. Liu, C. Deng, L. Tang, A. Qin, R. Hu, J. Z. Sun and B. Z. Tang, *J. Am. Chem. Soc.* 133, **2011**, 660.
83. X. Chen, Y. Zhou, X. Peng and J. Yoon, *Chem. Soc. Rev.* 39, **2010**, 2120.
84. B. M. Riederer, *Oxidation Proteomics: Curr. Proteomics* 6, **2009**, 51.
85. D. M. Townsend, K. D. Tew and H. Tapiero, *Pharmacother.* 57, **2003**, 145.
86. Y. Zhou and J. Yoon, *Chem. Soc. Rev.* 41, **2012**, 52.
87. M. Zhang, M. X. Yu, F. Y. Li, M. W. Zhu, M. Y. Li, Y. H. Gao, L. Li, Z. Q. Liu, J. P. Zhang and D. Q. Zhang, *J. Am. Chem. Soc.* 129, **2007**, 10322.
88. L. Peng, Z. Zhou, R. Wei, K. Li, P. Song and A. A. Tong, *Dyes Pigm.* 108, **2014**, 24.
89. J. Tong, Y. Wang, J. Mei, J. Wang, A. Qin, J. Z. Sun and B. Z. Tang, *Chem. - Eur. J.* 20, **2014**, 4661.
90. D. L. Rabenstein, *Nat. Prod. Rep.* 19, **2002**, 312.

91. Y. Yu, J. Liu, Z. Zhao, K. M. Ng, K. Q. Luo and B. Z. Tang, *Chem. Commun.* 48, **2012**, 6360.
92. X. Wang, J. Hu, T. Liu, G. Zhang and S. Liu, *J. Mater. Chem.* 22, **2012**, 8622.
93. X. Huang, X. Gu, G. Zhang and D. Zhang, *Chem. Commun.* 48, **2012**, 12195.
94. Z. Yang, W. Qin, J. W. Y. Lam, S. Chen, H. H. Y. Sung, I. D. Williams and B. Z. Tang, *Chem. Sci.*, 4, **2013**, 3725.
95. Y. Liu, Y. H. Tang, N. N. Barashkov, I. S. Irgibaeva, J. W. Y. Lam, R. R. Hu, D. Birimzhanova, Y. Yu and B. Z. Tang, *J. Am. Chem. Soc.* 132, **2010**, 13951.
96. G. He, H. Peng, T. Liu, M. Yang, Y. Zhang and Y. Fang, *J. Mater. Chem.* 19, **2009**, 7347.
97. R. Saferstein, *Criminalistics: An Introduction to Forensic Science*, **2006**.
98. Y. Li, L. Xu and B. Su, *Chem. Commun.* 48, **2012**, 4109.
99. Z. J. Zhao, S. M. Chen, X. Y. Shen, F. Mahtab, Y. Yu, P. Lu, J. W. Y. Lam, H. S. Kwok and B. Z. Tang, *Chem. Commun.* 46, **2010**, 686.
100. Z. Zhao, Z. Li, J. W. Y. Lam, J. L. Maldonado, G. Ramos-Ortiz, Y. Liu, W. Yuan, J. Xu, Q. Miao and B. Z. Tang, *Chem. Commun.* 47, **2011**, 6924.
101. X. Gu, J. Yao, G. Zhang, Y. Yan, C. Zhang, Q. Peng, Q. Liao, Y. Wu, Z. Xu and Y. Zhao, *Adv. Funct. Mater.* 22, **2012**, 4862.
102. Z. Zhao, D. Liu, F. Mahtab, L. Xin, Z. Shen, Y. Yu, C. Y. K. Chan, P. Lu, J. W. Y. Lam and H. H. Y. Sung, *Chem. Eur. J.* 17, **2011**, 5998.
103. Y. Li, Z. Li, Y. Wang, A. Compaan, T. Ren and W. J. Dong, *Energy Environ. Sci.* 6, **2013**, 2907.
104. J. Wang, J. Mei, R. Hu, J. Z. Sun, A. Qin and B. Z. Tang, *J. Am. Chem. Soc.* 134, **2012**, 9956.
105. J. Liang, Z. Chen, J. Yin, G. A. Yu and S. H. Liu, *Chem. Commun.* 49, **2013**, 3567.
106. J. J. Peterson, A. R. Davis, M. Werre, E. B. Coughlin and K. R. Carter, *ACS Appl. Mater. Interfaces* 3, **2011**, 1796.
107. C. Y. Y. Yu, R. T. K. Kwok, J. Mei, Y. Hong, S. Chen, J. W. Y. Lam and B. Z. Tang, *Chem. Commun.* 50, **2014**, 8134.
108. C. Ma, B. Xu, G. Xie, J. He, X. Zhou, B. Peng, L. Jiang, B. Xu, W. Tian, Z. Chi, S. Liu, Y. Zhang and J. Xu, *Chem. Commun.* 50, **2014**, 7374.



*CHAPTER*  
**2**

**Synthesis of Low Dimensional Organic  
Particles: A General Overview**

## 2.1. Introduction:

During last decades scientists involved themselves not only in fabrication of new low dimensional materials with desirable applications they also developed many new techniques and designed these to explore interesting properties in nano/micro range. Synthesis of nanoparticles ranging from 1-100nm and microparticles ranging from 1-100 $\mu$ m has been intensively pursued over the last 30 years, not only for their scientific interest, but also for their many technological applications. Organic polyhedron with diverse shapes, sizes and compositions are of interest because these factors not only attract fundamental interests but also effect physical properties and their applications such as field-effect transistors, chemical sensors, solar cells, memory elements, optical waveguides, lasers, and color-tunable displays etc [1-7]. However, rather weak supramolecular interactions, complicated mechanism of kinetic growth and the unclear correlation between crystal morphology and molecular configuration make it a great challenge to controllably synthesize a highly symmetric polyhedron from organic synthons. This includes zero dimensional (0-D) spherical or tetrahedral quantum dots, one-dimensional (1-D) nano rods and wires from small organic compound, two-dimensional (2-D) nanoplates, nano ribbon and nanotube, microcapsule, organic nano flower, sub-microtube and three dimensional highly symmetrical small molecular organic microcrystals with shapes, range from cubes through truncated cubes to rhombic dodecahedra [8-15]. The basic principle for the synthesis of low dimensional

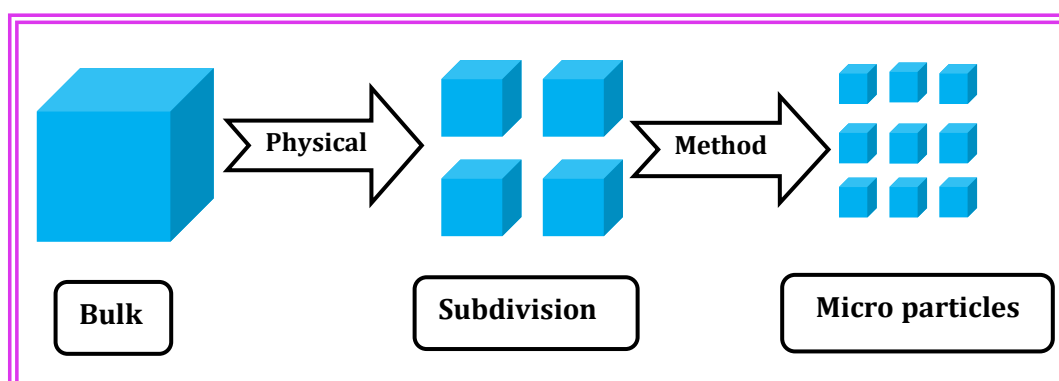


materials is to produce a large number of nuclei and to inhibit the growth and aggregation of grains. There are two different approaches to synthesize low dimensional materials:

- (i) Top-down approach, which utilized physical methods
- (ii) Bottom-up approach, which employs solution phase colloidal chemistry.

## 2.2. Top-Down method:

The “top-down” approach (Scheme 2.1) involves the production of the nanoparticles by breaking larger materials into fine particles, or other definition says “top-down” approach begins with a suitable starting material and then sculpts the functionality from the materials. Top-down approaches include attrition, repeated quenching and lithography. Attrition can produce microparticles ranging from a couple of tens to several hundreds of micrometers in diameter. However microparticles produced by attrition have a relatively broad size distribution, contain significant amount of impurities and defects.



**Scheme 2.1: Schematic representation of ‘top-down’ approach.**

There are several physical methods of this approach-(i) Electro spinning method, (ii) LASER ablation approach, (iii) Direct condensation method, (iv) Molecular beam deposition method and (v) Physical vapour deposition, etc.

**2.2.1. Electro spinning Method:** Electrospinning provides a simple and versatile method for generating ultrathin fibers from a rich variety of materials that includes polymers,

composite and ceramics. Electro spinning uses an electrical charge to draw very fine (typically on the microscale) fibres from a liquid. It shares characteristics of both electro spraying and conventional solution dry spinning of fibres. When a sufficiently high voltage is applied to a liquid droplet, the body of liquid becomes charged and electrostatic repulsion counteracts the surface tension and the droplet is stretched at a critical point a stream of liquid erupts from the surface. This point of eruption is known as the Taylor cone. If the molecular cohesion of the liquid is sufficiently high, stream breakup does not occur and a charged liquid jet is formed. As the jet dries in flight, the mode of current flow changes from ohmic to convective as the charge migrates to the surface of the fibre. The jet is then elongated by a whipping process caused by electrostatic repulsion initiated at small bends in the fibre, until it is finally deposited on the grounded collector. The elongation and thinning of the fibre resulting from this bending instability leads to the formation of uniform fibres with micrometer scale diameters. These ultrafine fibres have two main properties, a very high surface to volume ratio and a relatively defect free structure at the molecular level. This method is utilized for processing of rich variety of organic polymers, ceramics, and composite materials into ultrathin fibre with controllable diameter [16]. Now a day's electro spinning is one of the mostly accepted choices for preparing 1D microfiber.

**2.2.2. LASER ablation approach:** LASER ablation is the process of removing material from a solution surface by irradiating it with a laser beam. At low laser flux, the material is heated by absorbed laser energy and evaporates. At high laser flux, the material is typically converted to plasma. Usually, laser ablation refers to removing materials with a pulsed laser, but it is possible to ablate materials with a continuous wave laser beam if laser intensity is high enough. The depth over which the laser energy is absorbed and thus the amount of material removed by a single laser pulse, depends on the materials' optical properties and the laser wavelength and pulse length. In laser ablation synthesis,

nanomaterials are deposited on a substrate in vacuum or inert phase, where as in liquid environment, nanoparticles stabilized in colloidal solution in a variety of solvents. The fundamental (1064 nm) output from a Q-switched Nd:YAG laser or the IR output from the Nd:YAG operating at 10 Hz are focused onto the metal plate with 10-cm focal-length lens. The solution was continuously stirred during the ablation and the laser influence was varied from 30 to 80 mJ/pulse. By tuning laser wavelength, pulse width and total shot number, the size and phase of the microparticles can be controlled [17]. Recently, laser ablation technique applied for preparation of organic nanoparticles, where some phthalocyanines and aromatic hydrocarbons were adopted. In this method, organic crystalline powders suspended in a poor solvent are exposed to a laser beam, which induces fragmentation of the initial crystals. Consequently, the opaque suspension is converted into a transparent colloidal solution [18].

**2.2.3. Direct Condensation Method:** Direct condensation is a novel and versatile approach for the preparation of concentrated dispersions of organic nanoparticles by direct condensation of an organic material into a liquid dispersion medium. The apparatus consists of four main parts: a tube furnace, a double-walled heated-vapor injection tube, a condensation and receiving vessel, and a vacuum pumping system. The tube furnace is heated by resistive heating and can be purged by inert gas (argon) via a valve and a mass-flow control unit. It consists of a preheating zone for the inert gas stream and an evaporation zone containing a crucible filled with the organic material, which is evaporated into the inert-carrier-gas stream. The tube furnace is connected via a spherical joint to the vapor-injection tube, which guides the inert-carrier-gas stream and vapor of the organic material into a liquid condensation medium (vapor transport zone). This vapor-injection tube is constructed as a double-walled structure, where the inner wall is heated by resistive heating and the outer wall provides electrical and thermal insulation to the surrounding liquid condensation medium.

Three aromatic hydrocarbons (pentacene, rubrene, and tetracene) commonly applied in organic electronics were used for this study [19].

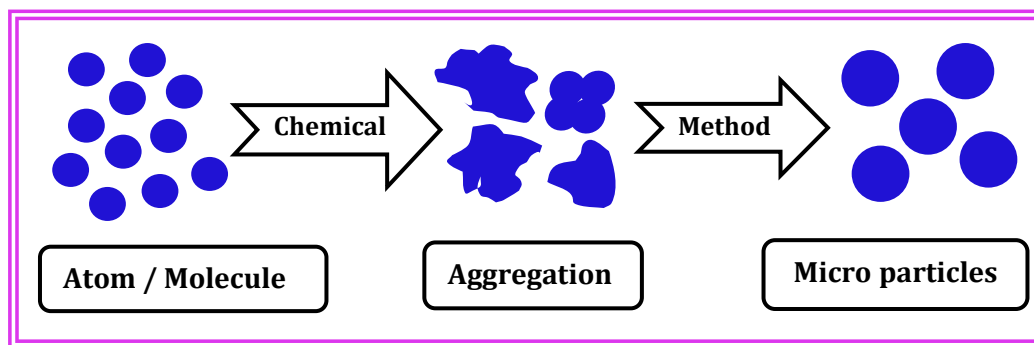
**2.2.4. Molecular beam deposition Method:** Molecular beam deposition is one of several methods of depositing single crystals. This method takes place in high vacuum or ultra-high vacuum ( $10^{-8}$  Pa). The most important aspect of this method is deposition rate which allow the films to grow epitaxially. The absence of carrier gases as well as the ultra high vacuum environment, results in the highest achievable purity of the grown films. This method is widely used in the manufacture of semiconductor devices [20]. This method is used to grow polycrystalline pentacene channel thin-film transistors.

**2.2.5. Physical vapor deposition Method:** Physical vapor deposition (PVD) describes a variety of vacuum deposition methods used to deposit thin films by the condensation of a vaporized form of the desired film material onto various work piece surfaces. The coating method involves purely physical processes such as high temperature vacuum evaporation with subsequent condensation, or plasma sputter bombardment. Yao *et al.* introduced the adsorbent-assisted PVD method to doped binary organic systems [21].

### 2.3. Bottom-Up method:

This approach refers to the building-up of material from the bottom- atom by atom, molecule by molecule or cluster by cluster (Scheme 2.2). The bottom-up approach can be grouped into two categories: thermodynamic equilibrium approach and kinetic approach. The thermodynamic approach consists of (i) generation of super saturation, (ii) nucleation, and (iii) growth. In kinetic approach, formation of nano/micro particles consists of limiting amount of precursors for the growth. The bottom-up approach consists of chemical methods are based on solution-phase colloidal chemistry. Uniformed size distributions of the

nano/micro particles with various sizes and shapes have been synthesized over the last ten years by using chemical methods. The advantage of the top-down approach is; it produces large quantity of nano/micro particles whereas it is very difficult to control the size of nano/micro particles. In contrast bottom-up approaches can be used to synthesize uniform nano/micro particles with controlled size and shape.



**Scheme 2.2: Schematic representation of 'bottom-up' approach.**

The growth of nano/micro particles involves the processes of precipitation of a solid phase from solution. For a particular solvent, there is certain solubility for a solute, whereby addition of any excess solute will result in precipitation and formation of nano/micro particles. Thus to form nano/micro particles and nucleation to occur the solution must be super saturated either by directly dissolving the solute at higher temperature and then cooling to low temperature or by adding foreign substance to make it super saturated [22,23]. The precipitation processes then basically consists of a nucleation step followed by particle growth stage [24]. Generally there are three kinds of nucleation processes: homogeneous nucleation, heterogeneous nucleation and secondary nucleation. Homogeneous nucleation occurs in the absence of a solid interface by combining solute molecules to produce nuclei. Fundamentals of homogenous nucleation demands that when the concentration of solute in a solvent exceeds its equilibrium solubility or temperature decreases below the phase transformation points, a new phase appears. A supersaturated solution possesses high Gibbs

free energy ( $\Delta G$ ). This free energy ( $\Delta G$ ) is the sum of free energy due to the formation of a new volume and free energy due to new surface created. For spherical particles,

$$\Delta G = \frac{4}{V} \pi r^3 K_B T \ln(S) + 4\pi r^2 \gamma$$

Where  $V$  is the molecular volume of the precipitated species,  $r$  is the radius of the nuclei,  $K_B$  is the Boltzmann constant,  $S$  is the saturation ratio and  $\gamma$  is the surface free energy per unit surface area. When  $S > 1$ ,  $\Delta G$  has a positive maxima at a critical size ( $r^*$ ). This maximum free energy is the activation energy for nucleation (Fig. 2.1). Nuclei larger than the critical size will further decrease their free energy for growth and form stable nuclei that grow to form particles. The critical nuclei size is-

$$\frac{d\Delta G}{dr} = 0 \qquad r^* = \frac{2V\gamma}{3K_B T \ln(S)}$$

After the initial nucleation, the super saturation of the growth species decreases and the change in Gibbs free energy reduces. When the concentration decreases below this specific concentration, nucleation stops and the particles continue to grow by molecular addition until the equilibrium concentration of the precipitated species is reached. Uniform size distribution is achieved through a short nucleation processes that generates all the particles obtained at the end of reaction followed by self-sharpening growth process. Due to large free energy for smaller particles than the larger ones, the smaller particles grow more rapidly than the larger one. On the other hand when the reactants are depleted due to particle growth, Ostwald ripening will occur where larger particles grow and smaller ones get smaller and finally dissolved. Actually Ostwald ripening occurs when saturation ratio ( $S$ ) decreases and corresponding critical size ( $r^*$ ) increases.

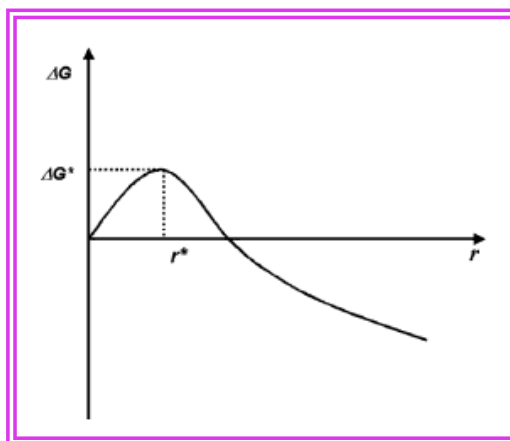


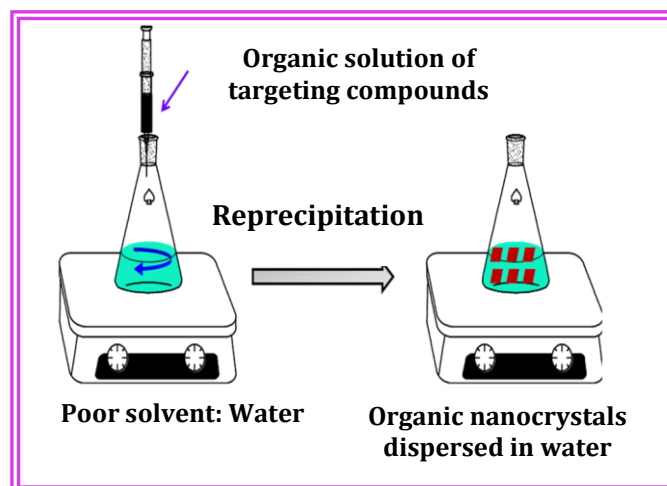
**Figure 2.1:** Plot of change in overall free energy ( $\Delta G$ ) as a function of particle size ( $r$ ).

If the reaction stops quickly at this stage the particles have a broad size distribution. In addition to this another type of growth processes occurs, where soluble species deposit on the solid surface, particles can grow by aggregation with other particles, which is known as secondary growth process. The rate of particle growth is much faster in secondary growth process than the growth occurs by molecular addition process.

The bottom-up approach consists of chemical methods are based on solution-phase colloidal chemistry. Uniformed size distributions of the microparticles with various sizes and shapes have been synthesized over the last ten years by using chemical methods. There are several chemical methods including (i) Reprecipitation, (ii) Chemical reduction, (iii) Microemulsion, (iv) Hydrothermal or Solvothermal, (v) Sonochemical, (vi) Sol-gel method, (vii) Post Chemistry and (viii) Direct Writing method for generation of organic microparticles.

**2.3.1. Reprecipitation Method:** Reprecipitation, which is a solvent displacement method, was first reported by Nakanishi and coworkers [25-27]. It provides a very simple and versatile way to prepare organic nanoparticle dispersions. The method involves a rapid mixing of a small amount of concentrated stock solution of the target compound dissolved in a good solvent with excess of a poor solvent. The schematic images of the reprecipitation

method are shown in Scheme 2.3. The great disparity between the solubilities of the target compound in the good and poor solvents and the good compatibility of the two solvents are essential for this method. It is supposed that the rapid mixing of the stock solution and the poor solvent changes the micro-environment of the target compound molecules. The molecules are exposed to the poor solvent surroundings in a very short time, inducing the nucleation and growth of the molecules to nanoparticles. The sudden exchanges of solubility from good to poor cause the precipitation, and when the concentration, temperature, and kinds of solvent are adequately selected, nanocrystals are stably dispersed in water, with usually giving the negative charged  $\zeta$ -potential on the surface of nanocrystals. The  $\zeta$ -potential helps nanocrystals for preventing their aggregation because of the created balanced stability by negative charged repulsion force of them.



**Scheme 2.3: The Scheme of Reprecipitation method.**

With this method, a series of organic nanoparticles were successfully fabricated by several groups. For example, after their pioneer work on this method, Nakanishi and coworkers prepared perylene nanoparticles and observed the emissions from both free excitons and self-trapped excitons [28, 29]. Horn and coworkers prepared nanoparticles from b-carotene and observed the influence of both supramolecular structure and particle size on



the absorption spectra [30]. Majima's group [31] and Barbara's group [32] prepared nanocrystals from perylene and a perylene derivative, respectively.

**2.3.2. Chemical reduction Method:** Although reprecipitation is a facile approach to organic nanoparticles, it is difficult to form kinetically stable nanoparticles dispersions. Large-scale synthesis is limited by the solubility of the target compound in the good solvent. Moreover, the heterogeneous environment of this method makes it difficult to precisely control the complicated nucleation process in the initial stages and the subsequent fast growth [33]. Yao and coworkers developed a colloid chemical reaction method to overcome these problems [34]. With this method, the perylene nanoparticles were prepared by the reduction of perylene perchlorate by  $\text{Br}^-$  anions [35] in the presence of cetyl trimethylammonium bromide (CTAB) in acetonitrile. The large-scale synthesis of perylene nanoparticles ranging from 25 to 90nm with a polydispersity of <10% was achieved by changing the molar ratio of CTAB to perylene perchlorate. The homogeneous solution phase in this method provides several advantages, including facile separation of the nucleation and growth stages and better controllability of the growth parameters, through which size control of the organic nanoparticles was realized.

**2.3.3. Microemulsion Method:** Among the different methods the microemulsion has been demonstrated as a very versatile and reproducible method that allows to control over the nanoparticle size and yields nanoparticles with a narrow size distribution. Microemulsions are homogeneous in macroscale and micro heterogeneous in nanoscale dispersion of two immiscible liquids consisting of nanosized domains of one or both liquids in the other, stabilized by an interfacial film of surface active molecules. The essential distinction between normal emulsion and microemulsion is their particle size and stability. Microemulsions are thermodynamically stable, single optically isotropic and usually form spontaneously.

Microemulsions have ultralow interfacial tension, large interfacial area and capacity to solubilize both aqueous and oil-soluble compounds. Depending on the proportion of various components and hydrophilic-lypophilic balance (HLB) value of the used surfactant microemulsions can be classified as water-in-oil (W/O), oil-in-water (O/W) and intermediate bicontinuous structural types that can turn reversibly from one type to the other. Organic nanoparticles of cholesterol, Rhovanil, and Rhodiarome have been synthesized in different microemulsions (AOT/heptane/water; Triton/decanol/water; CTABr/hexanol/water) by direct precipitation of the active compound in aqueous core. The size of the nanoparticles depends on different parameters such as the concentration of the organic molecules and the diameter of the water cores which is related to the ratio  $R = [\text{H}_2\text{O}]/[\text{surfactant}]$ . Different solvents are used to solubilize the organic molecules, but the average diameter of the particles does not change. The solvents are considered as a carrier vector for the organic molecules and do not influence the precipitation in a significant way [36].

**2.3.4. Hydrothermal or Solvothermal Method:** Performing a chemical reduction in a sealed vessel (bomb, autoclave etc.) solvent can be brought to temperatures well above their boiling points by the increase in autogenously pressure resulting from heating, is referred to as solvothermal method or hydrothermal processing [37]. The temperature and pressure above the critical point of any solvent is said to be supercritical. Supercritical fluids exhibits characteristics of both a liquid and gas: the interface of solids and supercritical fluids lack surface tension, yet supercritical fluids exhibits high viscosity and easily dissolve chemical compounds that would exhibits very low solubility under ambient condition. Cyanuric acid (CA) and melamine (M) are both highly hydrogen bonded solids melting at high temperatures, with limited solubility in most organic solvents. So the adduct formation in between these are quite difficult in normal condition. Rao *et al.* have synthesized the 1:1 hydrogen-bonded adduct between CA and M forming rosettes structure by

hydrothermal method. This drastic condition in reaction mixture can break the self hydrogen bonding interactions and help them to be solubilized [38].

**2.3.5. Sonochemical Method:** Nano/micro crystals with definite morphologies and optical properties were successfully fabricated from an organic functional low molecular weight compound, through an ultra-sonication technique. In a typical fabrication, silicon or quartz wafers with an area of  $1 \times 1 \text{ cm}^2$  were first suspended in organic molecule solutions with various solvents and concentrations. The solutions were subsequently put into a commercial ultrasonic cleaning bath in the open. The solvents volatilized as the sonication proceeded, and the organic molecules assembled into nano/micro crystals spontaneously on the surfaces of the substrates. Yao *et al.* undergoes controllable synthesis through sonication technique for the fabrication of 2,4,5-triphenylimidazole nanoparticles [39]. Sonication method can prove the indispensability for formation of well-defined lophine nanocrystals.

**2.3.6. Sol-gel Method:** A gel denotes a dilute mixture of at least two components, in which each of the components forms a separate continuous phase throughout the system. Generally, gels are divided into two groups, chemical gels and physical gels, depending on the type of interactions that hold the network structure together. The gels formed from low molecular mass organo-gelators (LMOGs) belong to the physical type, because the network structures are held together by non covalent interactions such as hydrogen bonding or  $\pi$ - $\pi$  stacking, and, in addition, solvophobic and entropy effects are also very important in the formation of organogels. It has been realized that forming organogels is a very effective way to construct organic 1D nanomaterials with a variety of structures and properties. Usually, long alkyl chains or steroidal groups are incorporated into most gelator molecular structures to achieve effective gelation, although these structural elements are normally inactive and undesirable for the optoelectronic properties. Park and coworkers reported a new class of

LMOGs, 1-cyano-trans-1,2-bis(3,5-bistrifluoromethyl-biphenyl)ethylene (CN-TFMBE) with simple  $\text{CF}_3$  substituents [40]. The thermo reversible gels were obtained by the gelation of dichloroethane by CN-TFMBE.

**2.3.7. Post Chemistry Method:** Post Chemistry involved the contamination of precipitate by an insoluble compounds after the major of the precipitate is formed. The supersaturated solution of the second material is formed on the surface of the particle and that offers nucleation sites to break supersaturation and cause the secondary precipitate to form. The impurities are trapped as mother liquor during aging of precipitate. The materials chosen for this work were aqueous tetrathiafulvalene (TTF) microparticles and 7,7',8,8'-tetracyanoquinodimethane (TCNQ) microstructures. TTF-TCNQ is a well-known organic charge-transfer (CT) salt that has a well-defined quasi-one dimensional structure with a high electronic conductivity [41]. TTF microparticles were prepared in water using surfactants. In this process, TCNQ acetonitrile solution were rapidly injected to develop TCNQ trapped TTF microparticles in order to improve their high electrical conductivity.

**2.3.8. Direct writing Method:** Direct writing is a method in which the fabrication and interconnection of nanodevices on semiconducting surfaces such as silicon wafer has been done. The capability to direct-write and pattern polymeric materials with interesting electronic and electrooptical properties at the nanoscale creates a number of opportunities since a large variety of monomers/polymers are available. Electrochemical Dip-Pen Nanolithography (E-DPN) is used to fabricate polythiophene nanostructures on semiconducting and insulating surfaces in the sub-100 nm regime. Using DPN techniques, nanostructures composed of organic [42,43], semiconducting [44], metallic materials [45] are easily obtained of controlled and well-defined nanometer shape and size. Liu *et al.* electrochemically polymerized 3,4-ethylenedioxythiophene (EDOT) at the AFM tip/substrate

interface to create poly-EDOT nanowires. Poly-EDOT is a well-known conducting polymer possessing interesting electrical and electrooptic properties, and of interest for antistatic, electrostatic, and conducting coatings as well as for light emitting diodes [46].

**2.3.9. Microwave Method:** The microwave processing of nanoparticles results in rapid heating of the reaction mixtures, particularly those containing water. As a consequence, the precipitation of particles from such solutions tends to be rapid and nearly simultaneous. This process leads to very small particle sizes and narrow size distributions within the solution and it offers the additional benefit of requiring very short reaction times. 1,1,4,4-Tetraphenyl-1,3-butadiene nanocrystals were fabricated by the microwave method, whose procedure is the conventional reprecipitation followed by the microwave irradiation. Using this method, monodisperse nanocrystals possessing the crystal structure different from that of bulk crystals were produced [47].

## 2.4. Stabilization of Microparticles:

During nucleation of any colloid, it faces several possible fates *i.e.* re-dissolution, coagulation and stabilization. Many chemical reaction syntheses for organic compounds are conducted at room temperature in the solution phase in which the reactant precursors are well dissolved and the target product is generated as a precipitate. The homogeneous solution phase makes it possible to continuously tune the super saturation during precipitation of the target product [48-50]. The greatest practical challenge is to prevent this coagulation. The stabilization of colloids and thus the means to preserve their finely dispersed state is a crucial aspect to consider during their synthesis [51]. At short interparticle distance, the van der Waals forces attract two molecules to each other. In the absence of repulsive forces opposed to the van der Waals forces, the colloidal particles aggregate. Consequently, the use of a

stabilizing agent able to induce a repulsive force opposed to the van der Waals forces is necessary to provide stable low dimensional particles in solution.

**2.4.1. Soft Template Method:** The template method is a straight forward way to fabricate nanostructures by inducing the target materials to grow according to the patterns of the templates. This strategy provides an easy way for the synthesis of nanomaterials with desired shape and size, and has been widely applied in the construction of 1D nanostructures. The templates adopted in this method can be generally divided into two sorts: soft and hard ones. So-called soft templates are those that can be dissolved in the liquid phase, including surfactant micelles, [52] complexes,[53] biomolecules,[54] and copolymers [55]. It is well known that micelles (or inverse micelles) with different shapes, such as spherical or rodlike, will be formed in the surfactant solutions when the concentration reaches the critical micelle concentration (CMC) [56]. These can then be used as soft templates for the fabrication of nanostructures. Yao and coworkers reported nanofibers of 1,3-diphenyl-2-pyrazoline (DP) induced by CTAB micelles [57]. It is found that the shape and size of the obtained nanostructures can be controlled by changing the molar ratio of DP to CTAB. It can be seen that at lower DP/CTAB molar ratios, CTAB tends to form spherical micelles, and increasing the DP/CTAB ratio will induce the sphere-to-rod transition of the micelles, which act as a template to direct the 1D growth of DP. With the same method, Wan and coworkers also prepared nanotubes from zinc mesotetra(4-pyridyl)porphyrin and constructed 3D arrays on substrates [58]. Zhang *et al.* used sodium dodecyl sulfate (SDS) micelles as templates to direct the 1D growth of pyrene molecules in an aqueous phase [59].

**2.4.2. Hard Template Method:** The synthesis of nanostructures with hard templates has developed independently in various fields of nanotechnology and it has become one of the most applied methods in the fabrication of inorganic 1D nanomaterials [60,61]. Possin

was the first to use this technique to prepare semiconductor nanowires in the 1970s [62]. In recent years, this technique has also been applied to prepare 1D nanomaterials from small organic compounds. Lee *et al.* reported the synthesis of organic nanowires by introducing 1,4-bis[2-(5-phenyloxazolyl)]benzene molecules into the AAO membranes by sublimation [63]. Li and coworkers fabricated C<sub>60</sub> nanotubes with this method by an easy dip-and-dry procedure, in which they dipped the anodized aluminum oxide (AAO) templates repeatedly into a C<sub>60</sub> solution, and evaporated the solvent during the intervals between dipping [64]. Yao's group reported the preparation of perylene [65] and dibenzoylmethane (DBM) [66] nanotubes by the dip-and-dry template method followed by heat treatment to increase the crystallinity.

## References:

1. A. L. Briseno, S. C. B. Mannsfeld, X. Lu, Y. Xiong, S. A. Jenekhe, Z. Bao and Y. Xia, *Nano Lett.* 7, **2007**, 668.
2. Y. S. Zhao, J. Wu and J. Huang, *J. Am. Chem. Soc.* 131, **2009**, 3158.
3. A. L. Briseno, T. W. Holcombe, A. I. Boukai, E. C. Garnett, S. W. Shelton, J. J. M. Frechet and P. Yang, *Nano Lett.* 10, **2010**, 334.
4. K. Xiao, J. Tao, Z. Pan, A. A. Poretzky, I. N. Ivanov, S. J. Pennycook and D. B. Geohegan, *Angew. Chem.* 119, **2007**, 2704.
5. K. Takazawa, Y. Kitahama, Y. Kimura and G. Kido, *Nano Lett.* 5, **2005**, 1293.
6. D. O'Carroll, I. Lieberwirth and G. Redmond, *Nat. Nanotechnol.* 2, **2007**, 180.
7. Y. Lei, Q. Liao, H. Fu and J. Yao, *J. Am. Chem. Soc.* 132, **2010**, 1742.
8. B.K. An, S.K. Kwon, S.D. Jung and S.Y. Park, *J. Am. Chem. Soc.*, 124, **2002**, 14410.
9. H. Yu and L. Qi, *Langmuir*, 25, **2009**, 6781.
10. K. Ujjiye-Ishii, E. Kwon, H. Kasai, H. Nakanishi and H. Oikawa, *Cryst. Growth & Design*, 8, **2008**, 369.
11. X. Zhang, X. Zhang, K. Zou, C. S. Lee and S. T. Lee, *J. Am. Chem. Soc.*, 129, **2007**, 3527.
12. Z. Wang, H. Mohwald and C. Gao, *ACS Nano*, 5, **2011**, 3930.
13. Y.S. Zhao, W. Yang, G. Zhang, Y. Ma and J. Yao, *Colloids Surf. A*, 277, **2006**, 111.
14. S. Zhao, W. Yang, D. Xiao, X. Sheng, X. Yang, Z. Shuai, Y. Luo and J. Yao, *Chem.Mater*, 17, **2005**, 6430.
15. Y. X. Zhang, C. Dong, J. A. Zapien, S. Ismathullakhan, Z. Kang, J. Jie, X. Zhang, J. C. Chang, C. S. Lee and S. T. Lee, *Angew. Chem. Int. Ed.*, 48, **2009**, 9121.
16. D. Li and Y. Xia, *Adv. Mater.*, 16, **2004**, 1151.
17. T. Asahi, T. Sugiyama and H. Masuhara, *Acc. Chem. Res.*, 41, **2008**, 1790.
18. Y. Tamaki, T. Asahi, and H. Masuhara, *J. Phys. Chem. A*, 106, **2002**, 2135.
19. S. Kostler, A. Rudorfer, A. Haase, V. Satzinger, G. Jakopic, and V. Ribitsch, *Adv. Mater.* 21, **2009**, 2505.
20. M. Shtein, J. Mapel, J.B. Benziger and S.R. Forrest, *Appl. Phys. Lett.*, 81, **2002**, 268.
21. Y.S. Zhao, H. Fu, F. Hu, A. Peng, W. Yang and J. Yao, *Adv. Mater.* 20, **2008**, 79.
22. X. Peng, J. Wickham and A. P. Alivisatos, *J. Am. Chem. Soc.* 120, **1998**, 5343.
23. C. B. Murray, C. R. Kagan and M. G. Bawendi, *Annu. Rev. Mater. Sci.* 30, **2000**, 545.
24. B. R Pamplin, *Crystal Growth*; Pergamon Press, New York, **1975**.
25. H. Kasai, H. S. Nalwa, H. Oikawa, S. Okada, H. Matsuda, N. Minami, A. Kakuta, K. Ono, A. Mukoh and H. Nakanishi, *Jpn. J. Appl. Phys.* 31, **1992**, 1132.
26. H. S. Nalwa, H. Kasai, H. Kamatani, S. Okada, H. Oikawa, H. Matsuda, A. Kakuta, A. Mukoh and H. Nakanishi, *Adv. Mater.* 5, **1993**, 758.
27. H. Kasai, H. Oikawa and H. Nakanishi, *Organic Mesoscopic Chemistry* (Eds: H. Masuhara, F. C. Schryver), *Blackwell Science, Oxford*, **1999**, 145.
28. H. Kasai, H. Kamatani, Y. Yoshikawa, S. Okada, H. Oikawa, A. Watanabe, O. Itoh and H. Nakanishi, *Chem. Lett.* 26, **1997**, 1181.
29. H. Oikawa, T. Mitsui, T. Onodera, H. Kasai, H. Nakanishi and T. Sekiguchi, *Jpn. J. Appl. Phys.* 42, **2003**, 111.
30. H. Auweter, H. Haberkorn, W. Heckmann, D. Horn, E. Lu" ddecke, J. Rieger and H. Weiss, *Angew. Chem. Int.*



- Ed.* 38, **1999**, 2188.
31. T. Tachikawa, H.-R. Chung, A. Masuhara, H. Kasai, H. Oikawa, H. Nakanishi, M. Fujitsuka and T. Majima, *J. Am. Chem. Soc.* 128, **2006**, 15944.
  32. A. J. Gesquiere, T. Uwada, T. Asahi, H. Masuhara and P. F. Barbara, *Nano Lett.* 5, **2005**, 1321.
  33. F. Bertorelle, D. Lavabre and S. Fery-Forgues, *J. Am. Chem. Soc.* 125, **2003**, 6244.
  34. L. Kang, Z. Wang, Z. Cao, Y. Ma, H. Fu and J. Yao, *J. Am. Chem. Soc.* 129, **2007**, 7305.
  35. C. V. Ristagno and H. J. Shine, *J. Org. Chem.* 36, **1971**, 4050.
  36. F. Debuigne, L. Jeuniau, M. Wiame and J. B. Nagy, *Langmuir*, 16, **2000**, 7605.
  37. F. Cansell, B. Chevalier, A. Demourgues, J. Etourneau, C. Even, Y. Garrabos, V. Pessey, S. Petit, A. Tressaud and F. Weill, *J. Mater. Chem.* 9, **1999**, 67.
  38. A. Ranganathan, V. R. Pedireddi, and C. N. R. Rao, *J. Am. Chem. Soc.* 121, **1999**, 1752-1753
  39. Y. S. Zhao, W. Yang and J. Yao, *Phys. Chem. Chem. Phys.*, 8, **2006**, 3300.
  40. B.K. An, D.S. Lee, J. S. Lee, Y. S. Park, H. S. Song and S. Y. Park, *J. Am. Chem. Soc.* 126, **2004**, 10232.
  41. J. Xiao, Z. Yin, H. Li, Q. Zhang, F. Boey, H. Zhang and Q. Zhang, *J. Am. Chem. Soc.* 132, **2010**, 6926.
  42. R. D. Piner, J. Zhu, F. Xu, S. H. Hong, and C. A. Mirkin, *Science*, 283, **1999**, 661.
  43. S. H. Hong, J. Zhu and C. A. Mirkin, *Science* 286, **1999**, 523.
  44. Y. Li, B. W. Maynor and J. Liu, *J. Am. Chem. Soc.* 123, **2001**, 2105.
  45. B. W. Maynor, Y. Li and J. Liu, *Langmuir* 17, **2001**, 2575.
  46. B. W. Maynor, S. F. Filocamo, M.W. Grinstaff and J. Liu, *J. Am. Chem. Soc.* 124, **2002**, 522.
  47. K. Baba, H. Kasai, S. Okada, H. Oikawa and H. Nakanishi, *Opt. Mater.* 21, **2002**, 591.
  48. C. B. Murray, C. R. Kagan and M. G. Bawendi, *Annu. Rev. Mater. Sci.* 30, **2000**, 545.
  49. Z. A. Peng and X. G. Peng, *J. Am. Chem. Soc.* 123, **2002**, 1389.
  50. Z. A. Peng and X. G. Peng, *J. Am. Chem. Soc.* 123, **2001**, 183.
  51. C. S. Hirtzel and R. Rajagopalan, *Colloidal Phenomena: Advanced Topics*; Noyes: New Jersey, **1985**, 27-39 and 73- 87.
  52. J. Chen, T. Herricks, M. Geissler and Y. Xia, *J. Am. Chem. Soc.* 126, **2004**, 10854.
  53. Y. Liu, J. Cao, J. Zeng, C. Li, Y. Qian and S. Zhang, *Eur. J. Inorg. Chem.* 4, **2003**, 644.
  54. H. A. Becerril, R. M. Stoltenberg, D. R. Wheeler, R. C. Davis, J. N. Harb, and A. T. Woolley, *J. Am. Chem. Soc.* 127, **2005**, 2828.
  55. C. Minelli, C. Hinderling, H. Heinzelmann, R. Pugin and M. Liley, *Langmuir*, 21, **2005**, 7080.
  56. M. J. Rosen, *Surfactants and Interfacial Phenomena*, 3rd ed., Wiley, New York **2004**.
  57. H. Fu, D. Xiao, J. Yao and G. Yang, *Angew. Chem. Int. Ed.* 42, **2003**, 2883.
  58. J.S. Hu, Y.G. Guo, H.P. Liang, L.J. Wan and L. Jiang, *J. Am. Chem. Soc.* 127, **2005**, 17090.
  59. X. Zhang, X. Zhang, W. Shi, X. Meng, C. Lee and S. Lee, *J. Phys. Chem. B*, 109, **2005**, 18777.
  60. C. R. Martin, *Acc. Chem. Res.* 28, **1995**, 61.
  61. C. R. Martin, *Science*, 266, **1994**, 1961.
  62. G. E. Possin, *Rev. Sci. Instrum.* 41, **1970**, 772.
  63. J.K. Lee, W. K. Koh, W.S. Chaeb and Y.R. Kim, *Chem. Commun.* **2002**, 138.
  64. H. Liu, Y. Li, L. Jiang, H. Luo, S. Xiao, H. Fang, H. Li, D. Zhu, D. Yu, J. Xu and B. Xiang, *J. Am. Chem. Soc.* 124, **2002**, 13370.

65. L. Zhao, W. Yang, Y. Ma, J. Yao, Y. Li and H. Liu, *Chem. Commun.* **2003**, 2442.  
66. L. Zhao, W. Yang, Y. Luo, T. Zhai, G. Zhang and J. Yao, *Chem. Eur. J.* **11**, **2005**, 3773.



*CHAPTER*

**3**

**Characterization  
Techniques**

Characterizations of the low dimensional materials are important to apply it for a particular application. A variety of techniques are employed for the characterization of low dimensional materials in dispersed state. Different experimental techniques that are used for characterization and Photophysical studies of our samples are described in the following section.

### 3.1. UV-Vis Spectroscopy:

The UV-Vis spectroscopy is one of the most common and fundamental technique to obtain useful information regarding the nature of aggregation of low dimensional organic materials [1,2]. Different compounds may have different absorption maxima and absorbance. The absorbance may be calculated from Lambert-Beer law which states that *‘the absorbance of a solution is directly proportional to the concentration of the absorbing species in the solution and the path length’*. Thus, for a fixed path length, UV-Vis spectroscopy can be used to determine the concentration of the absorber in a solution. Actually, UV-Vis spectrophotometer measures the intensity of light passing through a sample (I), and compares it to the intensity of light before it passes through the sample (I<sub>0</sub>). The ratio I/I<sub>0</sub> is called the transmittance, and is usually expressed as a percentage (%T). The absorbance, A, is based on the transmittance:

$$A = \epsilon cl = \log_{10} (I_0/I) = \log_{10} (100/T)$$

where ‘l’ is the path length through the sample, and ‘c’ the concentration of the absorbing species. For each species and wavelength, ‘ $\epsilon$ ’ is a constant known as the molar absorptivity or

extinction coefficient. This constant is a fundamental molecular property in a given solvent. A standardized spectrum is formed by removing the concentration dependence and determining the extinction co-efficient ( $\epsilon$ ) as a function of wavelength. A schematic diagram of a double beam UV-Visible spectrophotometer is shown in Fig.3.1.

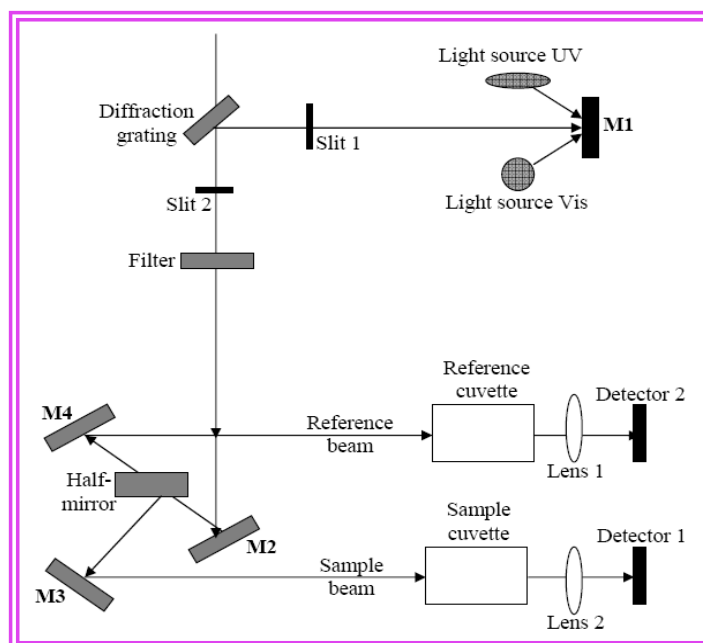


**Figure 3.1: Schematic diagram of a double beam UV-visible spectrophotometer (M1, M2, M3 and M4 are mirrors).**

The experimental set up in principle is very simple. In this spectrophotometer, the blazed holographic grating with self-aligning, energy-optimizing deuterium and tungsten-halogen lamps enhances precision across the UV-vis spectrum from 190 to 900 nm. A beam of light from a visible or UV light source is separated into its component wavelengths by diffraction grating. A monochromator selects different wavelengths which fall on the sample. Each monochromatic beam is split into two equal intensity beams by a beam splitter (a half mirrored device). Sample is well dispersed in suitable solvent and the pure solvent was used as a reference. The sample and the reference are taken in quartz cuvette (a small transparent container) because these are transparent throughout the UV, visible and near infrared regions. One beam *i.e.* the sample beam, passes through a cuvette containing a solution of the

compound being studied in a transparent solvent. The other beam, the reference, passes through an identical cuvette containing only the solvent. The transmitted intensity at different wavelengths are detected by a photo detector and given as an input to a computer. The intensity of the reference beam, which have been suffered little or no light absorption, is defined as ' $I_0$ '. The intensity of the sample beam is defined as ' $I$ '. Absorption of the solvent cancels out to give spectrum of the pure sample. The absorption is different at different wavelengths and is characteristic of the sample. The wavelength of the maximum absorbance is designated as ' $\lambda_{\max}$ '.

All the UV-vis spectroscopic study of low dimensional organic materials was made using a SHIMADZU UV-1800 Spectrophotometer in this thesis work. The photograph of the instrument is shown in Fig.3.2.



**Figure 3.2: SHIMADZU UV-1800 Spectrophotometer.**

### **3.2. Fluorescence Spectroscopy:**

Fluorescence spectroscopy is basically concerned with electronic and the associated vibrational states. In fluorescence spectroscopy, the species is first excited, by absorbing a photon, from its ground electronic state to one of the various vibrational states in the excited electronic state. Collisions with other molecules cause the excited molecule to lose vibrational energy until it reaches the lowest vibrational state of the excited electronic state. The Jablonski diagram (Fig.3.3) visualized the above process and the other relevant

transitions. Actually, photons with energies in the ultraviolet to the blue-green region of the spectrum are needed to trigger an electronic transition. Further, since the energy gap between the excited and ground electronic states is significantly larger than the thermal energy, thermodynamics predicts that molecules predominately reside in the electronic ground state.

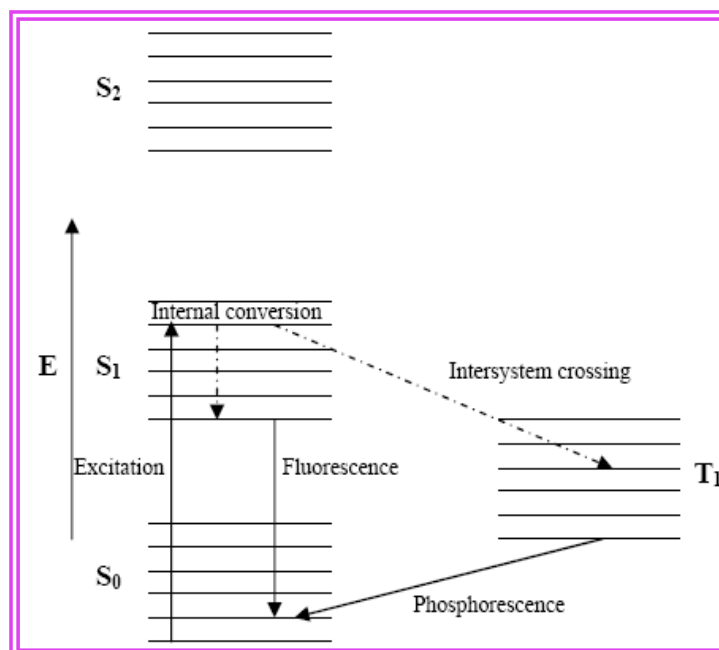


**Figure 3.3: The Jablonski diagram of fluorophore excitation, radiative decay and nonradiative decay pathways. [E=energy scale; S<sub>0</sub>=ground singlet electronic state; S<sub>1</sub>, S<sub>2</sub> = successively higher energy excited singlet electronic states; T<sub>1</sub> = lowest energy triplet state].**

Fluorescence occurs when a molecule absorbs photons from the UV-visible light spectrum (200-900 nm), causing transition to a high-energy electronic state and then emits photons as it returns to its initial state, in less than  $10^{-9}$  sec. Some energy, within the molecule, is lost through heat or vibration so that emitted energy is less than the exciting energy; *i.e.* the emission wavelength is always longer than the excitation wavelength. The difference between the excitation and emission wavelengths is called the Stokes shift. The Stokes shift describes the observation that fluorescence photons are longer in wavelength than the excitation radiation. The fluorescence absorption and emission spectra reflect the vibrational level structures in the ground state and the excited electronic states, respectively.

The Frank-Condon principle states the fact that the vibrational levels are not significantly altered during electronic transitions. The similarity of the vibrational level structures in the ground and excited electronic states often results in the absorption and emission spectra having mirror images to each other.

The measurement of fluorescence signals provides a sensitive method of monitoring the chemical environment of a fluorophore. A schematic representation of a fluorescence spectrophotometer is shown in Fig.3.4. The most common light source for fluorescence spectrophotometer is xenon arc lamps. These lamps provide a relatively uniform intensity over a broad spectral range from the ultraviolet to the near infrared. Photons impinge on the excitation monochromator, which selectively transmits light in a narrow range centred about the specified excitation wavelength. The transmitted light passes through adjustable slits that control magnitude and resolution by further limiting the range of transmitted light. The filtered light passes into the sample cell causing fluorescent emission by fluorophores within the sample. Emitted light enters the emission monochromator, which is positioned at a 90° angle from the excitation light path to eliminate background signal and minimize noise due to stray light. Again, emitted light is transmitted in a narrow range centred about the specified emission wavelength and exits through adjustable slits, finally entering the photomultiplier tube (PMT). The signal is amplified and creates a voltage that is proportional to the measured emitted intensity. Noise in the counting process arises primarily in the PMT. Therefore, spectral resolution and signal to noise ratio is directly related to the selected slit widths. The detector can either be single-channel or multichannel. The single channel detector can only detect the intensity of one wavelength at a time, while the multichannel detects the intensity at all wavelengths simultaneously, making the emission monochromator or filter unnecessary.



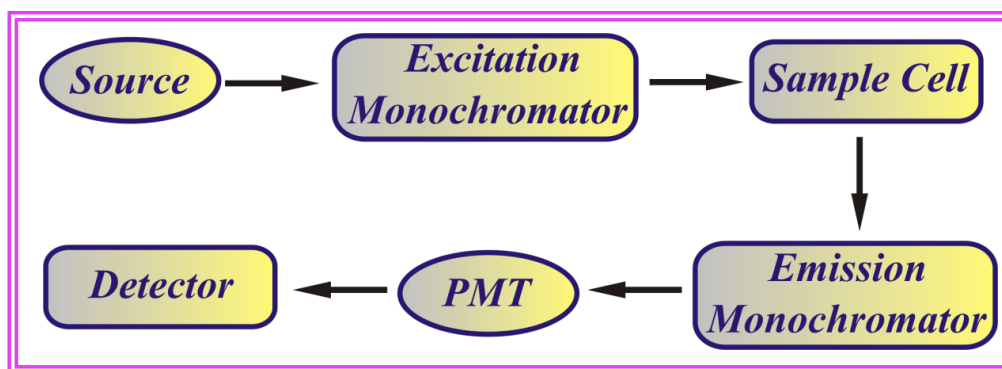


**Figure 3.4: Schematic diagram of photoluminescence set up.**



**Figure 3.5: HITACHI F-7000 Fluorescence Spectrophotometer.**

For spectral measurement, monochromator or band pass filters are placed in the excitation and emission light paths to select a specific spectral band. The excitation spectrum is defined as the fluorescent intensity measured as a function of excitation wavelength at a constant emission wavelength; the emission spectrum is the fluorescent intensity measured as a function of emission wavelength at a constant excitation wavelength. Fluorescence spectra of all the samples were obtained using a HITACHI F-7000 Fluorescence Spectrophotometer. The photograph of the instrument is shown in Fig.3.5.

### 3.3. Time-resolved Fluorescence Measurements:

#### 3.3.1. Time correlated single photon counting: Picosecond setup:

Picosecond fluorescence decays were recorded using picoseconds time resolution in a time correlated single photon counting (TCSPC) setup.



**Figure 3.6: TCSPC instrument, PTI, USA.**

The singlet state lifetime was measured by using TCSPC from PTI, USA (Fig.3.6), using the sub nanosecond pulsed LED source [290 nm, pulse width 600 ps (full width at half maximum) from Pico Quant, Germany] operating at high repetition rate of 10 MHz driven by PDL 800-B driver, Pico Quant, Germany. Lamp profiles was measured at the excitation wavelength 290 nm with a band pass of 3 nm using Ludox as the scatterer. A schematic representation of our TCSPC setup is shown in Fig.3.7.

The decay parameters were recovered using a non-linear iterative fitting procedure based on the Marquardt algorithm. De-convolution technique can determine the lifetime up to 150-200 ps. The quality of fit has been assessed over the entire decay, including the rising edge, and tested with a plot of weighted residuals and other statistical parameters *e.g.* the reduced  $\chi^2$  ratio. Several artifacts may arise and must be guarded against. Firstly, radio

frequency is frequently a source of noise. It is eliminated through proper grounding loop and choice of CFD level. Secondly, humidity may cause spurious signals from the MCP. Thirdly, long time stability of the laser and the sample should be checked.

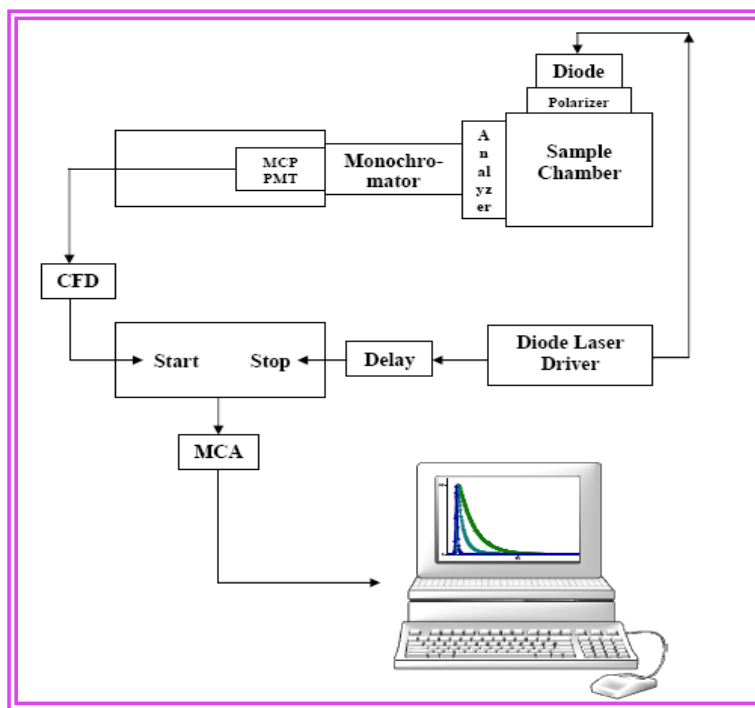


Figure 3.7: Time-correlated single photon counting (TCSPC) setup.

**3.3.2. Deconvolution procedure:** When the decay time is long compared to that of the excitation pulse, the excitation may be described as a  $\delta$ -function. However, when the lifetime is short, distortion of the experimental data occurs due to a finite decay time of the lamp pulse, response time of the photomultiplier and associated electronics. Since the measured decay function is now a convolution of the true fluorescence decay, it is necessary to deconvolute the data in order to extract the fluorescence lifetime.

The lifetime is calculated with the help of the “convolution integral”,

$$R(t') = \int_0^{t'} Y(t)P(t'-t) dt$$

where,  $R(t')$  is the fluorescence intensity at any time  $t'$ ,  $Y(t)$  is the intensity of the exciting light at time  $t$  and  $P(t'-t)$  is the response function of the experimental system. If  $P(t'-t)$  is equal to  $\exp[-(t'-t)/\tau]$ , *i.e.*, for single exponential decays, then,

$$R(t') = \exp(-t'/\tau) \int_0^{t'} Y(t) \exp(t/\tau) dt$$

The values  $R(t')$  and  $Y(t)$  as a function of time, measured by means of the MCA card are fed into a computer to determine the lifetime  $\tau$ .

The deconvolution is based on an iterative least square method [3, 4]. An excitation pulse profile is first recorded. Then the deconvolution starts with the mixing of the excitation pulse and a projected decay to form a new reconvoluted set. This data is compared with the experimentally obtained data and the difference is summed, generating the  $\chi^2$  function for the fit. The deconvolution proceeds through a series of such iterations until an insignificant change in  $\chi^2$  occurs between two successive iterations. The quality of fit is normally assessed by inspection of the reduced  $\chi^2$ , plot of the weighted residuals and the autocorrelation function of the residuals.

### 3.4. Spectroscopic study of molecular assemblies:

The photophysical properties of aggregated low dimensional organic materials are often distinctively different than in solution. Molecular arrangements in aggregated crystals can be complex due to the soft nature of the organic compounds. This is ascribed to specific intermolecular interactions, which are pre-formed by the sterical and electronic demands of the single molecules. While electronic couplings, *i.e.* the direct overlap of the molecular orbitals (MOs) of neighboring molecules, affect the electronic properties of the material [5], excitonic couplings, *i.e.* the interaction of transition dipole densities, affect the optical and photophysical properties [6]. Electronic couplings are from their nature of short-range order and thus depend substantially on the exact arrangement of adjacent molecules [5]. The excitonic coupling corresponds to half of the splitting of the excited states caused by the interaction of the molecules.

**3.4.1. H- vs. J-aggregates:** Increasing the pitch angle in a slipped stack arrangement changes the system from so called H-type to J-type aggregates (Fig.3.8). H-aggregates refer to ‘side-by-side’ oriented molecular transition dipole moments  $\mu$ . In H-aggregates, the lower of the two excited states which are generated by the excitonic interaction is forbidden, while the higher one is allowed. This has two important implications: (i) a hypsochromic (blue) shifted absorption spectra against solution, which corresponds to the excitonic coupling between the molecules; details of the spectral band shapes have been intensively investigated by Spano over the last decade [6] and (ii) a low radiative rate constant  $k_r$  due to the dipole-forbidden nature of the emitting state [7].

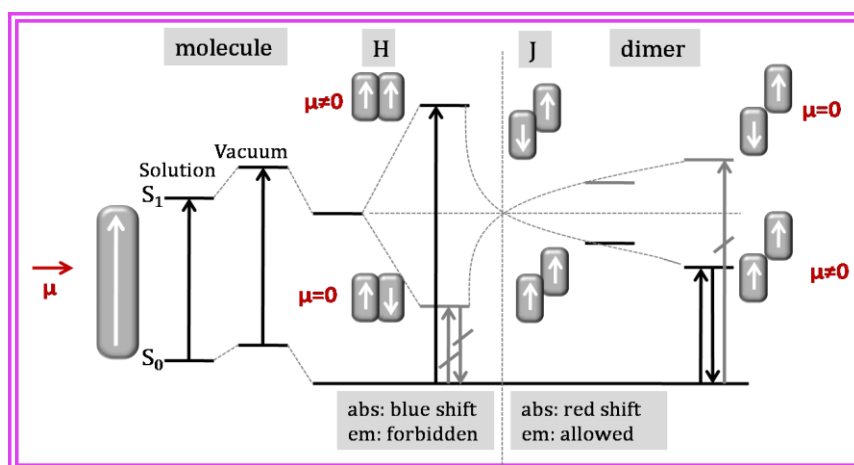


**Figure 3.8: Exciton coupling for a face-to-face dimer in a molecular crystal as obtained from quantum-chemical calculations: H- and J-aggregates and their impact on the absorption (abs) and emission (em) process.**

The radiative rate  $k_r$  goes to zero for ideal  $\pi$ -stacked arrangements. However, the validity of the selection rule will depend sensitively on (i) the strength of excitonic coupling; i.e. the effective  $k_r$  will significantly increase for weak splitting of the excited states due to Herzberg–Teller type coupling, and (ii) the inclined angle between the transition dipole moments, which gives intensity to the  $S_1$  state. Thus, radiative rate constants in H-aggregates can differ by orders of magnitude. J-aggregates on the other hand, dominated by ‘head-to-tail interactions’, display bathochromic (red) shifted absorption and high radiative rates [6]. For

simple slip-stacked crystals even the maximum slip along x in a 3D molecular crystal of half a molecular length generates only a very moderate bathochromic shift compared to the often large hypsochromic shift in H-aggregates. Due to the high radiative rates, J-aggregates are highly emissive, while H-aggregates are generally suspected to be less emissive due to the lowered radiative compared to the single molecule.

**3.4.2.  $\pi$ -stack vs. herringbone:** Perfect co-facial overlap ( $\pi$ -stack) of short and medium size chromophores at small intermolecular separations generate excimer-like band shapes with large bathochromically shifted and unstructured PL spectra. This is due to the partial intermolecular CT character of the respective optical transition, which leads to different intermolecular separations in the ground and first excited state. The intermolecular coordinate introduced by such interaction allows for efficient coupling of low-frequency breathing modes to the electronic transition, which gives rise to excimer emission [7]. The degree of  $\pi$ - $\pi$  overlap and intermolecular separation is crucial for the excimer features [8]. Hence, for herringbone arrangements, well-resolved emission band shapes of a relaxed exciton are observed, with vibronic features closely resembling the single molecule species [9]. Perfect side-by-side arrangements both in  $\pi$ -stacks and herringbone patterns give rise to H-type aggregation with strongly blue-shifted absorption spectra.

### 3.5. Scanning Electron Microscope (SEM):

The sample morphology was checked by a SEM machine (Fig.3.9). In SEM a high energy electron beam (0.2 KeV to 30 KeV) is focused on the sample surface within a size of nanometer to micrometer by means of various focusing lenses (schematically shown in Fig.3.10). In electron microscope, electrons are usually emitted from a hot filament. However, sometimes cold cathode (a cathode which emits electrons without heating) is also used. A cold cathode emits electrons under the application of a very high electric field. It is

also known as field emitter. Such SEM is known as FE-SEM (Field emission scanning electron microscope). It can able to give better image than hot filament SEM. There are several kinds of phenomena that occur as a result of the interaction between the incident electron beam and the atoms at the vicinity of the sample surface. Three major incidents are the emission of the secondary electrons (SE) due to the inelastic scattering, back scattered electrons (BSE) due to the elastic scattering and electromagnetic radiation generated by the electronic transition from an excited atom.



**Figure 3.9: ZEISS EVO 18 Scanning Electron Microscope.**

All of these emissions can be detected and mapped to produce an image of the sample surface. Imaging the sample surface by detecting the SE is the most commonly used technique for the topography of the surface. In this technique the low energy electrons ejected from the K cell of the atoms by the inelastic scattering of the incident electron beam are collected by a detector, which is basically a scintillated photomultiplier. The electrons are accelerated to a high energy by high bias voltage which finally hit the scintillator to produces photons, which are further, magnified by the photomultiplier and collected as a 2D intensity distribution. This intensity distribution is a one to one correspondence to the density of the SE. The density of SE is nearly independent to the atomic number of an atom.

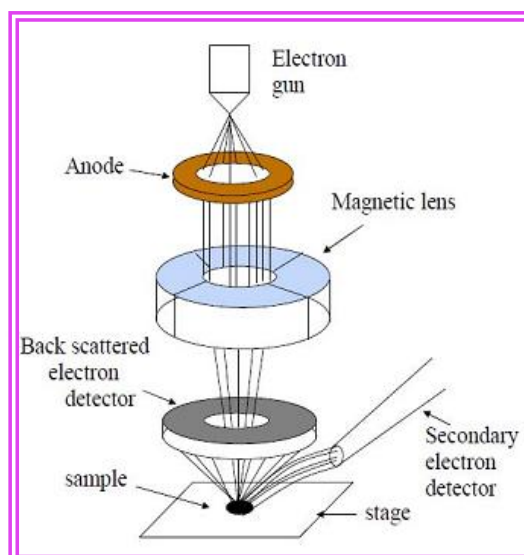


**Figure 3.10: Schematic diagram of the working principle of a Scanning Electron Microscope.**

It depends on the atomic density and the interaction area between the beam and the sample surface. The density of SE is least when the beam is perpendicular to the surface as the exposed area becomes the smallest. Thus we see relatively darker image for a flat surface and brighter image for a inclined surface situated at the edge. This phenomenon of SE makes the image topographically distinct. In most of the cases, we checked the sample morphology by means of a ZEISS EVO 18 scanning electron microscope. Our main requirement was to identify the grain size and shape of our polycrystalline samples. A circular Cu slab was used as the sample holder. Samples were mounted on the holder by conducting carbon tape and a gold coating was done over the sample surface in case the samples are insulating in nature in order to avoid the charging effect during the scan.

### **3.6. Optical, polarizing and fluorescence microscopy analysis:**

The past decade has witnessed an enormous growth in the application of optical microscopy for micron and submicron level investigations in a wide variety of disciplines [10, 11]. Rapid development of new fluorescent labels has accelerated the expansion of fluorescence microscopy in laboratory applications and research. Advances in digital imaging



and analysis have also enabled microscopes to acquire quantitative measurements quickly and efficiently on specimens ranging from photosensitive caged compounds and synthetic ceramic superconductors to real-time fluorescence microscopy of living cells in their natural environment.

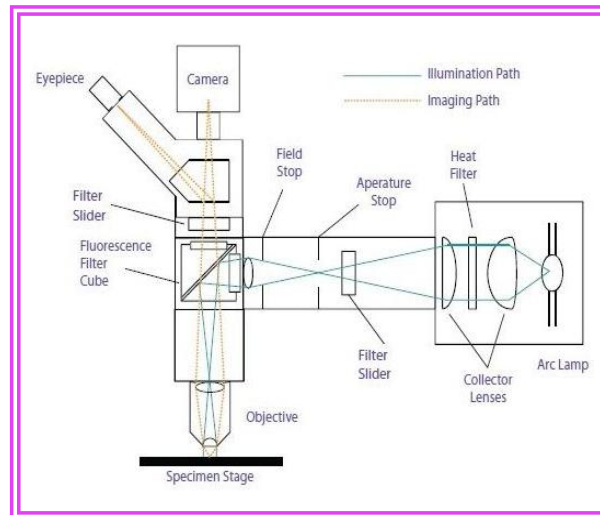


**Figure 3.11: Schematic diagram of the working principle of an optical microscope.**

All modern optical microscopes have the same 'structural' components (Fig.3.11):

1. Eye piece (ocular lens)
2. Objective turret, revolver, or revolving nose piece (to hold multiple objective lenses)
3. Objective lenses
4. Focus knobs (to move the stage): i) Coarse adjustment and ii) Fine adjustment
5. Stage (to hold the specimen)
6. Light source (a light or a mirror)
7. Diaphragm and condenser
8. Mechanical stage

Microscopy analysis is mainly three types:

**3.6.1. Optical microscopy study:** In a classic optical microscope, also known as the simple "light" microscope, visible light is sent through a series of lenses to magnify a sample. There are many types of microscopes, the most common and first is the optical microscope which uses light to image the sample. This is an optical instrument containing one or more lenses producing an enlarged image of a sample placed in the focal plane. Optical microscopes have refractive glass and occasionally of plastic or quartz, to focus light into the eye or another light detector. Mirror-based optical microscopes operate in the same manner. Typical magnification of a light microscope, assuming visible range light, is up to 1250x with a theoretical resolution limit of around 0.250 micrometres or 250 nanometres.

**3.6.2. Polarizing microscopy study:** A polarizing microscope is an optical microscope with the addition of polarizing filters that acts to polarize visible light. Polarizing Microscopes (PLM) uses two filters; a polarizer, positioned in the light path somewhere before the specimen (usually fixed to a left-right, or East-West position) and an analyzer (a second polarizer), placed in the optical pathway between the objective rear aperture and the observation tubes or camera port and an analyzer (a second polarizer), set to a North-South position, though it can be rotated on some microscope models. The analyzer can be slid in and out of the path of the source light. The professional grades are equipped with Bertrand Lens system, compensator plates: quartz wedge, mica (1/4 wavelength), and gypsum (full wavelength) part of the analyzer. Polarized light microscopy is capable of providing information on absorption color and optical path boundaries between minerals of differing refractive indices, in a manner similar to bright field illumination, but the technique can also distinguish between isotropic and anisotropic substances. Furthermore, the contrast-enhancing technique exploits the optical properties specific to anisotropy and reveals detailed

information concerning the structure and composition of materials that are invaluable for identification and diagnostic purposes.

**3.6.3. Fluorescence microscopy study:** The basic function of a fluorescence microscope is to irradiate the specimen with a desired and specific band of wavelengths, and then to separate the much weaker emitted fluorescence from the excitation light. The limits of detection are generally governed by two elements:

- The darkness of the background
- The removal of excitation light.

Excitation light is typically several hundred thousand to a million times brighter than the emitted fluorescence. Their individual molecules are able to absorb light for an extremely short time, usually billionths of a second and then to emit it again. However, the emitted light features a wavelength which is slightly shifted “towards red”. If, for example, blue light is absorbed, green light will be emitted immediately afterwards.



**Figure 3.12: NIKON ECLIPSE LV100POL optical microscope.**

All the Optical, polarizing and fluorescence microscopy analysis was made using a NIKON ECLIPSE LV100POL upright microscope equipped with a CCD camera (model no.

DS-Fil), polarizer-analyzer assembly and 12V-50W halogen lamps as the excitation source for the emission study (Fig.3.12). The samples for the optical microscopic study were prepared by placing a drop of colloidal solution onto a clean glass slide.

### 3.7. X-ray Diffraction (XRD):

X-ray diffraction (XRD) is a very important experimental technique that has long been used to explain the crystal structure of solids, including lattice constants and geometry, identification of unknown materials, orientation of single crystals, preferred orientation of polycrystals, defects, stresses etc. The atomic planes of a crystal cause an incident beam of X-rays to interfere with one another as they leave the crystal. If the incoming wave is split into two by slits and the two parts of the wave are allowed to interfere with each other, than a pattern is produced on the screen placed on the other side of the slits. Whether the two beams interfere constructively or destructively at particular paths that each of the wave takes from the split to the point on the wavelengths, the combination of two waves is perfectly constructive and the intensity is greatly enhanced. A regularly spaced series of slits has the same type of effect and is called a diffraction grating. When a crystal is bombarded with X-rays of a fixed wavelength and at certain incident angles, intense reflected X-rays are produced when the wavelengths of the scattered X-rays interfere constructively. In order for the waves to interfere constructively, the differences in the travel path must be equal to integer multiples of the wavelength. When this constructive interference occurs, a diffracted beam of X-rays will leave the crystal at an angle equal to that of the incident beam. A crystal grating is nothing but a three-dimensional diffraction grating. However, it cannot diffract visible light. This is because for the diffraction effect to be noticeable, the spacing between the slits in the grating should be of the same order of magnitude as the wavelength of incident radiations. In a crystal the distance between the lattice points corresponds to the dimensions

of atoms and molecules *i.e.* few angstroms. X-rays are radiations with wavelengths of this size and hence diffraction from the crystal is observed (Fig.3.13).

where,  $\lambda$  is the wavelength of the X-ray,  $\theta$  is the scattering angle and  $n$  is an integer.

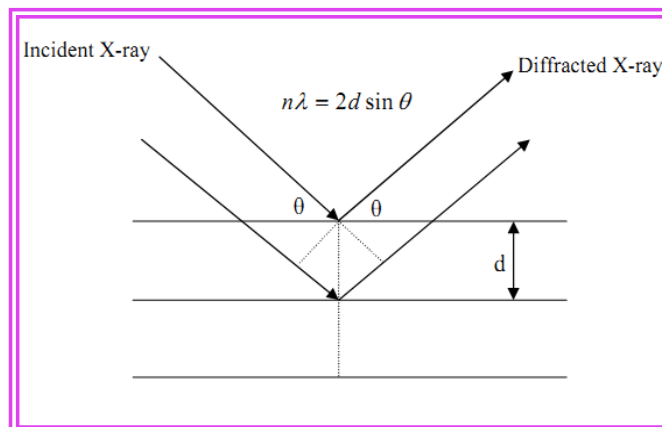


**Figure 3.13: Bragg's Law diagram.**

Most crystals can have many sets of planes passed through their atoms. Each set of planes has a specific inter planer distance and will give rise to a characteristic angle of diffracted X-rays. For a given set of lattice planes with an inter-plane distance of 'd', the condition for a diffraction to occur is given by Bragg's equation:

$$n\lambda = 2d \sin\theta$$

where,  $\lambda$  is the wavelength of the X-ray,  $\theta$  is the scattering angle and  $n$  is an integer.



**Figure 3.14: Rigaku Miniflex-II' X-ray diffractometer.**

A set of 'd-spaces' obtained from a single compound represent the set of planes that can be passed through the atoms and can be used for comparison with sets of d-spaces obtained from standard compounds. In 1913, the English physicists Sir W. H. Bragg and his son Sir W. L. Bragg were derived the above equation. They were awarded the Noble prize in physics in 1915 for their work in determining crystal structures beginning with NaCl, ZnS, and diamond. These energies X-rays can penetrate deep into the material and provide information about the structural arrangement of atoms and molecules.

The crystallinity and particle size of the microparticles are often experimentally determined by X-ray diffraction [12]. X-ray diffraction (XRD) data of the samples in the thesis are obtained using 'Rigaku Miniflex-II' X-ray diffractometer. The photograph of the instrument is shown below (Fig.3.14):

### 3.8. Single-crystal X-ray Diffraction:

Single-crystal X-ray Diffraction is a non-destructive analytical technique which provides detailed information about the internal lattice of crystalline substances, including unit cell dimensions, bond-lengths, bond-angles, and details of site-ordering. Max von Laue, in 1912, discovered that crystalline substances act as three-dimensional diffraction gratings for X-ray wavelengths similar to the spacing of planes in a crystal lattice [13]. X-ray diffraction is based on constructive interference of monochromatic X-rays and a crystalline sample. These X-rays are generated by a cathode ray tube, filtered to produce monochromatic radiation, collimated to concentrate, and directed toward the sample. The interaction of the incident rays with the sample produces constructive interference when conditions satisfy Bragg's Law ( $n\lambda=2d \sin\theta$ ). This law relates the wavelength of electromagnetic radiation to the diffraction angle and the lattice spacing in a crystalline sample. These diffracted X-rays are then detected, processed and counted. By changing the geometry of the

incident rays, the orientation of the centered crystal and the detector, all possible diffraction directions of the lattice should be attained.

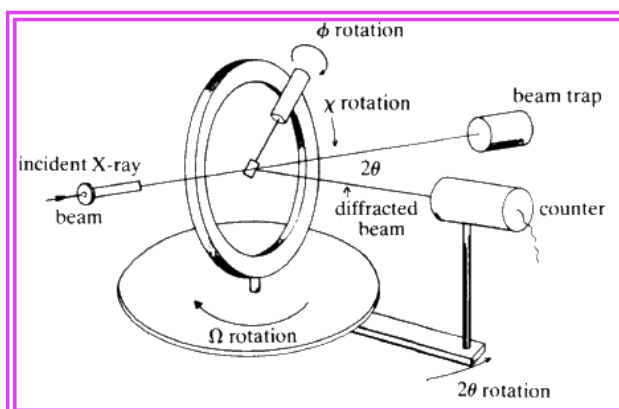


**Figure 3.15: Schematic diagram of Single-crystal X-ray diffractometer.**

X-ray diffractometers consist of three basic elements, an X-ray tube, a sample holder, and an X-ray detector. X-rays are generated in a cathode ray tube by heating a filament to produce electrons, accelerating the electrons toward a target by applying a voltage, and impact of the electrons with the target material. When electrons have sufficient energy to dislodge inner shell electrons of the target material, characteristic X-ray spectra are produced. These spectra consist of several components, the most common being  $K_{\alpha}$  and  $K_{\beta}$ .  $K_{\alpha}$  consists, in part, of  $K_{\alpha 1}$  and  $K_{\alpha 2}$ .  $K_{\alpha 1}$  has a slightly shorter wavelength and twice the intensity as  $K_{\alpha 2}$ . The specific wavelengths are characteristic of the target material. Filtering, by foils or crystal monochromators, is required to produce monochromatic X-rays needed for diffraction.  $K_{\alpha 1}$  and  $K_{\alpha 2}$  are sufficiently close in wavelength such that a weighted average of the two is used. Molybdenum is the most common target material for single-crystal diffraction, with Mo  $K_{\alpha}$  radiation =  $0.7107\text{\AA}$ . These X-rays are collimated and directed onto the sample. When the geometry of the incident X-rays impinging the sample satisfies the Bragg's equation, constructive interference occurs. A detector records and processes this X-ray signal and converts the signal to a count rate which is then output to a device such as a printer or computer monitor. Single-crystal diffractometers use either three or four circle

goniometers. These circles refer to the four angles ( $2\theta$ ,  $\chi$ ,  $\varphi$ , and  $\Omega$ ) that define the relationship between the crystal lattice, the incident ray and detector (Fig.3.15). Samples are mounted on thin glass fibers which are attached to brass pins and mounted onto goniometer heads. Adjustment of the X, Y and Z orthogonal directions allows centering of the crystal within the X-ray beam. X-rays leave the collimator and are directed at the crystal. Rays are either transmitted through the crystal, reflected off the surface, or diffracted by the crystal lattice. A beam stop is located directly opposite the collimator to block transmitted rays and prevent burn-out of the detector. Reflected rays are not picked up by the detector due to the angles involved. Diffracted rays at the correct orientation for the configuration are then collected by the detector. Modern single-crystal diffractometers use CCD (charge-coupled device) technology to transform the X-ray photons into an electrical signal which are then sent to a computer for processing.

Single crystal X-ray diffraction data was collected on a Bruker Nonius APEX-II CCD diffractometer (Fig.3.16) using graphite monochromated MoK $\alpha$  radiation ( $\lambda = 0.71073$  Å).

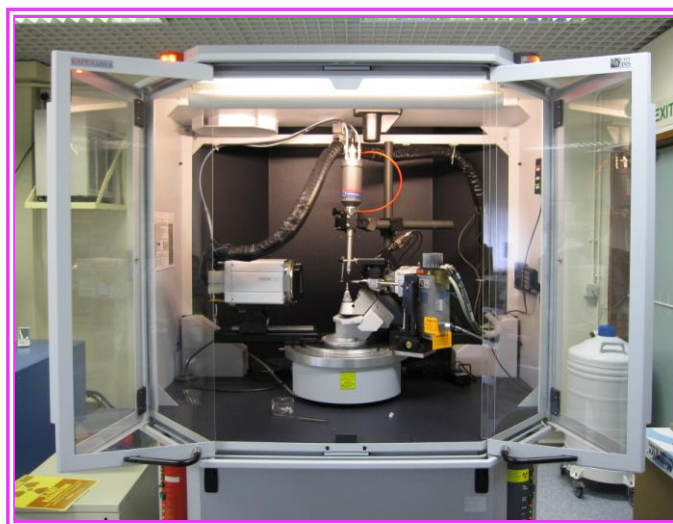


**Figure 3.16: Bruker APEX II CCD Single-crystal X-ray diffractometer.**

The intensity of X-rays in a diffraction pattern depending only upon the crystal structure is referred to as so called the structure factor:



$$F(hkl) = \sum_{j=1}^N f_j \exp[2\pi i (hx_j + ky_j + lz_j)] \quad \dots\dots\dots(1)$$

where  $h$ ,  $k$  and  $l$  are the indices of the diffraction planes (Bragg reflections),  $N$  is the number of atoms in the cell and  $(x_j, y_j, z_j)$  are the fractional coordinates of the  $j^{\text{th}}$  atom with scattering factor  $f_j$ . Each structure factor represents a diffracted beam which has an amplitude  $F(hkl)$  and a relative phase  $\varphi(hkl)$ .

The crystal structure can be obtained from the diffraction pattern if the electron density function is calculated at every point in a single unit cell:

$$\rho(x, y, z) = \frac{1}{V} \sum_h \sum_k \sum_l F(hkl) \cos [\exp[2\pi i (hx_j + ky_j + lz_j)] - \varphi(hkl)] \dots\dots\dots(2)$$

where the summation is over all values of  $h$ ,  $k$  and  $l$  and  $V$  is the volume of the unit cell. Since X-rays are diffracted from the whole crystal, the calculation yields the contents of the unit cell averaged over the whole crystal. In practice, the calculation of the electron density produces maps. The maxima on these maps represent the position of the atoms in the cell.

The structure factors are reciprocal space vectors whereas the electron density is from the real space. The calculation of the electron density is not then obtained directly from experimental measurements and the phases must be obtained by other methods. This is the so called phase problem. The most usual methods to overcome the phase problem are direct methods. With the calculated phases and structure factors amplitudes, a first electron density map is calculated, also approximate, from which the atomic positions will be obtained. The next step is the completion of the structure by Fourier synthesis and refinement of the structural parameters to optimize the fitting between the observed and calculated intensities in the diffraction pattern. The structural refinement is evaluated from the agreement between the calculated and the measured structure factors. Once the structure is determined and refined several geometrical parameters such as bond lengths, bond angles, torsion angles,  $\pi$ -stacking

and hydrogen-bond are evaluated and appropriate tables and graphics representing the structure are prepared. A standard file (CIF: crystal information file) containing all the information of the structure is created and can be used to evaluate their quality and possible problems.

**References:**

1. M. A. El-Sayed, *Acc. Chem. Res.*, 34, **2001**, 257.
2. C. Burda, X. Chen, R. Narayanan and M. A. El-Sayed, *Chem. Rev.*, 105, **2005**, 1025.
3. D. V. O'Connor and D. Phillips, *Time correlated single photon counting*; Academic Press: New York, **1984**.
4. B.J. Berne and R. Pecora, *Dynamic Light Scattering*, Courier Dover Publications, **2000**.
5. V. Coropceanu, J. Cornil, D. A. da Silva Filho, Y. Olivier, R. Silbey and J.-L. Brédas, *Chem. Rev.*, 107, **2007**, 926.
6. F. C. Spano, *Acc. Chem. Res.*, 43, **2010**, 429.
7. J. Gierschner, M. Ehni, H.-J. Egelhaaf, B. Milián Medina, D. Beljonne, H. Benmansour and G. C. Bazan, *J. Chem. Phys.*, 123, **2005**, 144914.
8. J. Gierschner, H.-G. Mack, D. Oelkrug, I. Waldner and H. Rau, *J. Phys. Chem. A*, 108, **2004**, 257.
9. C. C. Wu, O. J. Korovyanko, M. C. DeLong, Z. V. Vardeny, J. Gutierrez and J. P. Ferraris, *Synth. Met.*, 139, **2003**, 735.
10. B. Herman and J.J. Lemasters (eds.), *Optical Microscopy: Emerging Methods and Applications*. Academic Press, New York, **1993**, 441.
11. B. Herman, *Fluorescence Microscopy*. BIOS Scientific Publishers Ltd., Oxford, UK, **1998**, 170.
12. D. Zanchet, B. D. Hall and D. Uarte, *J. Phys. Chem. B*, 104, **2000**, 11013.
13. M. Laue, W. Friedrich and P. Knipping, *Ann. Phys. Lpz.*, 41, **1912**, 199.



*CHAPTER*

**4**

**Computational Study**

## 4.1. Introduction:

“Computational chemistry simulates chemical structures and reactions numerically, based in full or in part on the fundamental laws of physics.” - *Foresman and Frisch*

Theoretical chemistry is defined as the mathematical description of chemistry. When these mathematical methods are sufficiently well developed to be automated and implemented on a computer, we can talk about computational chemistry. Very few aspects of chemistry can be computed exactly, but almost every aspect of chemistry has been described in a qualitative or approximate quantitative computational scheme. The theoretical chemist must keep in mind that numbers obtained from theoretical calculations are not exact (they use many approximations), but they can offer a useful insight into real chemistry. Thus computational chemistry can be described as chemistry performed using computers rather than chemicals.

Computational chemistry is a branch of chemistry that uses principles of computer science to assist in solving chemical problems. It uses the results of theoretical chemistry, incorporated into efficient computer programs, to calculate the structures and properties of molecules and solids. Its necessity arises from the well-known fact that apart from relatively recent results concerning the hydrogen molecular ion, the quantum n-body problem cannot be solved analytically, much less in closed form. While its results normally complement the information obtained by chemical experiments, it can in some cases predict very much unobserved chemical phenomena. It is widely used in the design of new drugs and materials.

Examples of such properties are structure (*i.e.* the expected positions of the constituent atoms), absolute and relative (interaction) energies, electronic charge distributions, dipoles and higher multipole moments, vibrational frequencies, reactivity or other spectroscopic quantities, and cross sections for collision with other particles.

The methods employed cover both static and dynamic situations. In all cases the computer time and other resources (such as memory and disk space) increase rapidly with the size of the system being studied. The system can be a single molecule, a group of molecules, or a solid. Computational chemistry methods range from highly accurate to very approximate; highly accurate methods are typically feasible only for small systems. *Ab initio* methods are based entirely on theory from first principles. Other (typically less accurate) methods are called empirical or semi-empirical because they employ experimental results, often from acceptable models of atoms or related molecules, to approximate some elements of the underlying theory. Both *ab initio* and semi-empirical approaches involve approximations. These range from simplified forms of the first-principles equations that are easier or faster to solve, to approximations limiting the size of the system (for example, periodic boundary conditions), to fundamental approximations to the underlying equations that are required to achieve any solution to them at all.

## **4.2. Schrödinger Equation:**

In quantum mechanics, the Schrödinger equation describes how the quantum state of a physical system changes with time. It was formulated in late 1925, and published in 1926, by the Austrian physicist Erwin Schrödinger.

In classical mechanics, the equation of motion is Newton's second law, and equivalent formulations are the Euler-Lagrange equations and Hamilton's equations. In all these formulations, they are used to solve for the motion of a mechanical system, and

mathematically predict what the system will do at any time beyond the initial settings and configuration of the system.

In quantum mechanics, the analogue of Newton's law is Schrödinger's equation for a quantum system, usually atoms, molecules, and subatomic particles; free, bound, or localized. It is not a simple algebraic equation, but (in general) a linear partial differential equation. The differential equation encases the wave function of the system, also called the quantum state or state vector.

In the standard interpretation of quantum mechanics, the wave function is the most complete description that can be given to a physical system. Solutions to Schrödinger's equation describe not only molecular, atomic, and subatomic systems, but also macroscopic systems, possibly even the whole universe [1].

Like Newton's Second law, the Schrödinger equation can be mathematically transformed into other formulations such as Werner Heisenberg's matrix mechanics, and Richard Feynman's path integral formulation. Also like Newton's Second law, the Schrödinger equation describes time in a way that is inconvenient for relativistic theories, a problem that is not as severe in matrix mechanics and completely absent in the path integral formulation.

Four approximations are commonly (but not necessarily) made:

- Time independence; we are looking at states that are stationary in time.
- Neglect of relativistic effects; this is warranted unless the velocity of the electrons approaches the speed of light, which is the case only in heavy atoms with very high nuclear charge.
- Born-Oppenheimer approximation; separation of the motion of nuclei and electrons.
- Orbital approximation; the electrons are confined to certain regions of space.

**4.2.1. Time Dependent Equation:** The form of the Schrödinger equation depends on the physical situation. The most general form is the time-dependent Schrödinger equation, which gives a description of a system evolving with time [2].

$$i\hbar \frac{\partial}{\partial t} \Psi = \hat{H}\Psi$$

**Time-dependent Schrödinger equation (general)**

where  $\Psi$  is the wave function of the quantum system,  $i$  is the imaginary unit,  $\hbar$  is the reduced Planck constant, and  $\hat{H}$  is the Hamiltonian operator, which characterizes the total energy of any given wave function and takes different forms depending on the situation.

A wave function which satisfies the non-relativistic Schrödinger equation with  $V=0$ . In other words, this corresponds to a particle traveling freely through empty space. The most famous example is the non-relativistic Schrödinger equation for a single particle moving in an electric field (but not a magnetic field):

$$i\hbar \frac{\partial}{\partial t} \Psi(r,t) = -\frac{\hbar^2}{2m} \nabla^2 \Psi(r,t) + V(r,t)\Psi(r,t)$$

**Time-dependent Schrödinger equation (single non-relativistic particle)**

where  $m$  is the particle's mass,  $V$  is its potential energy,  $\nabla^2$  is the Laplacian, and  $\Psi$  is the wave function (more precisely, in this context, it is called the “position-space wave function”). In words, this equation could be described as “total energy equals kinetic energy plus potential energy”, but the terms take unfamiliar forms for reasons explained below.

Given the particular differential operators involved, this is a linear partial differential equation. It is also a wave equation, hence the name “Schrödinger wave equation”.

The term “Schrödinger equation” can refer to both the general equation (first box above), or the specific non relativistic version (second box above and variations thereof). The



general equation is indeed quite general, used throughout quantum mechanics, for everything from the Dirac equation to quantum field theory, by plugging in various complicated expressions for the Hamiltonian. The specific non relativistic version is a simplified approximation to reality, which is quite accurate in many situations, but very inaccurate in others.

To apply the Schrödinger equation, the Hamiltonian operator is set up for the system, accounting for the kinetic and potential energy of the particles constituting the system, then inserted into the Schrödinger equation. The resulting partial differential equation is solved for the wave function, which contains information about the system.

**4.2.2. Time Independent Equation:** The time dependent Schrödinger equation predicts that wave functions can form standing waves, called stationary states (also called “orbital’s”, as in atomic orbital’s or molecular orbital’s). These states are important in their own right, and moreover if the stationary states are classified and understood, then it becomes easier to solve the time-dependent Schrödinger equation for any state. The time-independent Schrödinger equation is the equation describing stationary states. (It is only used when the Hamiltonian itself is not dependent on time.)

$$E\Psi = \hat{H}\Psi$$

**Time-independent Schrödinger equation (*general*)**

In words, the equation states: When the Hamiltonian operator acts on the wave function  $\Psi$ , the result might be proportional to the same wave function  $\Psi$ . If it is, then  $\Psi$  is a stationary state, and the proportionality constant,  $E$ , is the energy of the state  $\Psi$ .

The time-independent Schrödinger equation is discussed further below. In linear algebra terminology, this equation is an Eigen value equation. As before, the most famous

manifestation is the non-relativistic Schrödinger equation for a single particle moving in an electric field (but not a magnetic field):

$$E\Psi(r) = -\frac{\hbar^2}{2m}\nabla^2\Psi(r) + V(r)\Psi(r)$$

**Time-independent Schrödinger equation (*single non-relativistic particle*)**

With definitions as above, the Schrödinger equation, and its solutions, introduced a breakthrough in thinking about physics. His equation was the first of its type, and solutions led to very unusual and unexpected consequences for the time.

### 4.3. Born-Oppenheimer approximation:

In quantum chemistry, the computation of the energy and wave function of an average-size molecule is a formidable task that is alleviated by the Born-Oppenheimer (BO) approximation, named after Max Born and J. Robert Oppenheimer. For instance the benzene molecule consists of 12 nuclei and 42 electrons. The time independent Schrödinger equation, which must be solved to obtain the energy and wave function of this molecule, is a partial differential Eigen value equation in 162 variables-the spatial coordinates of the electrons and the nuclei. The BO approximation makes it possible to compute the wave function in two less complicated consecutive steps. This approximation was proposed in 1927, in the early period of quantum mechanics, by Born and Oppenheimer and is still indispensable in quantum chemistry.

In basic terms, it allows the wave function of a molecule to be broken into its electronic and nuclear (vibrational, rotational) components.

$$\Psi_{\text{total}} = \psi_{\text{electronic}} \times \psi_{\text{nuclear}}$$

In the first step of the BO approximation the electronic Schrödinger equation is solved, yielding the wave function depending on electrons only. For benzene this wave function depends on 126 electronic coordinates. During this solution the nuclei are fixed in a certain configuration, very often the equilibrium configuration. If the effects of the quantum mechanical nuclear motion are to be studied, for instance because a vibrational spectrum is required, this electronic computation must be in nuclear coordinates. In the second step of the BO approximation this function serves as a potential in a Schrödinger equation containing only the nuclei-for benzene an equation in 36 variables.

The success of the BO approximation is due to the high ratio between nuclear and electronic masses. The approximation is an important tool of quantum chemistry; without it only the lightest molecule, H<sub>2</sub>, could be handled and all computations of molecular wave functions for larger molecules make use of it. Even in the cases where the BO approximation breaks down, it is used as a point of departure for the computations.

### **4.4. Molecular Mechanics:**

Molecular mechanics simulations use the laws of classical physics to predict the structures and properties of molecules. There are different molecular mechanics methods. Each one is characterized by its particular force field. These classical force fields are based on empirical results, averaged over a large number of molecules. Because of this extensive averaging, the results can be good for standard systems; no force field can be generally used for all molecular systems of interest. However, molecular mechanics methods cannot describe bond formation or bond breaking or predict molecular properties which depend on molecular orbital interactions.

## 4.5. Electronic Structure Methods:

Electronic structure methods use the law of quantum mechanics as the basis for their computations. Quantum mechanics states that the energy and other related properties of a molecule can be obtained by solving the Schrödinger equation,

$$H\psi = E\psi$$

However, exact solutions to the Schrodinger equation are not practical. Electronic structure methods are characterized by their various mathematical approximations to their solutions. There are two major classes of electronic structure methods:

- Semi-empirical methods use a simpler Hamiltonian than the correct molecular Hamiltonian and use a parameter whose values are adjusted to fit the experimental data. That means they solve an approximate form of the Schrodinger equation that depends on having approximate parameters available for the type of chemical system in question. There is no unique method for the choice of parameter. Ab initio force fields provide solutions to these problems.
- Ab initio methods use the correct Hamiltonian and do not use experimental data other than the values of the fundamental physical constants (*i.e.*,  $c$ ,  $h$ , mass and charges of electrons and nuclei). Moreover it is a relatively successful approach to perform vibrational spectra.

## 4.6. Semi-empirical Quantum Chemistry Methods:

Semi-empirical quantum chemistry attempts to address two limitations, namely slow speed and low accuracy, of the Hartree-Fock calculation by omitting or parameterizing certain integrals based on experimental data, such as ionization energies of atoms, or dipole moments of molecules. As a result, semi-empirical methods are very fast, applicable to large molecules, and may give accurate results when applied to molecules that are similar to the

molecules used for parameterization. On the downside, accuracy of semi-empirical methods is erratic on many systems.

Modern semi-empirical models are based on the Neglect of Diatomic Differential Overlap (NDDO) method in which the overlap matrix  $S$  is replaced by the unit matrix. This allows one to replace the Hartree-Fock secular equation  $[\mathbf{H}-\mathbf{E}\mathbf{S}] = 0$  with a simpler equation  $[\mathbf{H}-\mathbf{E}] = 0$ . Existing semi-empirical models differ by the further approximations that are made when evaluating one- and two-electron integrals and by the parameterization philosophy. Semi-empirical NDDO Models: MNDO, AM1, PM3, and PDDG/PM3.

Trends in vibrational frequencies in related systems are usually reproduced by semi-empirical calculations, but the errors are not as nicely systematic. When energy is concerned the results are not completely satisfactory, in spite of the fact that the methods are parameterized to reproduce heats of formation.

## 4.7. Ab initio Quantum Chemistry Methods:

Ab initio quantum chemistry methods are computational chemistry methods based on quantum chemistry [3]. The term *ab initio* was first used in quantum chemistry by Robert Parr and coworkers, including David Craig in a semi-empirical study on the excited states of benzene [4,5]. The background is described by Parr [6]. In its modern meaning ('from first principles of quantum mechanics') the term was used by Chen [7] (when quoting an unpublished 1955 MIT report by Allen and Nesbet), by Roothaan [8] and, in the title of an article, by Allen and Karo, [9] who also clearly define it.

Ab initio orbital molecular methods are useful to predict harmonic force constants and frequencies of normal modes. The ab initio methods first optimize the molecular geometry and then evaluate the second derivative at the equilibrium positions usually using analytical derivatives. Such methods provide reliable values for harmonic vibrational frequencies for

fairly large sized molecules. Additionally, such calculations can be used to predict barriers to internal rotation as well as relative stabilities of different conformers. The information obtained from structural parameters, conformational stabilities, force constants, vibrational frequencies as well as infrared and Raman band intensities gives significant contributions to the field of vibrational spectroscopy. Harmonic force constants in Cartesian coordinates can be directly derived from ab initio calculations. These force constants can be transformed to force constants in internal or symmetry coordinates. Ab initio calculations followed by normal coordinate analysis are very helpful in making reliable vibrational assignments. Band intensities from ab initio studies are another important output. Such band intensity data can also be very useful in making vibrational assignments.

If the quantum-mechanical force field is not corrected, especially in the case of large deviations from the experimental results, this omission can complicate the theoretical analysis of the vibrational spectrum of a molecule and lead to errors in the assignment of the experimental frequencies.

## 4.8. Hartree-Fock Methods:

In computational physics and chemistry, the Hartree-Fock (HF) method is a method of approximation for the determination of the ground-state wave function and ground-state energy of a quantum many-body system. The origin of the Hartree-Fock method dates back to the end of the 1920s, soon after the derivation of the Schrödinger equation in 1926. In 1927 D. R. Hartree introduced a procedure, which he called the self-consistent field method, to calculate approximate wave functions and energies for atoms and ions.

The simplest type of ab initio electronic structure calculation is the Hartree-Fock (HF) scheme, in which the instantaneous Coulombic electron-electron repulsion is not specifically taken into account. Only its average effect (mean field) is included in the calculation. This is a variational procedure; therefore, the obtained approximate energies, expressed in terms of

the system's wave function, are always equal to or greater than the exact energy, and tend to a limiting value called the Hartree-Fock limit as the size of the basis is increased [10]. Many types of calculations begin with a Hartree-Fock calculation and subsequently correct for electron-electron repulsion, referred to also as electronic correlation.

The Hartree-Fock method is typically used to solve the time-independent Schrödinger equation for a multi-electron atom or molecule as described in the Born-Oppenheimer approximation. Since there are no known solutions for many-electron systems (hydrogenic atoms and the diatomic hydrogen cation being notable one-electron exceptions), the problem is solved numerically. Due to the nonlinearities introduced by the Hartree-Fock approximation, the equations are solved using a nonlinear method.

## 4.9. Density Function Theory (DFT):

Density functional theory (DFT) is a quantum mechanical modeling method used in physics and chemistry to investigate the electronic structure (principally the ground state) of many-body systems, in particular atoms, molecules, and the condensed phases. With this theory, the properties of a many-electron system can be determined by using functional, *i.e.* functions of another function, which in this case are the spatially dependent electron density. Hence the name density functional theory comes from the use of functional of the electron density. DFT is among the most popular and versatile methods available in condensed-matter physics, computational physics, and computational chemistry.

DFT has been very popular for calculations in solid-state physics since the 1970s. However, DFT was not considered accurate enough for calculations in quantum chemistry until the 1990s, when the approximations used in the theory were greatly refined to better model the exchange and correlation interactions. In many cases the results of DFT calculations for solid-state systems agree quite satisfactorily with experimental data.

---

Computational costs are relatively low when compared to traditional methods, such as Hartree-Fock theory and its descendants based on the complex many-electron wave function.

Despite recent improvements, there are still difficulties in using density functional theory to properly describe intermolecular interactions, especially van der Waals forces (dispersion); charge transfer excitations; transition states, global potential energy surfaces and some other strongly correlated systems; and in calculations of the band gap in semiconductors. Its incomplete treatment of dispersion can adversely affect the accuracy of DFT (at least when used alone and uncorrected) in the treatment of systems which are dominated by dispersion (*e.g.* interacting noble gas atoms) [11] or where dispersion competes significantly with other effects (*e.g.* in bio molecules) [12]. The development of new DFT methods designed to overcome this problem, by alterations to the functional [13] or by the inclusion of additive terms [14-16], is a current research topic.

**4.9.1. Time Dependent Density Functional Theory (TDDFT):** TDDFT is an extension of density functional theory (DFT), and the conceptual and computational foundations are analogous to show that the (time-dependent) wave function is equivalent to the (time-dependent) electronic density, and then to derive the effective potential of a fictitious non-interacting system which returns the same density as any given interacting system. The issue of constructing such a system is more complex for TDDFT, most notably because the time-dependent effective potential at any given instant depends on value of the density at all previous times. Consequently the development of time-dependent approximations for the implementation of TDDFT is behind that of DFT, with applications routinely ignoring this memory requirement.

The most popular application of TDDFT is in the calculation of the energies of excited states of isolated systems and, less commonly, solids. Such calculations are based on the fact that the linear response function - that is, how the electron density changes when the



external potential changes - has poles at the exact excitation energies of a system. Such calculations require, in addition to the exchange-correlation potential, the exchange-correlation kernel the functional derivative of the exchange-correlation potential with respect to the density [17].

**4.9.2. Success of Density Functional Theory:** Kohn-Sham DFT is an important first-principles computational method to predict chemical properties accurately and to analyze and interpret these in convenient and simple chemical terms.

The reasons for its popularity and success are easy to understand. In the first place, the DFT approach is in principle exact. In particular, the Kohn-Sham method implies a one-electron picture of the many-electron systems but yields in principle the exact electron density (and related properties) and the total energy. The exact exchange-correlation (XC) functional is unknown, but the currently available XC functional provides in most cases already a 'chemical' accuracy of a few kcal/mol for binding energies. Moreover, the quest for more accurate ones based on a more detailed understanding of their essential properties is continuing.

In the past two decades, computational chemistry emerged as a mainstream tool used by all types of chemists, physicists and engineers who have an interest in research and development. DFT came to dominate quantum chemistry applications since the turn of the century.

In the second place, it preserves at all levels of approximation the appealing one-electron molecular orbital (MO) view on chemical reactions and properties. The computed orbitals are suitable for the typical MO-theoretical analyses and interpretations. The KS method effectively incorporates all correlation effects.

In the third place, it is a relatively efficient computational method, and its fundamental scaling properties do not deteriorate when methodological precision is

increased, in particular, when a more accurate XC functional is applied. Recent research paves the way to implementations that scale only linearly with the system size. This brings within reach the treatment by fundamental quantum chemical methods of systems with hundreds, maybe even thousands of atoms.

DFT gives superior accuracy to Hartree-Fock theory and semi-empirical approaches, and it is well suited for molecules containing metal atoms. In contrast to conventional ab initio methods (MP2, CI, CC), it enables accurate treatment of systems with several hundreds of atoms (or several thousand with QM/MM).

#### 4.10. Basis Sets:

A basis set in quantum chemistry is a set of functions used to create the molecular orbital, which are expanded as a linear combination of such functions with the weights or coefficients to be determined. Usually these functions are atomic orbital, in that they are centered on atoms. Otherwise, the functions are centered on bonds or lone pairs. Pairs of functions centered in the two lobes of a 'p' orbital have also been used. Additionally, basis sets composed of sets of plane waves down to a cutoff wavelength are often used, especially in calculations involving systems with periodic boundary conditions.

Today, there are hundreds of basis sets composed of Gaussian-type orbital (GTOs). The smallest of these are called 'minimal basis sets', and they are typically composed of the minimum number of basis functions required to represent all of the electrons on each atom. The largest of these can contain literally dozens to hundreds of basis functions on each atom.

A minimum basis set is one in which, on each atom in the molecule, a single basis function is used for each orbital in a Hartree-Fock calculation on the free atom. However, for atoms such as lithium, basis functions of p type are added to the basis functions corresponding to the 1s and 2s orbital of the free atom. For example, each atom in the second

---

period of the periodic system (Li - Ne) would have a basis set of five functions (two s functions and three p functions).

The most common addition to minimal basis sets is probably the addition of polarization functions, denoted (in the names of basis sets developed by Pople) by an asterisk, \*. Two asterisks, \*\*, indicate that polarization functions are also added to light atoms (hydrogen and helium). These are auxiliary functions with one additional node. For example, the only basis function located on a hydrogen atom in a minimal basis set would be a function approximating the 1s atomic orbital. When polarization is added to this basis set, a p-function is also added to the basis set. This adds some additional needed flexibility within the basis set, effectively allowing molecular orbital involving the hydrogen atoms to be more asymmetric about the hydrogen nucleus. This is an important result when considering accurate representations of bonding between atoms, because the very presence of the bonded atom makes the energetic environment of the electrons spherically asymmetric. Similarly, d-type functions can be added to a basis set with valence p orbital, and f-functions to a basis set with d-type orbital, and so on. Another, more precise notation indicates exactly which and how many functions are added to the basis set, such as (d,p).

Another common addition to basis sets is the addition of diffuse functions, denoted in Pople type sets by a plus sign, +, and in Dunning-type sets by “aug” (from “augmented”). Two plus signs indicate that diffuse functions are also added to light atoms (hydrogen and helium). These are very shallow Gaussian basis functions, which more accurately represent the "tail" portion of the atomic orbital, which are distant from the atomic nuclei. These additional basis functions can be important when considering anions and other large, “soft” molecular systems.

**4.10.1. Minimal basis sets:** The most common minimal basis set is STO-nG, where  $n$  is an integer. This  $n$  value represents the number of Gaussian primitive functions comprising

a single basis function. In these basis sets, the same number of Gaussian primitives comprises core and valence orbital. Minimal basis sets typically give rough results that are insufficient for research-quality publication, but are much cheaper than their larger counterparts.

Commonly used minimal basis sets of this type are:

- STO-3G
- STO-4G
- STO-6G
- STO-3G\* - Polarized version of STO-3G

There are several other minimum basis sets that have been used such as the MidiX basis sets.

**4.10.2. Split-valence basis sets:** During most molecular bonding, it is the valence electrons which principally take part in the bonding. In recognition of this fact, it is common to represent valence orbital by more than one basis function (each of which can in turn be composed of a fixed linear combination of primitive Gaussian functions). Basis sets in which there are multiple basis functions corresponding to each valence atomic orbital are called valence double, triple, quadruple-zeta, and so on, basis sets. Since the different orbital of the split have different spatial extents, the combination allows the electron density to adjust its spatial extent appropriate to the particular molecular environment. Minimum basis sets are fixed and are unable to adjust to different molecular environments.

**4.10.3. Pople basis sets:** The notation for the split-valence basis sets arising from the group of John Pople is typically X-YZg. In this case, X represents the number of primitive Gaussians comprising each core atomic orbital basis function. The Y and Z indicate that the valence orbital are composed of two basis functions each, the first one composed of a linear combination of Y primitive Gaussian functions, the other composed of a linear combination of Z primitive Gaussian functions. In this case, the presence of two numbers after the hyphens implies that this basis set is a split-valence double-zeta basis set. Split-valence triple-

and quadruple-zeta basis sets are also used, denoted as X-YZWg, X-YZWVg, etc. Here is a list of commonly used split-valence basis sets of this type:

- 3-21G
- 3-21G\* - Polarized
- 3-21+G - Diffuse functions
- 3-21+G\* - With polarization and diffuse functions
- 4-21G
- 4-31G
- 6-21G
- 6-31G
- 6-31G\*
- 6-31+G\*
- 6-31+G\*\*
- 6-31G(3df, 3pd)
- 6-311G
- 6-311G\*
- 6-311+G\*

The 6-31G\* basis set (defined for the atoms H through Zn) is a valence double-zeta polarized basis set that adds to the 6-31G set six *d*-type Cartesian-Gaussian polarization functions on each of the atoms Li through Ca and ten *f*-type Cartesian Gaussian polarization functions on each of the atoms Sc through Zn.

#### 4.11. Fukui Parameter:

The Fukui function or frontier function was introduced by Parr and Yang in 1984. This function is sensitive to the electron density at various points in a species to a change in the number of electrons in a species. In the aggregated structures of molecules, where strong interaction between different atomic centers's of similar kind of molecule take place, a second-order local reactivity descriptor (LRD) called Fukui function [18-20] may be used instead of electronic density. Fukui function is defined in terms of the derivative of  $\rho(r)$  electronic charge density with respect to total no. of electrons, N at constant geometry.

$$f(r) = \left[ \frac{\partial \rho(r)}{\partial N} \right]_{v(r)}$$

The function  $f(r)$  reflects the ability of a molecular site to accept or donate electrons. High values of  $f(r)$  are related to a high reactivity at point  $r$ . Since the number of electrons ‘N’ is a discrete variable [21], right and left derivatives of  $\rho(r)$  with respect to ‘N’ have emerged. By applying a finite difference approximation to the above equation, three definitions of Fukui functions depending on total electronic densities are obtained:

$$f^+(r) = \left[ \frac{\partial \rho(r)}{\partial N} \right]_{v(r)}^+ = \rho_{N+1}(r) - \rho_N(r)$$

$$f^-(r) = \left[ \frac{\partial \rho(r)}{\partial N} \right]_{v(r)}^- = \rho_N(r) - \rho_{N-1}(r)$$

$$f^0(r) = \left[ \frac{\partial \rho(r)}{\partial N} \right]_{v(r)}^0 = \frac{1}{2} [\rho_{N+1}(r) - \rho_{N-1}(r)]$$

Where  $\rho_{N+1}(r)$ ,  $\rho_N(r)$ , and  $\rho_{N-1}(r)$  are the electronic densities at point ‘r’ for the systems with N+1, N, and N-1 electrons, respectively. The first one,  $f^+(r)$ , has been associated to reactivity for a nucleophilic attack so that it measures the intramolecular reactivity at site ‘r’ toward a nucleophilic reagent. The second one,  $f^-(r)$ , has been associated to reactivity for electrophilic attack so that this function measures the intramolecular reactivity at site ‘r’ toward an electrophilic reagent. The third function,  $f^0(r)$ , refers to a radical and has been associated to reactivity towards radical attack.

Morell *et al.* [22-26] have proposed a local reactivity descriptor (LRD) which is called the dual descriptor (DD)  $f^2(r) \equiv \Delta f(r)$ . Morell and co-workers used the notation  $\Delta f(r)$ , but currently it has been replaced by the modern notation  $f^2(r)$  in order to highlight the fact that

this is a Fukui function of second order. Its physical meaning is to reveal nucleophilic and electrophilic sites on a molecular system at the same time. Mathematically, it is defined in terms of the derivative of the Fukui function,  $f(r)$ , with respect to the number of electrons,  $N$ . Through a Maxwell relation, this LRD may be interpreted as the variation of  $\eta$  (the molecular hardness which measures the resistance to charge transfer [27]) with respect to  $v(r)$ , the external potential. The definition of  $f^2(r)$  is shown below as indicated by Morell *et al.* [22,23]

$$\eta = \left[ \frac{\partial^2 E}{\partial N^2} \right]_v$$

$$f^2(r) = \left[ \frac{\partial f(r)}{\partial N} \right]_{v(r)} = \left[ \frac{\partial \eta}{\partial v(r)} \right]_N$$

As mentioned above,  $f^2(r)$  allows one to obtain simultaneously the preferable sites for nucleophilic attacks ( $f^2(r) > 0$ ) and the preferable sites for electrophilic attacks ( $f^2(r) < 0$ ) into the system at point ' $r$ '.

## 4.12. Computable Properties:

Using computational chemistry many molecular properties can be computed, these include:

- Bond energies, reaction energies, reaction pathways and mechanisms
- Structures of ground-, excited- and transition-states
- Atomic charges and electrostatic potentials
- Vibrational frequencies (IR and Raman)
- Transition energies and intensities for UV and IR spectra
- NMR chemical shifts
- Dipole moments, polarisabilities and hyperpolarisabilities

### 4.13. Conclusion:

Theoretical predictions about the structure and properties of molecules have come a long way since 1929. Even as early as 1959, the advances made in quantum chemistry were significant enough to warrant a review. In their famous “Broken Bottlenecks” article, Mulliken and Roothaan made their own pronouncement about the efficacy of quantum chemistry: Looking toward the future, it seems certain that colossal rewards lie ahead from large quantum–mechanical calculations of the structure of matter [28]. In 1980’s the scientists commented in various reviews of the quantum chemical literature: We are confident that by the year 2000, essentially all fields of chemistry will acknowledge the accuracy of Mulliken and Roothaan’s prophecy [29]. It is now time to note the accuracy of both prophecies, and to make a new one: We, as quantum chemists, now predict that by the year 2100, those “colossal rewards” will have been largely realized, and their consequences will be so striking that essentially all fields of science will acknowledge the accuracy of Mulliken and Roothaan’s prophecy. Computation of global reactivity descriptors (chemical hardness, chemical softness, ionization potential, electrophilicity index, chemical potential), polarizability and chemical hardness offer complementary information in combination with principles such as MHP and MPP. The future of computational approach to reactivity parameters is bright.



## References:

1. E. Schrödinger, *Physical Review*, 28, **1926**, 1049.
2. R. Shankar, *Principles of Quantum Mechanics (2nd ed.)*. Kluwer Academic/ Plenum Publishers, **1994**, 143.
3. I. N. Levine, *Quantum Chemistry*. Englewood Cliffs, New jersey: Prentice Hall, **1991**, 455.
4. R. G. Parr, "History of Quantum Chemistry".
5. R. G. Parr, D. P. Craig and I. G. Ross, *J. Chem. Phys.* 18, **1950**, 1561.
6. R. G. Parr, *Int. J. Quantum Chem.* 37, **1990**, 327.
7. T. C. Chen, *J. Chem. Phys.* 23, **1955**, 2200.
8. C. C. J. Roothaan, *J. Chem. Phys.* 28, **1958**, 982.
9. L. C. Allen and A. M. Karo, *Revs. Mod. Phys.* 32, **1960**, 275.
10. C. J. Cramer, *Essentials of Computational Chemistry*. Chichester: John Wiley & Sons, Ltd., **2002**, 153.
11. T. Van Mourik and R.J. Gdanitz, *J. Chem. Phys.* 116, **2002**, 9620.
12. J. Vondrasek, L. Bendova, V. Klusak and P. Hobza, *J. Am. Chem. Soc.* 127, **2005**, 2615.
13. S. Grimme, *J. Chem. Phys.* 124, **2006**, 34108.
14. U. Zimmerli, M. Parrinello and P. Koumoutsakos, *J. Chem. Phys.* 120, **2004**, 2693.
15. S. Grimme, *J. Comp. Chem.* 25, **2004**, 1463.
16. O. A. Von Lilienfeld, I. Tavernelli, U. Rothlisberger and D. Sebastiani, *Phys. Rev. Lett.* 93, **2004**, 153004.
17. M. E. Casida, C. Jamorski, F. Bohr, J. Guan and D. R. Salahub, *Theoretical and Computational Modeling of NLO and Electronic Materials*. Washington, D. C.: ACS Press. **1996**, 145.
18. P. Geerlings, F. De Proft and W. Langenaeker, *Chem. Rev.*, 103, **2003**, 1793.
19. R. G. Parr and W. Yang, *J. Am. Chem. Soc.*, 106, **1984**, 4049.
20. P. W. Ayers, W. Yang, L. J. Bartolotti and P. K. Chattaraj, Ed., *CRC Press. Taylor & Francis Group: Boca Raton, FL*, **2009**.
21. P. W. Ayers, *J. Math. Chem.*, 43, **2008**, 285.
22. C. Morell, A. Grand and A. T.Labbe, *J. Phys. Chem. A*, 109, **2005**, 205.
23. C. Morell, A. Grand and A. T.Labbe, *Chem. Phys. Lett.*, 425, **2006**, 342.
24. C. Cárdenas, N. Rabi, P. W. Ayers, C. Morell, P. Jaramillo and P. Fuentealba, *J. Phys. Chem. A*, 113, **2009**, 8660.
25. P.W.Ayers, C. Morell, F. De Proft and P. Geerlings, *Chem. Eur. J.*, 13, **2007**, 8240.
26. C.Morell, P. W. Ayers, A. Grand, S. Gutiérrez-Oliva and A. Toro-Labbé, *Phys. Chem. Chem. Phys.* 10, **2008**, 7239.
27. R.G.Parr and W.Yang, *Oxford Univ. Press: New York*, **1989**.
28. R.S.Mulliken and C.C.J. Roothaan, *Proc. U. S. Natl. Acad. Sci.* 45, **1959**, 394.
29. H.F. Schaefer, *Quantum Chemistry: The Development of Ab Initio Methods in Molecular Electronic Structure Theory*. Clarendon Press, Oxford. **1984**.



# CHAPTER 5

## **Aggregation Induced Emission Enhancement from Bathophenanthroline Micro Structures and Its Potential use as Sensor of Mercury ions in Water\***

\*A part of this chapter has been published in the article, “Prativa Mazumdar<sup>†</sup>, Debasish Das<sup>†</sup>, Gobinda Prasad Sahoo<sup>†</sup>, Guillermo Salgado-Morán<sup>‡</sup> and Ajay Misra<sup>†</sup>, *Phys. Chem. Chem. Phys.*, 2014, 16, 6283-6293.”

## 5.1. Introduction:

Aggregation induced emission enhancement (AIEE) based low dimensional materials are highly interesting due to their potential application as fluorescence sensor [1-4]. In the sensor research, mercury sensor is very essential in the present day, because mercury concentration increases in the food chain due to its bioaccumulation. Once mercury is introduced into the food chain, the environmental cycle causes serious threat to human health and ecology. Hence it is important to develop an extremely high sensitive, cost-effective  $\text{Hg}^{2+}$  sensor that can provide real-time determination of  $\text{Hg}^{2+}$  levels in the environment, water and food. Several methods, [5-7] such as atomic absorption and fluorescence spectroscopy, inductively coupled plasma atomic emission spectrometry, electrochemical sensing, and the use of piezoelectric quartz crystals, provide limits of detection at the parts-per-billion (ppb) level. Although the above approaches provide low detection limits, the methods are time-consuming and they lack the procedural simplicity for on-site analysis. To avoid this, alternative approaches using fluorescence based molecular sensors and chemo sensors have been actively pursued [8-12]. While fluorescence detection is highly sensitive, there is a continuous need for improving fluorophores with increased intensity and photo stability. However, most of these sensors display drawbacks in terms of actual applicability, such as the lack of water solubility, cross-sensitivity toward other metal ions, weak fluorescence enhancement factors, and short emission wavelengths [13].

Here, we have introduced a new low dimensional material of aggregated Bathophenanthroline where two free rotating phenyl rings are attached with the 1, 10 phenanthroline moiety at 4 and 7 position. Aggregated BA molecule exhibits AIEE effect and strong violet color fluorescence are observed under ultraviolet irradiation. We have also computed second order Fukui parameter for each atomic centre of BA as local reactivity descriptor to understand the possible site of interaction between the adjacent BA pairs in their aggregated form. The strong PL property of this novel low dimensional material is used to detect mercury ions in water at ppm level. Compare to other  $\text{Hg}^{2+}$  ion sensor, BA hydrosol is easy to prepare and it can selectively detect  $\text{Hg}^{2+}$  ions as low as ppm level. The drastic decrease of fluorescence of BA aggregates in presence of mercury ions have been explained as complex interplay between ground state complexation and external heavy atom induced perturbations by mercury ions.

## 5.2. Experimental:

**5.2.1. Materials:** Bathophenanthroline (BA) was purchased from Sigma-Aldrich Chemical Corp. Tetrahydrofuran (THF) and Mercuric Chloride, Cadmium Chloride, Manganese Chloride, Cobalt Chloride, Zinc Acetate, Ferrous Chloride, Copper Sulphate and Nickel Sulphate were purchased from E-Merck India Ltd. All the chemicals were of analytical grade and were used without further purification. Triply distilled deionised water was used throughout the experiment.

**5.2.2. Luminogen Preparation:** 0.05 M solution of BA was prepared using THF as good solvent. Then different amount of the above solution (1.25 $\mu\text{L}$  for Sample A, 2.5 $\mu\text{L}$  for Sample B, 5 $\mu\text{L}$  for Sample C, 20 $\mu\text{L}$  for Sample D, 50 $\mu\text{L}$  for Sample E, 100 $\mu\text{L}$  for Sample F) were rapidly injected into 5 ml water and allowed to stir for 2 min. Clearness of the solutions

gradually decreases and a milky white color was appeared. The solutions were allowed to stand for 30 min.

**5.2.3. Characterization:** UV-Vis absorption spectroscopy was used to characterize the optical properties and was measured in a 1cm quartz cuvette with a Shimadzu UV-1800 spectrophotometer. The spectra were recorded at room temperature in the range between 200 to 450 nm. Steady state fluorescence spectra were recorded using Hitachi F-7000 Fluorescence Spectrophotometer. Time-resolved fluorescence measurements were carried out under ambient conditions using a time-correlated single-photon counting (TCSPC) spectrometer [a picosecond diode laser (IBH, UK)]. All samples were excited using 280 nm picosecond diode laser and the emission was collected at 386 nm. Lamp profiles were measured with a band-pass of 3 nm using Ludox as the scatterer. The morphologies of the synthesized nano/micro structures were studied using ZEISS EVO 18 scanning electron microscope (SEM) operated at an accelerating voltage of 5 kV. Before SEM study samples were vacuum dries on a glass plate and a thin layer of Au was deposited onto the samples to minimize sample charging. Optical microscopy images were taken using NIKON ECLIPSE LV100POL upright microscope equipped with a 12V-50W mercury lamp. The samples for optical microscopic study were prepared by placing a drop of colloidal solution onto a clean glass slide. XRD was recorded in a 'Rigaku Miniflex-II' X-ray diffractometer using  $\text{CuK}\alpha$  radiation ( $\lambda=0.154056\text{nm}$ ). Scans were collected on dry samples in the range of  $10^{\circ}$ - $80^{\circ}$ . Samples for the XRD study of aggregated hydrosol were prepared by drying aqueous suspension of particles on a small glass slide followed by solvent evaporation under vacuum.

**5.2.4. Computational Method:** Quantum chemical calculations based on density functional theory (DFT) were carried out using a Gaussian09 program. Ground state geometry of BA was optimized and HOMO, LUMO energy gap this were performed using

the B3LYP functional and the 6-31G(d,p) basis set. The second order Fukui function,  $f^2(r)$  has been computed using this method to find out the possible mode of interaction between BA molecules in its aggregated state.

### 5.3. Result and Discussion:

**5.3.1. SEM Study:** SEM micrographs of Sample C, D and F are shown in Fig.5.1.

Comparison of SEM micrographs of these three samples shows three distinct morphologies *i.e.* micro rice (Sample C), micro rod (Sample D) and micro panicle (Sample F) respectively.

It is observed that one dimensional growth of particles from micro rice to micro rod to branch panicle geometry takes place with the increasing concentration of BA.

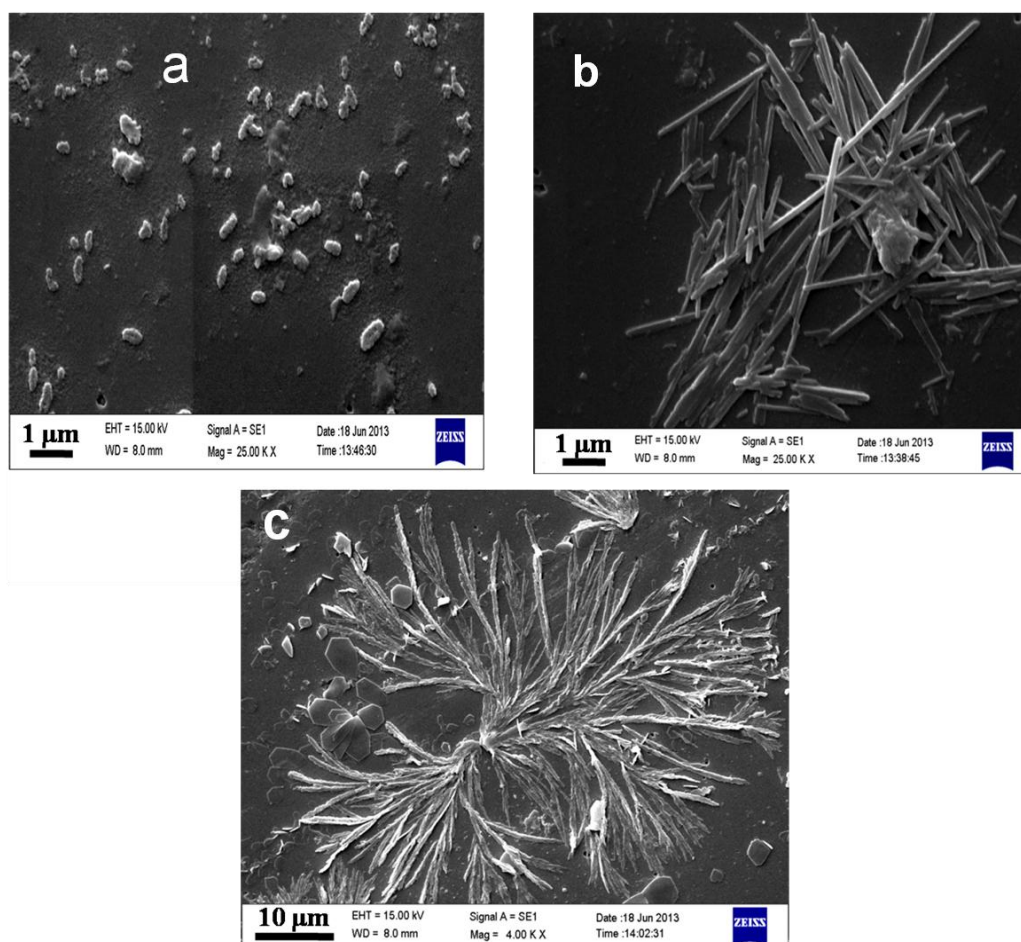


**Figure 5.1: SEM images of BA microstructures at different BA concentration (a)  $5 \times 10^{-5}$  M (Sample C) (b)  $2 \times 10^{-4}$  M (Sample D) (c)  $1 \times 10^{-3}$  M (Sample F).**

**5.3.2. Optical microscopic study:** The solid state luminescence property of BA was observed with optical microscopy which is a useful tool to observe the morphologies of the microstructure. Panicle shape morphology is observed for the Sample F (Fig.5.2). At low BA concentration, sizes of particles are too small to be detected by the present resolution of our microscope. Dark field's view of this Sample F using polarizer and analyzer assembly shows different colors depending on the direction of incident radiation and it suggests the anisotropic nature of synthesized microcrystal (Fig. 5.2b).

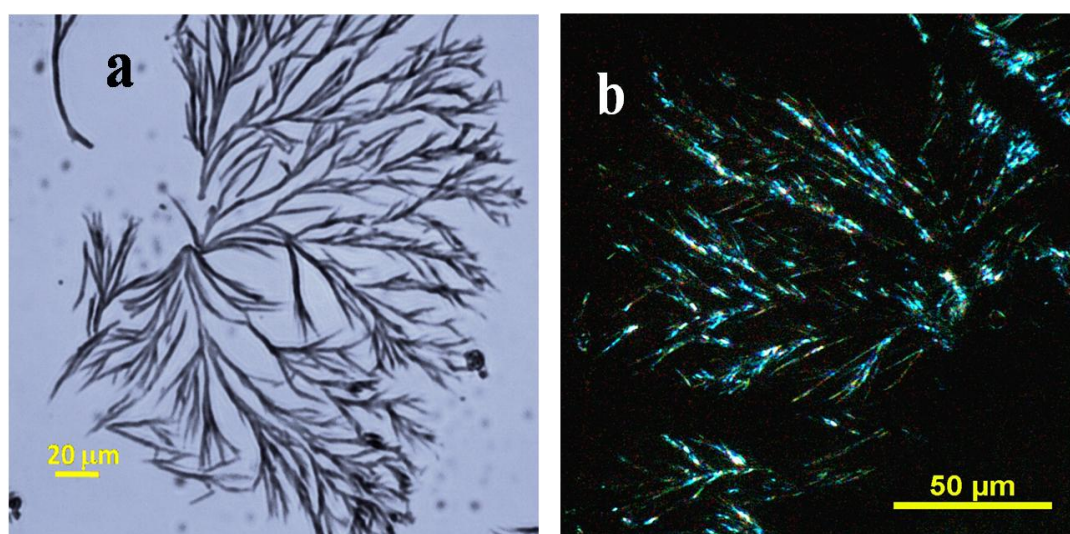


**Figure 5.2: (a) Optical microscopic images of BA microcrystals having  $1 \times 10^{-3}$  M BA (Sample F). (b) Polarized optical microscopy images of BA microcrystals having  $1 \times 10^{-3}$  M BA (Sample F).**

**5.3.3. XRD Study:** In view of the variety of microcrystals observed, a question comes in our mind; does this variety result from a change in crystal habit or the formation of different polymorphs? The problem is that the possibility of polymorphism is hard to study in our case because of small size of microcrystals. We didn't succeed in growing a single crystal of sufficient size, so that the crystal structure of BA can be known. XRD analysis was carried out in order to recheck the crystalline nature of Sample F (we did not succeed to prepare film with sufficient thickness for XRD measurements for other samples) and was compared with the powder XRD pattern of BA. XRD pattern of both the aggregated BA film and BA powder

are shown in Fig.5.3 (i) and 5.3(ii) respectively. BA film shows sharp XRD peaks and the position of the peaks are almost similar to that of powder BA. A sharp intense peak at  $2\theta = 16.99^\circ$  is observed for BA film and the corresponding 'd' value is 5.21Å. This sharp intense peak at  $2\theta = 16.99^\circ$  suggests that the microcrystal of BA aggregate grow along the plane with  $2\theta$  value  $16.99^\circ$ .

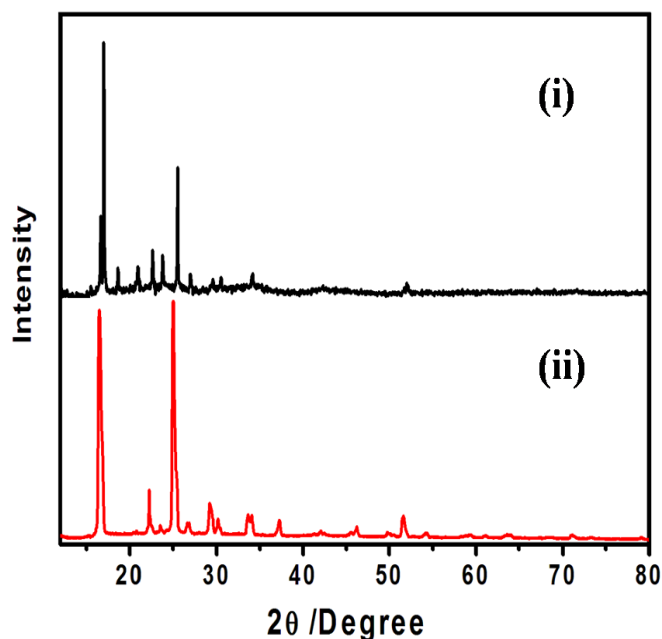


**Figure 5.3: XRD Patterns of (i) Film prepared from the microcrystal of Sample F and (ii) BA powder.**

**5.3.4. UV-Vis Study:** UV-Vis spectra of BA in THF show three distinct bands with peaks at 245, 272 and 305 nm respectively (Fig.5.4a). The absorption band with peaks at 245 and 272 nm band correspond to the  $\pi - \pi^*$  transition within phenyl and phenanthroline groups of BA and the weak broad shoulder at  $\sim 305$  nm is due to  $n - \pi^*$  transition within the phenanthroline ring of BA. Fig.5.4a also shows the absorption spectra of aggregated BA hydrosol having various BA concentrations. Nearly 5-10nm bathochromic shift of both the  $\pi - \pi^*$  and  $n - \pi^*$  transitions of phenanthroline moieties of BA in aggregated form are observed and compare to BA in THF. A closer look of the spectra illustrates red shift as the concentration of BA increases from  $1.25 \times 10^{-5}$  M to 0.2 mM and then shifted to blue with the



further increase of BA concentration. Red shifts of spectra are due to weak  $\pi - \pi$  interaction of BA in its aggregated form. On the other hand, with further increase in concentration ( $>0.2$  mM) of BA, agglomerated crystals become larger in size and there occurs crystal softening which is the manifestation of weak interactions among the neighboring BA molecules. This weak  $\pi - \pi$  interactions cause blue shift of spectra after reaching a maximum red shift at a concentration 0.2mM. Comparison of UV-Vis absorption spectra of BA in THF and in different volume fraction of water are shown in Fig.5.4b. It is observed that the spectra are affected very little with increasing volume fraction of water for a given concentration of BA. This small shift in the absorption spectra is due to weak aromatic  $\pi - \pi$  interaction of BA in its aggregated form [14].

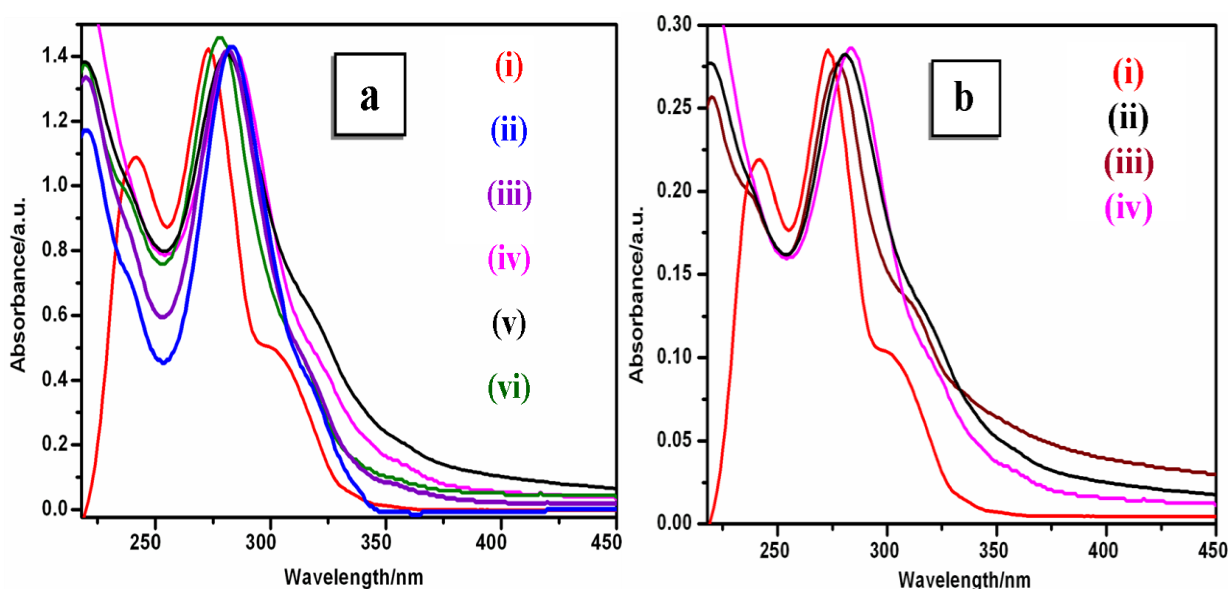


**Figure 5.4:** (a) UV-Vis absorption spectra of (i)  $5 \times 10^{-5}$  M BA (Mother), (ii)  $1.25 \times 10^{-5}$  M BA (Sample A), (iii)  $2.5 \times 10^{-5}$  M BA (Sample B), (iv)  $5 \times 10^{-5}$  M BA (Sample C), (v)  $2 \times 10^{-4}$  M BA (Sample D), (vi)  $5 \times 10^{-4}$  M BA (Sample E). (b) UV-Vis absorption spectra of  $5 \times 10^{-5}$  M BA in (i) 0% water (Mother), (ii) 20% water, (iii) 40 % water, (iv) 90 % water.

**5.3.5. Emission Study:** Fig.5.5 shows the PL spectra of BA in THF and the aggregated hydrosol of BA. It is observed that the diluted solution ( $5 \times 10^{-5}$  M) of BA in THF exhibits almost no emission upon photo excitation at 270 nm. But in its aggregated hydrosol, BA

exhibits intense broad emission having maximum at 386nm. PL spectra of BA hydrosol at different time interval after its preparation are shown in Fig.5.5a. PL intensity increases with time and reaches the maximum after 30min. Initially the mechanical shear stress leads to the increasing chances of most probable collisions; thus a portion of BA molecules clustered together to form tiny particles. The remaining portion of BA molecules presents in the solvent mixture then gradually deposited onto the initially formed particle in recrystallization pattern to give highly emissive aggregated structure. So with increasing time, the system attains an ordered cluster which restricts the free rotation of phenyl ring and as a result the enhanced emission of molecules appears.

Optimum concentration of BA for PL study is achieved by adding different volume of 0.05 M BA in THF into 5mL of water. It has been observed that the PL intensity increases with increasing concentration of BA and reaches a maximum value at  $5 \times 10^{-5}$  M BA. Further increase in BA concentration results gradual decrease of PL intensity keeping the peak position unaltered (Fig.5.5b). This suggests that  $5 \times 10^{-5}$  M is the optimum concentration of BA in solution below which aggregation of BA occur in such a way that it can form emissive crystalline structure but above this concentration molecules start to be aggregated in random orientation that break the regular crystalline structure and make it less emissive one [15].

Fig.5.5c shows the fluorescence emission spectra of BA at different volume fraction of poor solvent, water. In all the sets, the concentration of BA is fixed to  $5 \times 10^{-5}$  M. It is observed that PL intensity increases slowly up to 80% water fraction but suddenly an upward shift is observed when water fraction is 90% (Fig.5.5d). This increasing intensity of BA with increasing water content has been explained due to formation of more and more aggregated BA structure. Aggregated BA structures restrict the free rotation of phenyl groups of individual BA molecules and thus block the nonradiative deactivation channels of BA in its

excited states. Inset of Fig.5.5c also shows the change in color from colorless to blue under UV excitation.

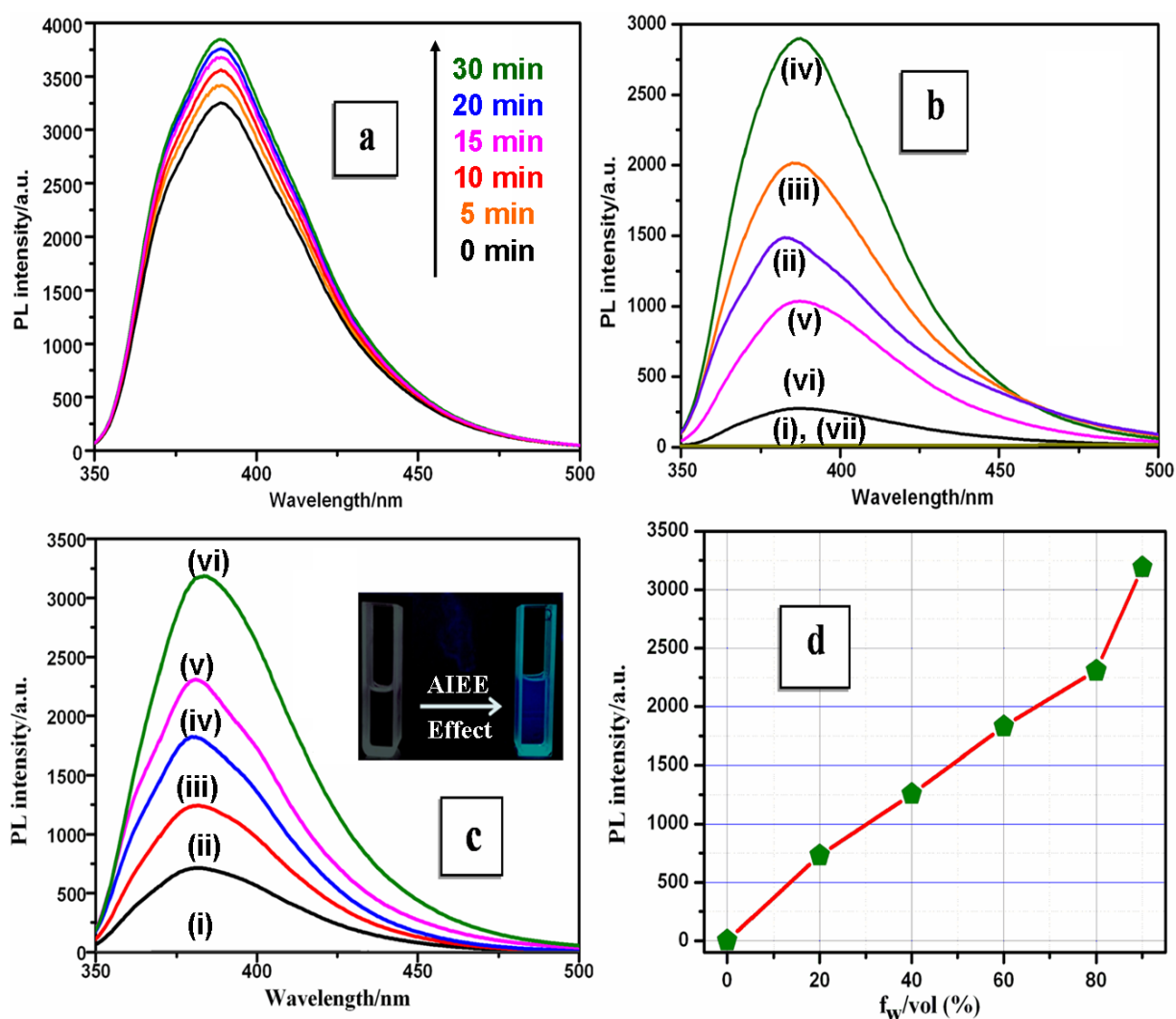


**Figure 5.5:** (a) Dependence of the PL intensity of BA immediate after its preparation with time in THF/water mixture (10:90 v/v). BA concentration:  $5 \times 10^{-5}$  M.  $\lambda_{\text{ex}}$ : 270 nm. (b) Emission spectra of (i)  $5 \times 10^{-5}$  M BA in THF (Mother) and (ii)  $1.25 \times 10^{-5}$  M BA (Sample A), (iii)  $2.5 \times 10^{-5}$  M BA (Sample B), (iv)  $5 \times 10^{-5}$  M BA (Sample C), (v)  $2 \times 10^{-4}$  M BA (Sample D), (vi)  $5 \times 10^{-4}$  M BA (Sample E), (vii)  $1 \times 10^{-3}$  M BA (Sample F) in THF/water mixture (10:90 v/v).  $\lambda_{\text{ex}}$ : 270 nm. (c) Emission spectra of freshly prepared BA ( $5 \times 10^{-5}$  M) in (i) 0% water (Mother), (ii) 20% water, (iii) 40% water, (iv) 60% water, (v) 80% water and (vi) 90% water.  $\lambda_{\text{ex}}$ : 270 nm. Inset: Fluorescence images of BA (0% and 90% H<sub>2</sub>O) under 270 nm illumination. (d) Plot of relative variation of PL intensity against water content ( $f_w$ ) in THF/water mixture. BA concentration:  $5 \times 10^{-5}$  M.  $\lambda_{\text{ex}}$ : 270 nm.

### 5.3.6. Time resolved Fluorescence Study:

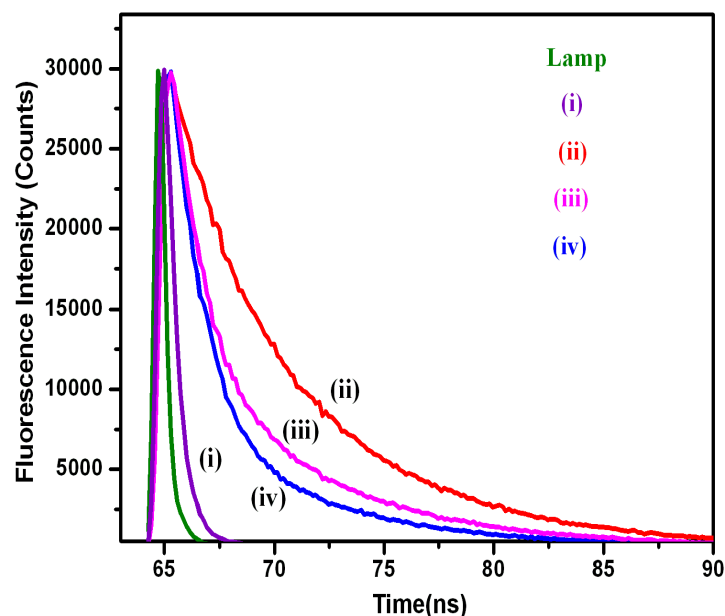


**Figure 5.6: Time-resolved fluorescence spectra of (i)  $5 \times 10^{-5}$  M BA (Mother), (ii)  $5 \times 10^{-5}$  M BA (Sample C), (iii)  $2 \times 10^{-4}$  M BA (Sample D) and (iv)  $5 \times 10^{-4}$  M BA (Sample E) at 386 nm emission. Excitation wavelength: 280 nm.**

In order to understand the nature of aggregate of BA luminogen, we have carried out time resolved fluorescence study of BA in THF and aggregated BA hydrosols with excitation at 280 nm and emissions are measured at 386nm. Decay profile of monomer and hydrosols are shown in Fig.5.6. Fluorescence lifetimes of the samples are measured by deconvoluting the response function from the decay curves. Fluorescence lifetime of diluted BA in THF is 0.37ns with very weak emission intensity. It took nearly 15-20 times more time to get comparable emission intensity as that of its aggregated hydrosols. Fluorescence decay profiles of aggregated BA hydrosols having reasonably higher emission intensity are fitted with bi-exponential decay. The observed components of lifetime for aggregated BA particles lie within  $\sim 1$ -2 ns and  $\sim 6$ -7 ns respectively. Our analyzed fluorescence lifetime data (table 5.1) also show that the weight percentage of 1-2 ns component increases and the 6-7 ns decreases with the increased concentration of BA. It seems that the  $\sim 1$ -2 ns component is due to the foregoing aggregates of BA in solution and  $\sim 6$ -7 ns can be assigned to the crystal

fluorescence lifetime where neighboring BA molecules are present in more rigid form causing the non-radiative reactivation of BA aggregates less probable. Since the crystalline nature of BA aggregates decreases due to crystal softening at higher concentration of BA, it is also reflected in the decreased weight percentage of 6-7 ns component as we go from sample C to D to E.

**Table 5.1: Fluorescence life time of Bathophenanthroline monomer in THF and aggregated hydrosols (Sample C, D, E) of BA in water**

Materials	$\tau_1$ (ns)	Contribution (%)	$\tau_2$ (ns)	Contribution (%)	$\chi^2$
Mother	0.37	100%			0.93
Sample C	2.3	32%	6.7	68%	1.1
Sample D	1.32	75%	6.64	25%	1.02
Sample E	1.2	83%	6.53	17%	0.97

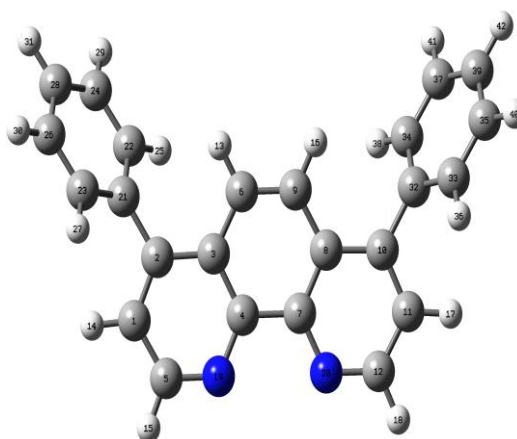
**5.3.7. Mechanism of AIEE effect:** Non emissive property in BA molecules is due to the free twisting of benzene moiety in solution phase and as a consequence of that BA molecules waste major part of its excitation energy through non radiative pathway.

In order to understand the distribution of electron density within the aromatic rings of BA, we have optimized the energy of BA using density functional theory (DFT) with B3LYP/6-31G (d) hybrid functional. Our computed HOMO electron density (Fig.5.7) illustrates that electron densities are localized within two phenyl and the phenanthroline groups of BA. On the other hand LUMO electron densities are localized among all the three aromatic rings of BA. This delocalization of excited electronic energy to the freely rotating phenyl groups is responsible to open up the non-radiative deactivation channels for excited BA in its isolated form in solution.

Again the optimized structure of BA using the DFT (B3LYP/ 6-31G(d)) level of theory shows that BA attain a torsionally distorted geometry where two phenyl rings are

present  $55.26^\circ$  out of plane with the phenanthroline group. This distorted out of plane structure of phenyl groups do not favor strong  $\pi$ - $\pi$  stacking interaction among the neighboring BA molecules. It is observed that, the distance between two BA molecules cannot be less than  $5.08\text{\AA}$  and this is in conformity with the calculated 'd' value ( $5.21\text{\AA}$ ) from XRD study. This larger intermolecular distance is responsible for weak overlap of aromatic  $\pi$  electrons between two neighboring BA molecules in its aggregated structures.

The possible mode of attachment of BA with other BA in their aggregated structures can be well understood theoretically using second order Fukui Parameter ( $f^2(r)$ ) as local reactivity descriptor for each atomic centre of BA (Table 5.2). Since negative value of  $f^2(r)$  is a preferable sites for electrophilic attack and positive  $f^2(r)$  values are the possible sites for nucleophilic attack, table 5.2 illustrates that  $C_{12}$  is a most nucleophilic center and  $C_{32}$  is most electrophilic center. Thus  $C_{12}$  of phenanthroline moiety mostly prefer to be closed with  $C_{32}$  atom of neighbouring BA molecule through electrostatic covalent attraction. This end to end attachment BA in its aggregated structures (Scheme 5.1) is one of the main reasons that BA shows AIEE effect instead of ACQ in its aggregates form.



**Optimized Structure of BA.**

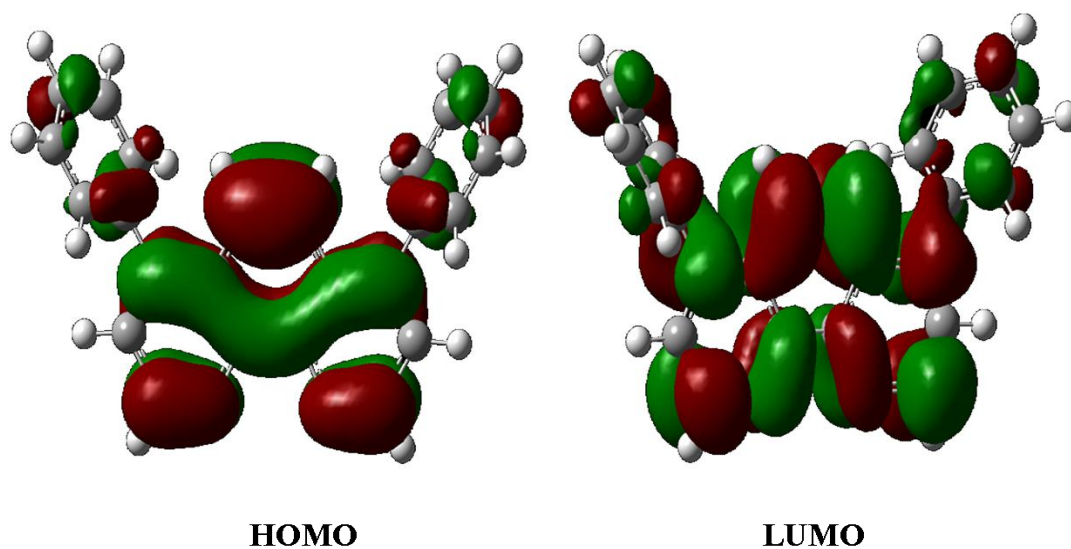
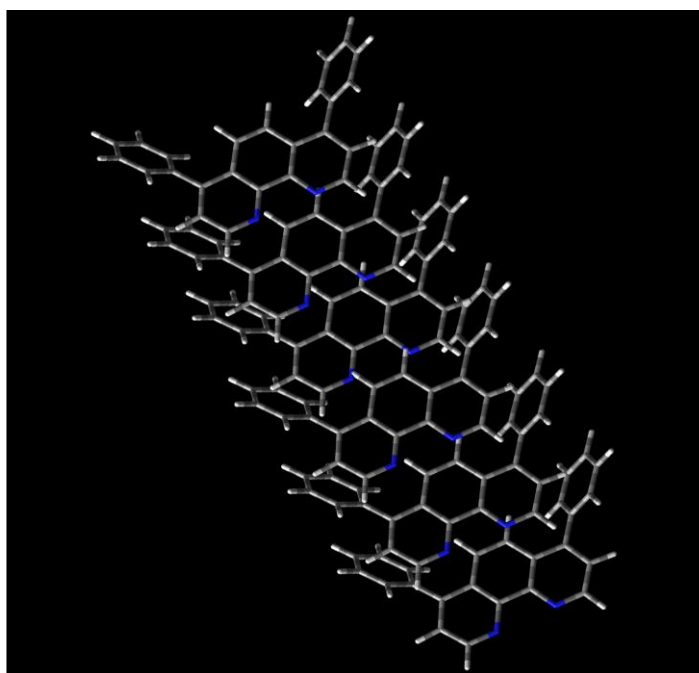


**Figure 5.7: Optimized structure and HOMO and LUMO electron densities of BA calculated using the DFT (B3LYP/ 6-31G (d)) level of theory.**



**Scheme 5.1: Packing motif of Bathophenanthroline through intermolecular covalent interaction.**

**Table 5.2: Electrophilic  $f^+(r)$  and nucleophilic  $f^-(r)$  condensed Fukui functions and second order Fukui parameter  $f^2(r)$  of Bathophenanthroline molecule calculated using DFT B3LYP 6-31G (d) level of theory**

<i>Atom</i>	<i>No.</i>	$f_k^+$	$f_k^-$	$f_k^2$	<i>Atom</i>	<i>No.</i>	$f_k^+$	$f_k^-$	$f_k^2$
C	1	-0.006	-0.014	0.008	C	22	0.003	-0.008	0.011
C	2	-0.072	-0.054	-0.018	C	23	-0.026	-0.01	-0.016
C	3	0.009	0.004	-0.013	C	24	-0.022	-0.008	-0.014
C	4	-0.012	-0.024	0.012	H	25	-0.003	-0.003	0
C	5	-0.083	-0.056	-0.027	C	26	-0.01	-0.019	0.009
C	6	-0.074	-0.09	0.016	H	27	-0.008	-0.01	0.002
C	7	-0.012	-0.024	0.012	C	28	-0.04	-0.05	0.01
C	8	-0.009	0.004	-0.013	H	29	-0.017	-0.017	0
C	9	-0.074	-0.09	0.016	H	30	-0.018	-0.018	0
C	10	-0.072	-0.054	-0.018	H	31	-0.018	-0.018	0
C	11	-0.006	-0.014	0.008	C	32	0.025	0.005	0.02
C	12	-0.083	-0.056	-0.027	C	33	-0.026	-0.01	-0.016
H	13	-0.023	-0.019	-0.004	C	34	0.003	-0.008	0.011
H	14	-0.024	-0.023	-0.001	C	35	-0.01	-0.019	0.009
H	15	-0.027	-0.026	-0.001	H	36	-0.008	-0.01	0.002
H	16	-0.023	-0.019	-0.004	C	37	-0.022	-0.008	-0.014
H	17	-0.024	-0.023	-0.001	H	38	-0.003	-0.003	0
H	18	-0.027	-0.026	-0.001	C	39	-0.04	-0.05	0.01
N	19	-0.037	-0.039	0.002	H	40	-0.018	-0.018	0
N	20	-0.037	-0.039	0.002	H	41	-0.017	-0.017	0
C	21	0.025	0.005	0.02	H	42	-0.018	-0.018	0

## 5.4. Mercury Sensor:

The most interesting application of this molecule opens a new channel of sensing mercury ion concentration in its aqueous solution by weak electrostatic attachment of  $\text{Hg}^{2+}$  with negative binding site of the molecule *i.e.* the nitrogen atoms. Fig.5.8a shows the appearance of a broad red shifted absorption band ( $\sim 360$  nm) upon addition of  $\text{Hg}^{2+}$  ion to BA hydrosol and this red shifted band increases in intensity with the increasing concentration of  $\text{Hg}^{2+}$  ions. This new red shifted band is due to the formation of ground state complex between  $\text{Hg}^{2+}$  ions and the electron donor nitrogen centre of BA through soft-soft combination. On the other hand, UV-vis absorption spectra of BA hydrosol in presence of



other metal ions *e.g.*  $\text{Cd}^{2+}$ ,  $\text{Cu}^{2+}$ ,  $\text{Fe}^{2+}$ ,  $\text{Co}^{2+}$ ,  $\text{Zn}^{2+}$ ,  $\text{Mn}^{2+}$ ,  $\text{Ni}^{2+}$  having same concentration as that of  $\text{Hg}^{2+}$ , show no red shifted broad absorption band (Fig.5.8c) and it rules out any ground state complexation between BA hydrosols and metal ions other than  $\text{Hg}^{2+}$  in this present study. Red shift of 272nm band in presence of all the metal ions may be attributed due to the change in dielectric constant of the medium.

Presence of  $\text{Hg}^{2+}$  ion also affects the PL spectra of BA hydrosol and it is shown in Fig.5.8b. Initially at a very low concentration of mercury ( $10^{-7}$  M), a sudden fall in emission intensity is observed and at higher concentration of  $\text{Hg}^{2+}$  ion *i.e.* above  $10^{-4}$  M, emission intensity decreases substantially. On the other hand the PL intensity of BA hydrosol (Fig.5.8d) in presence of other metal ions *e.g.*  $\text{Cd}^{2+}$ ,  $\text{Cu}^{2+}$ ,  $\text{Fe}^{2+}$ ,  $\text{Co}^{2+}$ ,  $\text{Zn}^{2+}$ ,  $\text{Mn}^{2+}$ ,  $\text{Ni}^{2+}$  also decreases but the decrease is much less compare to  $\text{Hg}^{2+}$ . This small decrease of PL intensity for other than  $\text{Hg}^{2+}$  ions has been attributed to external heavy atom induced quenching.

This fluorescence turn-off property of BA hydrosol in presence of  $\text{Hg}^{2+}$  ion is due to complex interplay of two types of effects *i.e.* the formation of ground state complexation between BA and  $\text{Hg}^{2+}$  and external heavy atom induced emission quenching by  $\text{Hg}^{2+}$ . Added  $\text{Hg}^{2+}$  ions can easily bind to the surface BA through its chelating nitrogen centre to form ground state complex. Again inter system crossing of BA is favored by  $\text{Hg}^{2+}$  induced spin-orbit coupling whose efficiency has a  $Z^4$  dependence ( $Z$  is atomic number of quencher) and it is responsible to depopulate the emissive  $S_1$  state of BA. Thus both the ground state complexation and heavy atom perturb depopulation of emissive  $S_1$  state of BA are responsible for mercury induced large fluorescence quenching of BA.

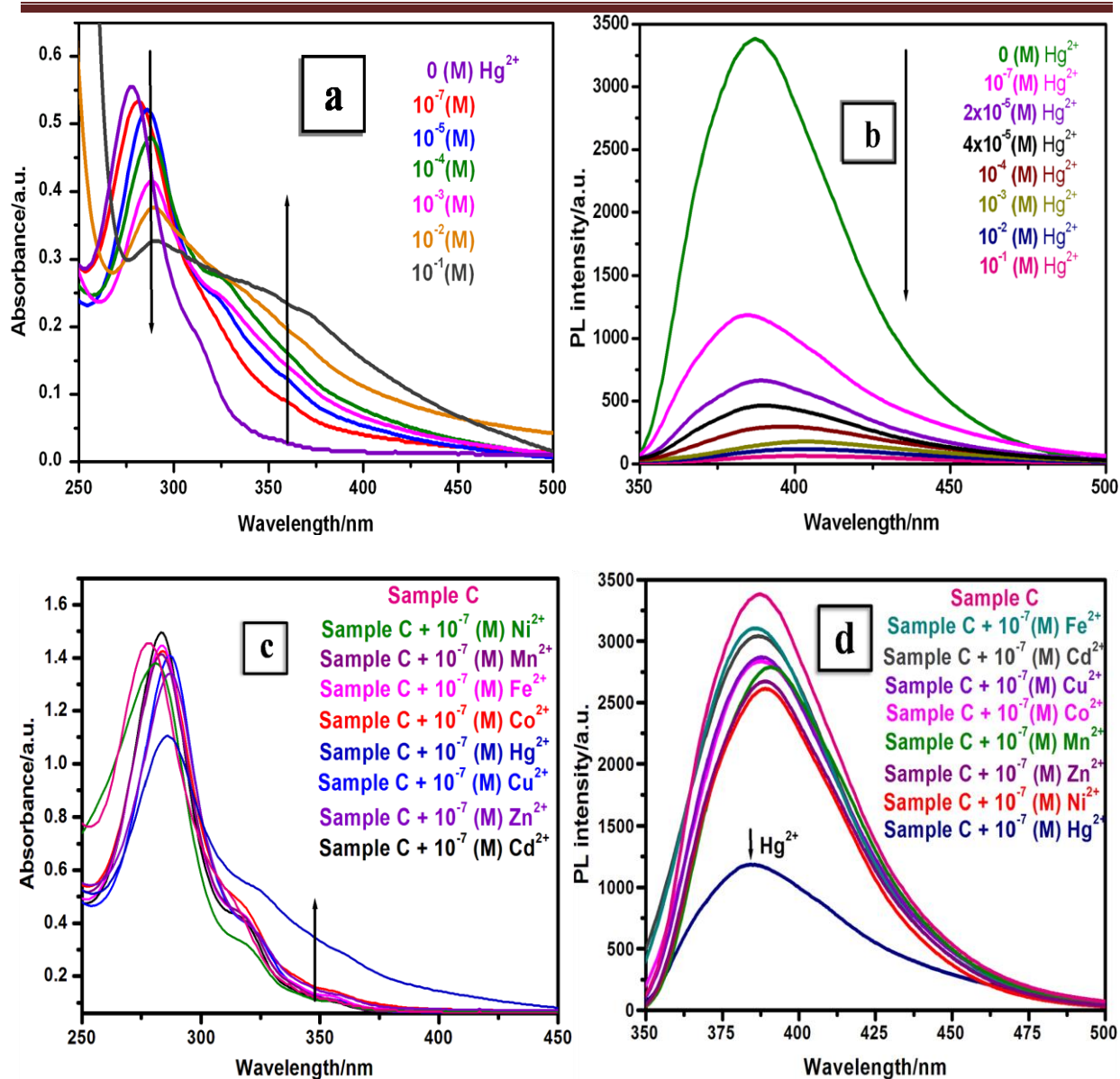


**Figure 5.8:** (a) UV-Vis absorption spectra of BA hydrosol upon addition of  $\text{Hg}^{2+}$  ions from 0.0 M to 0.1M (b) Fluorescence emission spectra of BA hydrosol upon addition of  $\text{Hg}^{2+}$  ions from 0.0 M to 0.1M. (c) UV-Vis absorption and (d) Emission spectra of Sample C in absence and presence of  $10^{-7}$  M various metal ions ( $\text{Ni}^{2+}$ ,  $\text{Mn}^{2+}$ ,  $\text{Cd}^{2+}$ ,  $\text{Co}^{2+}$ ,  $\text{Cu}^{2+}$ ,  $\text{Fe}^{2+}$ ,  $\text{Zn}^{2+}$ ,  $\text{Hg}^{2+}$ ).

## 5.5. Conclusion:

Our present synthesis of aggregated BA hydrosol is very interesting so far as its photophysical properties are concerned. BA has almost no emission in its diluted solution. But the aggregated hydrosol of BA shows strong emission and it is termed as aggregated induced emission enhancement (AIEE). BA has two freely rotating phenyl groups, which

after excitation transfer its energy through phenyl group rotation to the environment and it is responsible for quenching of BA emission in its diluted solution in THF. But in the aggregated hydrosol of BA, phenyl groups are no longer free to rotate and again due to weak aromatic  $\pi$ - $\pi$  interactions among the neighbouring BA molecules, strong AIEE effect is observed. Weak  $\pi$ - $\pi$  interaction among the BA molecules in aggregated form and its one dimensional growth with increasing BA concentration have been explained theoretically using second order Fukui parameter as local reactivity descriptor. Quenching of aggregated BA luminescence in presence of  $\text{Hg}^{2+}$  ions in water are being used as selective  $\text{Hg}^{2+}$  ion sensor in water at a very low concentrations. This quenching of BA emission by  $\text{Hg}^{2+}$  ions has been attributed to the complex interplay between ground state complexation and external heavy atom induced emission quenching by  $\text{Hg}^{2+}$  ions. Compare to other  $\text{Hg}^{2+}$  sensor BA hydrosol is easy to prepare.

**References:**

1. N. B. Shustova, A. F. Cozzolino, S. Reineke, M. Baldo and M. Dinca, *J. Am. Chem. Soc.*, 135, **2013**, 13326.
2. X. Li, G. Wang, X. Ding, Y. Chen, Y. Gou and Y. Lu, *Phys.Chem.Chem.Phys.*, 15, **2013**, 12800.
3. M. Wang, D. Zhang, G. Zhang and D. Zhu, *Chem. Commun*, **2008**, 4469.
4. A. Ito, S. Ishizaka and N. Kitamura, *Phys.Chem.Chem.Phys.*, 12, **2010**, 6641.
5. Y. Li, C. Chen, B. Li, J. Sun, J. Wang, Y. Gao, Y. Zhao and Z.J. Chai, *Anal. Atom. Spectrom.* 21, **2006**, 94.
6. M. Leermakers, W. Baeyens, P. Quevauviller and M. Horvat, *Trends Anal. Chem.* 24, **2005**, 383.
7. B. Valeur, *Wiley-VCH, Weinheim*, **2002**.
8. H. Komatsu, T. Miki, D. Citterio, T. Kubota, Y. Shindo, Y. Kitamura, K. Oka and K. Suzuki, *J.Am. Chem. Soc.* 127, **2005**, 10798.
9. X.J. Zhu, S.T. Fu, W.K. Wong, J.P. Guo and W.Y. Wong, *Angew. Chem., Int. Ed.* 45, **2005**, 3150.
10. J.V. Mello and N.S. Finney, *J. Am. Chem. Soc.* 127, **2005**, 10124.
11. E.M. Nolan and S.J.A. Lippard, *J. Am. Chem. Soc.* 125, **2003**, 14270.
12. A. Caballero, R. Martinez, V. Lioveras, I. Tatera, J. Vidal-Gancedo, K. Wurst, A. Tarraga, P. Molina and J. Veciana, *J. Am. Chem. Soc.* 127, **2005**, 15666.
13. J. Chen, A. Zheng, A. Chen, Y. Gao, C. He, X. Kai, G. Wu and Y. Chen, *Anal. Chim. Acta*, 599, **2007**, 134.
14. C. Shi, Z. Guo, Y. Yan, S. Zhu, Y. Xie, Y. S. Zhao, W. Zhu and H. Tian, *ACS Appl. Mater. Interfaces*, 5, **2013**, 192.
15. J. Liu, Q. Meng, X. Zhang, X. Lu, P. He, L. Jiang, H. Dong and W. Hu, *Chem. Commun.*, 49, **2013**, 1199.



# CHAPTER 6

## **Aggregation Induced Emission Enhancement of 4,4'-bis(diethylamino)benzophenone With an Exceptionally Large Blue Shift and Its Potential Use as Glucose Sensor\***

\*A part of this chapter has been published in the article, “Prativa Mazumdar<sup>†</sup>, Debasish Das<sup>†</sup>, Gobinda Prasad Sahoo<sup>†</sup>, Guillermo Salgado-Morán<sup>‡</sup> and Ajay Misra<sup>†</sup>, *Phys. Chem. Chem. Phys.*, 2015, 17, 3343-3354.”

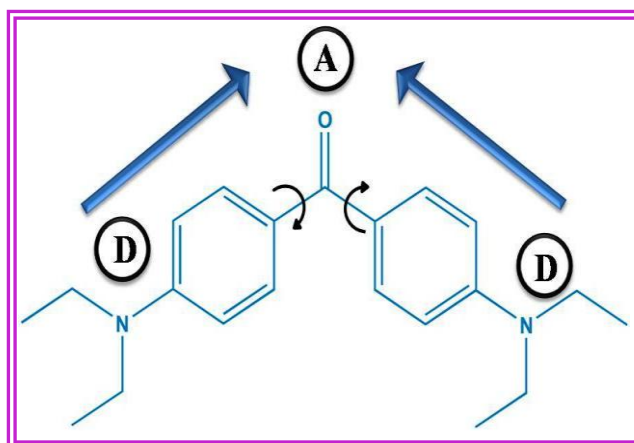
## 6.1. Introduction:

Aggregation induced emission enhancement (AIEE) based luminogen molecules with donor-acceptor (D-A) structure is one of the important materials now-a-days to get desired application in optoelectronic devices [1]. Due to facile manipulation of frontier orbital energy level, energy band gaps, carrier injection and transport balance of D-A molecules, the photoluminescence spectra can be easily shifted to the longer wavelengths [2-4]. In such intramolecular processes of a conjugated system with donor and acceptor subunits, the reaction product is usually called an intramolecular charge transfer (ICT) state. This fact greatly hinders the progress of D-A molecules to the short wavelength *i.e.* blue or ultraviolet region when they are used as active film in optoelectronic device. So the major challenge was to introduce a luminogen which prevents the most general red shifting but preserving the merits of D-A architecture.

AIEE effect has been utilized in various application fields. Amongst the different sensory system such as toxic metal sensors [5-7], volatile organic compounds sensor [8], explosives sensors etc [9] detection of saccharide *e.g.*, D-Glucose has been a great interest for long time due to its importance in medical diagnosis and bioprocessing. Though enzyme-based detection approaches are highly selective and effective but there are many limitations, including instability, difficult sterilization, slow sensor time lags and high cost [10]. An optical response is especially favored because it can be detected remotely. After a long research the best ligand identified for binding glucose in aqueous media is boronic acid [11-

13]. Singaram's group developed a series of two-component sensing system [14], but these glucose sensing systems are not only involving very complicated procedures to synthesize, but also not easy to be fabricated into device application.

Herein, a new low dimensional D-A material from 4,4'-bis(diethylamino) benzophenone (BZP) in which, two donor diethyl phenyl amine units are bridged by the acceptor keto group have been introduced (Scheme 6.1). Aggregated BZP molecule exhibits exceptional blue shifted PL spectra with a strong intense emission in its aggregated state than its dilute solution in any good solvent. This aggregation induced enhanced (AIE) blue emission are explained due to suppression of twisted intramolecular charge transfer (TICT) state in the aggregated structure and the blue shifted emission appears from the locally excited (LE) state of BZP in its aggregated structures. A broad red shifted emission band is also observed and it increases in intensity with increasing size of the aggregates. This broad emission originates from the excited intramolecular charge transfer (ICT) state of the relatively planar molecule present within the aggregated structures of BZP due to crystal softening. We have also used this aggregated material in fluorescence sensory probe and found its quenching efficiency in presence of D-Glucose. Quenching of blue emission from the aggregated structure has been explained due to the hydrogen bonding complexation between D-Glucose and BZP molecule present in the aggregated structures.



**Scheme 6.1: Molecular Structure of BZP.**

## 6.2. Experimental:

**6.2.1. Materials:** 4,4'-bis(diethylamino)benzophenone (BZP) and D-Glucose were purchased from Sigma-Aldrich Chemical Corp. Tetrahydrofuran (THF), Cyclohexane (CH), N, N dimethyl formamide (DMF) were purchased from E-Merck India Ltd. All the chemicals were of analytical grade and the purity were checked by UV-Vis spectroscopy. Triply distilled deionised water was used throughout the experiment.

**6.2.2. Fluorogen Preparation:** BZP aggregates were prepared through well known reprecipitation method. 0.01 M solution of BZP was prepared using THF as good solvent. Then different amount of the above solution (10 $\mu$ L for Sample A, 20 $\mu$ L for Sample B, 30 $\mu$ L for Sample C, 50 $\mu$ L for Sample D, 70 $\mu$ L for Sample E, 100 $\mu$ L for Sample F) were rapidly injected into 5 ml water and allowed to stir for 2 min. The final concentrations of BZP are 20 $\mu$ M, 40 $\mu$ M, 60 $\mu$ M, 100 $\mu$ M, 140 $\mu$ M and 200 $\mu$ M for Sample A, B, C, D, E and F respectively. Clearness of the solutions gradually decreases and milky white color was appeared. The solutions were allowed to stand for 30 min.

**6.2.3. Characterization:** UV-Vis absorption spectroscopy was used to characterize the optical properties and was measured in a 1cm quartz cuvette with a Shimadzu UV-1800 spectrophotometer. The spectra were recorded at room temperature in the range between 270 to 600 nm. Steady state fluorescence spectra were recorded using Hitachi F-7000 Fluorescence Spectrophotometer. Time-resolved fluorescence measurements were carried out under ambient conditions using a time-correlated single-photon counting (TCSPC) spectrometer [a picoseconds diode laser (IBH, UK)]. All samples were excited using 280 nm picoseconds diode laser and the emission was collected at 339 and 460 nm. Lamp profiles were measured with a band-pass of 3 nm using Ludox as the scatterer. The morphologies of the synthesized micro structures were studied using ZEISS EVO 18 scanning electron



microscope (SEM) operated at an accelerating voltage of 10 kV. Before SEM study samples were vacuum dried on a glass plate and a thin layer of Au was deposited onto the samples to minimize sample charging. Optical microscopy images were taken using NIKON ECLIPSE LV100POL upright microscope equipped with a 12V-50W mercury lamp. The samples for optical microscopic study were prepared by placing a drop of colloidal solution onto a clean glass slide.

**6.2.4. Computational Method:** Quantum chemical calculations were carried out using a Gaussian 09 program. Ground state geometry of BZP was optimized and HOMO, LUMO energy gap this were performed using DFT based B3LYP functional and the 6-31G(d,p) basis set. Excited state geometry of BZP was also carried out using TDDFT based B3LYP functional and the 6-31G(d,p) basis set. The second order Fukui function,  $f^2(r)$  has been computed using this method to find out the possible mode of interaction between BZP molecules in its aggregated state.

## 6.3. Results and Discussion:

**6.3.1. UV-Vis study:** Fig.6.1a shows the absorption spectrum of 60 $\mu$ M BZP in different nonaqueous good solvents at room temperature. There are two distinct absorption band of BZP in good solvent. The higher energy band at ~300-330 nm is due to  $n-\pi^*$  transition and the lower energy band at ~340-360 nm is due to  $\pi-\pi^*$  transition [15]. Both the shape and the peak positions are highly sensitive to the solvent polarity. With increasing dielectric constant of the medium from Cyclohexane (2.02) to DMF (38), a regular red shift of the  $\pi-\pi^*$  transition from 340 nm to 362 nm is observed (Fig.6.1a). Deconvolution of UV-Vis absorption spectra in cyclohexane medium using multiple Gaussian peaks shows two bands centered at 308 nm and 340 nm respectively (Fig.6.2). Gradual red shifts of UV-Vis absorption bands from 316 nm and 353 nm to 326 nm and 362 nm are observed as we increase the polarity of the

medium from THF to DMF. In addition to that, width of these bands also increases with raising the polarity of medium.

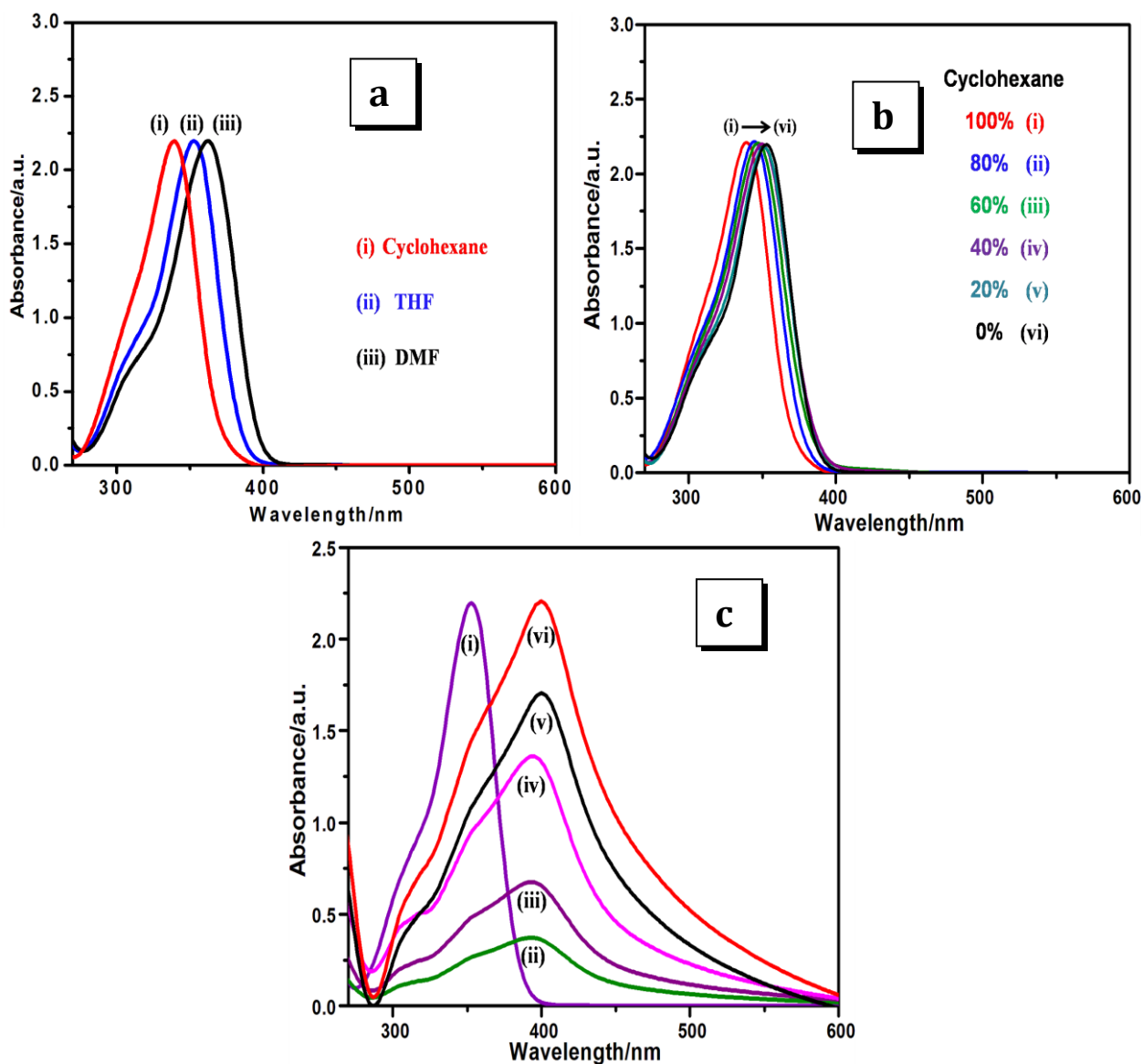


**Figure 6.1:** (a) Normalized UV-Vis absorption spectra of 60 μM BZP in good solvent of different solvent polarity. (b) Normalized UV-Vis absorption spectra of 60 μM BZP in Cyclohexane/THF mixture; (i) 100% cyclohexane, (ii) 80% cyclohexane, (iii) 40% cyclohexane, (iv) 20% cyclohexane, (v) 0% cyclohexane. (c) UV-Vis absorption spectra of (i) 60 μM BZP (mother), (ii) Sample A, (iii) Sample B, (iv) Sample C, (v) Sample D and (vi) Sample E.

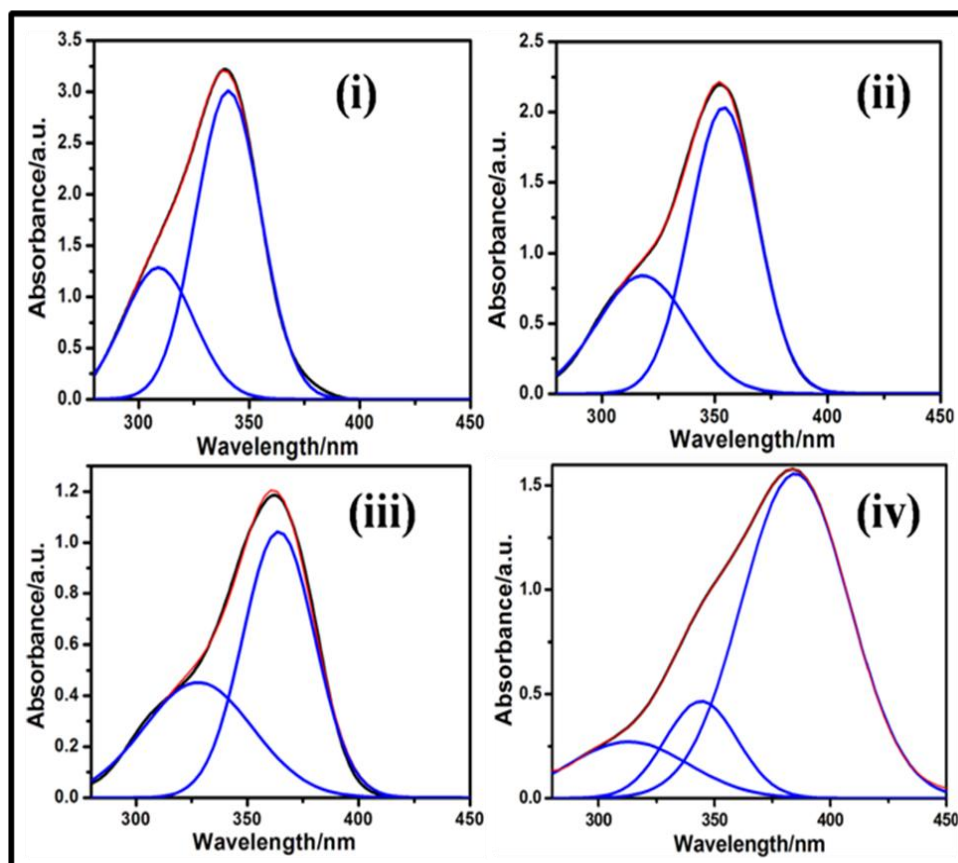


**Figure 6.2: Deconvolution with Gaussian functions of the UV-Vis absorption spectra: (i) BZP in CH, (ii) BZP in THF, (iii) BZP in DMF, (iv) BZP in water.**

The solvent polarity sensitivity of absorption spectra of 60 $\mu$ M BZP is further verified using different ratio of cyclohexane and THF as solvent (Fig.6.1b). The large bathochromic shift of the low energy band with increasing polarity of solvent suggest that the  $\pi$ - $\pi^*$  band has charge transfer character. The UV-Vis absorption study of aggregated hydrosol of BZP shows that apart from  $n$ - $\pi^*$  and  $\pi$ - $\pi^*$  band at 311 and 344 nm another red shifted absorption band is appeared, the intensity and broadening of this red shifted band increases with the increase of the aggregated structure (Fig.6.1c). It is observed that the broad red shifted band is centered at 398 nm (Fig.6.2) while deconvoluting the spectra using multi peak Gaussian functions. The band at 398 nm is assigned to the J-aggregates of BZP. In general, the J-aggregation band is distinctly red-shifted and appears as an intense narrow absorption band due to the motional narrowing [16,17], but that of BZP aggregates in Fig.6.1c is relatively broad. This result suggests that the molecules in aggregates may be oriented in a less optimal

way of J-aggregation. Lattice disorder is considered as one of the possible reasons of this inhomogeneous broadening of spectra [18].

**6.3.2. Emission study:** Fluorescence spectra of BZP in different nonaqueous solvents were recorded with an excitation at 300 nm (Fig.6.3a). A gradual bathochromic shift of emission band from 388 nm to 405 nm to 416 nm with decreasing intensity were observed as we increased the solvent polarity from cyclohexane ( $\epsilon=2.02$ ) to THF ( $\epsilon=7.5$ ) to DMF ( $\epsilon=38$ ). Polarity sensitive nature of emission spectra was further verified by using different volume ratio of cyclohexane / THF as solvent (Fig.6.3b). Shift of emission maxima and emission intensity as a function of different volume ratio of cyclohexane / THF are shown in Fig.6.3c. This broad and solvent polarity sensitive emission band originates from the polar twisted intramolecular charge transfer (TICT) state of BZP. Our DFT based computational study on both the ground and excited singlet state geometry of BZP show that the angle between two phenyl rings is  $\sim 45^\circ$  in  $S_0$  state and  $\sim 82^\circ$  in the  $S_1$  state and one of the diethyl amino group twisted about  $26^\circ$  in the  $S_1$  state compare to  $S_0$  state. Therefore, a highly polar TICT state is present in BZP which is further stabilized with increasing polarity of the medium. The decrease of emission intensity from TICT state with solvent polarity is due to the decreasing energy gap between  $^1(\text{TICT})$  and the low lying  $^3(\text{TICT})$  state. This decreasing energy gap open up the deactivation intersystem crossing (ISC) channel from  $^1(\text{TICT})$  to  $^3(\text{TICT})$  and thus decreases the emission intensity originating from  $^1(\text{TICT})$  state [19]. But the dramatic increase in photoluminescence (PL) intensity in its aggregated state compare to its molecular electronic state in good solvent under identical reaction condition inspires us to explore the aggregation induced emission enhancement (AIEE) effect.

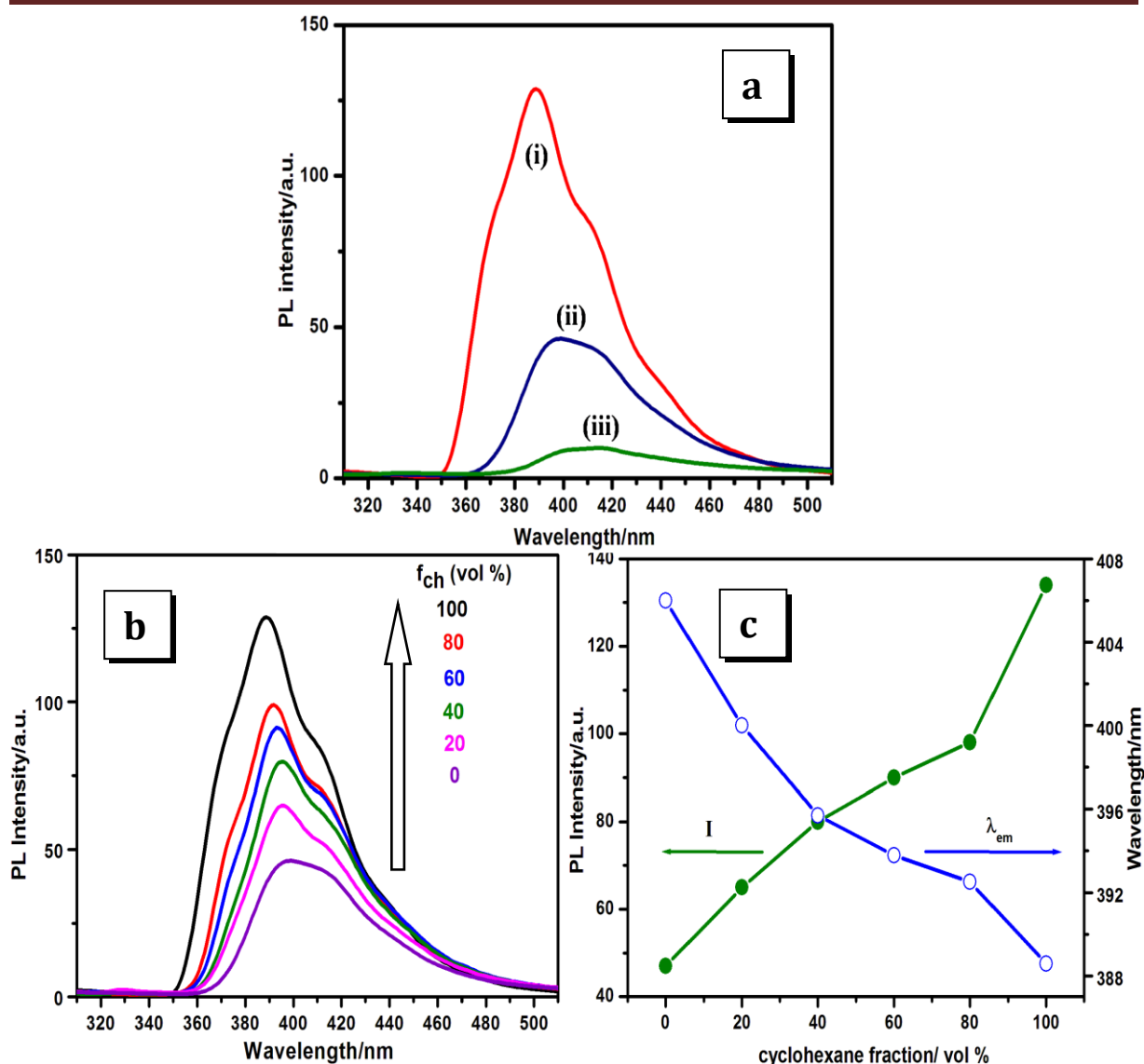


**Figure 6.3:** (a) Emission spectra of 60 $\mu$ M BZP in (i) Cyclohexane, (ii) THF and (iii) DMF.  $\lambda_{\text{ex}}$ : 300 nm. (b) Emission spectra of 60 $\mu$ M BZP in the CH/THF mixtures.  $\lambda_{\text{ex}}$ : 300 nm. (c) Plots of maximum emission intensity and wavelength ( $\lambda_{\text{em}}$ ) of BZP (conc. 60 $\mu$ M) versus cyclohexane fraction in the CH/THF mixtures.  $\lambda_{\text{ex}}$ : 300 nm.

In order to verify the stability of the luminogen, PL spectra of BZP hydrosol (Sample A) at different time interval after its preparation are shown in Fig.6.4a. PL intensity increases with time and reaches the maximum after 30min. Initially the mechanical shear stress leads to the increasing chances of most probable collisions; thus a portion of BZP molecules clustered together to form tiny particles. The remaining portion of BZP molecules presents in the solvent mixture then gradually deposited onto the initially formed particle in recrystallization

pattern to give highly emissive aggregated structure. So with increasing time, the system attains an ordered cluster which restricts the free rotation of diethyl aniline groups and as a result the enhanced emission of molecules appears. After 30 min a very small ~4% decrease is observed in the intensity of the spectra with increasing time. This may be due to the fluctuation of power of the excitation source after prolonged use.

PL spectra (Fig.6.4b) of BZP in THF/water mixtures (<80% water) are basically flat lines (320-380 nm) parallel to the abscissa and the emission intensity at around 430 nm gradually decreases (the inset of Fig.6.4b) as the water fraction ( $f_w$ ) increases. However, when a large amount of water (99%) is added to the solution in THF, the peak at around 430 nm disappears and a structured emission band with maxima at 339 nm is appeared. The PL intensity around 339 nm rises 580-fold as the water fraction is increased from 0% to 99%, (Fig.6.4c). Inset of Fig.6.4c shows the emission color of BZP in THF and aggregated BZP hydrosol under UV light illumination. No visual detection of emission color for BZP in THF indicates that the emission intensity is too weak to be observed in the naked eyes. The intense blue emission from aggregated BZP hydrosol suggests that AIEE occurs in our present case. Tang and Park groups first discovered the AIE/ AIEE phenomenon in 2001. Most of the reported AIE-active molecules are propeller-like shapes with weak  $\pi$ - $\pi$  stacking interactions.

The restriction of intramolecular rotation processes is proposed as the main mechanism for AIE. According to this mechanism, PL is enhanced in the solid state with a slight red shifted band than its emission from molecular state in good solvent. This cannot explain the present exceptional blue shift in the emission spectra of aggregated BZP. Another interesting feature of PL spectra of BZP hydrosol is that, the intensity of 339 nm band increases with the increasing concentration of BZP (*i.e.* increased size of aggregated structures), reaches a maxima and then decreases with further increase of BZP concentration.

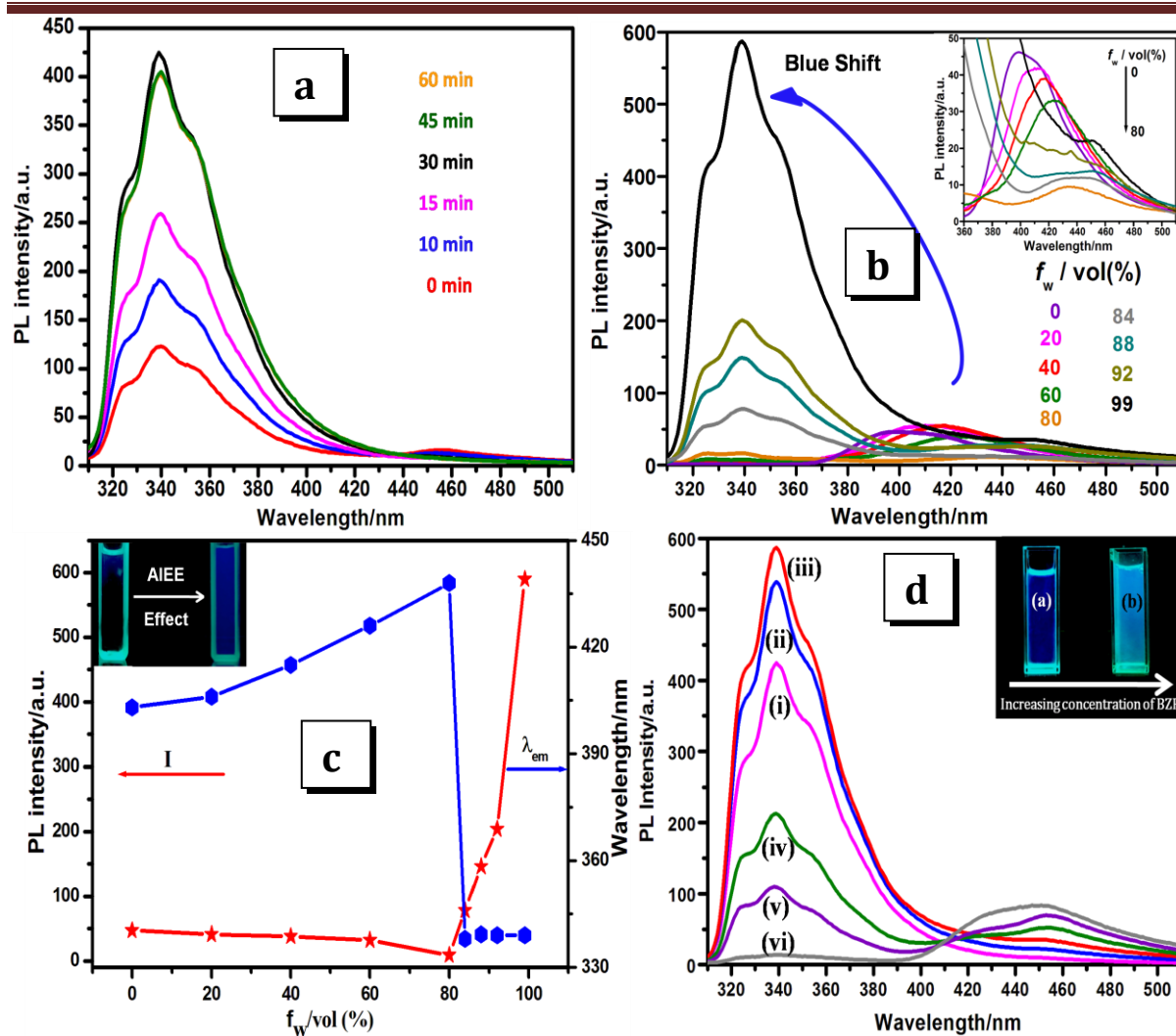


**Figure 6.4:** (a) Variation of PL intensity of BZP hydrosol immediate after its preparation with time in THF/water mixture (1:99 v/v); BZP concentration: 20 $\mu$ M and  $\lambda_{ex}$ : 300 nm. (b) PL spectra of BZP hydrosol prepared using different volume fraction of THF/water mixtures; BZP concentration: 60 $\mu$ M and  $\lambda_{ex}$ : 300 nm. (c) Plot of maximum emission intensity and wavelength ( $\lambda_{em}$ ) of BZP hydrosol prepared using different volume fraction of THF/water mixtures; BZP concentration: 60 $\mu$ M and  $\lambda_{ex}$ : 300 nm. Insets: PL images of BZP in THF (dark) and BZP hydrosol (blue) under UV light illumination. (d) PL spectra of (i) Sample A, (ii) Sample B, (iii) Sample C, (iv) Sample D (v) Sample E and (vi) Sample F;  $\lambda_{ex}$ : 300 nm. Inset: PL image of (a) Sample C and (b) Sample F under UV light illumination.

On the other hand, when we change the concentration of BZP keeping the water percentage same, another interesting feature of the emission spectrum *i.e.* a new broad and red shifted band with peak around 460 nm is appeared (Fig.6.4d). We also observed visual change of emission color when UV light is irradiated on THF/water solution containing 60 $\mu$ M and 200 $\mu$ M BZP in water (inset of Fig.6.4d). Two distinct colors *i.e.* deep blue and sky

blue emissions are observed from these hydrosols respectively. There two distinct emissions band *i.e.* one at 339 nm and the other one broad peak at 460 nm is due to two kind of conformer of BZP present within the aggregates. Ground state optimized geometry of BZP shows that the angle between the two phenyl rings is  $\sim 45^\circ$ . Though there is certain angle between the two phenyl rings of the BZP, they are not free to rotate even in the excited state due to restricted geometry in the aggregated structure. Since the Van der Waals force of attraction which is responsible for aggregation of BZP in water, diethyl aniline rings of BZP are almost twisted in low concentration, restricting its free rotation. Excitation of these BZP to its locally excited (LE) state results structured emission band with peak maxima at 339 nm. On the other hand at higher concentration of BZP, crystals get soften resulting lattice disordered. We presume that due to irregular packing of BZP in larger aggregates few molecules attain more planer geometry in their aggregates to allow the most feasible intramolecular charge transfer (ICT) process and the broad red shifted emission at 460 nm arises from the ICT state.

**6.3.3. Time resolved Fluorescence Study:** In order to understand the nature of emission spectra of aggregated BZP hydrosols and BZP in good solvent, we have carried out time resolved fluorescence study with excitation at 280 nm and emissions were measured at 405 nm for BZP in THF and at 339 and 460 nm for aggregated hydrosols. Decay profile of monomer and hydrosols with emission wavelength at 339 nm and 460 nm are shown in Fig.6.5a & 6.5b respectively. Fluorescence lifetimes of the samples are measured by deconvoluting the response function from the decay curves. Fluorescence lifetime of diluted BZP in THF is 0.49 ns with very weak emission intensity. It took nearly 30 times more to get comparable emission intensity as that of its aggregated hydrosols.



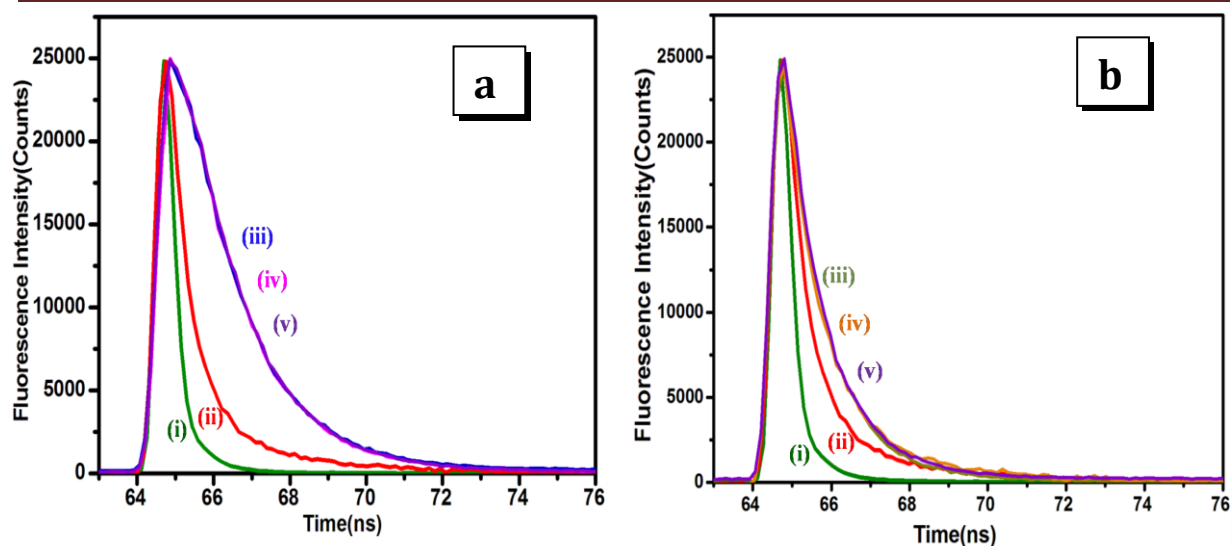


**Figure 6.5: (a) Time-resolved fluorescence spectra: (i) Lamp, (ii) 60 $\mu$ M BZP (mother), (iii) Sample A, (iv) Sample C and (v) Sample E; Excitation wavelength: 280 nm and Emission wavelength: 339 nm. (b) Time-resolved fluorescence spectra: (i) Lamp, (ii) 60 $\mu$ M BZP (mother), (iii) Sample C, (iv) Sample E and (v) Sample F. Excitation wavelength: 280 nm and Emission wavelength: 460 nm.**

Fluorescence decay profiles of aggregated BZP hydrosols having reasonably higher emission intensity are fitted with single exponential decay. The observed components of lifetime of aggregated BZP hydrosol at 339 nm peak position are within  $\sim 1.4$ - $1.5$  ns and the components corresponding to the peak position at 460 nm have fluorescence lifetime  $\sim 0.9$  ns. Fluorescence lifetime data as listed in table 6.1 illustrates that the fluorescence monitored at 339 nm has average lifetime  $\sim 1.5$  ns and the broad emission band at 460 nm has average lifetime  $\sim 0.9$  ns. Since all samples showing emission at 339 nm and 460 nm have similar average fluorescence lifetime, we may conclude that the emission from hydrosol comes from two different excited states. The  $\sim 1.5$  ns component of 339 nm band is due to locally excited BZP and the  $\sim 0.9$  ns component of 460 nm band is from ICT state of the relatively planer BZP present within the aggregated BZP.

**Table 6.1: Fluorescence life time of 4,4'-bis(diethylamino)benzophenone monomer in THF and aggregated hydrosols of BZP in water**

Materials	Emission Peak (nm)	$\tau$ (ns)	$\chi^2$
Mother	405 nm	0.49	0.9
Sample A	339 nm	1.46	0.99
Sample C	339 nm	1.48	1.1
	460 nm	0.92	0.97
Sample E	339 nm	1.41	0.96
	460 nm	0.9	0.93
Sample F	460 nm	0.94	0.95

**6.3.4. Mechanistic Discussion:** A systematic DFT investigation of the optimized geometry of the ground ( $S_0$ ) and lowest singlet excited ( $S_1$ ) states were performed to understand this new AIEE phenomenon. Ground state geometry shows that the dihedral angle between two phenyl rings is  $45.53^\circ$ . But in the excited singlet ( $S_1$ ) state, this angle changes to  $80.09^\circ$  (Fig.6.6a). These significant differences in the geometry changes from  $S_0$  to  $S_1$  may have a close relationship with the AIEE properties of the molecule. HOMO-LUMO electron distribution (Fig.6.6b) in the ground state of the molecule suggests that the TICT state is responsible for weak emission of this molecule in good solvent. But in aggregated state, rotation around intramolecular axis is completely restricted and the molecule attains relatively planar aggregated geometry where energy loss due to TICT is hindered. Thus in aggregated structures excitation of BZP occurs to its high energy locally excited (LE) state which shows intense blue shifted emission with structured vibronic band. This is known as aggregation induced locally excited (AILE) emission [20].

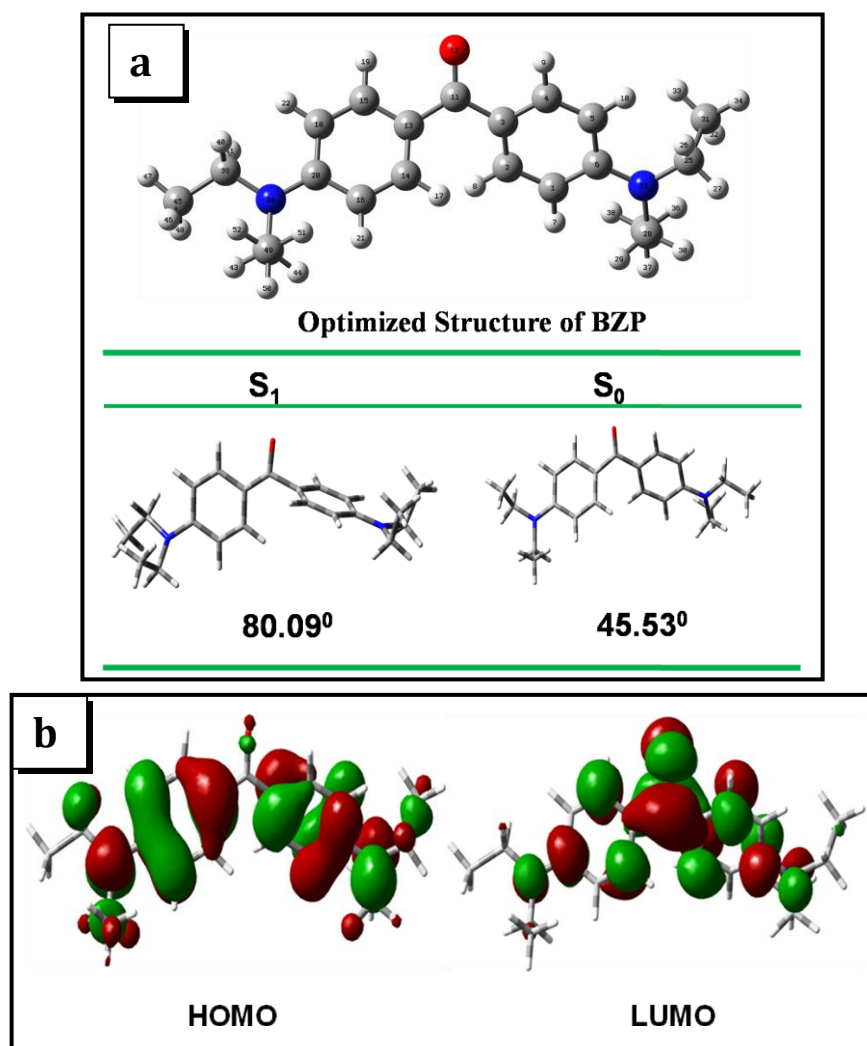


**Figure 6.6: (a) The optimized geometry and torsion angle between donor diethyl anilino and acceptor keto group of BZP at its ground state ( $S_0$ ) and lowest excited state ( $S_1$ ) using DFT B3LYP 6-31G (d) and TD DFT B3LYP 6-31G(d) level of theory respectively (b) Special distribution of electrons in HOMO and LUMO based on optimized geometry of BZP.**

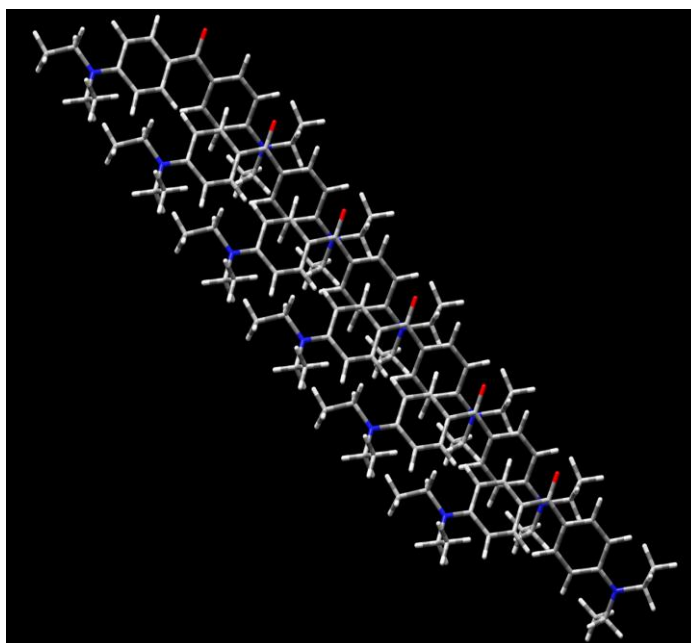
In case of larger aggregated structure, crystal softening occurs and this results to attain a more planer geometry of BZP than the molecule present at the tightly packed aggregates. These planer BZP molecules upon photo excitation undergo charge transfer between the donor diethyl aniline group and acceptor keto group.

**Table 6.2: Electrophilic  $f^+(r)$  and nucleophilic  $f^-(r)$  condensed Fukui functions and the second order Fukui parameter  $f^2(r)$  of BZP molecule calculated using DFT B3LYP 6-31G (d) level of theory**

<i>Atom</i>	<i>No.</i>	$f_k^+$	$f_k^-$	$f_k^2$	<i>Atom</i>	<i>No.</i>	$f_k^+$	$f_k^-$	$f_k^2$
C	1	-0.012	-0.052	0.04	H	27	-0.019	-0.022	0.003
C	2	-0.037	0.004	-0.041	C	28	0.007	0.016	-0.009
C	3	0.026	-0.07	0.096	H	29	-0.007	-0.015	0.008
C	4	-0.05	-0.002	-0.048	H	30	-0.019	-0.023	0.004
C	5	-0.01	-0.051	0.041	C	31	0.003	0.001	0.002
C	6	-0.079	-0.003	-0.076	H	32	-0.011	-0.012	0.001
H	7	-0.025	-0.018	-0.007	H	33	0.004	-0.002	0.006
H	8	-0.015	-0.012	-0.003	H	34	-0.019	-0.025	0.006
H	9	-0.018	-0.02	0.002	C	35	0.003	0.001	0.002
H	10	-0.026	-0.02	-0.006	H	36	-0.011	-0.014	0.003
C	11	-0.169	0.021	-0.19	H	37	-0.019	-0.023	0.004
O	12	-0.123	-0.039	-0.084	H	38	0.005	-0.002	0.007
C	13	0.026	-0.069	0.095	C	39	0.008	0.018	-0.01
C	14	-0.034	0.004	-0.038	H	40	-0.016	-0.029	0.013
C	15	-0.053	-0.003	-0.05	H	41	-0.008	-0.018	0.01
C	16	-0.013	-0.052	0.039	C	42	0.007	0.014	-0.007
H	17	-0.016	-0.011	-0.005	H	43	-0.019	-0.022	0.003
C	18	-0.008	-0.05	0.042	H	44	-0.005	-0.014	0.009
H	19	-0.018	-0.02	0.002	C	45	0.006	0.008	-0.002
C	20	-0.078	-0.003	-0.075	H	46	-0.008	-0.007	-0.001
H	21	-0.025	-0.018	-0.007	H	47	-0.015	-0.019	0.004
H	22	-0.026	-0.019	-0.007	H	48	-0.008	-0.01	0.002
N	23	-0.027	-0.125	0.098	C	49	0.003	0	0.003
N	24	-0.027	-0.128	0.101	H	50	-0.019	-0.023	0.004
C	25	0.008	0.015	-0.007	H	51	0.005	-0.002	0.007
H	26	-0.008	-0.018	0.01	H	52	-0.011	-0.013	0.002

The presence of two identical donor groups (diethyl aniline), further resonance stabilizes the intramolecular charge transfer (ICT) state. Vertical transition from the ICT state occurs to the repulsive part of the ground state potential energy surface resulting broad and structures less emission. Since crystal packing is strong in smaller aggregates, the emission from the LE state of BZP molecules *i.e.* at 339 nm is the only emissive state. This is further supported by our experimental observation, where we observed that the emission band

centered at 339 nm is decreased in intensity with the increased size of aggregated BZP (BZP concentration  $> 60\mu\text{M}$ ) structures. This increased size results crystal softening of the aggregates *i.e.* the loosening of aggregated BZP molecules and facilitate the internal charge transfer in planer geometry. It is observed that the emission intensity of LE band (339 nm) decreases and intensity of the broad red shifted band (460 nm) from ICT state increases (Fig.6.4d) with the increasing size of aggregates.



**Scheme 6.2: Packing pattern of BZP aggregates through intermolecular non-covalent interaction.**

Since we did not able to grow single crystal of BZP for X-ray study or no such data of this molecule is available in the literature, we have tried to understand the possible sites of interaction by computing second order Fukui parameter as local reactivity descriptors between the neighboring molecules in the crystalline form. Second order Fukui Parameter ( $f^2(r)$ ) as local reactivity descriptor for each atomic centre of BZP is listed in table 6.2. Since negative value of  $f^2(r)$  is a preferable sites for electrophilic attack and positive  $f^2(r)$  values are the possible sites for nucleophilic attack, table 6.2 illustrates that  $\text{C}_{11}$ ,  $\text{C}_{20}$ ,  $\text{C}_{14}$ ,  $\text{C}_{39}$ ,  $\text{H}_{17}$  are the most electrophilic center and  $\text{N}_{24}$ ,  $\text{C}_3$ ,  $\text{C}_5$ ,  $\text{C}_{13}$ ,  $\text{C}_{49}$  are most nucleophilic center. Thus

$N_{24}$  centre of one BZP molecule will be close enough to the  $C_{11}$  centre of another molecule through Van der Waals force of attraction. The possible arrangement of BZP in its aggregates state is shown in Scheme 6.2 and it helps to predict that BZP aggregates will prefer head to head slipped geometry in its aggregated structures.

**6.3.5. SEM & Optical Microscopic study:** SEM micrograph of Sample F is shown in Fig.6.7. From this micrograph it is observed that particles have mostly rectangular and higher polygon like morphologies with equal thickness. It seems a two dimensional growth of particles take place with the increasing concentration of BZP in solution.

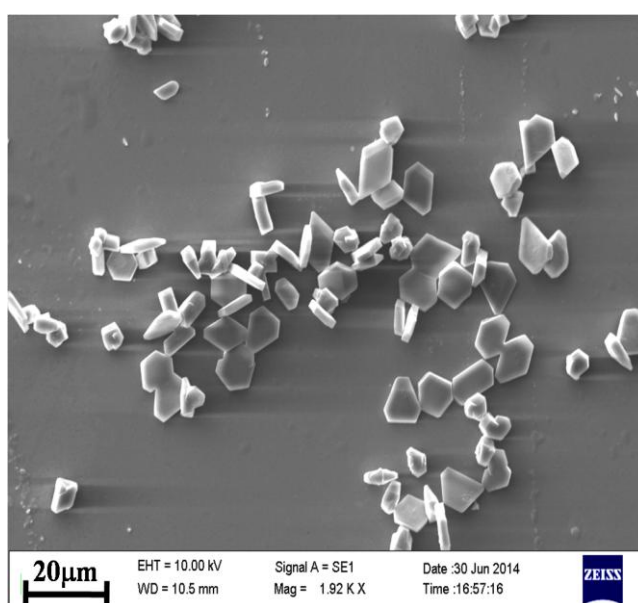


**Figure 6.7: SEM images of BZP microstructures of Sample F.**

Fig.6.8a shows the optical microscopic images of Sample F. The sizes of other samples are too small to be detected within the resolution of our optical microscope. The morphology of the microcrystals of Sample F though irregular but a clear two dimensional growth of crystals are noticeable. Fluorescence microscopic images of the crystals under UV excitation show distinct sky blue emission from the edges of crystals (Fig.6.8b). Initially we thought this emission may be due to crystal induced phosphorescence from BZP.

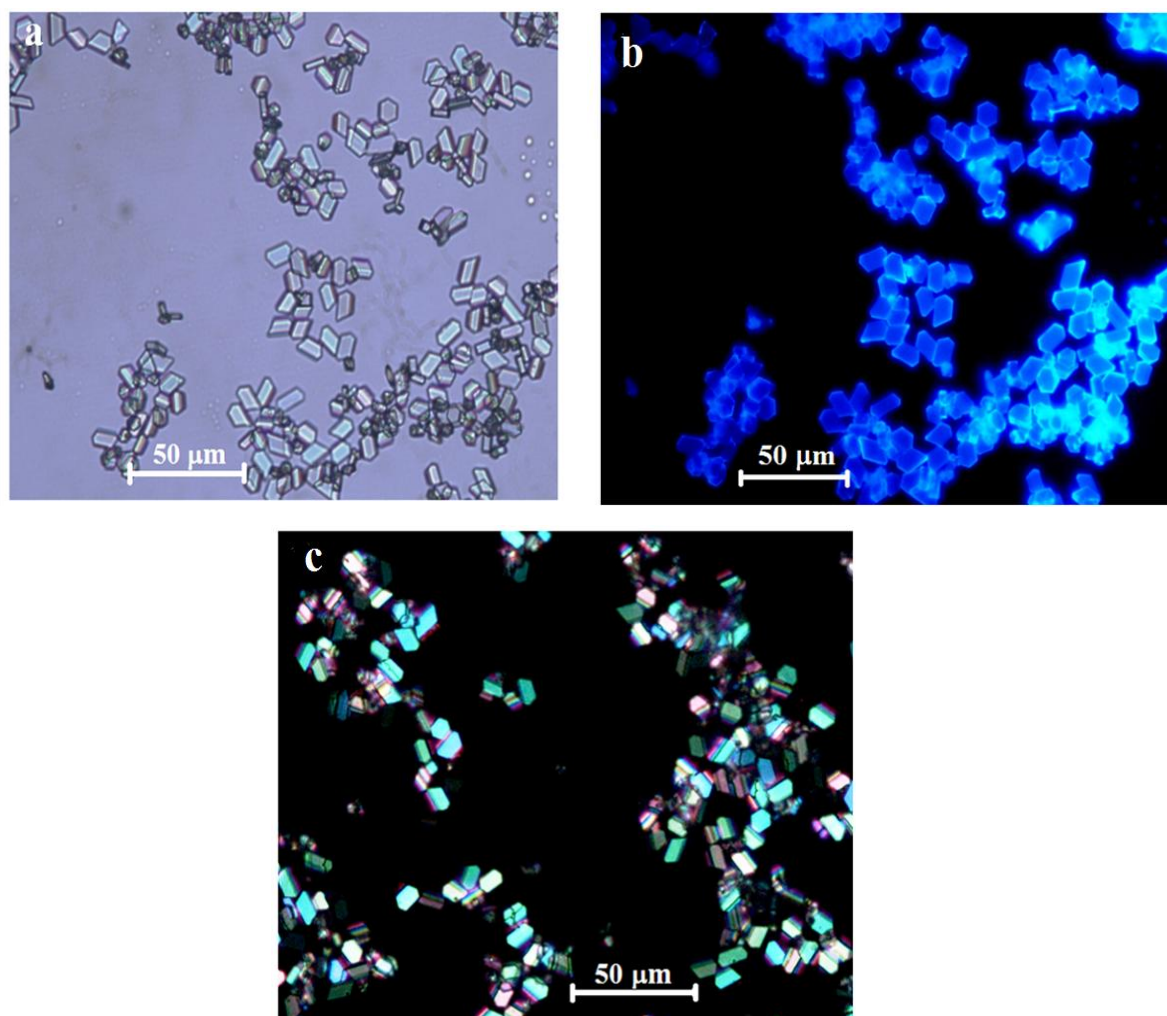


**Figure 6.8: (a) Optical microscopic images of BZP micro crystals of Sample F. (b) Optical fluorescence microscopic images of BZP micro crystals of Sample F; exciting under UV light, c) Optical polarized microscopic images of BZP micro crystals of Sample F.**

But the time resolved fluorescence emission study of Sample F monitored at 460 nm is found to be  $\sim 0.94$  ns and we presume that this faster fluorescence lifetime component is coming from other than triplet state of BZP. Now the deep blue emission from the crystal surface and distinct sky blue emission from the edges of crystals, it is clear that two types of emissive states are present within BZP aggregates.

Our UV-Vis study reveals that lattice disorder may be responsible for the inhomogeneous broadening of the 398 nm bands and the BZP molecules are present in less optimal way *i.e.* more planar form in the disordered sites. Since BZP is a donor-acceptor (D-A) type of molecule, the intramolecular charge transfer (ICT) state will get stabilized in this

planar geometry. During the two dimensional growth of aggregates, disordered sites are formed on the growing part *i.e.* edges of larger aggregates. Thus the sky blue emission from the growing edges of crystals is coming from the ICT state of BZP. On the other hand the strong blue emission from the crystal surface arises from locally excited (LE) state of BZP present in twisted form within the crystals. Dark field's view of this Sample F using polarizer and analyzer assembly shows different colors depending on the direction of incident radiation and it reveals the anisotropic nature of the synthesized microcrystal (Fig.6.8c).

#### 6.4. Glucose Sensor:

AIEE luminogens are useful analytical tools and have been judiciously utilized as sensitive and selective chemosensors and bioprobes. Sugars play important roles in biological processes such as metabolism. There is great demand for the development of convenient methods for selective recognition of sugars in aqueous media due to their obvious clinical and therapeutic values. For example, monitoring glucose levels in biological fluids such as urine and blood is essential for the management of diabetes. So here we introduce the most interesting turn off glucose sensing property of this aggregated luminogen. BZP molecules are aggregated in solid state through Van der Waals force of attraction with the neighboring molecules. Glucose is a hexose sugar possessing six hydroxyl groups in its open chain structure. With the help of this -OH groups, it will offer strong hydrogen bonding interaction with the electronegative N and O centers of BZP within the aggregates. This will cause loosening of crystal packing of BZP in the aggregated luminogen.

This loosening of crystal packing as well as hydrogen bonding interaction of glucose with the surface BZP molecules causes quenching of LE state emission of BZP within the luminogen. The decrease of LE state (339 nm) emission intensity with increasing glucose concentration is shown in Fig.6.9a. Small increase of emission intensity of 460 nm band with increasing glucose concentration is due to crystal softening as glucose is added to the



hydrosol of BZP aggregates. We also introduce a calibration curve where the change of the ratio of emission intensity with respect to the concentration of glucose is shown (Fig.6.9b). Our study shows that the minimum glucose concentration that can be detected using the above method is about 1.1 mM.

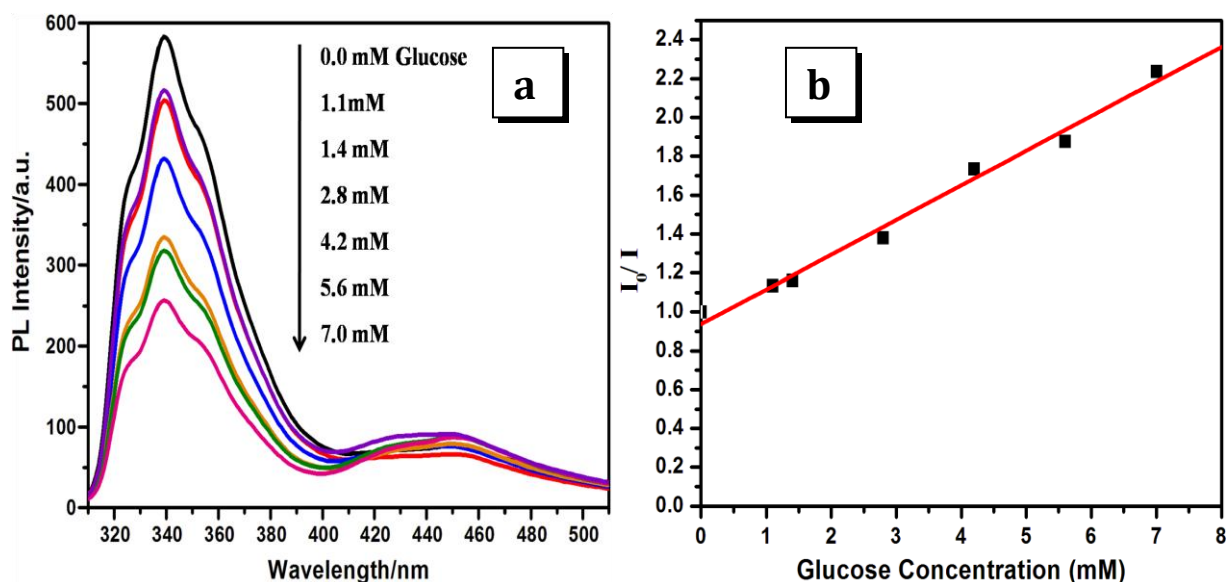


**Figure 6.9: (a) Fluorescence emission spectra of BZP hydrosol of Sample C upon addition of different concentration of D-Glucose, (b) Calibration curve: Plot of  $I_0 / I$  at 339 nm vs. concentration of D-Glucose.**

## 6.5. Conclusion:

In this chapter, we have introduced conjugated D-A moiety which exhibits broad and structure less fluorescence spectra in different kinds of solvents but in aggregated state blue shifted structured emission band is observed and it has been termed as aggregation induced locally excited emission enhancement (AILEE). Apart from AILEE, another broad red shifted band appears in the hydrosol with the increasing concentration of BZP. Simultaneous appearances of these two kinds of emission band in the aggregated hydrosols are rare in literature. Our extensive photo physical study of the hydrosol revealed that two types of emissive state are present in the aggregated structures of BZP. But with increasing concentration, lattice disordered is introduced to the microcrystals and the crystal softening

allow this molecule to attain a planer geometry in which ICT is more feasible. The broad red shifted band at 460 nm is appeared from the ICT state of the relatively larger aggregates. On the other hand intense blue emission from the aggregated hydrosols is coming from the locally excited (LE) states of the relatively twisted conformer of BZP present within the microcrystals. Our study also revealed that the AILEE band can be used for sensing glucose at a low concentration in aqueous solution. The strong quenching of AILEE emission in presence glucose is due to softening of aggregated structures of the luminogen.

**References:**

1. L. H. Xie, C. R. Yin, W. Y. Lai and Q. L. Fan, *Prog. Polym. Sci.* 37, **2012**, 1192.
2. L. J. Huo, J. H. Hou, S. Q. Zhang, H. Y. Chen and Y. Yang, *Angew.Chem.* 122, **2010**, 1542.
3. Y. J. Cheng, S. H. Yang and C. S. Hsu, *Chem. Rev.* 109, **2009**, 5868.
4. D. Majhi, S. K. Das, P. K. Sahu, S. Md. Pratik, A. Kumar and M. Sarkar, *Phys. Chem. Chem. Phys.*, 16, **2014**, 18349.
5. J. E. Kwon, S. Lee, Y. You, K.H. Baek, K. Ohkubo, J. Cho, S. Fukuzumi, I. Shin, S. Y. Park and W. Nam, *Inorg. Chem.*, 51, **2012**, 8760.
6. Y. Peng, Y.M. Dong, M. Dong and Y.W. Wang, *J. Org. Chem.*, 77, **2012**, 9072.
7. E. Ranyuk, C. M. Douaihy, A. Bessmertnykh, F. Denat, A. Averin, I. Beletskaya and R. Guilard, *Org. Lett.*, 11, **2009**, 987.
8. L. Qian, B. Tong, J. Shen, J. Shi, J. Zhi, Y. Dong, F. Yang, Y.Dong, J. W. Y. Lam, Y. Liu and B.Z. Tang, *J. Phys.Chem. B*, 113, **2009**, 9098.
9. G. Vamvounis, P. E. Shaw and P. L. Burn, *J. Mater. Chem. C*, 1, **2013**, 1322.
10. A. Heller and B. Feldman, *Chem. Rev.*, 108, **2008**, 2482.
11. N. Dicesare and J.R. Lakowicz, *Chem. Comm.* **2001**, 2022.
12. R. Badugu, J.R. Lakowicz and C.D. Geddes, *Sensors and Actuators B*, 104,**2005**, 103.
13. N. Dicesare and J.R. Lakowicz, *J. Phy. Chem. A*, 105, **2001**, 6834.
14. D.B. Cordes, S. Gamsey, Z. Sharrett, A. Miller, P. Thoniyot, R.A. Wessling and B. Singaram, *Langmuir*, 21, **2005**, 6540.
15. J. A. Mondal, H. N. Ghosh, T. K. Ghanty, T. Mukherjee and D. K. Palit, *J. Phys. Chem. A*, 110, **2006**, 3432.
16. L. M. Ilharco, R. B. de Barros, *Langmuir*, 16, **2000**, 9331.
17. A. Eisfeld, J. S. Briggs, *Chem. Phys.* 281, **2002**, 61.
18. E. W. Knapp, *Chem. Phys.* 85, **1984**, 73.
19. K. Bhattacharyya and M. Chowdhury, *Chem. Rev.* 93, **1993**, 507.
20. Z.F. An, C. Zheng, R.F. Chen, J. Yin, J.J. Xiao, H.F. Shi, Y. Tao, Y. Qian and W. Huang, *Chem. Eur. J.*, 18, **2012**, 15655.



# CHAPTER 7

## Proton Triggered Emission and Selective Sensing of Picric Acid by the Fluorescent Aggregates of 6,7-dimethyl-2,3-bis-(2-pyridyl)-quinoxaline\*

\*A part of this chapter has been published in the article, “Prativa Mazumdar<sup>†</sup>, Samir Maity<sup>†</sup>, Milan Shyamal<sup>†</sup>, Debasish Das<sup>†</sup>, Gobinda Prasad Sahoo<sup>†</sup> and Ajay Misra<sup>†</sup>, *Phys. Chem. Chem. Phys.*, 2016, 18, 7055- 7067.”

## 7.1. Introduction:

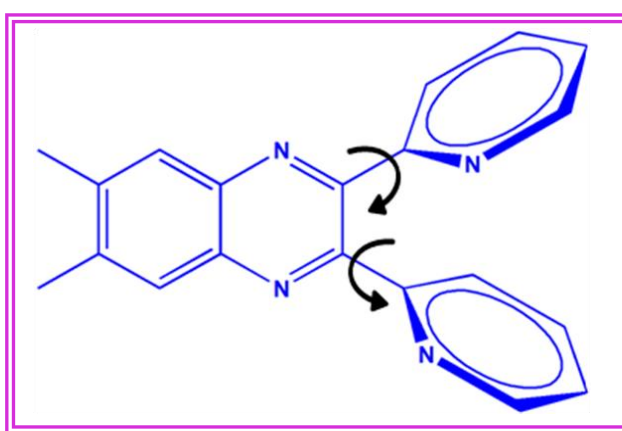
The unique characteristic of aggregation induced emission enhancement (AIEE) based luminogens differentiate it from the conventional luminophores and focused on the exploration of their utilities in the development of optical sensors and other important applications. Functional chromophore containing embedded recognition elements showing shifts in both absorption and emission upon acid/base stimuli are of immense interest for their innately potential applications in sensors [1-6]. Great effort has been devoted to the molecular design, modification [7-10] and origin of the spectral shift upon protonation of functional chromophores but in most investigations the spectral shift in presence of acid stimuli shows hypsochromic shift due to protonation. Since lone pairs of heteroatom lose conjugation, this hypsochromism in spectra is an obvious incident [11]. But proton triggered bathochromic shift is very rare.

Materials using non-covalent interactions *e.g.* hydrogen bonding and  $\pi$ -stacking, is being continuously explored in the field of sensing chemistry [12-14]. Depending on the nature of the interaction and the constituents involved, this selectivity can then be used in a wide variety of chemo-sensing processes [15]. Due to high selectivity and sensitivity, fluorescent chemo-sensors have found potential applications in the detection of environmentally important analytes such as nitroaromatic (NA) explosives [15]. Most commonly this fluorescence sensing is occurred by photoinduced electron transfer (PET) mechanism that depends on the excited state energy gap between the fluorophore and the

quencher, and binding efficiency of the fluorophore and the quencher molecules also [16]. Nitroaromatic compounds are electron deficient and they prefer to form aromatic  $\pi$ -interactions complexes with the electron-rich aromatic host [17]. The presence of nitro groups can further enhance the complexation through hydrogen bonds with suitable donor groups on the host molecules. Among the different nitroaromatic compounds, picric acid (PA) is one of the powerful explosive. PA is also a non-biodegradable environmental pollutant, which causes several problems to human health, such as skin irritation, skin allergy, cancer and respiratory system and liver damage [18]. Large quantities of PA are used in the pharmaceutical, dye and firework industries as a chemical reagent and released into the environment [19]. Thus the development of a fast and selective method for the detection of PA is highly desirable. In the past few years, different types of effective fluorescent sensors emerged for PA. Although the first selective sensor for PA was reported in 2004, this field needs to be explored further for suitable sensors [20]. In 2012, intermolecular charge transfer (ICT) based probes were reported by Kumar *et al.* [21]. However, many of the previously reported sensors had several drawbacks which include low binding affinity to PA and interference from other nitro compounds. Most of PA sensor systems were studied in molecular state. Further the lack of stability of organic fluorophore in water limit the detection of water soluble nitro-aromatic. But the fluorescent hydrosol has this advantage over other organic sensors.

Here we report a low dimensional material from 6,7-dimethyl-2,3-bis-(2-pyridyl)-quinoxaline (BPQ) where two free twisting pyridyl rings, attached to the 2 and 3 position of 6,7-dimethyl quinoxaline moiety are seized in solid phase by restriction of intramolecular free rotation (Scheme 7.1). It exhibits strong AIEE effect and is manifested by changing the colorless solution to blue color in aggregate state under UV irradiation. Another interesting part of BPQ hydrosol is its proton triggered tunable aggregation induced emission

enhancement (AIEE) and intramolecular charge transfer (ICT) property. In presence of proton, an unusual bathochromic shift is observed in both absorption and emission spectra and the color of hydrosol changes from blue to green. The pH triggered bathochromic shift in emission has been explained due to the introduction of charge transfer character in BPQ upon protonation to its pyridyl group. This aggregated BPQ hydrosol is utilized in sensing picric acid which is a powerful explosive among the different nitroaromatic compounds. It can selectively sense PA by forming ground state complexation with PA in its aggregated state.



Scheme 7.1: Chemical Structure of BPQ.

## 7.2. Experimental:

**7.2.1. Materials:** 6,7-dimethyl-2,3-bis-(2-pyridyl)-quinoxaline (BPQ) was purchased from Sigma-Aldrich Chemical Corp. Tetrahydrofuran (THF), Hydrochloric acid (HCl), Sodium hydroxide (NaOH), picric acid (PA), dinitro benzene (DNB), 4-nitrophenol (NP), 2,4-dinitrophenol (DNP), 3,5-dinitrobenzoic acid (3,5-DNBA), 3-nitrobenzoic acid (3-NBA), 4-nitroaniline (NA) and 2,4-dinitro toluene (DNT) were purchased from E-Merck India Ltd. The purity of these chemicals was checked spectrophotometrically. Triply distilled deionised water was used throughout the experiment.

**7.2.2. Preparation of aggregates:** 0.02(M) solution of BPQ was prepared using THF as good solvent. Different amount of the above solution (10 $\mu$ L for Sample A, 20 $\mu$ L for Sample B, 30 $\mu$ L for Sample C, 100 $\mu$ L for Sample D) were injected drop wise into 1:9 (v/v) ratio of THF/water and allowed to stir for 2 min. The final concentrations of BPQ were 40 $\mu$ M, 80 $\mu$ M, 120 $\mu$ M, 400 $\mu$ M for Sample A,B,C,D respectively. Clearness of the solutions was gradually decreased and a milky white color was appeared. Then the solutions were allowed to stand for 20 min.

For pH variation study, pH of the medium was adjusted by adding different amount of 0.1(M) HCl and 0.1(M) NaOH and the subsequent measurement of pH by using a pH meter. All solutions were prepared on the same day to study their absorbance, steady-state and time-resolved fluorescence measurements.

**7.2.3. Characterization:** The UV-Vis spectroscopy was used to characterize the optical properties and was measured in a 1cm quartz cuvette with a Shimadzu UV-1800 spectrophotometer. The spectra were recorded at room temperature in the range between 230 nm to 450 nm. Steady state fluorescence spectra were recorded using Hitachi F-7000 Fluorescence Spectrophotometer. Time-resolved fluorescence measurements were carried out under ambient conditions using a time-correlated single-photon counting (TCSPC) spectrometer [a picosecond diode laser (IBH, UK)] all samples were excited using 376 nm picosecond diode laser and the emission were collected at 398 nm and 468 nm depending upon the nature of emission of the sample. Lamp profiles were measured with a band-pass of 3 nm using Ludox as the scatterer. All pH measurements were made with an ORION VERSASTAR. The morphologies of the synthesized nano/micro structures were studied using ZEISS EVO 18 scanning electron microscope (SEM) operated at an accelerating voltage of 5 kV. Before SEM study samples were vacuum dries on a glass plate and a thin



layer of Au was deposited onto the samples to minimize sample charging. Optical microscopy images were taken using an NIKON ECLIPSE LV100POL upright microscope equipped with a 12V-50W mercury lamp. The samples for optical microscopic study were prepared by placing a drop of colloidal solution onto a clean glass slide. Single crystal X-ray diffraction data was collected on a Bruker Nonius APEX-II CCD diffractometer using graphite monochromated MoK $\alpha$  radiation ( $\lambda = 0.71073 \text{ \AA}$ ). All the experiments were carried out at room temperature.

**7.2.4. Computational Method:** Ground state geometry, HOMO, LUMO energy gap and electronic charge distribution of BPQ were computed using DFT based hybrid functional (B3LYP) and 6-31G(d,p) basis set. Excited state optimization of the protonated and neutral structures of BPQ were carried out by TDDFT with 6-31G(d,p) basis set. All the computations on BPQ were carried out using Gaussian-09 software package program.

## 7.3. Results and Discussion:

**7.3.1. UV-Vis Absorption Properties:** Fig.7.1a outlines the absorption spectra of 80 $\mu$ M BPQ in THF. There are two distinct absorption bands in the UV-Vis spectra of BPQ. The band in the region 230 nm-280 nm is structured one and 310 nm-380 nm band is broad and structureless. The high energy structure band is the  $S_0 \rightarrow S_1$  transition of the quinoxaline group and the broad structureless band which is solvent polarity sensitive arises due to charge transfer from pyridyl groups attached at 2 and 3 positions to quinoxaline. A clear bathochromic shift of the broad band is observed (Fig.7.1a) as the polarity of the medium is increased from cyclohexane ( $\epsilon=2.02$ ) to THF ( $\epsilon= 7.5$ ) to DMSO ( $\epsilon=48$ ). But the structure band is insensitive towards solvent polarity except the relative change of intensities of the vibronic bands. UV-Vis absorption spectra of the stock solution (80 $\mu$ M BPQ in THF) and the aggregated hydrosol (different concentration of BPQ in THF was added to a fixed volume

fraction of water) are shown in Fig.7.1b. Though spectral position of hydrosol remain in the same position as that of the stock solution, the intensity of absorption band increases with the increasing concentration of BPQ in the hydrosol. Charge transfer state of BPQ in the aggregates behaves like Frankel exciton and is more stable than the charge transfer state of free molecule. This is reflected in the increased absorption of CT band of hydrosol than the free BPQ in good solvent having same BPQ concentration (Sample B) (Fig.7.1b). Increasing absorbance of hydrosol with increasing BPQ concentration is due to increased number of excitonic state within the aggregates. UV-Vis absorption spectra of hydrosol for a fixed BPQ concentration and increasing volume percentage of water are shown in Fig.7.1c. It is observed that the absorption intensity of hydrosol increases with slight red shift of the CT band, with the increasing volume percentage of water in the solvent mixture.

The increasing number of particles resulting from increased water volume percentage is responsible for higher absorption of excitonic state and the bathochromic shift of spectra is due to enhanced dielectric constant of the medium. A closer look of CT band (Fig.7.1a) illustrates its asymmetric nature *i.e.* the band is the superposition of two Gaussian peaks with maxima at 339 nm and 352 nm. The dipoles of two pyridyl rings are present in oblique orientation. Now the interaction energy between two identical chromophores with one in an excited electronic state may be given by this general form.

$$E_{\text{interaction}} = \Delta E \pm E_{\text{resonance}} \quad \dots\dots\dots (i)$$

Where  $\Delta E$  contains electrostatic polarization and dispersion contribution and  $E_{\text{resonance}}$  is the resonance interactions between two pyridyl groups (Scheme 7.2). This effectively split the excited state charge transfer surface into two states. The  $E_{\text{resonance}}$  can be calculated from the spectral splitting lines  $\bar{\nu}$  and  $\bar{\nu}'$  and it is found to be  $2840\text{cm}^{-1}$ .

Temperature variation absorption study of aggregated BPQ (Sample B) is shown in Fig.7.1d. Fig.7.1d illustrates a small blue shift from 352 nm to 349 nm and coalescence of the

asymmetric CT band as the temperature is increased from 20<sup>0</sup>C to 70<sup>0</sup>C. The increasing temperature causes crystal softening which results less favor charge transfer orientation of quinoxaline and pyridyl groups. On the other hand, two pyridyl groups take less favored orientations for mutual interaction which leads to coalescence of the splitted band with increasing temperature.

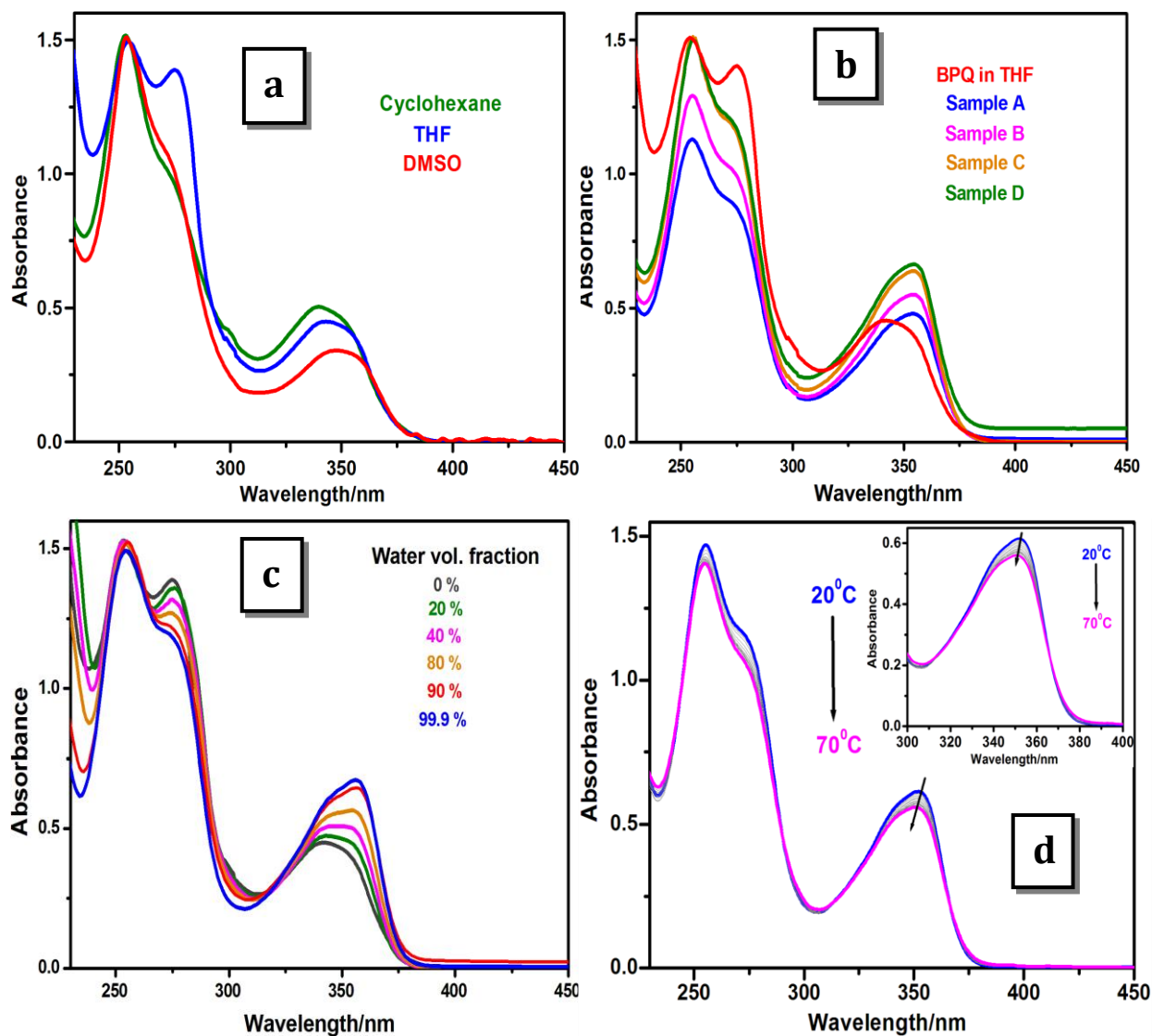
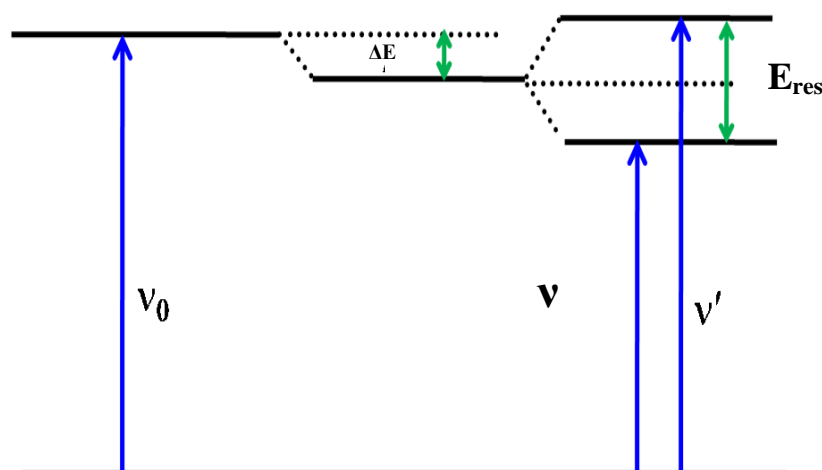


**Figure 7.1:** (a) UV-Vis absorption spectra of 80 $\mu$ M BPQ in (i) Cyclohexane, (ii) THF and (iii) DMSO. (b) UV-Vis absorption spectra of (i) 80 $\mu$ M BPQ in THF, (ii) Sample A (40 $\mu$ M BPQ), (iii) Sample B (80 $\mu$ M BPQ), (iv) Sample C (120 $\mu$ M BPQ) and (v) Sample D (400 $\mu$ M BPQ). (c) UV-Vis absorption spectra of 80 $\mu$ M BPQ in (i) 0% water (BPQ in THF), (ii) 20% water, (iii) 40% water, (iv) 80% water, (v) 90% water and (vi) 99.9% water. (d) Variable temperature absorption spectra of aggregated BPQ in THF/water mixture (10:90 v/v). BPQ concentration: 80 $\mu$ M.

Scheme 7.2: Energy level diagram



**7.3.2. Photoluminescence study:** The primary way to test whether a compound is AIEE active or not is to make a comparison of the emission spectra between its aggregated and molecular state. Since THF is a good solvent for BPQ and water is a poor one, aggregation of BPQ takes place with the increasing volume fraction of water in the solution. It is observed that the fluorescence of BPQ is gradually intensified when water is progressively added into its THF solution (Fig.7.2a). As the volume fraction of water ( $f_w$ ) reaches 90%, the luminogenic molecules are aggregated into particles and emit intense blue light with emission maximum at 398 nm. The PL intensity is increased about 475 times at  $f_w = 90%$  compare to  $f_w = 0%$  at same BPQ concentration (80 $\mu$ M) under identical measurement conditions, indicating the excellent AIEE property of BPQ (Fig.7.2b). Rotations and large amplitude vibrations of pyridyl groups (scheme 1) effectively deactivate the excited BPQ in good solvent through non radiative process and making it non-emissive. On the other hand, restriction of the intramolecular rotations and large amplitude vibrations of pyridyl groups of BPQ in the aggregates block the channel of nonradiative decay and make the molecule a strong emitter. A decrease in the PL intensity of BPQ hydrosol with a blue shift in emission peak from 398 nm to 396 nm is observed when the water fraction is increased from 90% to 99.9% (Fig.7.2b). This is due to the possible formation of amorphous agglomerate with

random stacking structures. In mixed solvent (THF-water) with low water content, the BPQ molecules steadily assemble in an ordered fashion to form more emissive, crystalline aggregates. But in higher water content, BPQ molecules may quickly agglomerate in a random fashion to introduce crystal softening within the crystalline aggregates. The change of emission color from colorless to intense blue in presence of 0% and 90% water content under UV irradiation is shown in the inset of Fig.7.2b.

We also followed the time course of spectral evolution of BPQ hydrosol in 90% volume percentage of water (Fig.7.2c). PL intensity increases with time and reaches the maximum intensity after 20 min of its preparation. Initially the mechanical shear stress leads to the increasing chances of most probable collisions; thus a portion of BPQ molecules clustered together to form tiny particles. The remaining portion of BPQ molecules present in the solvent mixture then gradually deposited onto the initially formed particle in recrystallization pattern to give highly emissive aggregated structures. The system thus attains an ordered cluster which restricts the free rotation and large amplitude vibrations of BPQ with time and the enhanced emission from the aggregated hydrosol is observed.

Optimum concentration of BPQ for PL study is achieved by adding different volume of 20mM BPQ in THF-water mixture (10:90 v/v). It has been observed that the PL intensity increases with increasing concentration of BPQ reaches a maximum at 80 $\mu$ M and then decreases with further increase in BPQ concentration (Fig.7.2d). This suggests that 80 $\mu$ M is the optimum concentration of BPQ in solution below which aggregation of BPQ occurs in such a way that it can form emissive crystalline structure but with further increase (>80  $\mu$ M) in concentration BPQ orient in random fashion to soften the microcrystals and is responsible for decreasing emission intensity from hydrosol.

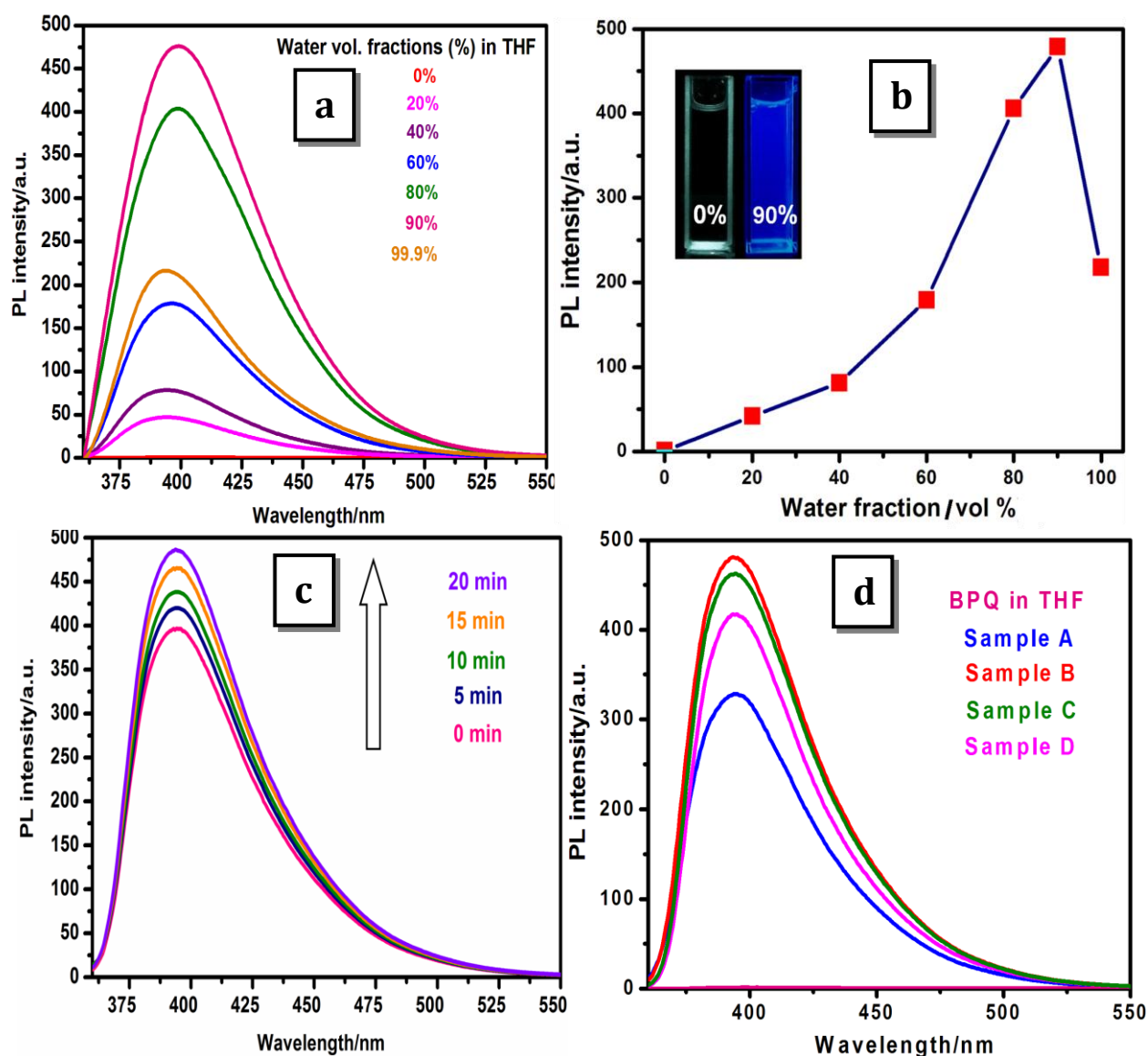


**Figure 7.2:** (a) Emission spectra of freshly prepared BPQ (80µM) in (i) 0% water (BPQ in THF), (ii) 20% water, (iii) 40% water, (iv) 60% water, (v) 80% water, (vi) 90% water and (vii) 99.9% water.  $\lambda_{ex}$ : 350 nm. (b) Plot of relative variation of PL intensity against water content ( $f_w$ ) in THF/water mixture. BPQ concentration: 80µM.  $\lambda_{ex}$ : 350 nm. Insets: Fluorescence images of BPQ (0% and 90% H<sub>2</sub>O) under 367 nm illumination. (c) Dependence of the PL intensity of BPQ immediate after its preparation with time in THF/water mixture (10:90 v/v). BPQ concentration: 80µM.  $\lambda_{ex}$ : 350 nm. (d) Emission spectra of (i) 80µM BPQ in THF, (ii) Sample A (40µM BPQ), (iii) Sample B (80µM BPQ), (iv) Sample C (120µM BPQ) and (v) Sample D (400µM BPQ) in THF/water mixture (10:90 v/v).  $\lambda_{ex}$ : 350 nm.

**7.3.3. SEM Study:** Scanning electron microscopic (SEM) study was carried out to study the morphology of the aggregated BPQ in the hydrosol. At low BPQ concentration, small crystalline microparticles (Sample C) are observed (Fig.7.3a). But at higher concentration of

BPQ, molecules are packed in two-dimensional fashion (Sample D) to form crystalline hexagonal plate like geometry with equal thickness as shown in Fig.7.3b. It seems a two dimensional growth of particles of length  $\sim 15\text{-}20\mu\text{m}$  and width  $\sim 8\text{-}10\mu\text{m}$ , take place with the increasing concentration of BPQ in solution. Most of the micro plates have smooth surface, suggesting that the luminogenic molecules (BPQ) are arranged uniformly within the crystals.

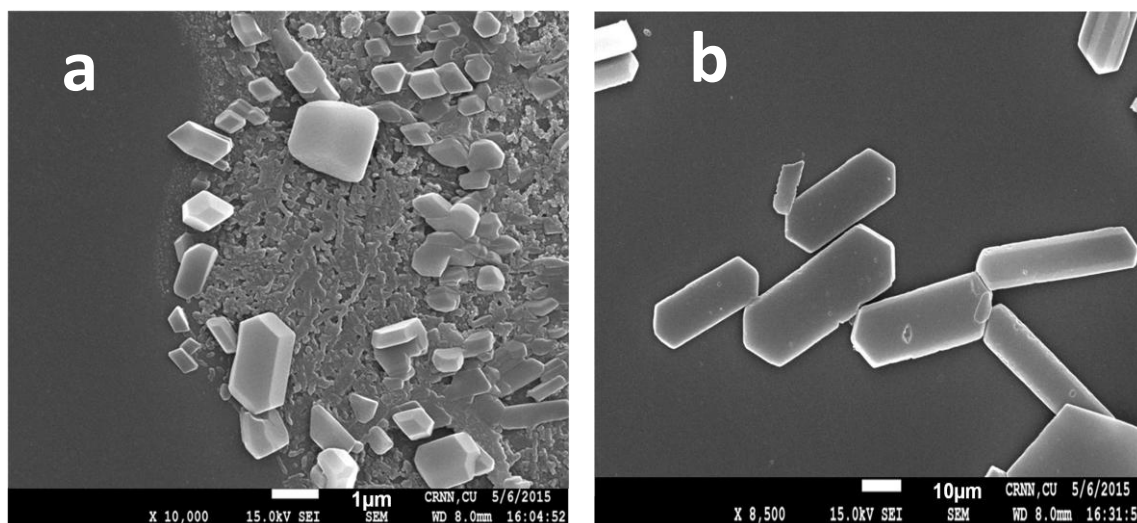


**Figure 7.3: SEM images of BPQ microstructures at concentration (a) Sample C (120 $\mu\text{M}$  BPQ) and (b) Sample D (400 $\mu\text{M}$  BPQ).**

**7.3.4. Optical Microscopic Study:** Fig.7.4a shows the optical microscopic images of Sample D. The sizes of other Samples (A, B and C) are too small to be detected within the resolution of our optical microscope. The morphology of the aggregated crystals of Sample D is hexagonal plate like and a clear two dimensional growth of crystals are noticeable. Fluorescence microscopic image of the crystals under UV excitation is shown in Fig.7.4b. The micro plates are highly luminescent, emitting intense blue light upon UV excitation. This color resembles to the color of aggregates shown in the inset of Fig.7.2b and it suggests that the nonemissive BPQ molecule becomes blue emitter in its aggregated state. Dark field's view of Sample D using polarizer, analyzer assembly shows different colors depending on the

direction of incident radiation and it reveals the anisotropic nature of the synthesized microcrystal (Fig.7.4c).

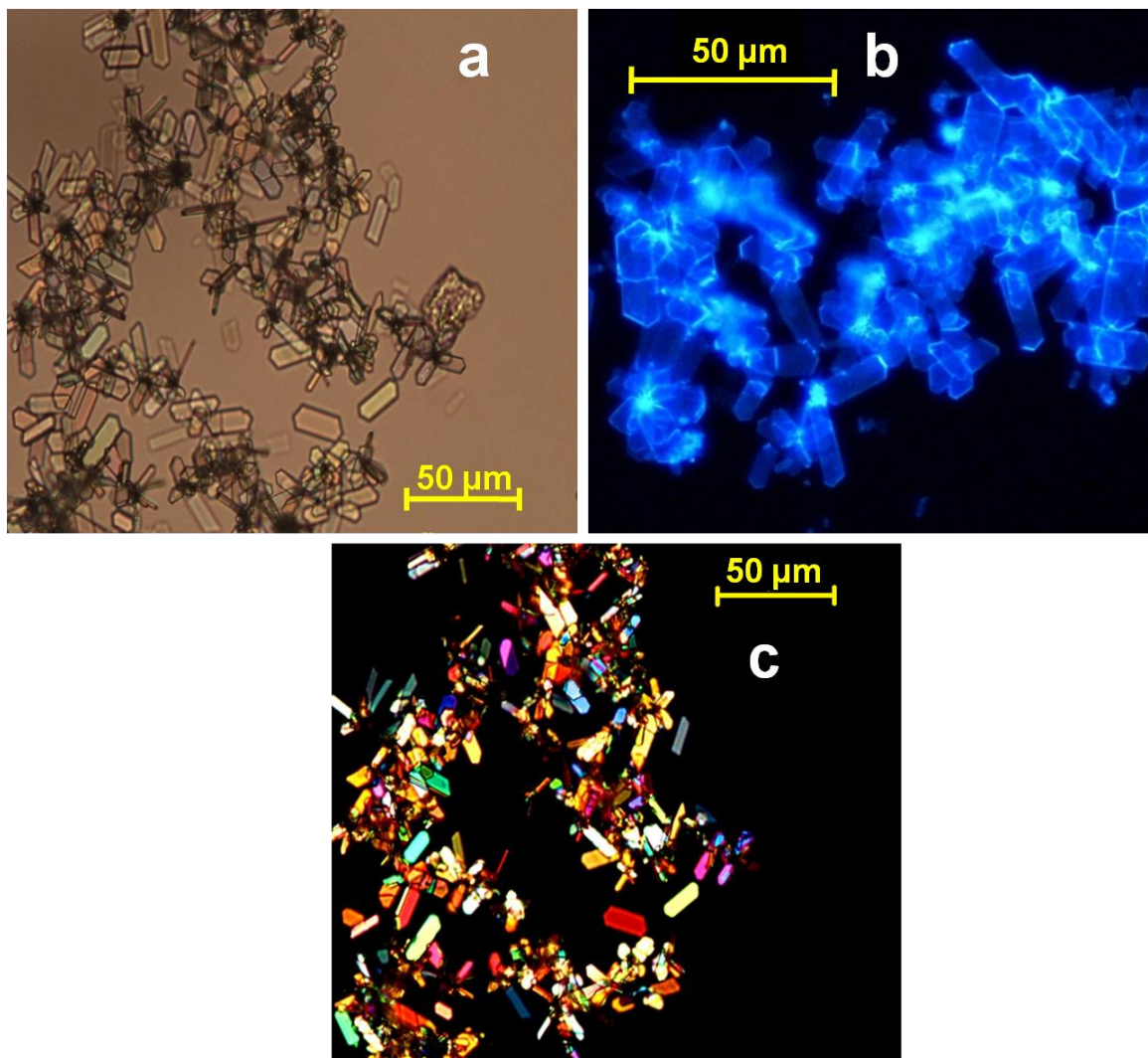


**Figure 7.4:** (a) Optical microscopic images of BPQ microcrystals have Sample D (400µM BPQ), (b) Fluorescence microscopic images of BPQ microcrystals have Sample D (400µM BPQ); exciting under UV light, (c) Polarized microscopic images of BPQ microcrystals having Sample D (400µM BPQ).

**7.3.5. Crystallographic study:** Single crystals with a highly ordered molecular packing structure can be used to directly determine the relationship between the aggregated state and PL properties by slow evaporation of a THF solution of BPQ. Single crystals of BPQ suitable for X-ray structural analysis were obtained. ORTEP drawing of BPQ displayed



in Fig.7.5a proves that that the molecules are not planar. Instead, they adopt a twisted conformation owing to the propeller-shaped structure.

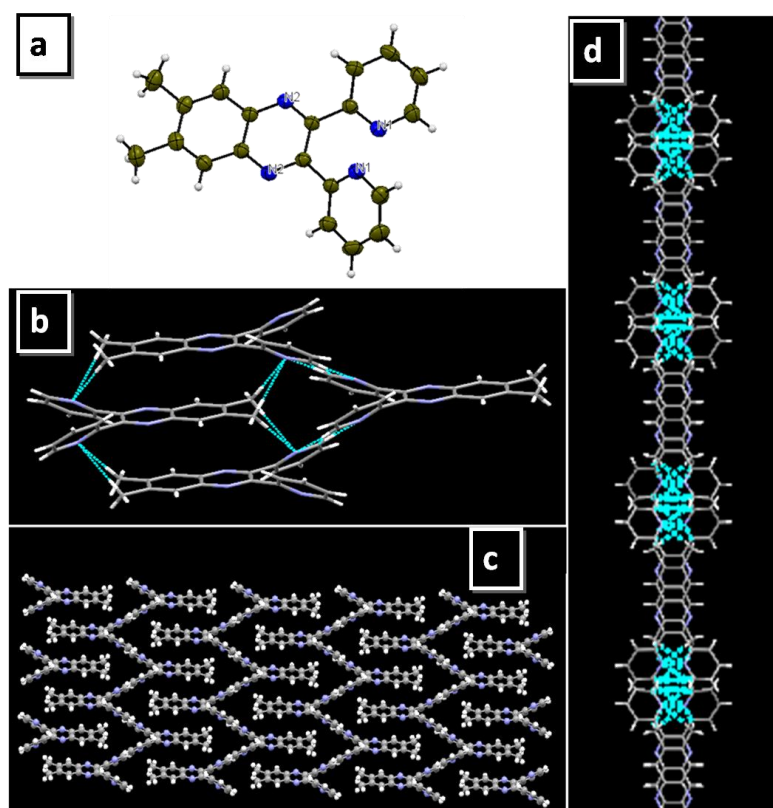


**Figure 7.5: (a) ORTEP diagram of BPQ, (b) Intramolecular Hydrogen bonding interaction in the single crystal lattice of BPQ, (c) Polymeric view of the molecular packing, (d) Belt like arrangement in Z-direction of BPQ crystal lattice.**

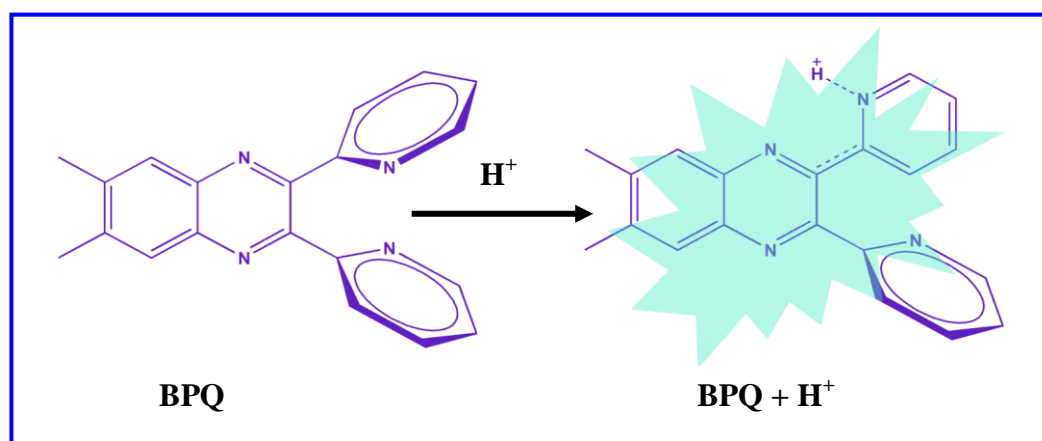
Crystallographic analysis of BPQ reveals that the torsion angle between the pyridyl ring and the quinoxaline moiety is merely  $117.8^\circ$ . Here also, like most of the AIEE active molecule,  $\pi$ - $\pi$  stacking interaction on account of extremely twisted aromatic ring in the crystalline state is absent. In particular, intermolecular hydrogen bonds are formed between the methyl Hydrogen and the pyridyl nitrogen, which enhances the close packing and consequently enhanced emission in the crystalline state (fig.7.5b). These forces help the molecules to further rigidify their conformations to the energy loss via the nonradiative relaxation channel to enhance the emission efficiency. Fig.7.5c and Fig.7.5d exhibit the

polymeric view and belt like view of this aggregated BPQ molecule. Details of crystal data were summarized in table 7.1.

**Table 7.1 Crystal data and structure refinement for 6,7-dimethyl-2,3-bis-(2-pyridyl)-quinoxaline (BPQ)**

Identification code	BPQ
Empirical formula	C <sub>20</sub> H <sub>16</sub> N <sub>4</sub>
Formula weight	312.37
Temperature	296K
Wavelength	0.71073 Å
Crystal system	Monoclinic
Space group	C2/c
Unit cell dimensions	a=16.433(2) Å
	b=13.111(2) Å
	c=7.6207(10) Å
Angles	α=90°
	β=99.243°(10)
	γ=90°
Volume	1620.6(4) Å <sup>3</sup>
Z	4
Absorption coefficient	0.079 mm <sup>-1</sup>
F(000)	656
Crystal shape	Plate
Crystal colour	Colorless
Theta range for data collection	5.101-35.21 deg
Calculated density	1.280 g/m <sup>3</sup>
Completeness to theta = 35.21	98.2%
Limiting indices	-26<=h<=26, -21<=k<=21, -12<=l<=12
Refinement method	Full-matrix least-squares on F <sup>2</sup>
Goodness-of-fit on F <sup>2</sup>	0.991
R <sub>1</sub> [I > 2σ(I)]	0.0750
wR <sub>2</sub> [I > 2σ(I)]	0.2156

**7.3.6. pH dependent photophysical properties:** The hydroxonium ion is one of the most important charged species that plays an important role in biological processes occurring in living cells and tissues such as proliferation and apoptosis, multidrug resistance, ion transport, endocytosis and muscle contraction. An interesting feature of the present compound is its pronounced effect of photophysical behavior upon protonation (Scheme 7.3).

**Scheme 7.3: The proposed mechanism of BPQ for sensing  $H^+$** 

**Absorption spectra of BPQ at different pH:** The UV-Vis absorption spectra of BPQ hydrosol recorded at different pH values are shown in Fig.7.6a. Protonated BPQ in the acidic pH shows broad absorption with absorption maxima at 361 nm. Absorption maxima of the deprotonated forms in the basic pH ( $>7$ ) medium is at 354 nm. At higher pH ( $>7$ ) absorption spectrum is similar to that of aggregated hydrosol in water. The spectra measured at higher pH are basically the same that of pH $\sim$ 5. The broadening and red shift of the emission spectra at pH $<$ 5 suggest the enhancement of charge transfer character in BPQ upon protonation [23].

**Fluorescence spectra of BPQ at different pH:** Photoluminescence (PL) spectra of BPQ hydrosol at different pH are shown in Fig.7.6b. No change in PL spectra of the hydrosol is observed at pH $\geq$ 5. But at pH less than 5, a new red shifted broad emission band having maxima at 468 nm is appeared.

An isoemissive point between peak maxima 398 nm and 468 nm is observed and it indicates equilibrium between protonated and deprotonated species of BPQ. It is also observed that the milky hydrosol slowly turned into clear solution with increasing  $H^+$  concentration in the medium. We presume that the broad emission band at 468 nm is due to the charge transfer emission from the dissolved protonated  $BPQH^+$  in the solution.

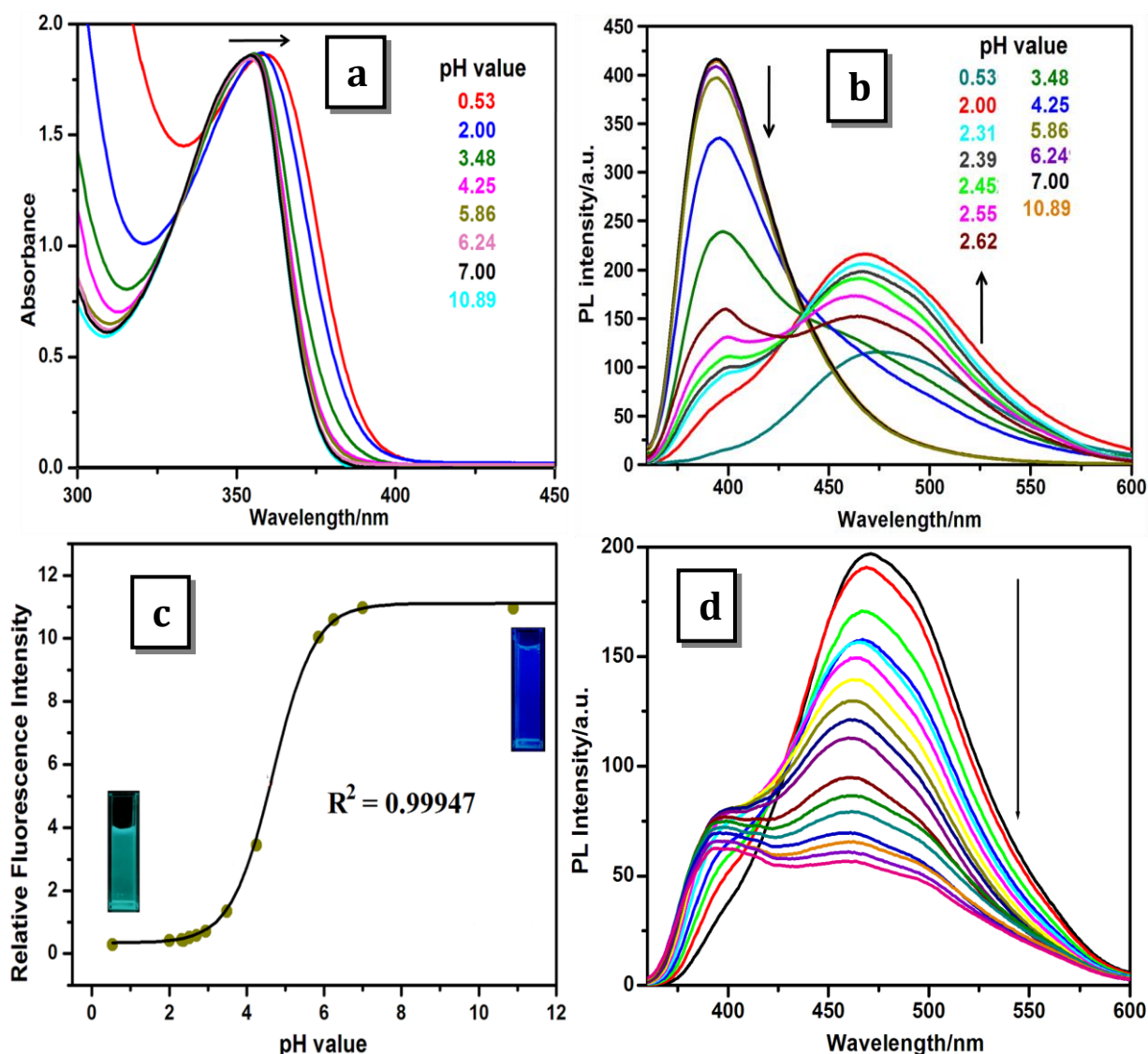


**Figure 7.6:** (a) Normalized UV-Vis absorption spectra of BPQ hydrosol (80 $\mu$ M) in THF/water mixture (10:90 v/v) at different pH of the medium (pH ~ 1.0-11.0). (b) PL spectra of BPQ hydrosol (80 $\mu$ M) in THF/water mixture (10:90 v/v) at different pH of the medium (pH ~ 1.0-11.0).  $\lambda_{\text{ex}}$ : 350 nm. (c) Ratiometric calibration curve of  $I_{398}/I_{468}$  (intensity at 398 nm vs. intensity at 468 nm as a function of pH of the medium and pH dependent color shift from green to blue with decreasing concentration of  $\text{H}^+$  ion in the medium under 367 nm illumination. (d) PL spectra of protonated BPQ in water/THF mixture.  $\lambda_{\text{ex}}$ : 350 nm.

Addition of less polar THF to this acidic hydrosol (Fig.7.6d) shows blue shift and decreasing intensity of the 468 nm broad band and hence it confirms the charge transfer character of the band. A visual change in color (Fig.7.6c) from blue to green under UV light excitation at higher (pH>4, blue) and lower pH (pH<4, green) is observed indicating the

charge transfer character of BPQ in the acidic solution. It is further observed that the intensity of 468 nm band decreases at higher  $H^+$  ion concentrations ( $pH < 1$ ). This suggests that at higher  $H^+$  ion concentrations, the nitrogen centre of quinoxaline unit get protonated and hence the charge transfer character of the molecule as a whole decreases.

We also investigated the reversibility of protonation/deprotonation processes of BPQ in its hydrosol. It is observed that the switch between blue and green emission can be repeated without fatigue by alternate addition of NaOH and HCl and the process is nondestructive in nature (Fig.7.7a). The red shift of  $\sim 70$  nm in the fluorescence of BPQ when being introduced with HCl and the recovery toward the initial blue emission ( $\lambda_{em} = 398$  nm) demonstrate the significant fluorescent switching properties of the BPQ hydrosol under protonation/deprotonation stimuli (Fig.7.7b).

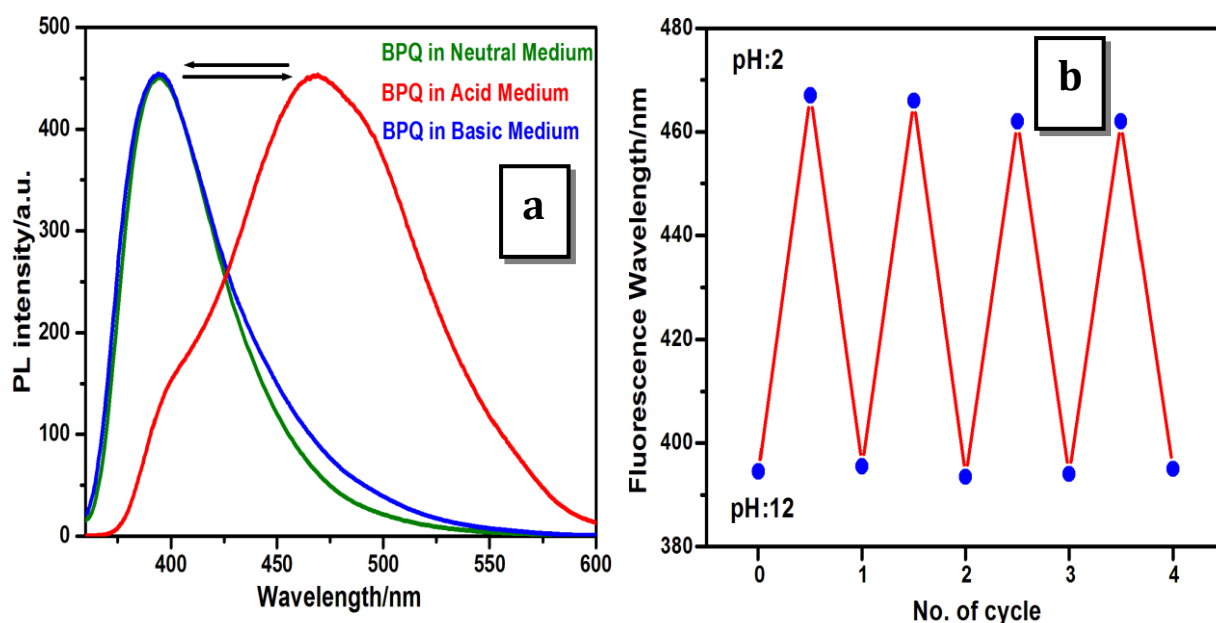


**Figure 7.7: (a) Normalized PL spectra of aggregated BPQ by changing pH of the medium by acidic and basic solvent. (b) Reversible switching of the emission wavelength of BPQ by repeated adding of acid and alkali to the medium.**

**7.3.7. Time resolved Fluorescence Study:** In order to understand the nature of aggregate of BPQ luminogen, we have carried out time resolved fluorescence study of aggregated BPQ hydrosols with excitation at 376 nm and emissions are measured at 398 nm

and 468 nm for deprotonated and protonated BPQ hydrosols respectively. Decay profile of deprotonated and protonated hydrosols of BPQ are shown in Fig.7.8a.

Fluorescence lifetime of diluted BPQ in THF is difficult to measure due to very weak emission intensity of the monomer. Fluorescence lifetimes of BPQ hydrosols are measured by deconvoluting the response function from the decay curves. The decay profiles of aggregated BPQ hydrosols having reasonably higher emission intensity are fitted with bi-exponential decay. The observed components of lifetime for aggregated BPQ lie within  $\sim 0.2$  ns and  $\sim 0.8$ - $1.0$  ns respectively.

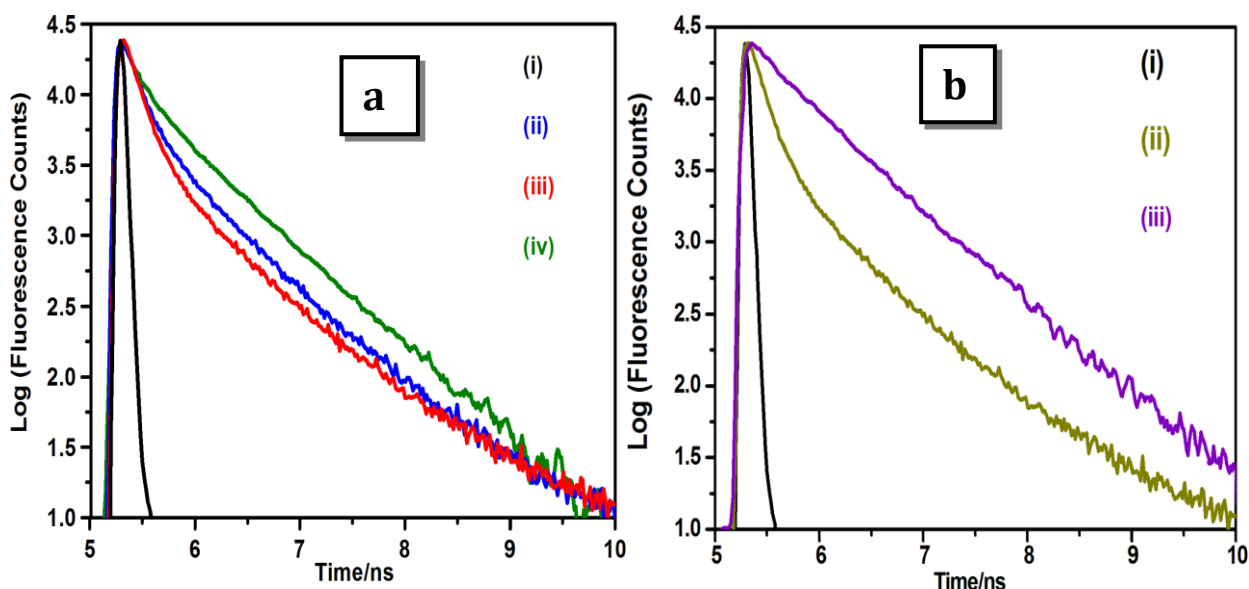


**Figure 7.8:** Fluorescence decay profile of spectra (a) (i) Lamp, (ii) Sample A ( $40\mu\text{M}$  BPQ), (iii) Sample B ( $80\mu\text{M}$  BPQ) and (iv) Sample B ( $80\mu\text{M}$  BPQ) in pH $\sim 2$  medium at ( $\lambda_{\text{emi}}$ : 398 nm). (b) (i) Lamp, (ii) Sample B ( $80\mu\text{M}$  BPQ) at ( $\lambda_{\text{emi}}$ : 398 nm), (iii) Sample B ( $80\mu\text{M}$  BPQ) in pH $\sim 2$  medium at ( $\lambda_{\text{emi}}$ : 468 nm). Excitation wavelength: 376 nm.

The weight percentage of shorter component ( $\sim 0.2$  ns) increases and the longer component ( $\sim 1.0$  ns) decreases with the increasing size of the aggregates. BPQ molecules within the aggregates are facing two types of micro environments *i.e.* surface bound BPQ and BPQ within the inner core of the microcrystals. The excited inner core BPQ molecules behave like Frenkel excitons whose fluorescence lifetime ( $\sim 0.2$  ns) is much shorter than the surface bound molecules. Now with increasing size of the aggregates, the number of surface

bound BPQ decreases and hence the weight percentage of the longer component decreases. On the other hand, with decreasing pH (<4) of the medium, dissolution of BPQ from aggregate to solution takes place and hence the size of the aggregate decreases. The number of surface bound BPQ increases with decreasing size of aggregates and it is reflected in the increasing weight percentage of the fluorescence lifetime of the surface bound molecules *i.e.* ~1.0ns component (table 7.2). The competition between ICT and AIEE character at much higher proton concentration generate a new peak at longer wavelength (468 nm). Interestingly the lifetime of protonated BPQ at this peak is fitted with single exponential decay and the value is ~0.8ns. This 0.8ns component arises solely from the solvated BPQH<sup>+</sup> upon excitation to its ICT state (Fig.7.8b).

**Table 7.2: Fluorescence lifetime of aggregated hydrosols of 6,7-dimethyl-2,3-bis-(2-pyridyl)-quinoxaline (BPQ) in water (Sample A and Sample B) and Sample B in pH~ 2.**

Sample	$\tau_1$ (ns)	Contribution (%)	$\tau_2$ (ns)	Contribution (%)	$\chi^2$
Sample A ( $\lambda_{\text{emi}}$ : 398 nm)	0.187	79.9	0.963	20.1	0.94
Sample B ( $\lambda_{\text{emi}}$ : 398 nm)	0.188	88.6	1.063	11.4	0.99
Sample B in pH~2 ( $\lambda_{\text{emi}}$ : 398 nm)	0.163	38.6	0.834	61.4	0.96
Sample B in pH~2 ( $\lambda_{\text{emi}}$ : 468 nm)			0.846	100	0.92

**7.3.8. Mechanism of proton triggered tuning AIEE and ICT effect:** It was well documented that the spatial conformation of molecules played an important role in determining their stacking modes and thus influenced the properties of the resulting aggregate. In BPQ molecule, two pyridyl units are attached to the 2, 3 positions of 6, 7-dimethyl quinoxaline moiety through single bond. The coplanar arrangement of these two

rings with quinoxaline groups are avoided due to steric forces and the BPQ as a whole prefer to attain a twisted geometry.

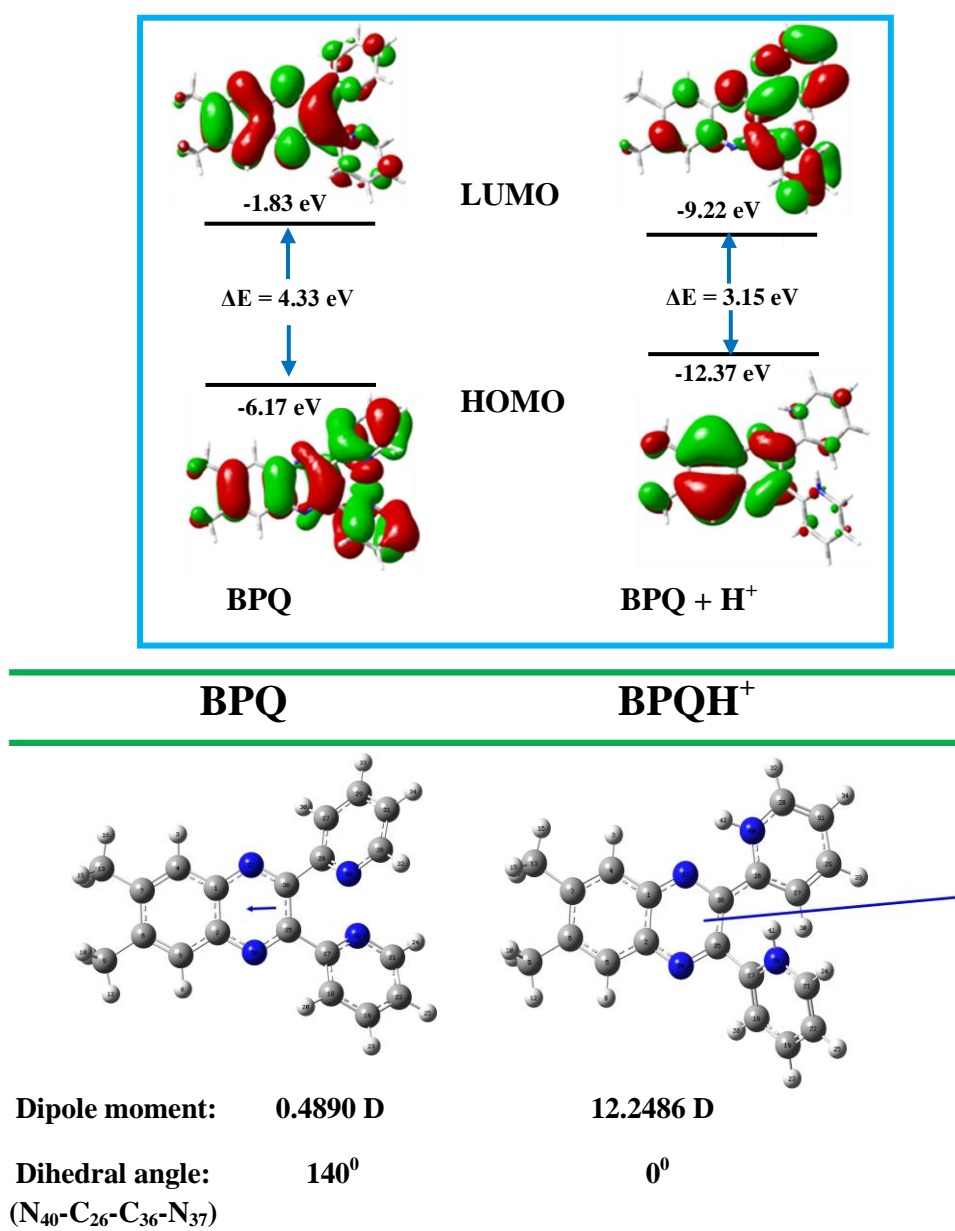


**Figure 7.9:** Theoretically calculated frontier orbital of BPQ and BPQH<sup>+</sup> calculated by using the DFT B3LYP/6-31G(d,p) basis set. The optimized geometry, dipole moment and dihedral angle between two nitrogen of pyridyl and quinoxaline moiety of BPQ and BPQH<sup>+</sup> molecule at its lowest excited state ( $S_1$ ) calculated by using the TDDFT B3LYP/6-31G(d,p) basis set.

Optimized ground state geometry of BPQ using DFT/B3LYP/6-31G(d,p) level of theory shows that both the pyridyl unit prefer to remain  $\sim 140^\circ$  out of plane of the quinoxaline ring. The twisted pyridyl ring will increase the stacking distance between two immediate



neighbors at about  $\sim 5\text{\AA}$  within the aggregates and it results much weaker intermolecular  $\pi$ - $\pi$  stacking interaction. The free rotation of two pyridyl groups is also hindered in the aggregated state to make the molecule AIEE active. But a significant conformational change of BPQ is observed in acidic medium. The frontier molecular orbital (FMO) of BPQ and BPQH<sup>+</sup> calculated using DFT/B3LYP/6-31G(d,p) level of theory are shown in Fig.7.9.

HOMO electron densities of BPQ are localized within the quinoxaline and pyridyl moiety separately and the electron densities are shifted from donor pyridyl to acceptor quinoxaline moiety in its LUMO. This delocalization of excited electronic energy with the freely rotating pyridyl group is responsible to open up the non-radiative deactivation channels for excited BPQ in its isolated form in solution and allow the charge transfer from donor pyridyl group to acceptor quinoxaline group. On the other hand though electron density on the protonated pyridyl group is absent in HOMO of BPQH<sup>+</sup>, the electron density is shifted to pyridyl group in its LUMO. This drift of electron density from quinoxaline group to pyridyl group in the excited state is due to the formation of strongly electron-withdrawing pyridinium ion, which triggered the intramolecular charge transfer between the quinoxaline donor and the pyridinium acceptor. In acidic medium, the proton (H<sup>+</sup>) is first attached with nitrogen atom of the pyridyl groups since the pK<sub>a</sub> value of pyridyl unit (5.25) is much higher than that of quinoxaline (0.6). Through aromatic conjugation, the quinoxaline loses electron density while the pyridinium ion gains electron density. Thus a prominent intramolecular charge transfer character from donor quinoxaline to acceptor protonated pyridyl group takes place and it is reflected in the lowering of HOMO and LUMO energy gap after protonation from 4.33eV to 3.15eV as shown in Fig.7.9. This aromatic conjugation stabilizes the LUMO mostly and causes red-shift of both the absorption and emission spectra of BPQH<sup>+</sup> (Fig.7.6a and 7.6b).

Introduction of ICT character in protonated BPQ is further supported from the excited state optimized geometry of both protonated and deprotonated BPQ molecule (Fig.7.9). BPQ is in twisted form, both in its ground and excited state and the twisted angle between quinoxaline and pyridyl group is  $\sim 140^\circ$ . On the other hand, planarity ( $N_{40}-C_{26}-C_{36}-N_{37} \sim 10^\circ$ ) of one of the pyridyl group is introduced after protonation in the ground state and dihedral angle  $N_{40}-C_{26}-C_{36}-N_{37}$  decreases to zero in the excited state. Meanwhile, it induces the dipole moments in the reversed directions (Fig.7.9). An enhanced value of dipole moment from 0.489 D to 12.2486 D is also observed after protonation. This enhancement of dipole moment supports the introduction of planarity and at the same time ICT character in  $BPQH^+$ .

#### 7.4. Picric acid Sensor:

UV-Vis spectra of BPQ hydrosol in presence of picric acid generate a new peak at longer wavelength region *i.e.* at 400 nm (Fig.7.10a). The broad red shifted band at 400 nm gradually becomes prominent with the increase of picric acid concentration to a fixed amount of BPQ hydrosol. Being a strong electron deficient molecule, PA can easily be attracted towards electron rich aggregated BPQ to form non fluorescent ground state complex and the red shifted (400 nm) band is the charge transfer band [22]. But the addition of other nitroaromatic compounds to BPQ hydrosol do not show any change in the absorption spectrum because their electron deficiency cannot reach to such extent to form strong complex with fluorescent BPQ hydrosol.

The fluorescence spectrum of BPQ hydrosol exhibits an intense emission peak at 398 nm. This fluorescence is effectively quenched upon addition of PA. Fig.7.10b shows the changes in the fluorescence spectrum upon titration of the hydrosol against picric acid. Gradual addition of PA to BPQ hydrosol, the emission intensity decreases, but the PL spectral profile remains unchanged.

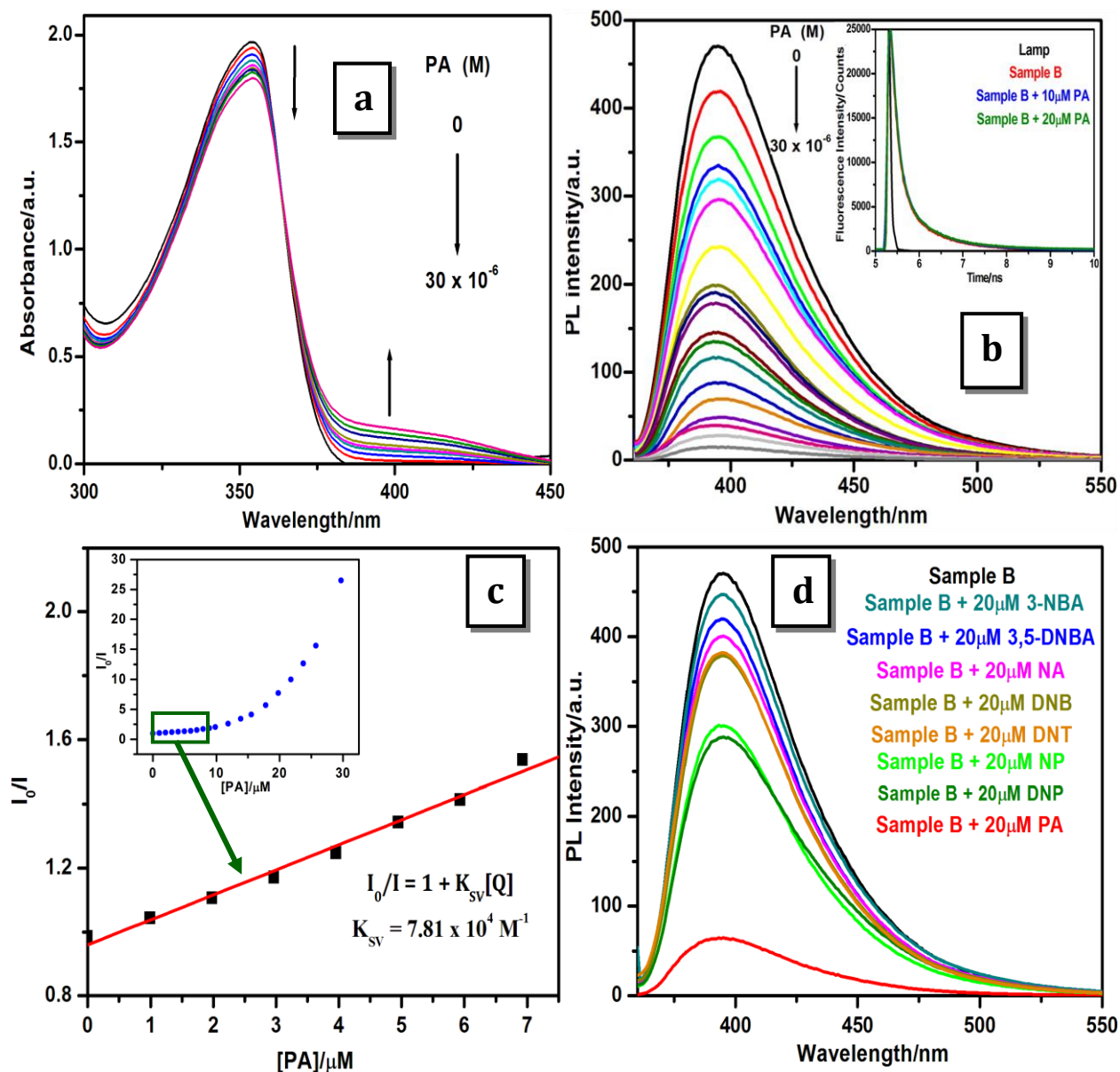


**Figure 7.10:** (a) UV-Vis spectra and (b) Fluorescence spectra of BPQ hydrosol (80 $\mu\text{M}$  BPQ) after the addition of different amounts of PA. The inset shows the variation of fluorescence lifetime of BPQ hydrosol (80 $\mu\text{M}$  BPQ) in absence and presence of PA (10 and 20 $\mu\text{M}$ ) at ( $\lambda_{\text{emi}}$ : 398 nm). Excitation wavelength: 376 nm. (c) Stern-Volmer curve of corresponding fluorescence quenching in presence of different amount of PA. The inset shows a plot of  $I_0/I$  versus [PA] for BPQ hydrosol. (d) Comparison of fluorescence quenching of BPQ hydrosol in presence of different aromatic nitro compounds (20 $\mu\text{M}$ ).

The plot of  $I_0/I$  versus [PA] shows an upward curvature instead of linear relationship (inset of Fig.7.10c), indicating that quenching efficiency increases with increasing concentration of quencher and may be termed as super amplified quenching effect [24-27]. The unique phenomenon could be attributed to the 3-dimensional morphology of the

aggregates that generate more small cavities to enable the small explosive molecules to enter through electrostatic interactions and offer more diffusion channels for the excitons to migrate, allowing them to be more quickly annihilated by the explosive quenchers. Equation  $I_0/I = 1.146 + 0.329e^{0.14684[PA]}$  is obtained by fitting the concave curve of Fig.7.10c. From this equation, quantitative analysis can be realized. But the curvature nature of this Stern-Volmer plot may be due to either static or dynamic pathway. This ambiguity is resolved by measuring fluorescence lifetime of BPQ hydrosol in presence and absence of PA (inset of Fig.7.10b) [28,29]. Our measured fluorescent decay curves of BPQ hydrosol both in presence and absence of PA are fitted with bi-exponential decay and the fitted components are identical for both the cases (inset of Fig.7.10b). This unchanged fluorescence lifetime of BPQ hydrosol in the presence of PA indicates that the fluorescence quenching takes place through ground state complexation *i.e.* static quenching mechanism. At low concentration of PA (inset of Fig.7.10c) a linear Stern-Volmer plot is obtained with quenching constant value  $7.81 \times 10^4 \text{ M}^{-1}$ .

Fluorescence quenching of BPQ in presence of different aromatic nitro compounds (3-NBA, 3,5-DNBA, NA, DNB, DNT, NP, DNP, PA) are also studied (Fig.7.10d) and it is observed that the quenching efficiency of PA is much higher than other nitro aromatics. The lowest detection limit of PA was calculated using  $3\sigma$  method [30] and the value is  $0.77\mu\text{M}$ .

## 7.5. Conclusion:

In conclusion, we have introduced a low dimensional aggregated hydrosol from the pyridyl substituted quinoxaline (BPQ) that possesses remarkable AIEE properties. Aggregation has induced significant enhancements in its fluorescence efficiency compared with its dilute solution in good solvent. The behavior has been explained due to restriction of intramolecular rotation and large amplitude vibrational modes in its aggregated states. In addition, we have presented the proton-triggered red shifted luminescence of BPQ hydrosol.

Computation of HOMO, LUMO electron densities of BPQ and BPQH<sup>+</sup> reveals extended conjugation of electron density between quinoxaline and pyridyl group takes place upon photoexcitation of BPQH<sup>+</sup>. This ICT in BPQH<sup>+</sup> causes the switching of emission from blue to green in presence of excess H<sup>+</sup> ions. Thus, introduction of an AIEE unit to the traditional pH sensitive fluorophores is an efficient route to expand their practical application to both solution and solid states. Such results also provide valuable information on the future design of new fluorescent probes, whose light-emitting behavior can be readily tuned by simply varying the environmental conditions. Another excellent utility of this AIEE active molecule is its selective sensitivity towards picric acid (PA) with quenching constant  $7.81 \times 10^4 \text{ M}^{-1}$ . It is further explained with the help of both steady state and time resolved emission study that the fluorescence quenching of BPQ hydrosol in presence of picric acid takes place through static quenching mechanism.

## References:

1. E. L. Spitler and M. M. Haley, *Tetrahedron*, 64, **2008**, 11469.
2. D. Knapton, S. J. Rowan and C. Weder, *Macromolecules*, 39, **2006**, 651.
3. P. K. Iyer, J. B. Beck, C. Weder and S. J. Rowan, *Chem. Commun.*, **2005**, 319.
4. J. J. Lavigne and E. V. Anslyn, *Angew. Chem., Int. Ed.*, 38, **1999**, 3666.
5. C. Dou, L. Han, S. Zhao, H. Zhang and Y. Wang, *J. Phys. Chem. Lett.*, 2, **2011**, 666.
6. E. A. Davey, A. J. Zuccherro, O. Trapp and U. H. F. Bunz, *J. Am. Chem. Soc.* 133, **2011**, 7716.
7. A. J. Zuccherro, J. N. Wilson and U. H. F. Bunz, *J. Am. Chem. Soc.* 128, **2006**, 11872.
8. Z. Yang, W. Qin, J. W. Y. Lam, S. Chen, H. H. Y. Sung, I. D. Williams and B. Z. Tang, *Chem. Sci.* 4, **2013**, 3725.
9. J. Tolosa, K. M. Solntsev, L. M. Tolbert and U. H. F. Bunz, *J. Org. Chem.* 75, **2010**, 523.
10. S. Ma, J. Zhang, J. Chen, L. Wang, B. Xu and W. Tian, *Chin. J. Chem.* 31, **2013**, 1418.
11. J. Chen, S. Ma, J. Zhang, L. Wang, L. Ye, B. Li, B. Xu and W. Tian, *J. Phys. Chem. Lett.* 5, **2014**, 2781.
12. R. Murugavel and M. P. Singh, *New J. Chem.*, 34, **2010**, 1846.
13. B. Szczesna and Z. U. Lipkowska, *New J. Chem.*, 26, **2002**, 243.
14. P. K. Thallapally, A. K. Katz, H. L. Carrell and G. R. Desiraju, *Chem. Commun.*, **2002**, 344.
15. K. K. Kartha, A. Sandeep, V. K. Praveen and A. Ajayaghosh, *Chem. Rec.*, 15, **2015**, 252.
16. N. Niamnont, N. Kimpitak, K. Wongravee, P. Rashatasakhon, K. K. Baldrige, J. S. Siegel and M. Sukwattanasinitt, *Chem. Commun.*, 49, **2013**, 780.
17. N. Dey, S. K. Samanta and S. Bhattacharya, *ACS Appl. Mater. Interfaces*, 5, **2013**, 8394.
18. V. Bhalla, A. Gupta, M. Kumar, D. S. S. Rao and S. K. Prasad, *ACS Appl. Mater. Interfaces*, 5, **2013**, 672.
19. M. Kumar, S. I. Reja and V. Bhalla, *Org. Lett.*, 14, **2012**, 6084.
20. R. Ni, R. B. Tong, C. C. Guo, G. L. Shen and R. Q. Yu, *Talanta*, 63, **2004**, 251.
21. V. Bhalla, A. Gupta and M. Kumar, *Org. Lett.* 4, **2012**, 13112.
22. K. K. Kartha, V. K. Praveen, S. S. Babu, S. Cherumukkil and A. Ajayaghosh, *Chem. Asian J.*, 10, **2015**, 2250.
23. S. Shanmugaraju, D. Samanta, B. Gole and P. S. Mukherjee, *Dalton Trans.*, 40, **2011**, 12333.
24. W. Wei, R. Lu, S. Tang and X. Liu, *J. Mater. Chem. A*, 3, **2015**, 4604.
25. K. Acharyya and P. S. Mukherjee, *Chem. Commun.*, 50, **2014**, 15788.
26. S. Sanda, S. Parshamoni, S. Biswas and S. Konar, *Chem. Commun.*, 51, **2015**, 6576.
27. J. Wang, J. Mei, W. Yuan, P. Lu, A. Qin, J. Sun, Y. Mac and B. Z. Tang, *J. Mater. Chem.*, 21, **2011**, 4056.
28. P. Lu, J. W. Lam, J. Z. Liu, C. K. Jim, W. Z. Yuan, N. Xie, Y. C. Zhong, Q. Hu, K. S. Wong, K. K. Cheuk and B. Z. Tang, *Macromol. Rapid Commun.* 31, **2010**, 834.
29. X. Sun, Y. Wang and Y. Lei, *Chem. Soc. Rev.* 31, **2015**, DOI: 10.1039/c5cs00496a.
30. Y.B. Ruan, A.F. Li, J.S. Zhao, J.S. Shen and Y.B. Jiang, *Chem. Commun.*, 46, **2010**, 4938.



# CHAPTER 8

## **Proton Induced Green Emission from AIEE active 2,2' Biquinoline Hydrosol and its Selective Fluorescence Turn-on Sensing Property towards Zn<sup>2+</sup> ion in Water\***

\*A part of this chapter has been communicated in the article “Prativa Mazumdar<sup>†</sup>, Samir Maity<sup>†</sup>, Debasish Das<sup>†</sup>, Sadhan Samanta<sup>†</sup>, Milan Shyamal<sup>†</sup> and Ajay Misra<sup>†</sup>, *Sens. Actuator B-Chem.*,2016, (Communicated).”

## 8.1. Introduction:

The AIEE materials have in turn brought tremendous research interests from both academic and technological areas. AIEgens have shown incredibly splendid performance as sensor [1,2]. Fluorescent chemosensors are widely used as powerful tools to spy on neutral and ionic species owing to their high sensitivity, selectivity, versatility and relatively simple handling [3]. Single hosts that can independently recognize two guest species with distinct spectral responses via the same or different channels have already emerged and have gradually become a new research focus [4]. This paradigm shift from selective to differential receptors resulted from a desire to overcome difficulties such as cross-talk, a larger invasive effect etc [5]. Thus, some interesting dual analytes fluorescent probes have been reported as conventional chemo sensor towards metal ion/metal ion, anion/metal ion and anion/anion either simultaneously or consecutively but in most of the cases bi-functional materials are used as host [6-8]. But dual sensing features by changing conformation of the host are still rare.

Zinc is an essential trace element that is necessary to plants, animals and microorganisms [9]. Zinc is believed to be an essential factor in many biological processes such as brain function and pathology, gene transcription, immune function and mammalian reproduction [10, 11] as well as some pathological processes, such as Alzheimer's disease, epilepsy, ischemic stroke, and infantile diarrhea [12-14]. Although most zinc ions are tightly bound to enzymes and proteins, the physiological roles of free zinc pools in certain tissues

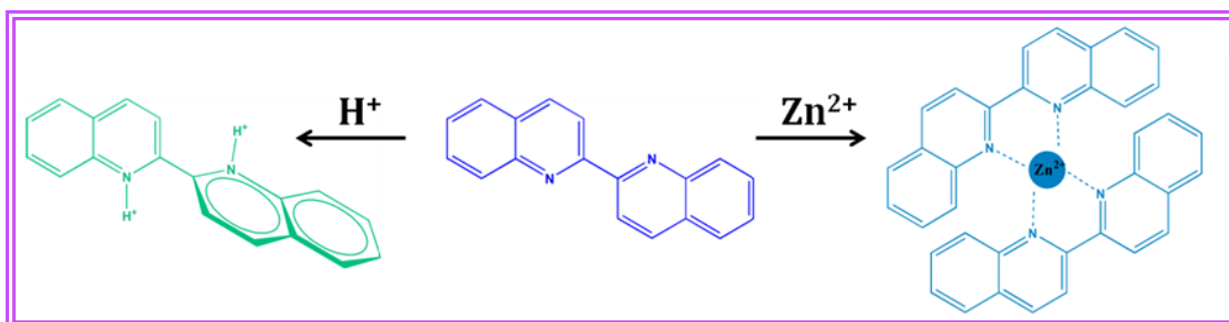


await to be explored [15]. Unlike other biological transition metal  $Zn^{2+}$  is spectroscopically and magnetically silent because of its  $d^{10}$  electron configuration. Thus the development of sensors for the facile detection of  $Zn^{2+}$  is of great importance in environmental monitoring and biological assays.

In case of sensor research work, the pH dependent fluorescence intensity of ligand is also an interesting topic of study. pH is highly critical to all life forms and a small change in environmental pH can devastate a number of plant and animal lives. Monitoring the pH level is thus crucial to the preservation of our living environment. Protonation of some heteroatom-containing groups such as pyridinyl, amino will significantly change their electron-withdrawing properties [16,17]. This will have an obvious effect on the emission color or intensity of fluorophores with these pH-sensitive groups. Since lone pairs of heteroatom lose conjugation upon protonation, this hypsochromism in spectra is an obvious incident. But proton induced bathochromic shift is very rare.

We are interested to explore a new AIEE based system *i.e.* heteroatom containing luminogen 2,2' biquinoline (BQN) which has two free rotating quinoline rings connecting with each other through a single bond. But in aggregated state this free rotation is restricted which induced enhancement of emission and changes its emission color from colorless to blue upon UV excitation. This AIEE active species can selectively sense zinc ion in its aggregated state through ground state complexation. Upon complexation with a suitable metal ion, a metal induced planarization is incorporated to the system and as result of this large enhancement of conjugation length and intra ligand charge transfer (ILCT) [18-20] are occurred. Meanwhile this probe can senses acidic medium by introducing charge transfer character with a drastic change in color from blue to yellowish green. This broad red shifting is due to attachment of proton to the electron donating nitrogen centers of BQN and this

introduces internal charge transfer (ICT) character within BQN. So this single molecule can sense dual guests independently through skeleton modification, shown in Scheme 8.1.



Scheme 8.1: Dual sensing of proton and  $Zn^{2+}$  ions independently by BQN.

## 8.2. Experimental:

**8.2.1. Materials:** 2,2' biquinoline (BQN) was purchased from Sigma-Aldrich Chemical Corp. Tetrahydrofuran (THF), Hydrochloric acid (HCl), Sodium hydroxide (NaOH), Mercuric Chloride, Cadmium Chloride, Manganese Chloride, Cobalt Chloride, Zinc Acetate, Copper Sulphate, Nickel Sulphate, Magnesium Chloride, Potassium Chloride, Sodium Chloride, Silver Nitrate, Calcium Chloride and Lead Nitrate were purchased from E-Merck India Ltd. The purity of these chemicals was checked spectrophotometrically. Triply distilled deionised water was used throughout the experiment.

**8.2.2. Preparation of aggregates:** 0.05(M) solution of BQN was prepared in THF. Different amount of the above solution (10 $\mu$ L for Sample A, 20 $\mu$ L for Sample B, 30 $\mu$ L for Sample C, 50 $\mu$ L for Sample D, 100 $\mu$ L for Sample E) were injected drop wise into 5ml water and allowed to stir for 2min. The final concentrations of BQN are 100 $\mu$ M, 200 $\mu$ M, 300 $\mu$ M, 500 $\mu$ M, 1000 $\mu$ M for Sample A, B, C, D and E respectively. Clearness of the solutions was gradually decreased and a milky white color was appeared. Then the solutions were allowed to stand for 20 min.

**8.2.3. pH dependent experiments:** pH of the medium during pH variation study was adjusted by adding different amount of 0.1(M) HCl and 0.1(M) NaOH and the subsequent measurement of pH by using a pH meter. All solutions were prepared on the same day to study their absorbance, steady-state and time-resolved fluorescence measurements.

**8.2.4. Characterization:** The UV-Vis spectroscopy was used to characterize the optical properties and was measured in a 1cm quartz cuvette with a Shimadzu UV-1800 spectrophotometer. The spectra were recorded at room temperature in the range between 230 nm to 400 nm. Steady state fluorescence spectra were recorded using Hitachi F-7000 Fluorescence Spectrophotometer. Time-resolved fluorescence measurements were carried out under ambient conditions using a time-correlated single-photon counting (TCSPC) spectrometer [a picosecond diode laser (IBH, UK)]. All samples were excited using 370 nm picoseconds diode laser and the emission was collected at 396 nm, 450 nm and 497 nm. Lamp profiles were measured with a band-pass of 3 nm using Ludox as the scatterer. All pH measurements were made with an ORION VERSASTAR. The morphologies of the synthesized nano/micro structures were studied using ZEISS EVO 18 scanning electron microscope (SEM) operated at an accelerating voltage of 5 kV. Before SEM study samples were vacuum dries on a glass plate and a thin layer of Au was deposited onto the samples to minimize sample charging. Optical microscopy images were taken using an NIKON ECLIPSE LV100POL upright microscope equipped with a 12V-50W mercury lamp. The samples for optical microscopic study were prepared by placing a drop of colloidal solution onto a clean glass slide. Single crystal X-ray diffraction data was collected on a Bruker Nonius APEX-II CCD diffractometer using graphite monochromated MoK $\alpha$  radiation ( $\lambda = 0.71073 \text{ \AA}$ ). All the experiments were carried out at room temperature.

**8.2.5. Computational Method:** Quantum chemical calculations based on density functional theory (DFT) were carried out using a Gaussian09 program. Ground state geometry of BQN was optimized and dipole moment, HOMO, LUMO energy gap and electronic charge distribution were performed using the B3LYP hybrid functional with 6-31G(d,p) basis. The resulting geometry was used as starting geometries for optimization of its protonated forms as well its Zn complex. Excited states computations were carried out using TD-DFT B3LYP/6-31G(d,p) level of theory.

### 8.3. Results and Discussion:

**8.3.1. Absorption Study:** The optical properties of the compounds are investigated both in solution and in the aggregated state. The UV-Vis absorption spectrum of BQN in THF is shown in Fig.8.1 and two groups of bands are detected. The first intense band at ~250 nm is due to  $\pi$ - $\pi^*$  transition between two quinoline and the second set of bands ~312-336 nm corresponds to the charge transfer from nitrogen centre of quinoline to the  $\pi$  electron framework of benzene ring within the same quinoline moiety [21].

UV-Vis spectra of aggregated hydrosol show small red shift and broadening of the overall spectra with a new absorption tail in the long wavelength region (Fig.8.1). Red shifts of spectra are due to weak  $\pi$  -  $\pi$  interaction of BQN in its aggregated form. This newly grown band at 350-390 nm has been assigned to the charge transfer transition from nitrogen centre of one pyridyl to the phenyl ring of another quinoline ring [21]. It is assumed that BQN takes planer orientation in its aggregated structure which insists charge transfer between the two quinoline groups of BQN. Further the long tail of the absorption band has been explained due to Mie's scattering of light by the aggregated BQN hydrosol.

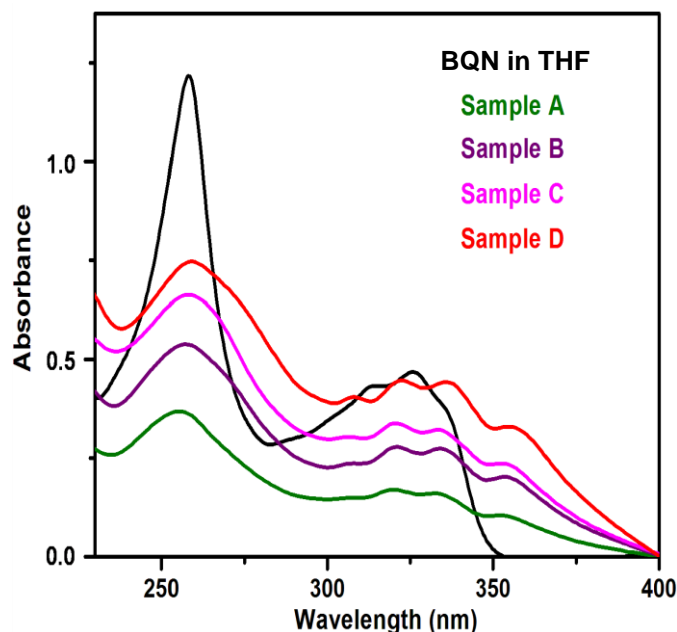


**Figure 8.1:** UV-Vis absorption spectra of (i) 300 $\mu$ M BQN in THF, (ii) 100 $\mu$ M BQN (Sample A), (iii) 200 $\mu$ M BQN (Sample B), (iv) 300 $\mu$ M BQN (Sample C), (v) 500 $\mu$ M BQN (Sample D).

### 8.3.2. Aggregation induced emission enhancement effect: 2,2' biquinoline

(BQN) is soluble in THF and shows a very weak PL spectra with maximum at 388 nm. The fluorescence is largely intensified in presence of non-solvent *i.e.* water. PL intensity is slowly increased upon addition of 60% water and then increased sharply with further increase of water percentage (Fig.8.2a). Images of solutions containing BQN in THF and BQN hydrosol (99% vol of water) under UV excitation are shown in the inset of Fig.8.2a. The change in color from colorless (BQN in THF) to deep blue (BQN hydrosol) suggests the AIEE property of BQN. Careful inspection of PL spectra reveals that a small red shift of peak  $\sim$ 412 nm is observed when a small amount of water *i.e.* up to 20% water is added into the THF solution of BQN but the emission spectrum is shifted to blue when water content exceeds 20%. The emission maxima of BQN hydrosol (99% water) show nearly  $\sim$ 16 nm blue shift compare to hydrosol in 20% water (Fig.8.2b).

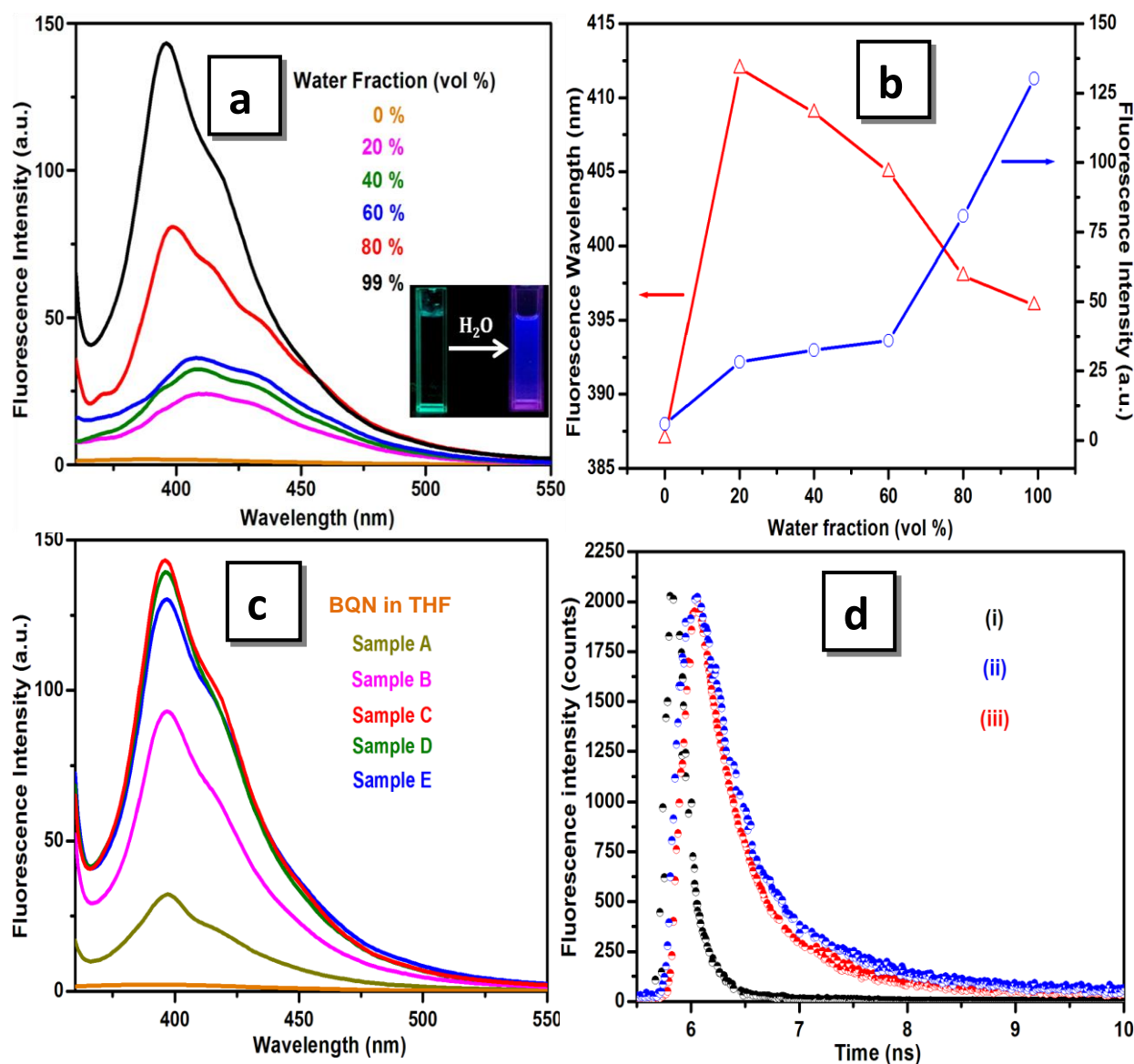


Figure 8.2: (a) Emission spectra of BQN (300 μM) in (i) 0% water (BQN in THF), (ii) 20% water, (iii) 40% water, (iv) 60% water, (v) 80% water and (vi) 99% water.  $\lambda_{ex}$ : 350 nm.

Insets: Images of BQN (0% and 99% H<sub>2</sub>O) under 367 nm illumination. (b) Plot of maximum emission wavelength ( $\lambda_{em}$ ) and intensity of BQN hydrosol prepared using different volume fraction of THF/water mixtures; BQN concentration: 300 μM and  $\lambda_{ex}$ : 350 nm. (c) PL spectra of (i) Sample A, (ii) Sample B, (iii) Sample C, (iv) Sample D (v) Sample E and (vi) 300 μM BQN in THF;  $\lambda_{ex}$ : 350 nm. (d) Fluorescence decay profile of spectra (i) Lamp, (ii) Sample A (100 μM BQN), (iii) Sample C (300 μM BQN) at ( $\lambda_{em}$ : 396 nm).

Excitation wavelength: 370 nm.

In aggregated BQN, surface molecules are more flexible and facing towards polar water, whereas the molecules within the core of the aggregates are more rigid and facing non polar environment. In relatively low water content (20%) small aggregated nuclei from BQN

are formed for a fixed BQN concentration compare to higher water content (99%). So the number of surface molecules decreases with increasing the percentage of water in THF/water mixture. The increasing numbers of molecules facing the non-polar inner core of the aggregates are responsible for the blue shift of emission at high water content.

Adding different volume of 0.05M BQN in THF into 5ml of water, it has been observed that the PL intensity increases with increasing concentration of BQN, reaches a maximum value for Sample C (300 $\mu$ M BQN). Further increase of BQN concentration results gradual decrease of PL intensity keeping the peak position unaltered (Fig.8.2c). Thus 300 $\mu$ M is the optimum concentration of BQN in solution below which aggregation of BQN occurs in such a way that it can form emissive crystalline aggregates. But above this concentration molecules start to aggregate in random fashion that break the regular crystalline structures and makes it less emissive one.

In order to understand the nature of aggregation, we carried out time resolved fluorescence study of aggregated BQN hydrosols with excitation at 370 nm and emissions were measured at 396 nm. Decay profile of BQN hydrosols (Sample A and Sample C) are shown in Fig.8.2d. Fluorescence decay profiles of aggregated BQN hydrosols having reasonably higher emission intensity are fitted with bi-exponential decay. The observed components of lifetime lie within  $\sim$ 0.3ns and  $\sim$ 1.2ns respectively (table 8.1).

The weight percentage of shorter component ( $\sim$ 0.3ns) increases and the longer component ( $\sim$ 1.2ns) decreases with the increasing size of the aggregates. BQN molecules present within the aggregates are facing two types of micro environments *i.e.* surface bound BQN and BQN within the inner core of the microcrystals. The excited inner core BQN molecules behave like Frenkel excitons whose fluorescence lifetime ( $\sim$ 0.3ns) is much shorter than the surface bound molecules. Now with increasing size of the aggregates, the number of

surface bound BQN decreases and hence the weight percentage of the longer component decreases.

**Table 8.1: Fluorescence life time of aggregated hydrosols of 2,2' biquinoline (BQN) (Sample A and Sample C).**

Sample	$\tau_1$ (ns)	Contribution (%)	$\tau_2$ (ns)	Contribution (%)	$\chi^2$
Sample A ( $\lambda_{\text{emi}}$ : 396 nm)	0.270	89.34	1.02	10.66	1.01
Sample C ( $\lambda_{\text{emi}}$ : 396 nm)	0.291	96.75	1.34	3.25	1.05

**8.3.3. SEM and Optical Microscopic study:** SEM images of Sample C, D and E are studied and the gradual changes in morphology as shown in Fig.8.3a-c are observed. Rod shaped morphology is obtained at a very low concentration of BQN (Sample C). A regular two dimensional growth is observed from micro rod to microplates with the increasing concentration of BQN.

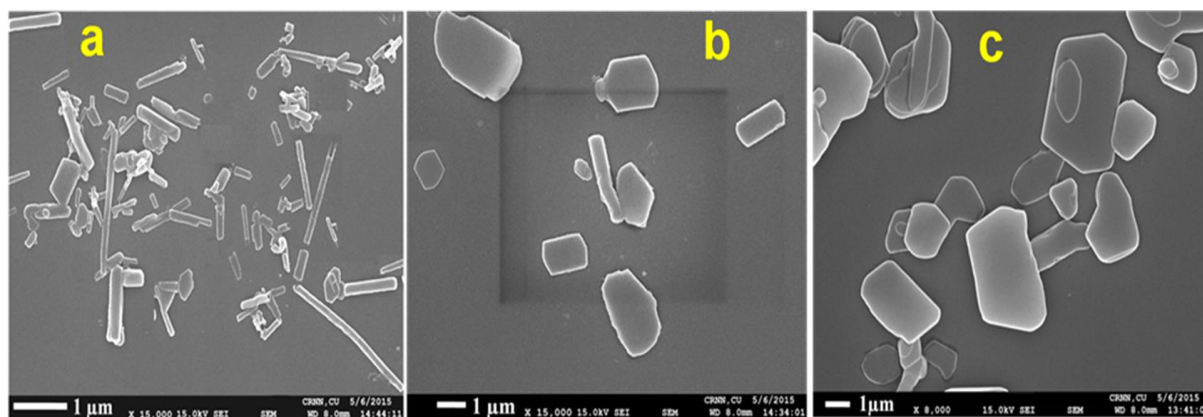


**Figure 8.3: SEM images of BQN microstructures at different BQN concentration (a) 300 $\mu$ M (Sample C) (b) 500 $\mu$ M (Sample D) and (c) 1000 $\mu$ M (Sample E).**

Fig.8.4a shows the fluorescence microscopic images of Sample E. The sizes of other samples are too small to be detected within the resolution of our optical microscope. The morphology of the aggregated crystals of Sample E is rectangular plate shaped. Fluorescence



microscopic images of the crystals under UV excitation show distinct blue emission from the surface of crystals (Fig.8.4a). This color is also similar to the observed color of hydrosol shown in the inset of Fig.8.2a. Dark field's view of Sample E using polarizer and analyzer assembly shows different colors depending on the direction of incident radiation and it reveals the anisotropic nature as well as birefringent property of the microcrystals (Fig.8.4b).

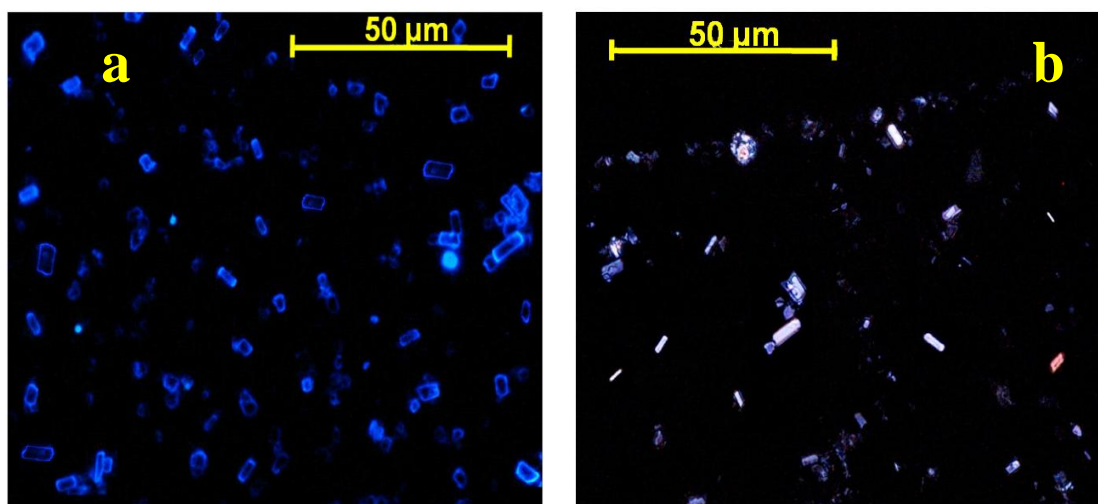


**Figure 8.4: (a) Fluorescence microscopic images of BQN microcrystals of Sample E (1000µM); under UV excitation, (b) Polarized microscopic images of BQN microcrystals of Sample E (1000µM).**

## 8.4. Proton and Zinc(II) sensor:

**8.4.1. Proton induced Photophysical Properties:** Protons play critical roles in many cellular events such as cell growth apoptosis, calcium regulation, endocytosis, etc. Thus, protons have become one of the most important sensing targets to be detected among the other species in vivo.

UV-Vis absorption spectra of BQN hydrosol at different pH are shown in Fig.8.5a. With the increase of pH from ~3 to ~10, the absorption spectra of aggregated BQN hydrosol exhibit similar spectral bands like the aggregated one but at pH < 3, a new red shifted broad band at ~354 nm is observed (Fig.8.5a) instead of structured band. This broad nature of band suggests the formation of protonated charge transfer species in the ground state. In case of

fluorescence spectra, no detectable change compare to aggregated hydrosol is observed at  $\text{pH} > 3$ . But at lower  $\text{pH} (< 3)$  the band at  $\sim 396$  nm of the aggregated BQN hydrosol decreases and a new red shifted intense emission band at  $\sim 497$  nm is appeared (Fig.8.5b).

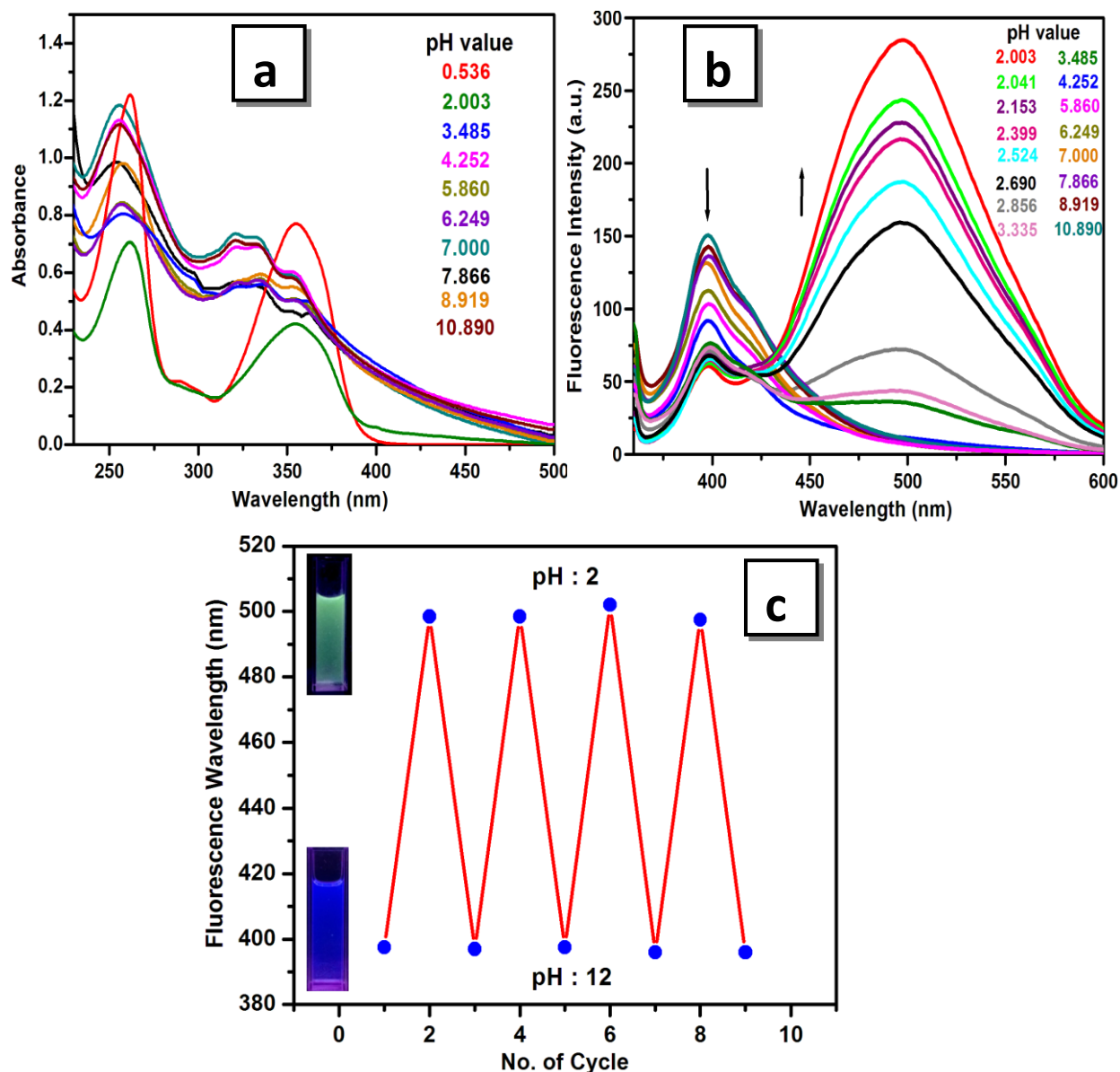


**Figure 8.5:** (a) UV-Vis absorption spectra of BQN hydrosol ( $300\mu\text{M}$ ) in THF/water mixture (1:99 v/v) at different pH of the medium ( $\text{pH} \sim 1.0-11.0$ ). (b) PL spectra of BQN hydrosol ( $300\mu\text{M}$ ) in THF/water mixture (1:99 v/v) at different pH of the medium ( $\text{pH} \sim 2.0-11.0$ ).  $\lambda_{\text{ex}}$ : 350 nm. (c) Reversible switching of the emission wavelength of BQN by repeated addition of acid and alkali to the medium. pH dependent color shift from blue to yellowish green in presence of  $\text{H}^+$  ion in the medium under 367 nm illumination.

This proton sensitivity at lower pH range also exhibit a distinct change in color from deep blue to yellowish green under UV excitation (Fig.8.5c). The two nitrogen atoms of BQN are equivalent *i.e* facing identical chemical environment. At high proton concentration, these two electrons rich nitrogen centers are protonated. This protonated BQN is ionic and is soluble in polar water. Reversibility of proton sensing of BQN hydrosol is studied by changing the pH of the medium from pH=2 to pH=12. The turn on and off of the 497 nm band is observed as the pH of the medium changes from pH=2 to pH=12 and vice versa (Fig.8.5c).

**8.4.2. Fluorogenic Zn(II) sensing:** Recent progress in the area of fluorophore-based chemosensors has contributed significantly to the development of a variety of probes based on quinoline, dansyl, anthracene and fluorescein for the sensing of  $Zn^{2+}$ [22-28]. Since quinoline is well known for its metal chelating ability, we have used BQN as selective sensing of metal ion. BQN itself is insoluble in water, so BQN hydrosol has been used for selective detection of metal ions in water. Since metal ions are water soluble, the development of water soluble fluorescent probe like BQN hydrosol will be highly useful in the real world applications.

Fig.8.6a displays the absorption spectra of aggregated BQN taken in the course of titration with  $Zn^{2+}$ . Addition of  $Zn^{2+}$  showed significant decrease of the absorption band (306 nm-352 nm) of aggregated BQN hydrosol with the concomitant formation of a new red-shifted absorption band at 357 nm indicating formation of ground state complexation with BQN. The 357 nm band corresponds to the intramolecular charge transfer from nitrogen center to the phenyl ring of molecule as mentioned in the section 8.3.1. This charge transfer is possible when BQN takes its planar conformation. The long tail absorption (380-500 nm) in Fig.8.6a arises due to Mie's scattering of light by the particles in the hydrosol. Absorbance of

this long tail part decreases with increasing concentration of  $Zn^{2+}$  and the overall spectra become sharper. On the other hand, the milky solution of BQN hydrosol become clear upon gradual addition of  $Zn^{2+}$  in the hydrosol. These observations suggest that  $Zn^{2+}$ -BQN complex is soluble in water. The overall planarization of BQN upon complexation with  $Zn^{2+}$  is responsible for the increased absorbance of the charge transfer band appeared at  $\sim 357$  nm. However, titration with other metal ions do not show much change in the absorption properties of BQN hydrosol.

The emission spectra of BQN hydrosol upon titration with  $Zn^{2+}$  are shown in Fig.8.6b. The hydrophobic BQN molecules form aggregates in aqueous solution and exhibit emission with maximum at 396 nm. Addition of  $Zn^{2+}$  ions into the solution gradually red-shifts the spectrum and show broad band with increasing intensity having peak maxima at  $\sim 450$  nm. The fluorescence enhancement is highly desirable, because many reported fluorescent chemosensors generally undergo fluorescence quenching upon binding with this metal ions through energy or electron transfer mechanism [29]. Selective fluorescence enhancement by  $Zn^{2+}$  could be due to restriction of free rotation of BQN by forming chelate with zinc ion. Biquinoline is a well known bidentate chelating ligand with strong affinity towards electropositive metal ion to form stable complexes. Among these, the complex with zinc ion is highly emissive and moreover a color change of the hydrosol upon addition of zinc ion from blue to sky blue under UV light illumination is shown in the inset of Fig.8.6b.

In order to find out the binding stoichiometry of BQN and zinc ion, Job's plot has been done with the increasing mole fraction of added metal ion in BQN hydrosol (Fig.8.6c). The maxima of the plot at  $\sim 0.334$  suggests the 2:1 binding ratio between BQN and  $Zn^{2+}$  ion.

Fluorescence intensity at 450 nm increases with the increasing concentration of  $Zn^{2+}$ , reaches a maximum value when all the BQN molecules are eached out from the aggregated hydrosol to make complex with the added  $Zn^{2+}$  (Fig.8.6d). This indicates that saturation is

reached at higher metal concentration. Furthermore, to confirm the higher selectivity of BQN toward  $Zn^{2+}$ , we determined the dissociation constant of complex. Considering a 2:1 complex formation, the dissociation constant ( $K_d$ ) was calculated on the basis of the titration curve of the sensor BQN with  $Zn^{2+}$  by nonlinear curve fitting of the emission intensity at 450 nm (Fig.8.6d). The  $K_d$  value of complex was estimated as  $\sim 25.8\mu M$  ( $R^2 = 0.994$ ), which clearly demonstrates the potent binding affinity of BQN toward  $Zn^{2+}$  ions.

The pH effect on the fluorescence intensity of aggregated BQN in the presence of  $Zn^{2+}$  at 450 nm were determined in the pH range 2.0 to 8.0 with a fixed concentration (150  $\mu M$ ) of  $Zn^{2+}$  (fig.8.7a). As the pH of the solution is varied from  $\sim 3.8$  to 2.0, a small decrease in PL intensity at 450 nm is observed and this is due to the protonation of nitrogen center of BQN. But a constant intensity is exhibited from this system between pH  $\sim 4.2$  to 7.8. It indicates that BQN possess the highest sensing ability under biological pH range.

The selective binding ability of BQN with  $Zn^{2+}$  over other metal ions was investigated by measuring the fluorescence of BQN hydrosol with other competitive cations having same concentration. No significant changes of fluorescence of the aggregated hydrosol were observed when  $Cd^{2+}$ ,  $Mn^{2+}$ ,  $Co^{2+}$ ,  $Pb^{2+}$ ,  $Mg^{2+}$ ,  $K^+$ ,  $Na^+$ ,  $Ca^{2+}$  were added to the hydrosol (Fig.8.7b). On the other hand, addition of  $Ag^+$ ,  $Ni^{2+}$ ,  $Cu^{2+}$ ,  $Hg^{2+}$  to the hydrosol cause quenching of emission intensity and this is due to chelation induced fluorescence quenching (CHEQ) [24]. On the basis of the above observations, the selective recognition of  $Zn^{2+}$  by the BQN hydrosol over a number of other cations is indicative of the fact that the bidentate ligand better satisfies the geometrical requirements of a tetrahedral  $Zn^{2+}$  complex. From the mechanistic viewpoint, since zinc ion has fully occupied d-orbital, it does not lead to metal to ligand charge transfer (MLCT) or ligand to metal charge transfer (LMCT) emission.

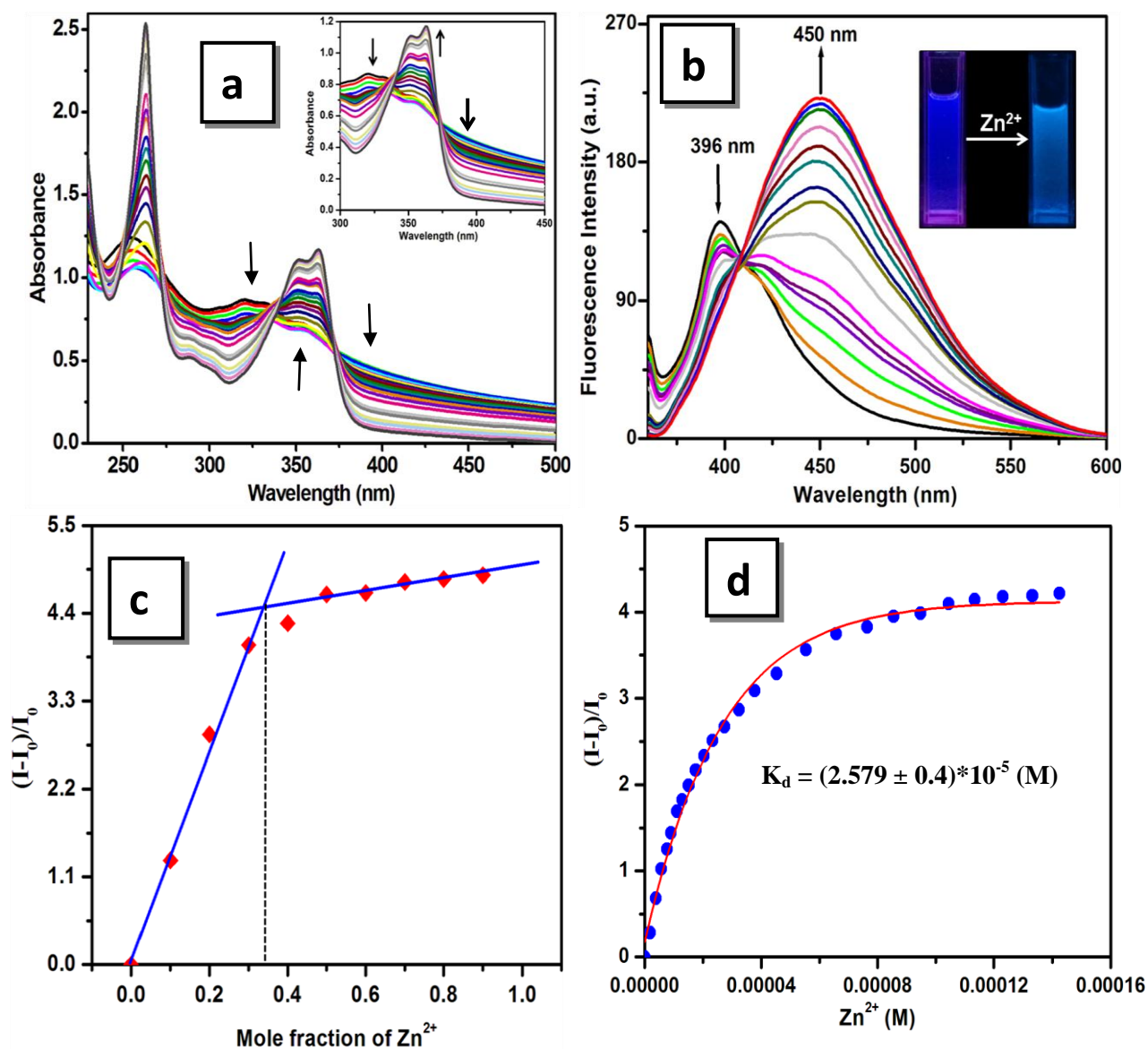
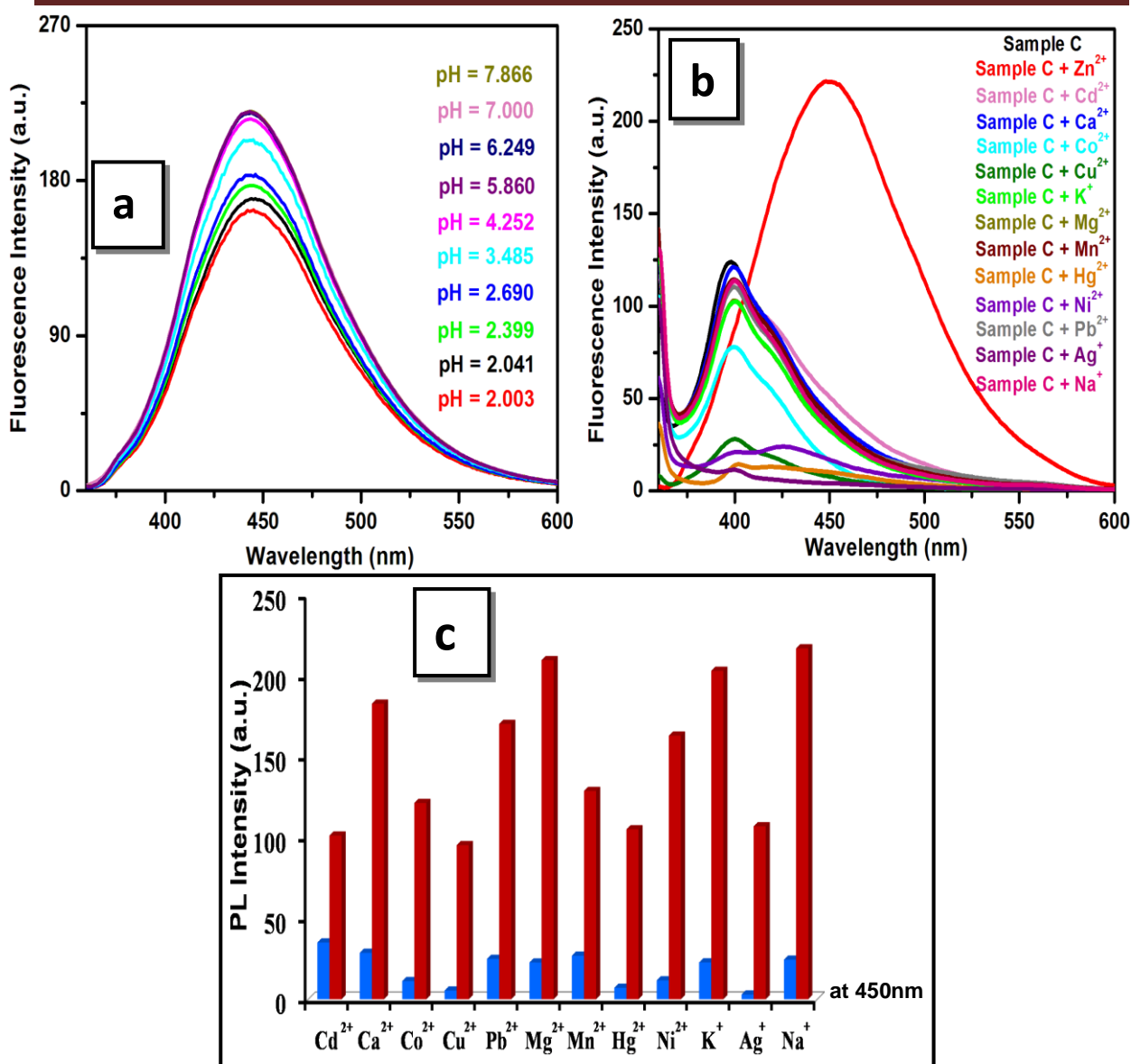


Figure 8.6: (a) UV-vis absorption spectra of BQN (300 μM) in THF/Water (1:99 v/v) mixture upon addition of Zn<sup>2+</sup> ion (0 μM - 150 μM). (b) Fluorescence titration spectra of BQN (300 μM) in THF/water (1:99 v/v) upon addition of Zn<sup>2+</sup> ion (0 μM - 150 μM).  $\lambda_{ex} = 350$  nm. Arrows indicate the direction of spectral change with increasing Zn<sup>2+</sup>. Inset: Shows the visible change of emission color in absence and in presence of zinc ion under 367 nm illumination. (c) Job's plot for the determination of stoichiometry of Zn<sup>2+</sup> and BQN in the complex. (d) Plot of 450 nm emission of BQN-Zn<sup>2+</sup> complex as a function of the Zn<sup>2+</sup> concentration:  $\lambda_{ex} = 350$  nm. Determination of dissociation constant ( $K_d$ ) by nonlinear fit of the curve.



**Figure 8.7:** (a) Fluorescence response of BQN (300 μM) in THF/H<sub>2</sub>O (1:99 v/v) mixture in presence and in absence of Zn<sup>2+</sup> (150 μM) at different pH. (b) Fluorescence spectra of BQN (300 μM) hydrosol in presence of different metal ions (Zn<sup>2+</sup>, Cd<sup>2+</sup>, Ca<sup>2+</sup>, Co<sup>2+</sup>, Cu<sup>2+</sup>, K<sup>+</sup>, Mg<sup>2+</sup>, Hg<sup>2+</sup>, Mn<sup>2+</sup>, Ni<sup>2+</sup>, Pb<sup>2+</sup>, Ag<sup>+</sup>, Na<sup>+</sup>) of concentration 100 μM.  $\lambda_{\text{ex}} = 350 \text{ nm}$ . (c) The blue bars represent the emission intensity of Sample C in the presence of other cations (100 μM). The red bars represent the emission intensity upon subsequent addition of 100 μM of Zn<sup>2+</sup> to the above solution. (All the emission spectra were taken with  $\lambda_{\text{ex}}: 350 \text{ nm}$  and  $\lambda_{\text{em}}: 450 \text{ nm}$ ).

Thus ion binding leads to a red shift in absorption and emission maxima in response to planarization of the biquinoline unit, extending the effective conjugation length, in conjunction with perturbation of the electronic system. Although many transition metals

induce such response, a selective fluorescence response to  $\text{Zn}^{2+}$  has been attributed to the closed-shell  $d^{10}$  configuration of  $\text{Zn}^{2+}$  and its diamagnetic property; thus fluorophore-appended ligands tend to remain emissive. In contrast, other metal ions are likely to be encountered in the environment are paramagnetic and typically efficient emission quenchers. Heavier  $d^{10}$  ions ( $\text{Hg}^{2+}$ ) also tend to yield less emissive complexes due to quenching via the classic heavy atom effect.

In order to check the interference of other metal ions we have compared the ratiometric emission intensity changes of BQN hydrosol in presence of  $\text{Zn}^{2+}$  as well as equivalent amount of other metal ions (Fig.8.7c). As shown in Fig.8.7c, all competitive cations including more electrophilic competitors such as  $\text{Hg}^{2+}$ ,  $\text{Cd}^{2+}$  and  $\text{Ag}^+$  caused no obvious changes. Therefore, the BQN hydrosol shows selective sensing property towards  $\text{Zn}^{2+}$  ions in water.

**8.4.3. Time Resolved Emission Study:** In order to understand the mechanism of ratiometric emission changes of hydrosol in acidic medium, time resolved emission study at the two emission bands (396 nm and 497 nm) are carried out. Time resolved emission data at 396 nm are fitted with bi-exponential decay and the measured emission lifetimes are 0.3ns (41%) and 3.0ns (59%) respectively (Fig.8.8a). The faster decay component (0.3ns) is due to charge transfer exciton (Frankel exciton) within the aggregated structure and the longer one (3.0ns) arises from the excited protonated BQN species. On the other hand the decay at 497 nm is fitted with single exponential decay having emission lifetime 3.0ns (100%) (Fig.8.8b). Thus the emission band at 497 nm arises solely from the excited protonated BQN.

In presence of zinc ion BQN undergoes a different mode of attachment with metal at the same time a change of conformation also exhibited by it. Metal induced emission decay at ~450 nm is fitted with bi exponential decay curve and the components are 1.05ns (95.32%)



and 3.4ns (4.68%) (Fig.8.8b). Components corresponds to the aggregated BQN is completely absent indicating that aggregated BQN have broken down in presence of zinc ion. Incorporation of zinc, the major contributed component (1.05ns) is resembled with that of the component present in aggregated BQN as monomer part. This component arises from the decay of excited intra ligand charge transfer state of fully conjugated BQN molecule. The second smaller contributed component at~3.4ns is due to the existence of interligand charge transfer form nitrogen centre of BQN to the phenyl framework of another BQN moiety through metal centre. So emission is enhanced only due to the metal induced planarization of fully conjugated BQN.

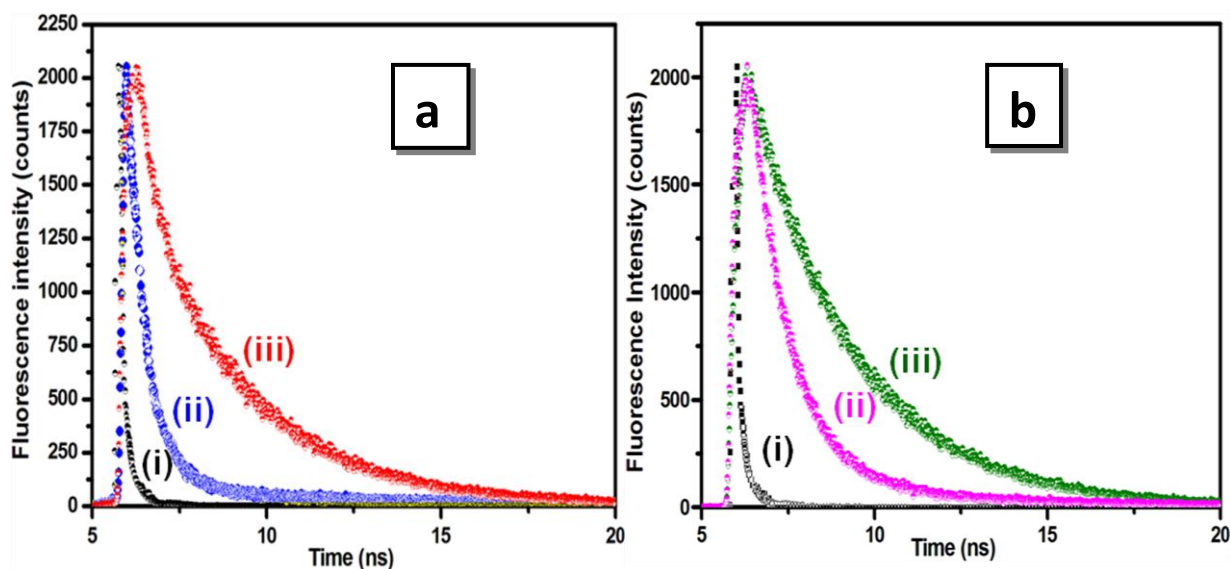


**Figure 8.8:** Fluorescence decay profile of (a) (i) Lamp, (ii) Sample C (300 $\mu$ M BQN) and (iii) Sample C (300 $\mu$ M BQN) in pH~2 medium at ( $\lambda_{em}$ : 396 nm). (b) (i) Lamp, (ii) Sample C (300 $\mu$ M BQN) in presence of 150 $\mu$ M Zn<sup>2+</sup> ion at ( $\lambda_{em}$ : 450 nm), (iii) Sample C (300 $\mu$ M BQN) in pH~2 medium at ( $\lambda_{em}$ : 497 nm). Excitation wavelength: 370 nm.

#### 8.4.4. Density Functional Theory (DFT) based computational study:

Ground state energy optimization as a function of dihedral angle between the two quinoline planes using DFT based computation with B3LYP hybrid functional and 6-31G(d,p) basis shows two stable conformers of BQN *i.e.* one having the dihedral angle~30<sup>0</sup> (cis) and the other one at 180<sup>0</sup> (trans planar) (Fig.8.9a). Dipole moment of the cis and trans conformers are

2.629 D and 0.003 D respectively. The polar cis conformation of BQN partly introduces ICT character in this molecule. On the other hand excited state geometry optimization shows that the dihedral angle of cis ( $30^{\circ}$ ) conformer changes to  $0^{\circ}$  and that of trans ( $180^{\circ}$ ) remain unchanged. Though the trans ( $180^{\circ}$ ) geometry of BQN is more stable, the free rotation makes it non emissive in molecular state. But in the hydrosol, aggregation of this molecule restricts the free rotation around its single bond and makes it AIEE active. This restricted intramolecular rotation (RIR) is the main reason of AIEE effect of BQN.

The AIEE active BQN can exhibit dual sensitivity towards proton and zinc ion. In presence of proton, the nitrogen centre of this molecule is protonated and as a result, proton triggered emission is observed. Geometry optimization shows that the dihedral angle of trans ( $180^{\circ}$ ) conformer changes to  $140^{\circ}$  upon protonation (Fig.8.9b) and the dipole moment of the protonated species changes to 0.59D compare to 0.003 D of the unprotonated species. Increased dipole moment of the protonated BQN, suggests the existence of strong charge transfer character in its twisted form. On the other hand, computation of electronic charge density of the protonated BQN shows that the electronic charge is mainly localized at benzene ring of BQN in its HOMO and the charge density drifted towards another protonated nitrogen centre of quinoline ring in its LUMO (Fig.8.9c). This signifies the existence of charge transfer character of the protonated BQN.

Again, the ground state optimized structure of 1:2 complex of  $Zn^{2+}$  and BQN shows that the two BQN units attain cis planer conformation upon complexation with  $Zn^{2+}$  ion (Fig.8.9d) to form a tetrahedral shaped geometry. Comparing the geometry of both protonated BQN and BQN- $Zn^{2+}$  complex, it is observed that the emission from protonated BQN is red shifted due to twisted intramolecular charge transfer character in trans form and bathochromic shift from BQN- $Zn^{2+}$  complex is due to the metal induced enhanced conjugation of this molecule in cis form which is absent in its molecular state due to steric

effects of BQN. But zinc ion forcefully rotates BQN to its cis form in its ground state during complexation.

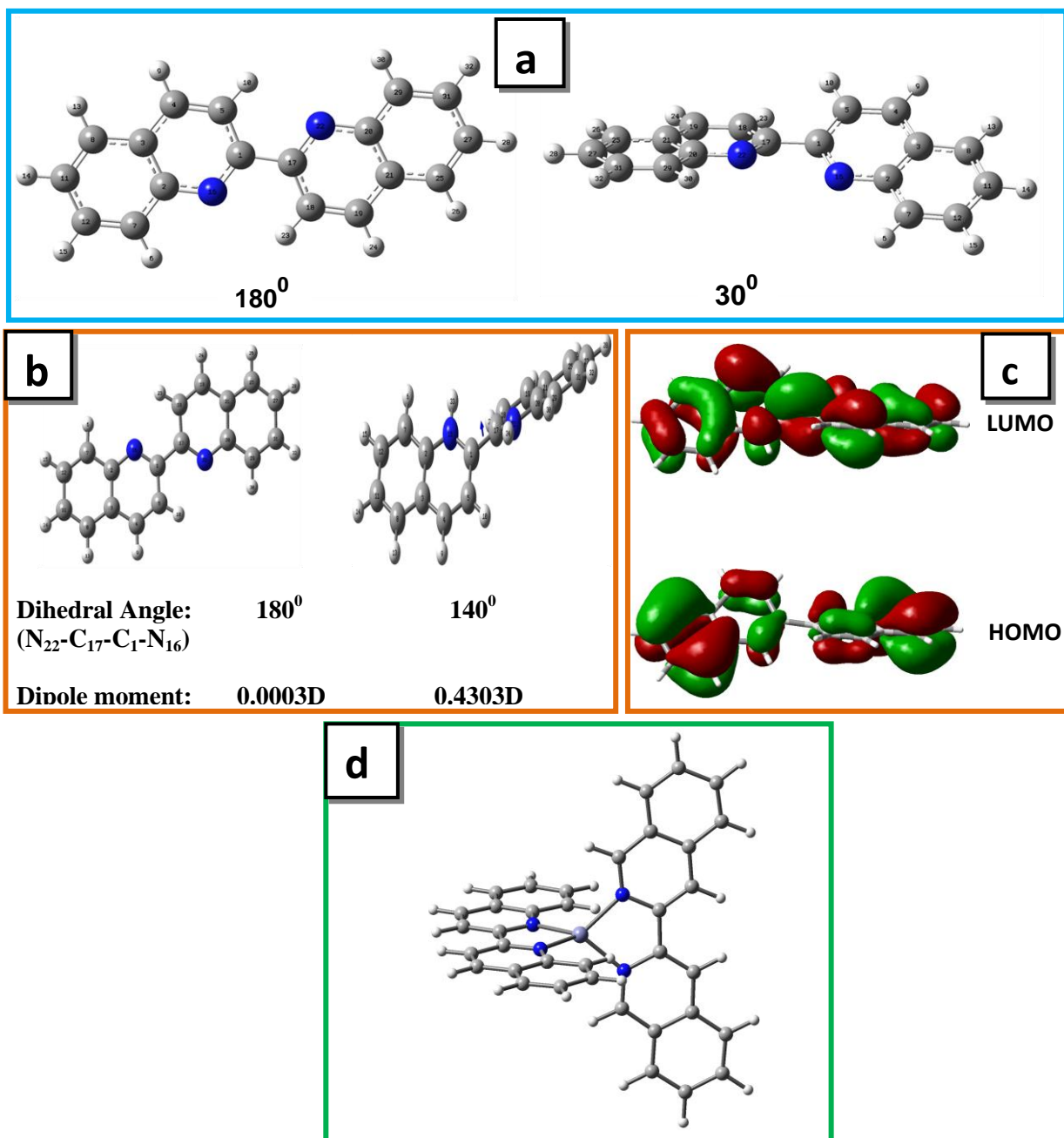


Figure 8.9: (a) Ground state Optimized geometry of two conformers of BQN ( $180^{\circ}$  and  $30^{\circ}$ ) using DFT based method with B3LYP/6-31G(d,p) basis sets. (b) Optimized geometry with dihedral angle and dipole moment (c) HOMO-LUMO electronic distribution of BQN and Protonated BQN in ground state. (d) Optimized structure of BQN-Zn<sup>2+</sup> complex (2:1) using DFT based method with B3LYP/6-31G(d,p) basis sets.

## 8.5. Conclusion:

In summary, a new low dimensional material of BQN is introduced and its optical sensing properties are investigated. Though BQN is weakly emissive in its molecular state, the aggregated hydrosol is highly emissive, demonstrating a novel phenomenon of aggregation induced emission enhancement (AIEE). On the other hand, optical output of aggregated BQN is switched on by  $H^+$  and  $Zn^{2+}$  ion. Proton sensitivity of this molecule changes its color from blue to yellowish green with a large red shift ( $\sim 101$  nm) in emission spectra due to the introduction of charge transfer character in its protonated form. A red shift in emission maxima of BQN with fluorescence enhancement in presence of  $Zn^{2+}$  has been explained due to the metal induced planarization of BQN. The Job's plot indicates the 2:1 binding mode complexation between BQN and  $Zn^{2+}$ . The selective recognition of this AIEE active BQN towards proton and zinc ion through skeleton modification is another example for this rare combination (metal ion / proton) of ratiometric fluorescent probe. Again the sensing of water soluble metal ions using water soluble fluorescent probes is highly demanding because most of the fluorescent probes are insoluble or weakly soluble in water. Therefore our investigation is one step forward in searching for a water soluble fluorescent probe for sensing water soluble metal ions as well as proton concentration.

## References:

1. H. Ma, C. He, X. Li, O. Ablikim, S. Zhang and M. Zhang, *Sens. Actuators B: Chem.*, 230, **2016**, 746.
2. X. Lou, Y. Zhuang, X. Zuo, Y. Jia, Y. Hong, X. Min, Z. Zhang, X. Xu, N. Liu, F. Xia and B. Z. Tang, *Anal. Chem.*, 87, **2015**, 6822.
3. T. Ueno and T. Nagano, *Nat. Methods* 8, **2011**, 642.
4. S.K. Kim and J. L. Sessler, *Chem. Soc. Rev.* 39, **2010**, 3784.
5. H. Komatsu, T. Miki, D. Citterio, T. Kubota, Y. Shindo, Y. Kitamura, K. Oka and K. Suzuki, *J. Am. Chem. Soc.* 127, **2005**, 10798.
6. M. Dong, Y. Peng, Y.-M. Dong, N. Tang and Y. W. Wang, *Org. Lett.* 14, **2012**, 130.
7. Y.M. Dong, Y. Peng, M. Dong and Y.W. Wang, *J. Org. Chem.* 76, **2011**, 6962.
8. M. Dong, Y.W. Wang and Y. Peng, *Org. Lett.* 12, **2010**, 5310.
9. W. Mertz, *Science* 213, **1981**, 4514.
10. C. J. Frederickson, J.Y. Koh and A. I. Bush, *Nat. Rev. Neurosci.*, 6, **2005**, 449.
11. S.C. Burdette and S. J. Lippard, *Proc. Natl. Acad. Sci. U.S.A.* 100, **2003**, 3605.
12. C. F. Walker and R. E. Black, *Annu. Rev. Nutr.* 24, **2004**, 255.
13. J. Y. Koh, S. W. Suh, B. J. Gwag, Y. Y. He, C. Y. Hsu and C. W. Choi, *Science* 272, **1996**, 1013.
14. A. I. Bush, W. H. Pettingell, G. Multhaup, M. Paradis, J. P. Vonsattel, J. F. Gusella, K. Beyreuther, C. L. Masters and R. E. Tanzi, *Science*, 265, **1994**, 1464.
15. M. Mahato, D. Dey, S. Pal, S. Saha, A. Ghosh, K. Harms and H. P. Nayek, *RSC Adv.* 4, **2014**, 64725.
16. A. J. Zuccherro, J. N. Wilson and U. H. F. Bunz, *J. Am. Chem. Soc.* 128, **2006**, 11872.
17. Z. Yang, W. Qin, J. W. Y. Lam, S. Chen, H. H. Y. Sung, I. D. Williams and B. Z. Tang, *Chem. Sci.* 4, **2013**, 3725.
18. R. C. Smith, A. G. Tennyson and S. J. Lippard, *Inorg. Chem.*, 45, **2006**, 6222.
19. A. Ajayaghosh, P. Carol and S. Sreejith, *J. Am. Chem. Soc.*, 127, **2005**, 14962.
20. L. Tian, W. Zhang, B. Yang, P. Lu, M. Zhang, D. Lu, Y. Ma and J. Shen, *J. Phys. Chem. B*, 109, **2005**, 6944.
21. D. Pucci, A. Crispini, M. Ghedini, E. I. Szerb and M. L. Deda, *Dalton Trans.*, 40, **2011**, 4614.
22. D. A. Pearce, N. Jotterand, I. S. Carrico and B. Imperiali, *J. Am. Chem. Soc.* 123, **2001**, 5160.
23. T. Koike, T. Watanabe, S. Aoki, E. Kimura and M. Shiro, *J. Am. Chem. Soc.* 118, **1996**, 12696.
24. R. B. Thompson, B. P. Maliwal, V. L. Felliccia, C. A. Fierke and K. McCall, *Anal. Chem.* 70, **1998**, 4717.
25. T. Hirano, K. Kikuchi, Y. Urano, T. Higushi and T. Nagano, *J. Am. Chem. Soc.* 122, **2000**, 12399.
26. G. K. Walkup, S. C. Burdette, S. J. Lippard and R. Y. Tsien, *J. Am. Chem. Soc.* 122, **2000**, 5644.
27. K. R. Gee, Z.L. Zhou, W.J. Qian and R. Kennedy, *J. Am. Chem. Soc.* 124, **2002**, 776.
28. S. C. Burdette, C. J. Frederickson, W. Bu and S. J. Lippard, *J. Am. Chem. Soc.* 125, **2003**, 1778.
29. A. W. Varnes, R. B. Dodson and E. L. Wehry, *J. Am. Chem. Soc.* 94, **1972**, 946.



## List of Publications

1. \***P. Mazumdar**, D. Das, G. P. Sahoo, G. S. Morán and A. Misra, Aggregation induced emission enhancement from Bathophenanthroline microstructures and its potential use as sensor of mercury ions in water, [\*Phys. Chem. Chem. Phys.\*](#), 2014, 16, 6283- 6293.
2. \***P. Mazumdar**, D. Das, G. P. Sahoo, G. S. Morán and A. Misra, Aggregation induced emission enhancement of 4,4'-bis(diethylamino)benzophenone with an exceptionally large blue shift and its potential use as glucose sensor, [\*Phys. Chem. Chem. Phys.\*](#), 2015, 17, 3343- 3354.
3. S. Ash, H. Beg, **P. Mazumdar**, G. S. Morán and A. Misra, Polarizability, hardness and Electrophilicity as global descriptors for intramolecular proton transfer reaction path, [\*Comp. Theor. Chem.\*](#), 2014, 1031, 50-55.
4. D. Das, G. P. Sahoo, **P. Mazumdar**, A. Maity, D. Chattopadhyay, G. S. Morán and A. Misra, Morphology directing synthesis of benzo[a]pyrene microstructures and their photo physical Properties, [\*J. Mol. Liq.\*](#), 2015, 206, 47-55.
5. \***P. Mazumdar**, S. Maity, M. Shyamal. D. Das, G. P. Sahoo and A. Misra, Proton triggered emission and selective sensing of picric acid by the fluorescent aggregates of 6,7-dimethyl-2,3-bis-(2-pyridyl)-quinoxaline, [\*Phys. Chem. Chem. Phys.\*](#), 2016, 18, 7055-7067.
6. S. Maity, **P. Mazumdar**, M. Shyamal, G. P. Sahoo and A. Misra, Crystal induced phosphorescence From Benz(a)anthracene microcrystals at room temperature, [\*Spectrochim. Acta Mol. Biomol.\*](#) 2016, 157, 61-68.
7. M. Shyamal, **P. Mazumdar**, S. Maity, G. P. Sahoo, G. S. Moran and A. Misra, Pyrene Scaffold as Real-Time Fluorescent Turn-on Chemosensor for Selective Detection of Trace-Level Al(III) and Its Aggregation-Induced Emission Enhancement, [\*J. Phys. Chem. A\*](#), 2016, 120, 210-220.

8. D. Das, **P. Mazumdar**, A. Maity, S. Tripathy, S. Roy, D. Chattopadhyay and A. Misra, Aggregation induced emission from  $\alpha$ -naphthoflavone microstructures and its cyto-toxicity, [\*J. Photochem. Photobiol. B\*](#), 2016, 156, 1-10.
9. M. Shyamal, **P. Mazumdar**, S. Maity, S. Samanta, G. P. Sahoo and A. Misra, Highly Selective Turn-On Fluorogenic Chemosensor for Robust Quantification of Zn(II) Based on Aggregation Induced Emission Enhancement Feature, [\*ACS Sensors\*](#), 2016, 1, 739-747.
10. A. Maity, **P. Mazumdar**, S. Samanta, D. Das, M. Shyamal, G.P. Sahoo and A. Misra, Morphology directing synthesis of 1-aminopyrene microstructures and its super quenching effect towards nitro aromatics, [\*J. Mol. Liq.\*](#), 2016, 221, 358-367.
11. \***P. Mazumdar**, S. Maity, D. Das, S. Samanta, M. Shyamal and A. Misra, Proton Induced Green Emission from AIEE active 2,2' Biquinoline Hydrosol and its Selective Fluorescence Turn-on Sensing Property towards Zn<sup>2+</sup> ion in Water, [\*Sens. Actuator B-Chem\*](#), 2016, (Communicated).

---

\* These are included in this thesis.